Coulomb Explosion Imaging and Covariance Analysis of Concurrent Fragmentation Mechanisms

Tiffany Rae Walmsley

Jesus College
University of Oxford

A thesis submitted for the degree of Doctor of Philosophy

Hilary 2024

Abstract

This thesis uses Coulomb explosion imaging and covariance analysis to characterise concurrent fragmentation processes generating identical sets of products via different reaction pathways, highlighting the potential of extending these methods to study the photochemistry of larger, more chemically relevant species than those that have previously been studied.

The photodissociation dynamics of CH_2I_2 at 202.5 nm were investigated using site-selective ionisation at the I 4d orbitals using photons of 95 eV. A concerted three-body dissociation process was assigned using charge transfer features and time-dependent covariance. Dynamic changes to the C-I internuclear distances and I-C-I bond angle were characterised, demonstrating the potential of Coulomb explosion imaging to simultaneously map potential energy surfaces of reaction dynamics along multiple degrees of freedom.

Site-selective ionisation of 1- and 2-iodopropane at the I 4d orbitals was carried out using photons of 95 eV. Modified three-dimensional momentum covariance analysis techniques were used to disentangle fragmentation processes generating the same sets of products as well as the individual steps of multi-step fragmentation mechanisms. Observable isomeric differences demonstrated the sensitivity of individual fragmentation processes, and the corresponding nuclear dynamics, to the geometry and charge distribution of the parent polycation species.

Iodobenzene was site-selectively ionised at the I 4d orbitals using photons of 120 eV, and valence-shell ionisation was also conducted using 800 nm laser pulses. Covariance analysis techniques were employed to analyse the range of products generated from stable and metastable phenyl cations and polycations, demonstrating how concurrent fragmentation processes generating long-lived species in lowly-charged cationic states can be characterised. Valence-shell ionisation could initially ionise more atomic sites than just iodine, leading to fragmentation channels that were not observed with site-selective, inner-shell ionisation. Both ionisation regimes generated similar sets of products but on different relative timescales due to initially populating different electronic excited states. Each ionisation regime results in many observable fragmentation processes, but photoelectron information is required to relate specific fragmentation channels to specific ionisation and charge generation/redistribution processes.

Coulomb Explosion Imaging and Covariance Analysis of Concurrent Fragmentation Mechanisms

Tiffany Rae Walmsley

Jesus College

University of Oxford

A thesis submitted for the degree of

Doctor of Philosophy

Hilary 2024

Acknowledgements

Firstly, thank you to my supervisor, Dr Michael Burt, for his support with and enthusiasm towards all aspects of this project. It has been a great privilege to be a part of the Burt research group, and I am incredibly grateful for all the advice and expertise you have given and all the opportunities I've had whilst here. I extend these thanks to Dr Emily Warne, whose perspective has been incredibly valuable and paramount to many aspects of this work. Infinite thanks for all of the lab, career, and general life wisdom you have passed on to me.

Thank you to the soon to be Dr's James Unwin and Joe McManus. Thank you for persevering and putting up with me over these last 4 years and laughing with/at me and all of my many mistakes. Thank you to all the past and present members of the Burt, Brouard, and Vallance groups, whose camaraderie has seen me through some very high highs and some very low lows. Special thanks to part two students Luke and Harvey for their work on the VMI ion optics used in the lab, Fabiola for her diligence and patience in the preliminary work on $C_2H_2Br_2$, and EPSRC Summer intern student Suzanne for going above and beyond with iodobenzene analysis.

A huge thanks to the many collaborators I have worked with throughout this DPhil. Thank you to all the staff at DESY, XFEL, and SACLA, without whom, most of this work would not exist, and to external collaborators at other institutions for their continued enthusiasm and involvement in post-beamtime analysis. I am especially grateful to Dr Ruaridh Forbes and Dr Felix Allum for facilitating so many opportunities to learn and grow over these years. I am incredibly thankful for the many hours spent talking through and building upon ideas each week with you and your inspiring motivation towards our work.

Thank you to my amazing friends who have cheered me along every step of the way. To the wonderful friends I have made at Jesus College through choir, the garden, and the MCR committee, thank you for the sense of community and belonging I found with you all. To Heon, Maya, and Agnes: what an enormous privilege it is to exist in the same timeline of the universe as you all. I am extremely grateful to have you in my life and to have been able to experience Oxford with you.

To my family, thank you for your unwavering support and belief in me. It has been hard to be far from you for so long, but thank you for always pushing me and encouraging me to follow what I love. Thank you for humouring me by

listening to my non-stop waffling and for the safe space you provide at home when I need a break. I love you all so!

To Daniel, I could not have done any of this if it wasn't for you. You continue to push me beyond what I think I can do, no matter how much I fight it. Thank you for everything you do and for being my rock through all of this, I love you.

Abstract

This thesis uses Coulomb explosion imaging and covariance analysis to characterise concurrent fragmentation processes generating identical sets of products via different reaction pathways, highlighting the potential of extending these methods to study the photochemistry of larger, more chemically relevant species than those that have previously been studied.

The photodissociation dynamics of CH_2I_2 at 202.5 nm were investigated using site-selective ionisation at the I 4d orbitals using photons of 95 eV. A concerted three-body dissociation process was assigned using charge transfer features and time-dependent covariance. Dynamic changes to the C-I internuclear distances and I-C-I bond angle were characterised, demonstrating the potential of Coulomb explosion imaging to simultaneously map potential energy surfaces of reaction dynamics along multiple degrees of freedom.

Site-selective ionisation of 1- and 2-iodopropane at the I 4d orbitals was carried out using photons of 95 eV. Modified three-dimensional momentum covariance analysis techniques were used to disentangle fragmentation processes generating the same sets of products as well as the individual steps of multi-step fragmentation mechanisms. Observable isomeric differences demonstrated the sensitivity of individual fragmentation processes, and the corresponding nuclear dynamics, to the geometry and charge distribution of the parent polycation species.

Iodobenzene was site-selectively ionised at the I 4d orbitals using photons of 120 eV, and valence-shell ionisation was also conducted using 800 nm laser pulses. Covariance analysis techniques were employed to analyse the range of products generated from stable and metastable phenyl cations and polycations, demonstrating how concurrent fragmentation processes generating long-lived species in lowly-charged cationic states can be characterised. Valence-shell ionisation could initially ionise more atomic sites than just iodine, leading to fragmentation channels that were not observed with site-selective, inner-shell ionisation. Both ionisation regimes generated similar sets of products but on different relative timescales due to initially populating different electronic excited states. Each ionisation regime results in many observable fragmentation processes, but photoelectron information is required to relate specific fragmentation channels to specific ionisation and charge generation/redistribution processes.

Contents

List of Figures

List of Abbreviations

1D, 2D, 3D . . One-, two-, or three-dimensional, referring to spatial dimensions

AM . . . . . Auger-Meitner

BBO . . . . . BaB_2O_4

BOA . . . . . Born-Oppenheimer Approximation

CAMP . . . . (Max Planck Advanced Study Group (ASG) within the Center for Free Electron Laser Science (CFEL)) CFEL-ASG Multi-Purpose instrument

CDF . . . . . Cumulative distribution function

CEI . . . . . Coulomb explosion imaging

COB . . . . . Classical over the barrier

DAQ . . . . . Data Acquisition

FEL . . . . . Free electron Laser

FLASH . . . . Free electron laser Hamburg

FWHM . . . . Full width half maximum

HOMO . . . . Highest occupied molecular orbital

IB . . . . . Iodobenzene

IP . . . . . Iodopropane

IR . . . . . Infra-red

KER . . . . . Kinetic energy released

LASER . . . . Light amplification of stimulated emission of radiation

MCP . . . . . Micro channel plate

NIR . . . . . Near-infrared

PES . . . . . Potential energy surface

PImMS . . . . Pixel imaging mass spectrometry

SACLA . . . . SPring-8 Angstrom Compact free electron LAser

SASE . . . . . Self Amplified Spontaneous Emission

SFI . . . . . Strong Field Ionisation

SMI . . . . . Spatial Map imaging

TOF . . . . . Time-of-flight

UV . . . . . Ultra-violet

VMI . . . . . Velocity map imaging

XUV . . . . . Soft-Xray / extreme UV

Publications

1 The role of momentum partitioning in covariance ion imaging analysis.
T. Walmsley*, J. W. McManus*, Y. Kumagai, K. Nagaya, J. Harries, H. Iwayama, M. N. R. Ashfold, M. Britton, P. H. Bucksbaum, B. Downes-Ward, T. Driver, D. Heathcote, P. Hockett, A. J. Howard, J. W. L. Lee, Y. Liu, E. Kukk, D. Milsesevic, R. S. Minns, A. Niozu, J. Niskanen, A. J. Orr-Ewing, S. Owada, P. A. Robertson, D. Rolles, A. Rudenko, K. Ueda, J. Unwin, C. Vallance, M. Brouard, M. Burt, F. Allum, and R. Forbes, *The Journal of Physical Chemistry A4*, 2024 (*These authors contributed equally)

2 Direct momentum imaging of charge transfer following site-selective ionization.
F. Allum, Y. Kumagai, K. Nagaya, J. Harries, H. Iwayama, M. Britton, P. H. Bucksbaum, M. Burt, M. Brouard, B. Downes-Ward, T. Driver, D. Heathcote, P. Hockett, A. J. Howard, J. W. L. Lee, Y. Liu, E. Kukk, J. W. McManus, D. Milsesevic, A. Niozu, J. Niskanen, A. J. Orr-Ewing, S. Owada, P. A. Robertson, A. Rudenko, K. Ueda, J. Unwin, C. Vallance, T. Walmsley, R. S. Minns, D. Rolles, M. N. R. Ashfold, R. Forbes, *Physical Review A*, 2023, 108(4), 043113

3 Exploring the Ultrafast and Isomer-Dependent Photodissociation of Iodothiophenes via Site-Selective Ionization.
W. O. Razmus, F. Allum, J. Harries, Y. Kumagai, K. Nagaya, S. Bhattacharyya, M. Britton, M. Brouard, P. H. Bucksbaum, K. Cheung, S. W. Crane, M. Fushitani, I. Gabalski, T. Gejo, A. Ghrist, D. Heathcote, Y. Hikosaka, A. Hishikawa, P. Hockett, E. Jones, E. Kukk, H. Iwayama, H. V. S. Lam, J. W. McManus, D. Milsesevic, J. Mikosch, S. Minemoto, A. Niozu, A. J. Orr-Ewing, S. Owada, D. Rolles, A. Rudenko, D. Townsend, K. Ueda, J. Unwin, C. Vallance, A. Venkatachalam, S.-i. Wada, T. Walmsley, E. M. Warne, J. Woodhouse, M. Burt, M. N. R. Ashfold, R. S. Minns, R. Forbes, *Physical Chemistry Chemical Physics*, 26, no. 16, 2024, 12725-12737

4 X-ray induced Coulomb explosion imaging of transient excited-state structural rearrangements in CS_2.
J. Unwin, F. Allum, M. Britton, I. Gabalski, H. Bromberger, M. Brouard, P. H. Bucksbaum, T. Driver, N. Ekanayake, D. Garg, E. Gougoula, D. Heathcote, A. J. Howard, P. Hockett, D. M. P. Holland, S. Kumar, C.-s. Lam, J. W. L. Lee, J. McManus, J. Mikosch, D. Milesevic, R. S. Minns, C. C. Papadopoulou,

C. Passow, W. O. Razmus, A. Röder, A. Rouzée, M. Schuurman, A. Simao, A. Stolow, A. Tul-Noor, C. Vallance, T. Walmsley, D. Rolles, B. Erk, M. Burt, R. Forbes *communications Physics*, 2023, 6(1), 309

5 Characterizing the multi-dimensional reaction dynamics of dihalomethanes using XUV-induced Coulomb explosion imaging.
T. Walmsley, J. Unwin, F. Allum, S. Bari, R. Boll, K. Borne, M. Brouard, P. Bucksbaum, N. Ekanayake, B. Erk, R. Forbes, A. J. Howard, P. Eng-Johnsson, J. W. L. Lee, Z. Liu, B. Manschwetus, R. Mason, C. Passow, J. Peschel, D. Rivas, D. Rolles, A. Rörig, A. Rouzée, C. Vallance, F. Ziaee, M. Burt, *The Journal of Chemical Physics*, 2023, 159, 144302

6 Time-Resolved X-ray Photoelectron Spectroscopy: Ultrafast Dynamics in CS_2 Probed at the S 2p Edge.
I. Gabalski, F. Allum, I. Seidu, M. Britton, G. Brenner, H. Bromberger, M. Brouard, P. H. Bucksbaum, M. Burt, J. P. Cryan, T. Driver, N. Ekanayake, B. Erk, D. Garg, E. Gougoula, D. Heathcote, P. Hockett, D. M. P. Holland, A. J. Howard, S. Kumar, J. W. L. Lee, S. Li, J. W. McManus, J. Mikosch, D. Milesevic, R. S. Minns, S. Neville, A. Tul-Noor, C. C. Papadopoulou, C. Passow, W. O. Razmus, A. Röder, A. Rouzeée, A. Simao, J. Unwin, C. Vallance, T. Walmsley, J. Wang, D. Rolles, A. Stolow, M. S. Schuurman, R. Forbes, *The Journal of Physical Chemistry Letters*, 2023, 17, 7126-7133

7 Disentangling sequential and concerted fragmentations of molecular polycations with covariant native frame analysis.
J. W. McManus*, T. Walmsley*, K. Nagaya, J. Harries, Y. Kumagai, H. Iwayama, M. N. R. Ashfold, M. Britton, P. H. Bucksbaum, B. Downes-Ward, T. Driver, D. Heathcote, P. Hockett, A. J. Howard, J. W. L. Lee, Y. Liu, E. Kukk, D. Milsesevic, R. S. Minns, A. Niozu, J. Niskanen, A. J. Orr-Ewing, S. Owada, P. A. Robertson, D. Rolles, A. Rudenko, K. Ueda, J. Unwin, C. Vallance, M. Brouard, M. Burt, F. Allum, and R. Forbes, *Physical Chemistry Chemical Physics*, 2022, 24, 22699-22709 (*These authors contributed equally)

Future Publications

1 Concurrent Pathways and Metastable States: Covariance Imaging Analysis of XUV-Ionisation Products.
T. Walmsley, F. Allum, M. Britton, M. Brouard, P. H. Bucksbaum, M. Fushitani, I. Gabalski, T. Gejo, J. Harries, P. Hockett, A. J. Howard, H. Iwayama, Y. Kumagai, E. Kukk, C.-s. Lam, S. Lim, R. S. Minns, J. W. McManus, K. Nagaya, S. Nishimuro, J. Niskanen, A. Niozu, S. Owada, W. O. Razmus, D. Rolles, J. Somper, K. Ueda, J. Unwin, S.-i. Wada, J. Woodhouse, R. Forbes, E. M. Warne, and M. Burt

2 Characterising the Overlapping Photodissociation Channels of Iodobenzene at 200 nm Using Coulomb Explosion Imaging.
J. Unwin, W. O. Razmus, F. Allum, M. Britton, M. Brouard, P. H. Bucksbaum, M. Fushitani, I. Gabalski, T. Gejo, J. Harries, P. Hockett, A. J. Howard, H. Iwayama, Y. Kumagai, E. Kukk, C.-s. Lam, S. Lim, R. S. Minns, J. W. McManus, K. Nagaya, S. Nishimuro, J. Niskanen, A. Niozu, S. Owada, W. O. Razmus, D. Rolles, J. Somper, K. Ueda, S.-i. Wada, T. Walmsley, J. Woodhouse, M. Burt, and E. M. Warne

If it's not broke, break it.

— Serena van der Woodsen, Gossip Girl

1 Introduction

Contents

1.1 Mapping Molecular Reaction Dynamics

Light-matter interactions happen all around us: many are crucial to day-to-day life, such as the interaction of light with our eyes so that we can see, or the absorption of light by chlorophyll in plants, leading to photosynthesis. Some reactions are to our detriment, such as the photo-initiated breakdown of the ozone layer[1–5] or the ultraviolet (UV)-degradation of DNA.[6] To gain a fuller understanding of how light interacts with complex systems and the ensuing photochemistry, it is useful to first consider and study the ultrafast reaction dynamics of smaller molecules.

Chemical structures can be studied using Coulomb explosion imaging (CEI). A molecule is firstly highly ionised by the removal of several electrons using ultrafast (femtosecond) and intense lasers (which are discussed in detail in Chapter 2). If the

resultant cationic state on the molecule is unstable, and charge is located on two or more atomic sites, their mutual Coulombic repulsion can disrupt or break chemical bonds, forming highly energetic ionic fragments. Coulomb's law states that the energy (E) released in a Coulomb explosion is inversely proportional to the separation (r_{ij}) between two charges (q_i,q_j), and proportional to the product of the two charges:

$$E = \frac{q_i q_j e^2}{4\pi\epsilon_0 r_{ij}}, \tag{1.1.0.1}$$

where e is the charge on an electron, and ϵ_0 is the vacuum permittivity. The kinetic energy of a Coulomb explosion and the correlated momenta of co-fragments are directly related to the geometrical properties of the compound at the instance of the explosion.[7, 8] CEI effectively 'freezes' the instantaneous structure of a molecule and allows time-dependent chemistry to be mapped by measuring the evolution of molecular properties (such as geometry) as a function of the time spent evolving along a reaction pathway.[9–13]

The capabilities of CEI to study time-dependent reaction dynamics have frequently been demonstrated using diatomics and small molecules (e.g., CH_3I).[14–23] However, as the size of a molecule increases, the number of possible fragmentation channels that can competitively occur also increase. Moreover, it becomes harder to generate a charge on every atom in the compound to completely atomise the molecule, which can lead to the formation of products comprising several atoms in varying geometries and, potentially, metastable states. As a result, disentangling the vast array of fragmentation channels accessible to large molecules induced by CEI is not straightforward. More intricate analysis procedures are required to study larger, more chemically relevant compounds. In this thesis, new methods are presented that extend the capabilities of CEI and correlated ion imaging methods to disentangle concurrent fragmentation channels arising in larger molecules than have historically been studied using CEI. The methods presented allow individual fragmentation channels to be independently characterised in detail, including characterisation of the nuclear dynamics and metastable lifetimes of intermediate products.

1.2 Light-matter Interactions

When a photon is incident on a molecule, if it is absorbed, the internal energy of the molecule increases, leading to the population of excited electronic states. If the energy of a photon is great enough, electrons can be liberated, leaving behind a molecule in an excited cationic state. Excited states can be described by potential energy curves (PECs) or surfaces (PESs) that illustrate how the potential energy of a state varies with parameters such as bond length or bond angle. An example of a simulated PEC is given in Figure 1.1 for the singlet S_1 excited state of CH_2I_2, showing how the potential energy of the state depends on the I-C-I bond angle when both C-I bond lengths are fixed at 2.2Å.

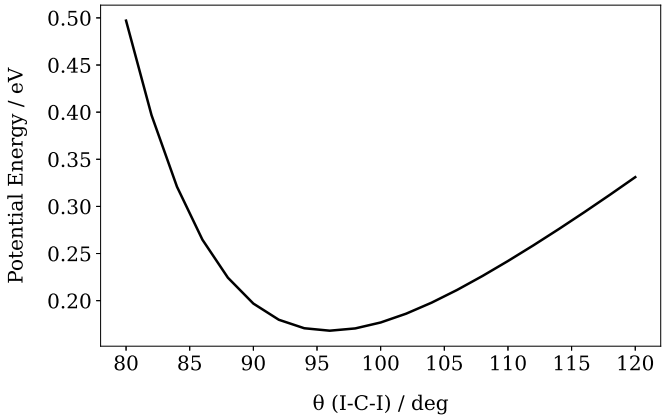

Figure 1.1: A simulated potential energy curve for the singlet S_1 excited state of CH_2I_2, showing how the potential energy (relative to the energy of the neutral ground state) depends on the I-C-I bond angle when both C-I bond lengths are fixed at 2.2 Å, simulated by Z. Liu.

After photoabsorption and excitation, an excited molecule will act to minimise its energy depending on the nature and structure of the populated excited state. This can result in structural changes to the molecule such as changes to bond lengths and angles, isomerisation, or even dissociation. The amount of kinetic energy that fragments gain from dissociation is dependent on the incident photon energy ($E = \hbar\omega$, where $\hbar$ is the reduced Planck's constant and ω is the angular frequency of the photon), the energy requirements of the dissociation process taking

place, and the sum of the internal energy, ΣE_{int} (rotational, vibrational, and/or electronic), of the products.[24] This can be formulated as:

$$\text{KE} = \hbar\omega - \Sigma D_0 - \Sigma E_{\text{int}}, \tag{1.2.0.1}$$

where KE is the translational energy disposed into fragments upon dissociation and ΣD_0 is the sum of the dissociation energies of any bonds broken. Alternatively, the system may relax back to its ground state by emission of a photon through radiative processes such as fluorescence, or redistribute internal energy via intramolecular vibrational redistribution (IVR).[25–29]

The Born-Oppenheimer approximation (BOA) assumes that the momentum of an atomic nucleus is negligible compared to the momenta of electrons due to their large difference in mass, and so nuclear and electronic potential interactions can generally be ignored for excitation processes. However, the BOA breaks down when electronic PESs with similar energies overlap and nuclear vibrational and electronic excited states become coupled, forming conical intersections that mediate non-radiative transitions between excited states.[30, 31] Internal energy can then redistribute between states of the same spin multiplicity via internal conversion (IC) or between states of different spin multiplicity via intersystem crossing (ISC).[32–34] Therefore, the photochemical response of a molecule to a photon of a specific wavelength is not limited to only one set of products; interactions between PESs can allow several excited states to be populated, leading to a range of products being created by the same photon wavelength, and concurrent photochemistry that is difficult to disentangle.[35]

1.3 Coulomb Explosion Imaging of Concurrent Fragmentation Channels

CEI can be performed using intense (on the order of $10^{13-15}\,\text{W}\,\text{cm}^{-2}$) laser pulses with ultra-short pulse durations (tens of femtoseconds) that are comparable to the timescales of chemical reactions. When the pulse duration is shorter than the timescales for nuclear re-arrangement (typically tens to hundreds of femtoseconds),

CEI effectively freezes the instantaneous geometry of the molecule, and so the momenta of ionic products can be used to infer geometrical properties of their chemical origin at the instance of the interaction with the ionising pulse.[7, 8, 36–39] As such, CEI has proven itself to be a valuable tool in characterising physical properties (for example, the structures of isomers and chiral molecules)[40–44] as well as in exploring field-induced processes such as rotation, alignment, and orientation of molecules, clusters, and droplets.[45–49] Furthermore, CEI can be used to track physical changes to a molecule as a function of time (such as dissociation,[8, 12, 16, 20, 21, 50–54] roaming,[55] and proton migration)[56] when coupled with femtosecond pump-probe spectroscopy.

In pump-probe spectroscopy, molecular excited states are prepared by a pump pulse, which initiates a chemical process. A second laser pulse–the probe pulse–is then used to ionise the molecule (and induce Coulomb explosion) at different delays relative to the interaction of the pump pulse with the molecule. Often, UV pulses are used to initiate chemical reactions via single photon absorption regimes. By varying the relative arrival times of the pump and probe pulses at the sample, the evolution of the molecular properties can be mapped as a function of the time spent evolving on an excited state PES.[9–13] Therefore, in principle, CEI coupled with pump-probe spectroscopy can be used to follow structural changes to a molecule. The simplest type of structural change is a two-body ballistic fragmentation, which breaks one chemical bond of a molecule whose centre of mass lies along the bond dissociation vector. The two products of such a fragmentation recoil with equal and opposite momenta and with little rotational excitation. When the centre of mass does not lie along a bond dissociation vector, as in CH_2BrI, two-body C-I dissociation becomes complicated due to induced rotational excitation in the CH_2Br product, centred around the heavy Br substituent that acts as an 'anchor'.[20, 51, 57]

Fragmentation processes breaking at least two chemical bonds can be classified simply as either concerted or sequential mechanisms. For a general system ABC, concerted processes can be written as

$$\mathrm{ABC} \rightarrow \mathrm{A} + \mathrm{B} + \mathrm{C}. \tag{1.3.0.1}$$

The timescale between two bonds breaking is generally less than the vibrational period of the first bond breaking (the primary bond). In other words, the two bonds cleave within such a fast time frame that the two events are not independent and cannot be uniquely distinguished. However, there generally tends to be some degree of asynchronicity if the two bond environments are not equal.[58, 59] On the other hand, in a sequential process, the timescale between two bonds breaking is long enough that the two bond-breaking events are considered independent. In general, a sequential fragmentation mechanism of a system ABC can be written as

$$\mathrm{ABC} \rightarrow \mathrm{A} + \mathrm{BC} \rightarrow \mathrm{A} + \mathrm{B} + \mathrm{C} \tag{1.3.0.2}$$

The first bond is broken in a primary process, generating at least one metastable intermediate (BC) product, which decays into secondary products (B + C). Depending on the geometry of the molecule, the primary bond-breaking process can produce rotationally excited intermediate species. If the rotational period is shorter than its metastable lifetime, the intermediate loses all 'memory' of its initial orientation relative to the primary co-fragment prior to secondary fragmentation.[58, 59]

Distributions of fragment products are not only complicated by the number of PESs accessed during the excitation phase, but ionisation processes can also influence fragmentation and nuclear dynamics based on how and where charge is generated on the molecule. Depending on whether inner-shell (Chapter 2, Section 2.2.2) or valence-shell electrons (Chapter 2, Section 2.2.3) are removed, charge is generated and redistributed differently. As a result, a range of parent cations in a range of internally excited states can be created, each with its own related fragmentation channels. Therefore, the range of fragmentation regimes accessed by the probe-pulse alone can be just as complicated as those induced by a pump-pulse. To accurately distinguish and characterise pump-induced fragmentation channels, nuclear dynamics induced by the probe also need to be fully deconvoluted. To extend time-dependent CEI to larger and more chemically relevant and interesting molecules, it is important to first be able to disentangle competing and simultaneously occurring fragmentation pathways.

1.4 Outline of Thesis

This thesis aims to address and extend the capabilities of ion imaging experiments by developing and applying new extensions to correlated ion momentum analysis methods. The findings that are presented throughout showcase the high levels of information that can be uncovered and retrieved from complicated experimental data. The outcomes of these analysis procedures demonstrate how a comprehensive understanding of competing fragmentation channels of neutral and polycationic molecules can be obtained from CEI and correlations between the momenta of detected ions. This includes the characterisation of multi-dimensional structural changes and mechanisms involving metastable states. Furthermore, this thesis highlights how the generation of lowly charged parent cations can lead to a vast range of competing fragmentation processes, which could complicate the application of CEI in time-resolved studies.

Advanced ion-imaging methods have been used to separately analyse pump- and probe-induced dynamics of iodo-substituted hydrocarbons of increasing size and complexity. The strong photoabsorbing ability of iodine is exploited to induce fragmentation of molecular systems ranging from diiodomethane to iodobenzene. The gas-phase chemistry of such compounds can be considered models of the more complicated dynamics that take place in larger structures.[60–62]

This thesis is set out in the following format. Chapter 2 outlines the experimental methods and analytic techniques used throughout this thesis. Chapter 3 presents a UV-pump extreme UV/soft X-ray (XUV)-probe experiment on CH_2I_2, where ion correlation methods were used to map multidimensional structural changes to the molecule as a function of time. Chapter 4 presents the range of XUV-induced fragmentation processes induced in 1- and 2-iodopropane by ionisation at the I 4d edge and demonstrates how the initial geometry of the isomer influences the charge generation and redistribution processes and the ensuing nuclear dynamics. This chapter also exemplifies analytical methods that can be used to disentangle complicated ion spectra. Chapter 5 uses site-selective XUV-ionisation of iodobenzene at the I 4d edge to probe the stability of phenyl cations and polycations and

demonstrates the possibility of extending CEI and ion correlation techniques to larger structures, whilst also outlining the current limitations of state-of-the-art experiments. Chapter 6 compares XUV- and infrared (IR)-induced CEI regimes of iodobenzene, and discusses how different charge generation processes affect the distribution of observable fragmentation channels. Finally, Chapter 7 will discuss the conclusions drawn from this work, as well as the potential of future work that would build upon the methods and results presented here.

RA: You're just using initials now?

SC: Yeah. They save time.

RA: Well, not if you have to translate.

— Ryan Atwood & Seth Cohen, The O.C.

2

Techniques

Contents

2.1 Introduction

In this chapter, the experimental and analytical methods used to carry out CEI throughout this thesis are discussed.

Firstly, the different types of lasers used to induce photochemistry in this thesis will be discussed, followed by methods to detect the nascent ionic fragments. Information on the different laser and spectrometer facilities used to generate the data presented in this thesis will be outlined, but more specific details will be given in the corresponding results chapters. Following this, different types of correlated ion imaging analysis techniques will be discussed and how to interpret their results.

2.2 Experimental Methods

2.2.1 Ionisation Using Femtosecond Lasers

The properties of a probe laser pulse control how efficiently a molecule can become ionised, as well as the type of ionisation it experiences. If the photon energy is larger than the ionisation potential of an atomic or molecular system, a valence-shell electron can be liberated. The energy of the photon in excess of the ionisation potential can be transferred to the electron as kinetic energy. (The momentum of the photon absorbed is also partitioned between the electron and resultant ion.) If the energy of the photon energy is less than the ionisation potential, then ionisation is instead possible if the intensity of light is high enough to operate under a multiphoton regime where two or more photons, whose summed energy is equal to or in excess of the ionisation potential, are absorbed.[63] By varying the parameters of the laser pulse, such as intensity, pulse duration, and phase relationships, different ionisation and/or dissociation regimes can be accessed.[64, 65] Two ionisation regimes will be considered here; inner-shell ionisation and valence-shell ionisation.

2.2.2 Inner-shell Ionisation

Site-selective, inner-shell ionisation can be induced using extreme UV/soft X-ray (XUV) photons, which have wavelengths within the range of high-energy UV

(∼120 nm) to low-energy X-ray (∼10 nm). In this thesis, XUV pulses are generated at X-ray free-electron lasers (FELs), which operate based on self-amplified spontaneous emission (SASE) to emit intense (10^{12}-10^{14} W cm^{-2}), ultrashort (2 fs-300 fs), and high repetition rate radiation, such that single-photon and multi-photon regimes are accessible. Briefly (and typically), a picosecond laser is used to irradiate a photocathode, generating a beam of electrons that are then accelerated to relativistic speeds via a superconducting linear accelerator (an undulator comprising a long, periodic arrangement of dipole magnets with alternating polarity (Figure 2.1)). The alternating magnetic field experienced by the electrons forces them to oscillate and emit spontaneous XUV radiation via SASE. At the beginning of the undulator, the radiation emitted by the electrons is incoherent but, as the electrons travel through the undulator, they interact collectively with their own XUV radiation, resulting in coherent XUV output and electron bunches separated by the resonant wavelength.[66–69] The XUV output pulses are ultrashort, with high peak power and spatial coherence.[70] The advances in generating narrowband pulses and wavelength tunability achieved at these FELs make them valuable in femtosecond experiments. Inner-shell ionisation is used to induce Coulomb explosions in Chapter 3, Chapter 4, and Chapter 5. In Chapter 3, the XUV photons are generated using the Free electron LASer in Hamburg (FLASH), Germany. In Chapter 4 and Chapter 5, the XUV photons are generated using the soft X-ray beamline BL1 at Spring-8 Angstrom Compact free electron LAser (SACLA), Japan.

XUV-ionisation is mostly independent of the geometry of a sample and most favourably ionises the atomic site with the highest absorption cross section at the utilised wavelength, which often corresponds to inner-shell electrons. Therefore, by tuning the wavelength of the XUV laser, atomic-orbital selective ionisation can be achieved.[7] Ionisation by removal of inner-shell core electrons can generate highly charged cationic states through photo-electron and Auger electron emission (Figure 2.2). Removing an inner-shell electron leaves behind an electron vacancy that can be filled by the relaxation of another electron from a higher energy orbital. This is a radiative decay process that releases another photon that can go on to

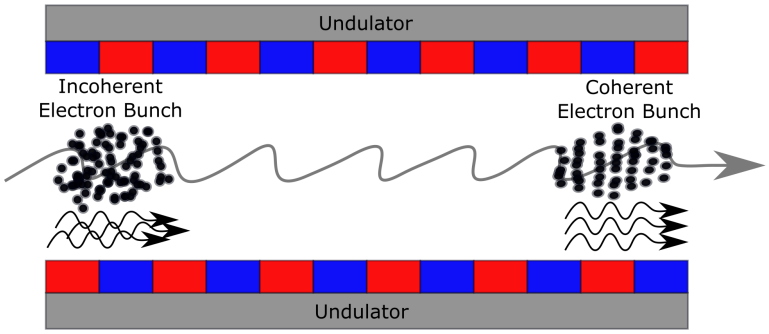

Figure 2.1: A depiction of an undulator: an incoherent electron bunch enters the undulator and emits incoherent XUV radiation. As the electrons travel through the undulator, they interact with their own emission, and interference between waves produces coherent XUV radiation and coherent electron bunches separated by the resonant wavelength.

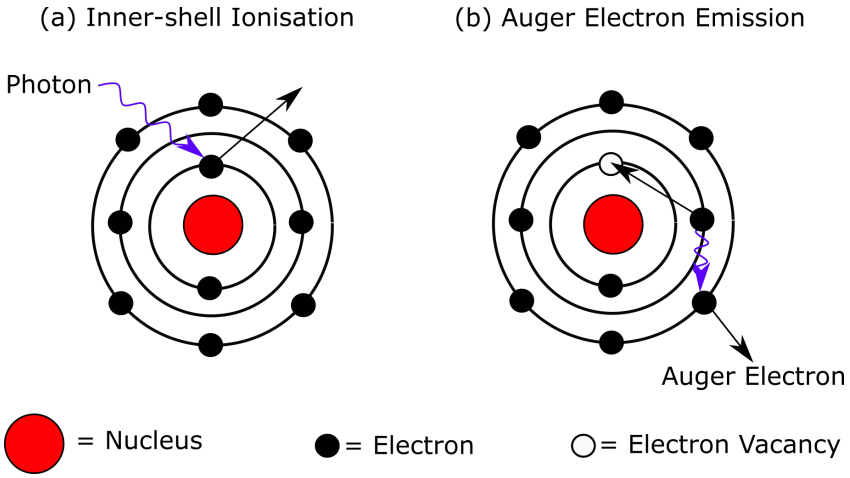

Figure 2.2: A depiction of the Auger-Meitner process. (a) A photon is absorbed, leading to the ejection of an inner-shell electron, which leaves behind an electron vacancy. (b) The electron vacancy is filled by the decay of an electron in a higher energy orbital, releasing another photon that can remove further Auger electrons.

remove another electron, referred to as an Auger electron. These electrons can collide with other outer and inner electrons, triggering a cascade of ionisation events occurring usually within a few tens of femtoseconds via Auger-Meitner (AM) decay. This leads to rapid and efficient charge multiplication.[7, 71]

The time taken for the AM process to generate the final charge on the parent is dependent on the XUV pulse duration, but also on the electronic distribution across the molecule.[72] AM cascades build up high charges that can redistribute across

the molecule, often leading to highly energetic Coulomb explosions. Although the time taken to reach a final charge state via AM decay is short, it is also finite (tens of fs), and charge redistribution processes occurring on timescales competitive with AM decay can result in additional structural distortion before Coulomb explosion occurs.[72] Vibrational excitation gained during ionisation can cause the molecule to expand and the resultant kinetic energy of fragments of a Coulomb explosion can be less than that expected from a Coulomb explosion of a molecule in its ground state geometry in the same final cationic state.

In atoms, AM decay is well established, following photon absorption and electron rearrangement.[73] However, the AM decay process in molecules is more complicated, due in part to competition between charge delocalisation, AM cascades, and Coulomb explosion.[74] Site-selective ionisation is often thought to be a 'molecular scissor' since the XUV radiation can be tuned to ionise molecules at specific electronic sites and break specific bonds.[75–78] However, due to competing charge generation and redistribution processes occurring within the timeframe of the AM decay, charge does not necessarily remain on the site-selectively ionised atom, and a range of bonds can theoretically be broken.[79] Secondary and tertiary AM decays and non-direct ionisation processes can populate a range of excited cationic states, each of which are defined by their own fragmentation or relaxation pathways.[74, 76, 77, 80–86] Therefore, the distribution of products generated by 'site-selective' ionisation has a greater dependence on the distribution of final cationic states and charge distributions than on primary ionisation processes.[87, 88]

2.2.3 Valence-shell Ionisation

Valence-shell ionisation (or strong field ionisation (SFI)) is used to induce Coulomb explosions in Chapter 6 and uses short (tens of femtoseconds) but intense (on the order of $10^{13-15}\,\mathrm{W\,cm^{-2}}$), laser pulses comprising low energy photons (e.g., infra-red (IR)) to liberate valence-shell electrons. Such laser pulses have electric field strengths comparable to the electrostatic Coulomb attraction between valence

electrons and the atomic nucleus, and their pulse durations are comparable to the timescales of molecular dissociative dynamics.[89]

Intense and ultrashort laser pulses are a result of the self-focusing and self-phase modulation abilities of a laser gain medium, which is enclosed in a highly reflective cavity and amplifies input radiation to generate laser output. The refractive index of the gain medium is dependent on the intensity of the input radiation beam. This effect (called the Kerr effect) is due to electric field distortions of the atomic energy levels in the gain medium, occurring usually within femtoseconds. The intensity profile of the input beam is usually assumed to be Gaussian, with high intensity at the centre and weaker intensity at its edges. The Kerr effect effectively focuses the laser beam like a lens, such that the central intensity is amplified and the intensity of the edge of the beam is weakened. Ultrafast (narrow) laser pulses are generated by combining many resonant frequencies spread around a central laser frequency. All frequencies must oscillate with a fixed phase relationship to produce a laser train of ultrashort pulses, which is ensured by the Kerr effect (termed mode-locking).[90] Table-top lasers operating with wavelengths (e.g., IR or near-infrared (NIR)) and intensities within the 'dipole oasis' (shown in Figure 2.3) can be described using the dipole approximation, which neglects any effect of the photon momentum on the momentum gain of ionised electrons, and considers that the laser produces a homogeneous, time-dependent electric field, neglecting the corresponding magnetic component of the laser field.[91]

Applying an external, oscillating laser electric field to an atomic or molecular system forces the valence electron density to localise opposite the field polarisation vector due to electrostatic repulsion. The result is deformation of the $1/r$ electron Coulomb potential wells, as depicted in Figure 2.4.[89] The electron experiences combined forces of the ion core and oscillating external electric field, which results in a time-dependent deformation of the electron potential well.[92]

The precise regime that SFI of an atom follows is governed by the Keldysh parameter (γ), which characterises the relationship between ionisation potential

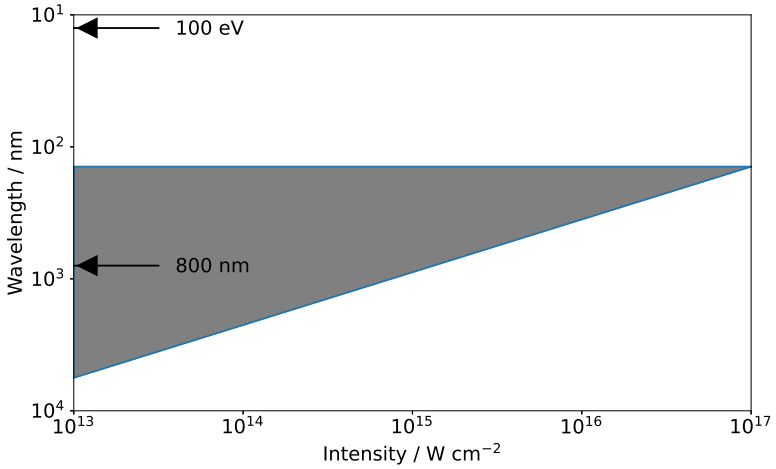

Figure 2.3: The 'dipole oasis': the shaded region–a function of wavelength and intensity–demonstrates the laser parameters that allow for tunnelling ionisation theory to be applied to atomic valence-shell ionisation.[91]

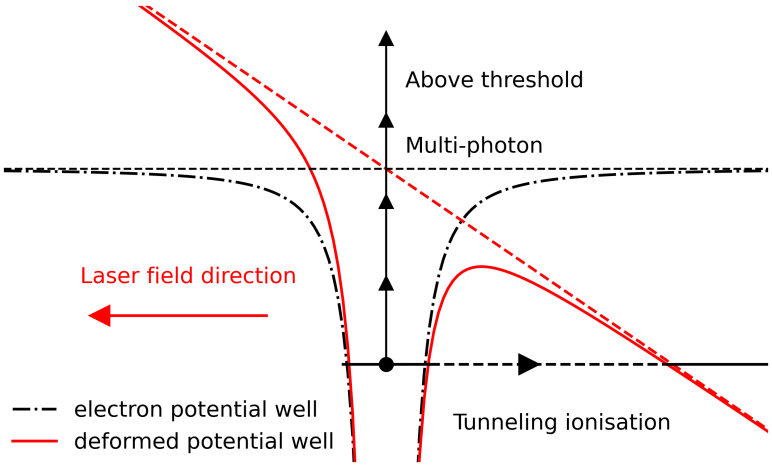

Figure 2.4: A simplistic depiction of strong field ionisation, showing how a one-dimensional electron potential becomes deformed under the application of a strong electric field, allowing electrons to escape via tunnelling or multi-photon/above threshold ionisation regimes.

(IP) and the electric field:[93, 94]

$$\gamma = \sqrt{\frac{IP}{2U_p}} \tag{2.2.3.1}$$

where U_p is the ponderomotive energy of the interaction of a free electron within the electric field (i.e. the average kinetic energy gained by a free electron undergoing field-induced harmonic motion during the electrons' oscillating orbit in the ionisation continuum), which depends on the intensity (I_0) and wavelength (λ_0) of the laser

field by the following equation:[95, 96]

$$U_p = \frac{I_0 e^2 \lambda_0^2}{8\pi^2 m_e \varepsilon_0 c^3}, \tag{2.2.3.2}$$

where e and m_e are the charge and mass of an electron, respectively, ε_0 is the vacuum permittivity, and c is the speed of light.

Two contrasting limiting cases are defined by the Keldysh parameter: when $\gamma > 1$, ionisation occurs via a multiphoton, above-threshold ionisation (ATI) regime, and when $\gamma < 1$, ionisation is dominated by a tunnelling mechanism.[93, 97]

The multiphoton regime occurs when the ionisation energy of an electron is greater than the ponderomotive potential of the laser field. Ionisation can occur via the absorption of several photons providing enough energy to the electron that it can escape classically over the top of its potential well into the ionisation continuum. ATI is a subset of multiphoton ionisation occurring when the number of photons absorbed is greater than the minimum number of photons required for ionisation, as depicted in Figure 2.4.[39, 62, 64, 95, 98–100] However, if the ponderomotive potential of the laser field is approximately equal to the electron binding energy, the potential well can become sufficiently deformed, forming a quasi-static, small potential barrier to the ionisation continuum. In this case, an electron may tunnel through the classically forbidden region during each oscillatory peak of the laser field. [101] The position of an electron during tunnelling ionisation depends on the stage of the field's oscillation at which ionisation occurred. It is possible that the electric field direction can reverse before the electron reaches the other side of the potential barrier, returning it to its valence position. Therefore, the tunnelling ionisation probability depends on the width of the potential barrier, the strength of the external electric field, and the stage of the field's oscillatory cycle relative to when the ionisation process began. Tunnelling ionisation and multiphoton regimes are not exclusive: the transition between regimes is smooth, and both can occur within the $\gamma \approx 1$ range.[92] The distinction between both regimes can be also complicated in cases where both occur, such as photons from the laser field being absorbed during tunnelling ionisation.[97] Alternatively, if $\gamma \ll$

1, the electron potential well is deformed so much that the energy barrier to the ionisation continuum is lower than the electron's binding energy and the electron can escape via over-the-barrier ionisation.

Once an electron has been removed, it can still interact with the atom from which it came. Depending on the shape and time period of the oscillations of the laser field, if the field reverses direction, the free electron can be accelerated back towards its parent cation and interact with the nuclei or remaining electrons.[102] The energy of the returning electron is dependent on its ionisation potential and the ponderomotive energy of the laser field:[62]

$$\mathrm{E} = \mathrm{I_p} + 3.2\mathrm{U_p}. \tag{2.2.3.3}$$

Electron re-collision can induce a wide range of effects, such as high harmonic generation (HHG)[103], and double ionisation.[104–106]

SFI of molecules is more complicated than SFI of atoms and cannot be described as simply with the Keldysh parameter due to their increased complexity, density of states, and degrees of freedom. SFI processes can be sensitive to the alignment or orientation of molecules with the laser field:[107, 108] electrons are typically removed from the highest occupied molecular orbital (HOMO) but, other lower-lying MOs may be preferably ionised if their size, shape, and orientation are more accessible by the laser field over the HOMO.[109–112] Furthermore, strong fields can not only ionise but induce molecular dissociation by interacting and coupling with molecular PESs to form 'dressed', non-adiabatic surfaces that are analytically inseparable in terms of the laser and individual PES components.[64, 65, 98, 100, 113–117] Nuclear wavepackets evolving on dressed dissociative and cationic surfaces lead to molecular fragmentation and combining this with the array of different ionisation interactions with the field can result in molecules and products in a range of cationic states and, within those, a range of internally excited states.[102] In the cases where double ionisation occurs, charge can redistribute across the molecule, resulting in a Coulomb explosion of recoiling fragments with momenta corresponding to the geometry of the molecule at the instance of the explosion.

2.2.4 Velocity Map Imaging Time-of-Flight Mass Spectrometry

To measure the momenta of fragments produced in Coulomb explosions, velocity map imaging (VMI) techniques are used. Figure 2.5 shows a schematic for a generic VMI spectrometer, which separates ions produced by laser-induced ionisation by their mass-to-charge ratio (m/z) and focuses ions with the same momenta within the plane of the detector (p_x, p_y) to the same position (x, y) on the detector, regardless of their origin position within the spectrometer. The spectrometer usually comprises two differentially pumped vacuum chambers (a source chamber and an experiment chamber) that operate under ultra-high vacuum conditions that can be achieved using a turbomolecular vacuum pump, backed by a roughing vacuum pump. An energetically 'cold' molecular beam is prepared by expanding a gaseous sample from a high-pressure region to a low-pressure region through a nozzle. Collisions between individual molecules, as they pass through the nozzle, convert rotational and vibration energy into translational energy along the direction of the molecular beam. The molecular beam can be pulsed so that it arrives at the interaction region at the same time as the laser pulse. The molecular beam intersects the probe-laser pulses perpendicularly within the reaction chamber, generating ionic products that are accelerated down the time of flight (ToF) drift region and focused onto a detector by the electric field produced by ion optic electrode plates. Ions of the same charge receive equal energy from the electric field. Their resultant terminal velocity is inversely proportional to the square root of the ion's mass. Therefore, ions separate by their (m/z) down the length of the field-free ToF drift region, where smaller m/z fragments arrive at the detector first, and larger m/z last.

The focus and magnification of ion momenta can be achieved by applying specific voltage ratios to the ion optic electrodes. Changing the voltage ratios changes the form of the overall electric field, which acts as an electrostatic lens (Figure 2.6). Ion optics usually comprise a repeller, extractor, ground, and lens electrode and ions are created by the ionisation source within the repeller and extractor, with any anisotropy of the laser field generally reflected in the distribution of ions.

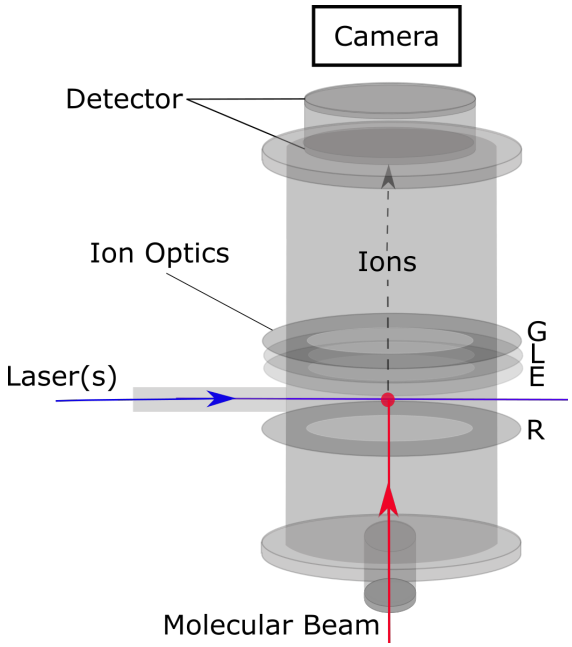

Figure 2.5: A cartoon schematic of a generic VMI spectrometer. The laser(s) and molecular beam interact perpendicularly within the four-electrode ion optic set-up (R = repeller; E = extractor, L = lens, G = ground), and resultant ions are accelerated towards a detector (usually comprising micro-channel plates (MCPs)) and imaged by a camera.

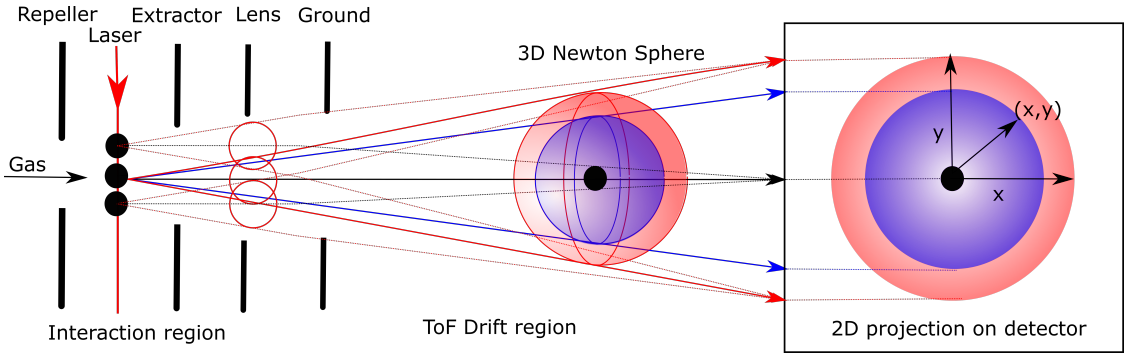

Figure 2.6: A cartoon schematic depicting velocity map imaging of a 3D Newton sphere, which is projected onto a 2D plane. A gaseous sample is perpendicularly intersected by the laser beam within the repeller and extractor plates, producing ionic fragments that form a 3D Newton sphere that is accelerated down the ToF drift region. Focusing on the detector is accomplished via a lens plate. Ions with the same momentum in the plane of the detector are focused to the same (x, y) position on the detector, regardless of their spatial position within the interaction region.[118]

The combination of voltages applied to these electrodes creates an electric field gradient potential 'hill'. Fragments generated between the repeller and the extractor electrodes are accelerated down this hill into a field-free ToF region and towards the detector. This is shown in Figure 2.7, which shows an electronic potential energy surface generated in SIMION. For a given m/z, ions can be generated with forwards or backwards momenta with respect to the detector at the end of the ToF drift region.[119] These form the beginning and the end of a 'Newton sphere', which expands as it progresses along the ToF drift region due to the range of fragment momenta. Ionic fragments can also have momentum within the plane parallel to that of the detector, forming a 3D Newton sphere. Fragments generated by the same process form a sphere with radii proportional to the magnitude of their momenta.[120] As a result, the corresponding Newton sphere for a given m/z can comprise concentric spheres corresponding to the same m/z generated by different processes, as shown in Figure 2.6. Fragmentation processes not occurring parallel to the ToF axis generate products with momenta contributions within the plane parallel to the detector/perpendicular to the ToF axis.

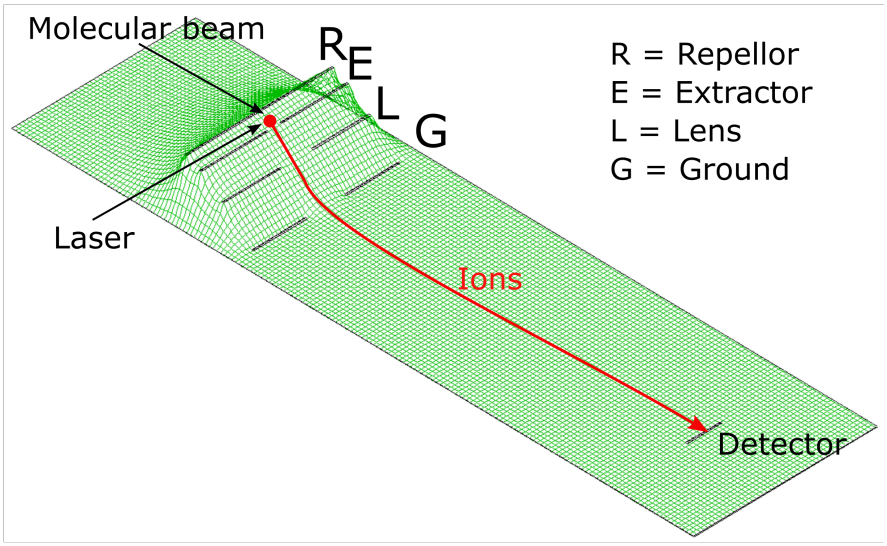

Figure 2.7: A potential energy surface for the in-house spectrometer in Oxford, simulated in SIMION.[121]

The focusing ability of VMI is demonstrated in Figure 2.6, which shows how momenta of ions with the same m/z but produced in different fragmentation processes form concentric, 3D Newton spheres that are projected onto the 2D detector plane. As a result, individual scattering distributions of specific m/z ratios can be retrieved.[120] Moreover, for each m/z, momenta and angular distributions of fragments of specific photochemical processes can be resolved. Hence, VMI is applicable to and useful for many different experimental configurations.[122, 123] The repeller, extractor, and ground electrodes of a VMI ion optic setup produce an extraction, acceleration, and field-free drift region, respectively. The addition of an Einzel lens electrode allows for control over the degree of focus and magnification of the VMI images.[118] By varying the voltages on the electrodes, the gradient of the potential hill can be altered to change the acceleration of ions onto the detector. The Newton spheres of ions that are accelerated faster have less time to expand down the ToF region and hit the detector with lower radii. The converse is true for ions accelerated more slowly. This allows the magnification of a VMI spectrometer to be tuned to look more closely at ions produced with high or low momenta. Notably, by changing the voltages on the ion optics, a second type of focusing is accessible, spatial map imaging (SMI), which maps ions produced in the same position within the ionising source to the same position on the detector. SMI can be useful in configuring the experimental setup to characterise the focus of the laser within the interaction region. In pump-probe experiments, SMI can be used to determine whether the foci of the pump and probe laser pulses are overlapped within the reaction chamber but also has applications in solid-state and surface mapping experiments.[124, 125]

2.2.5 Ion Event Detection

One type of position-sensitive detector is made of two micro-channel plate (MCP) detectors, coupled with a scintillator (such as a phosphor screen) or anode detector (Section 2.2.8). When individual ions hit the detector, the MCPs act as signal amplifiers. The ions hit the first MCP, which generates a cascade of electrons

that hit and release more electrons from the second MCP. These electrons hit the scintillator, causing a clustered photon emission that can then be detected by a fast imaging camera, such as PImMS (Pixel Imaging Mass Spectrometry), which is a charge-coupled device (CCD) camera that records images every 25 ns when using a PImMS2 sensor.[126] Work presented here collected at FLASH or within the in-house laboratory in Oxford used a PImMS camera equipped with a PImMS2 sensor to record x, y, and times of flight for multiple ion hits within the same acquisition cycle (i.e. laser shot), using four diode memory registers per pixel. At FEL facilities, a data acquisition system (DAQ) also records many other necessary parameters, such as laser pulse energies and laser shot identifiers, which are important values for analysis procedures.

For an ion event to be registered by a pixel on a fast imaging camera, the photons released by the detector must reach a certain threshold. As a result of the signal amplification process occurring in the detector, clusters of multiple pixels activated per ion hit can be recorded, overestimating the true ion count per image taken by the camera. Furthermore, the detector screen may be non-homogenous, resulting in some hits being over weighted. Cluster profiles tend to be approximately Gaussian, with the highest brightness generally at the centre of the cluster (Figure 2.8). The earliest a pixel can detect a cluster is at the actual time of the ion hit on the detector, and since pixels at the centre of the cluster tend to receive the highest intensity of photons, these pixels generally reach the detection threshold first and receive the earliest time-code per cluster. It is possible to assign the actual position and arrival time of an ion at the detector from the spread and the earliest time-code recorded for each cluster using a 'centroiding' code, which utilises a nearest-neighbour algorithm (implemented using Python code, Appendix A) to locate the centre of Gaussian clusters over a user-specified time window (Figure 2.9).[126] For every i^{th} pixel in a given cluster, a weighting factor is assigned that is determined by its timecode (T_i) relative to the earliest timecode (T_0) recorded for the cluster. The centre of the cluster (C) can be determined from

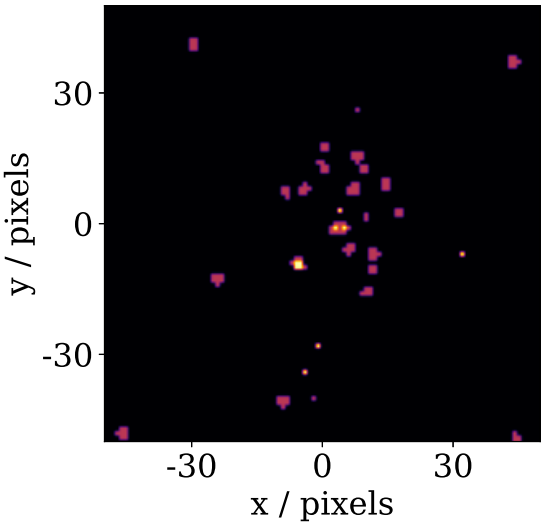

Figure 2.8: Example cluster distributions obtained for ion hits on a section of a dual MCP P47 detector, recorded using a PImMS2 sensor.

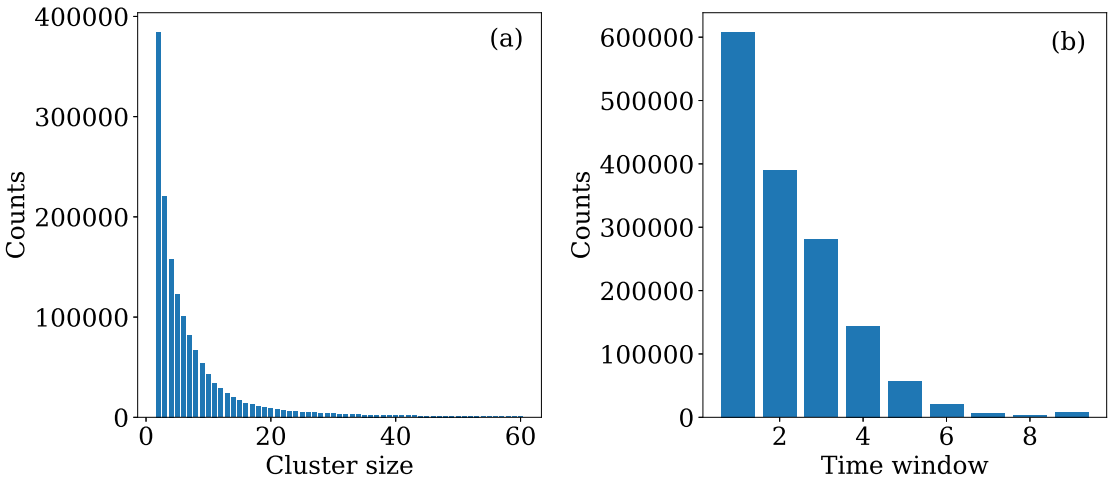

Figure 2.9: Example distributions obtained via the centroiding algorithm for (a) cluster size, which shows the range of sizes of clusters per ion hit, and (b) time window, which shows the range of time codes activated per ion hit.

these timecodes and the coordinates of pixels (r_i):[127]

$$C = \frac{\Sigma_{i=1}^{N} r_i (T_i - T_0 + 1)^{-1}}{\Sigma_{i=1}^{N} (T_i - T_0 + 1)^{-1}}. \tag{2.2.5.1}$$

2.2.6 Ion Images

The location of an ionic fragment within its corresponding Newton sphere is dependent on the orientation of the fragmentation mechanism relative to the ToF axis and the momentum imparted into the fragment. The radial position of an ion (r) within the spherical polar distribution is dependent on velocity (v) and time (t) by the classical equation $r = vt$. Therefore, the kinetic energy (E) of a fragment with mass m is related to the radial position by:

$$E = \frac{mr^2}{2t^2}. \tag{2.2.6.1}$$

When a Newton sphere is projected onto a detector, the 3D spherical polar distribution is projected via Abel transformation into 2D Cartesian coordinates, and the observed KE distribution is skewed. Fragments that have large momenta parallel to the ToF axis, but low momenta perpendicular to the ToF axis, are found at the centre of the 2D projection such that, despite having high KE, their radial position on the detector suggests low KE (Figure 2.10(a)).

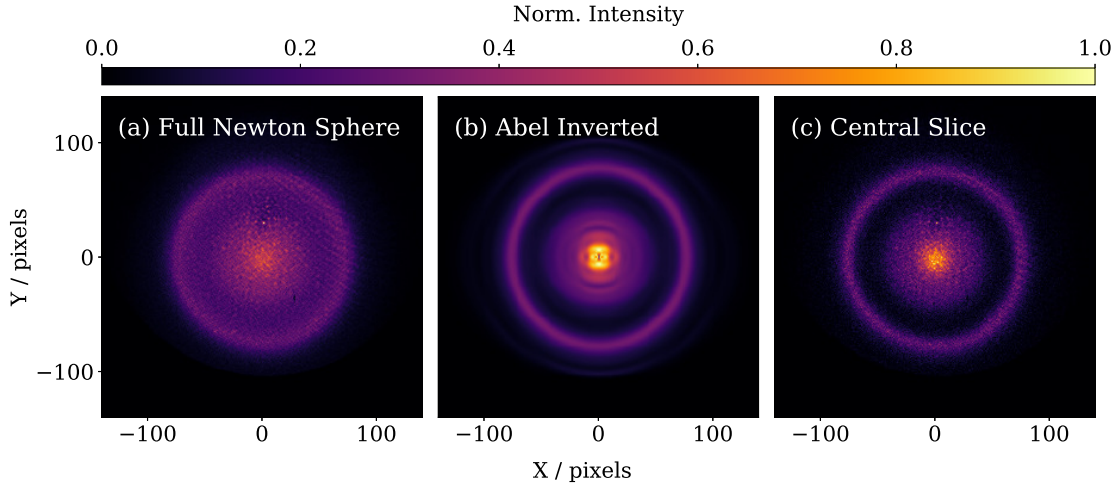

Figure 2.10: I^+ ion images (produced via XUV-ionisation of CH_2I_2 at FLASH), captured by a PImMS2 sensor. (a) The ion image for the full Newton Sphere; (b) the Abel inverted image of (a); (c) the ion image obtained by selecting a narrow range of the I^+ ToF peak, selecting a central slice of the 3D Newton Sphere.

In general, because the dimensionality of the Newton sphere is reduced by the 2D projection, the 3D distribution should not be recoverable. However, by assuming

that the original scattering distribution was cylindrically symmetric, 3D energy and momentum information can be approximately recovered from the 2D projection via an inverse Abel transformation (Abel inversion). This is because a cylindrically symmetric distribution can be made dependent on just two variables, r and θ (angle), which is the same number of variables as the 2D Cartesian projection.[120] This assumes that no 3D information was lost in the projection of the 2D Newton sphere. The Abel inversion process describes the variables r and θ as a truncated sum of Legendre polynomials. Specifically, the pBASEX Abel inversion method uses radial basis functions and a least-squares linear regression to retrieve coefficients describing the original 3D distribution.[128] However, this technique can result in noisy low KE regions and misleading substructures within KE ranges, as shown in Figure 2.10(b).

More accurate KE distributions can be retrieved from ion images by instead selecting only ions that fall within the centre of an ion species' time of flight range–in other words, selecting only the centre of the Newton sphere (Figure 2.10(c)). A compromise must be made between the width of the selected ToF region and the poorer signal-to-noise ratio that comes with fewer statistics.

2.2.7 Radius To Kinetic Energy Conversion

The KE of fragments created in a Coulomb explosion should be proportional to the square of the radial position of the ion hit on a detector (r^2).[120] It is possible to simulate the relationship between these two variables using ion trajectory simulation software such as SIMION.[121] In Figure 2.7, an electronic potential energy surface generated in SIMION is shown for the in-house spectrometer in Oxford. The particle kinetic energies used in the simulation can be varied and their hit position on the detector can be recorded. However, due to inaccuracies and approximations used in the simulation (e.g., space charge effects and aberrations are ignored), the two variables obtained from the simulation may not perfectly follow a square relationship. Instead, by fitting a polynomial, coefficients relating kinetic energy and radius can be obtained. In the work presented in this thesis, an approximate relationship between the two variables was obtained using a fifth-order polynomial. It is worth

noting that results obtained from simulations assume perfect VMI conditions but ion trajectories may behave differently in an experimental setting due to factors such as vibrations or vacuum dynamics.

2.2.8 3D Momentum Distributions

Data that was taken at the Spring-8 Angstrom Compact free electron LAser (SACLA) facility in Japan is presented in this thesis in Chapter 4 and Chapter 5. There, ion images were recorded using a detector comprising coupled MCPs and a hexanode delay line detector, rather than a scintillator and fast imaging camera as described above.[129] Ions hits on the MCPs of the detector generate electrons, which are then incident on anode delay line wires. This generates a reduced voltage on each wire, and two corresponding signals travel to either end of each wire. The difference in the propagation times of the two signals is used to calculate the spatial position of ion hits on the detector, along with the time of flights of ions recorded relative to the 60 Hz trigger of the FEL laser. The high ToF resolution achieved using delay line detectors essentially records very fine slices of the Newton sphere, which can be used to reconstruct the momentum distribution along the ToF axis with high accuracy and recover full 3D momentum distributions of multiple ions detected per laser shot, without the need for approximations, inversion, or compromised selections of the data set.[120]

2.3 Covariance Analysis

In mass spectrometry, it is difficult to untangle different reaction mechanisms leading to fragments with the same m/z. To understand these fragmentation pathways in greater detail, it is desirable to detect at least two charged co-fragments coming from the same molecule. In coincidence experiments, the primary condition is that, on average, less than one parent molecule is ionised per laser shot so that products created and detected in a single laser shot are assumed to come from the same molecule. Therefore, structural and/or electronic information describing the

causal fragmentation process can be obtained using techniques such as photoion-photoion coincidence (PIPICO) or photoelectron-photoion-photoion coincidence (PEPIPICO).[119, 130–132] Because coincidence experiments operate under low ion count rates, experiments can often require long acquisition times for good signal-to-noise ratios.[119, 130, 133] However, at FEL facilities, where limited experimental time is given to the user, high ion count rates (e.g., a comparable or greater number of ions detected than atoms in the target molecule) are utilised to obtain data with meaningful statistics within the allotted user time. These high count rates mean that the many detected fragments per laser shot are likely created from multiple parent molecules and, therefore, cannot be correlated through coincidence techniques.

Instead, to obtain information describing reaction processes creating two charged fragments, a complementary method to coincidence, covariance analysis, can be used. This is a statistical method for quantifying the linear correlation between two variables of interest (e.g., ToF or ion velocity) using the product of the deviations from their respective mean values, averaged over a large number of measurements (e.g., laser shots).[120, 134, 135] All covariance analysis methods used in this thesis were implemented using Python code. Example Python functions are given in the Appendices and the appropriate appendix is referenced within each of the following subsections.

2.3.1 Two-fold Covariance

An equation describing two-fold covariance, which is the covariance between two variables A and B, is given below:

$$\mathrm{cov}(A,B) = \langle (A - \langle A \rangle)(B - \langle B \rangle) \rangle = \langle AB \rangle - \langle A \rangle \langle B \rangle \tag{2.3.1.1}$$

where the expectation value of a variable ($\langle A \rangle$) is the signal measured averaged over M experimental cycles (i.e. laser shots):[119]

$$\langle A \rangle = \frac{1}{M_{\mathrm{shots}}} \Sigma_i^{M_{\mathrm{shots}}} A_i. \tag{2.3.1.2}$$

The $\langle AB \rangle$ term (also called the Sij term) is the correlated contributions to the covariance, and the $\langle A \rangle \langle B \rangle$ term (also called the SiSj term) is an estimate for

uncorrelated contributions to correct for any possible false correlations calculated in the first term. (This can be thought of as a background subtraction to isolate only correlated ion signals.) If $A = B$, the covariance results contain autocorrelation information, also termed variance, with an intensity equal to $\langle A^2 \rangle - \langle A \rangle^2$.[119] If A and B are both greater than their mean values (or if they are both less than their respective means), then the covariance will be positive, and A and B are assumed to be correlated. If A is greater than its mean and B is less than its mean (or vice versa), then the covariance will be negative, and A and B are assumed to be anticorrelated. If there is no correlation between A and B, then the covariance is zero.[136] In this thesis, only positive covariances are considered, and negative covariances are set to zero for simplicity of interpretation.

Covariance analysis requires the detection of at least two charged particles. Therefore, covariance analysis cannot be used to distinguish fragments produced in processes where only one charged product is generated, such as dissociative ionisation. Covariance observed between two ionic fragments is therefore (usually) a result of Coulomb explosion interactions. Next, different types of two-fold covariance representations–and how they can be used to disentangle different reaction mechanisms occurring in experiments–will be explained.

2.3.2 ToF-ToF Covariance Analysis

In mass spectrometry, variations in the mass spectrum of ions created per laser shot can be averaged out over many laser shots. The result is an accurate representation of the relative abundance of ions created via the interactions with the laser fields. ToF-ToF covariance (Appendix B) can be calculated to identify probable reaction pathways by assigning correlated ion pairs. In Equation 2.3.1.1, variable A is a ToF mass spectrum (which gives the intensity of ions detected per timebin ranging from 1 to n) and variable B is the transpose of the ToF mass spectrum. The multiplication of the data formatted in a column and row, respectively, results in a matrix consisting of $\mathrm{cov}(\mathrm{ToF}_i, \mathrm{ToF}_j) = c_{ij}$ elements.[119, 137]

$$\mathrm{cov}(\mathrm{ToF},\ \mathrm{ToF}^T) = \begin{pmatrix} c_{1,1} & c_{1,2} & \cdots & c_{1,n} \\ c_{2,1} & c_{2,2} & \cdots & c_{2,n} \\ \vdots & \vdots & \ddots & \vdots \\ c_{n,1} & c_{n,2} & \cdots & c_{n,n} \end{pmatrix} \tag{2.3.2.1}$$

Example mass spectra are given in Figure 2.11(a) and (b), which show the fragments of 1- and 2-iodopropane (C_3H_7I), respectively, produced following XUV-ionisation at the I 4d orbitals. The corresponding ToF-ToF covariance maps are given in (c) and (d), which show the correlated ion pairs produced via XUV-induced Coulomb explosions. These data sets have ToF resolutions high enough to distinguish fragmentation channels that produce alkyl cations with differing numbers of hydrogen atoms. Diagonal auto-variance ($\mathrm{var}(X) = \mathrm{cov}(X, x)$) lines with a positive gradient are visible.[130] Noise around the autovariance features in these examples is a result of 'shadowing' in the ToF (where some ion hits were assigned a slightly higher ToF) due to mismatches in the post-experiment data reconstruction process.

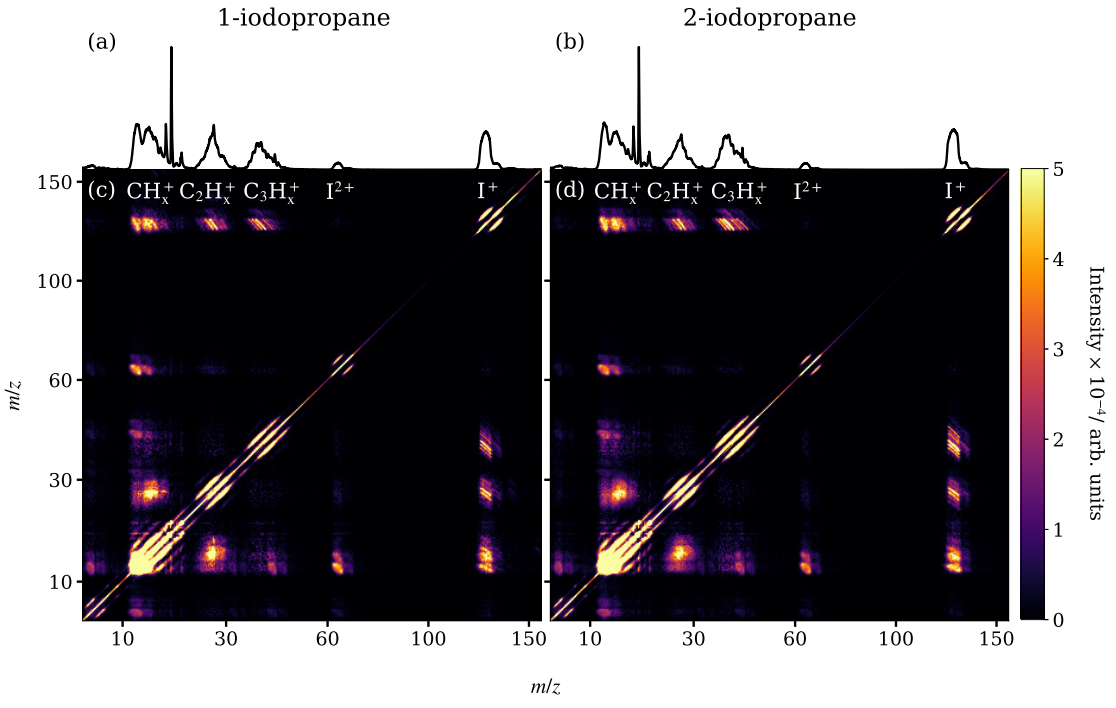

Figure 2.11: (a) and (b) are mass spectra recorded for fragments produced from XUV-ionisation of 1- and 2-iodopropane, respectively. (c) and (d) are the corresponding ToF-ToF covariance maps. Note the non-linear m/z axes.

Two-body Coulomb explosions, such as processes producing I^+ and $C_3H_7{}^+$, are characterised by a linear feature with a gradient of -1 because the co-fragments are produced with equal and opposite momenta. This means that, for explosions occurring parallel to the ToF axis of a spectrometer, one ion will be ejected towards the detector, with positive momentum along the ToF axis, and will arrive with an 'early' ToF within its own Newton sphere following velocity map imaging. The other ion is ejected away from the detector, with negative momentum along the ToF axis, and will arrive with a 'late' ToF within its own Newton sphere. The ToFs of the two ions will therefore be anti-correlated.[138] Fragmentation processes producing more than two fragments can result in blurred and diffuse ToF-ToF covariance features due to fragment momenta components acting in all three dimensions relative to one of the bond-breaking vectors. To conserve linear momentum, the momenta of all products along the ToF axis sum to zero. However, the momenta of only two ions along the ToF axis are often not back-to-back and the ToFs of the ions are not necessarily anti-correlated. The gradients of the corresponding ToF-ToF covariance features are related to the partitioning of momenta among the products and can, therefore, be used to infer the fragmentation processes generating these ions.

Consider a three-body fragmentation of a molecular dication, occurring concertedly, generating two charged products and a neutral co-product:

$$ABC^{2+} \rightarrow A^+ + B^+ + C. \tag{2.3.2.2}$$

The momenta of these three products is conserved in a plane. If the initial orientation of these three fragments is purely random, the feature in the ToF-ToF covariance map appears circular or elliptical.[138] Typically, three-body *sequential* fragmentation of a dication can be categorised into two regimes. The first of these is a delayed charge separation channel, following a primary dissociation into a neutral product and dication intermediate (AB^{2+}), which undergoes a secondary fragmentation via Coulomb explosion into two cationic products after some metastable lifetime.

$$ABC^{2+} \rightarrow AB^{2+} + C \rightarrow A^+ + B^+ + C. \tag{2.3.2.3}$$

If the kinetic energy released (KER) into products of the primary dissociation step is zero, the secondary products A^+ and B^+ recoil with equal and opposite momenta and the appearance of the corresponding feature in the ToF-ToF covariance is linear, with a gradient of -1, as in the true two-body case. The feature may be broadened if the KER of the primary dissociation step is non-zero and imparts some momentum into the intermediate.[138] A second type of sequential process follows a primary Coulomb explosion into two charged products, one of which is a metastable intermediate (BC^+) that further decays into cationic and neutral secondary products:

$$ABC^{2+} \rightarrow A^+ + BC^+ \rightarrow A^+ + B^+ + C. \tag{2.3.2.4}$$

The primary products have equal and opposite momenta and, if the KER of the secondary dissociation step is zero, then the velocity (v) of the secondary products will be equal to the velocity of the intermediate.

$$v_{BC} = v_B = v_C \tag{2.3.2.5}$$

The partitioning of momenta (p) in the secondary products is therefore related to the momenta of the primary products according to the partitioning of mass (m) in the secondary dissociation:

$$p_B = \frac{m_B}{m_{BC}} p_{BC} = -\frac{m_B}{m_{BC}} p_A. \tag{2.3.2.6}$$

As a result, the gradients of these features in the ToF-ToF covariance map are shallower than -1, at an angle of $\tan^{-1}(m_B/m_{BC})$. However, the KER of the secondary dissociation process is usually non-zero, and so this angle will be altered. If the KER takes a range of values (and is expected to be distributed as a Gaussian around some central value), the ToF-ToF covariance feature will also broaden.

Like a mass spectrum, the areas of different intensities in the ToF-ToF covariance map are representative of the relative contribution of various co-fragments to the overall mass spectrum of ions produced in Coulomb explosions. The summed intensity of a specific ToF-ToF covariance feature is directly proportional to the relative probability of a fragmentation channel generating that pair of ions.[137]

The number of parent molecules within the interaction region of the laser and molecular beam is assumed to follow a Poisson distribution. The products of induced photochemical reactions therefore are also expected to obey Poisson statistics, and so the covariance exhibited between two ions (A, B) is proportional to the number of parent molecules undergoing fragmentation into A and B.[119, 130] It is worth noting that the interpretation of the intensities of covariance features should be regarded with some caution as, for example, the detection efficiency of different ion species on the detector may result in slightly skewed yields.

ToF-ToF covariance is useful for determining which ions are produced in the same Coulomb explosion. However, ToF-ToF covariance features do not necessarily come from only one fragmentation channel but can be composed of contributions arising from different fragmentation pathways or different initial parent charge states that generate the same pairs of ion species. Therefore, ToF-ToF covariance alone is not sufficient to assign which fragmentation channels give rise to certain pairs of ions. To understand the different processes that generate the same correlated ion pairs, it is useful to analyse the relative recoil of the two ions.

2.3.3 Recoil-frame Covariance Analysis

To deduce the relative recoil angle between two fragment ions, as well as the KER of the explosion, recoil-frame covariance can be implemented (Appendix C), which makes use of the position-sensitive information gained in VMI experiments. Data is firstly filtered by m/z to select a reference ion (A) and an ion of interest (B). The correlations between signal intensities in each pixel of the VMI images of the two ions are calculated. This is demonstrated in Figure 2.12: (a) and (b) are the ion images of ion A and ion B, respectively. Pixels where ions have been detected are labelled 1-4, corresponding to different 'laser shots'. For each laser shot, covariance maps are plotted in (c)-(f), showing the relative positions of ion hits on the detector. Since the orientation of the gas molecule within the spectrometer is random relative to the ToF axis, each covariance map is rotationally transformed so that the trajectory of the reference ion is the same in each case, allowing all

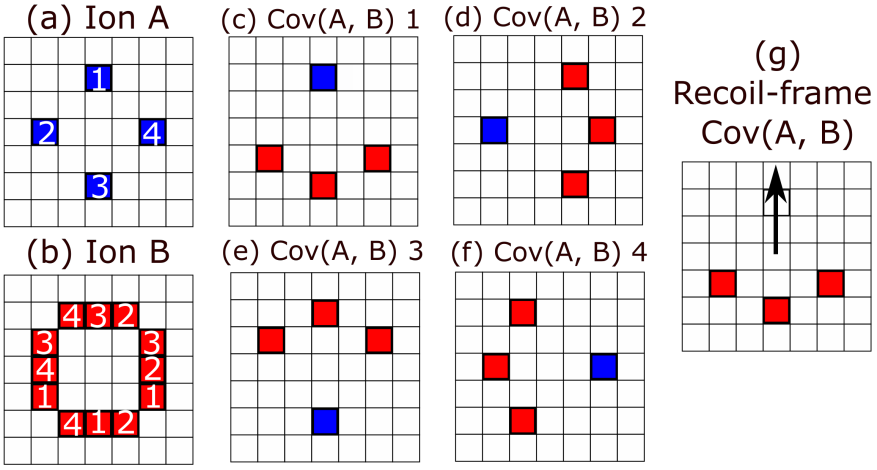

Figure 2.12: Schematics depicting the process of generating recoil-frame covariance maps. (a) and (b) are the ion images of ion A and ion B, respectively. (c)-(f) are covariance maps for laser shots 1-4. (g) is the total recoil-frame covariance map, where (c)-(f) have each been rotated such that the position of ion A is the same in each case.

maps to be averaged.[120, 139] This yields the recoil-frame covariance map in (g), which shows the position of ion B hitting the detector relative to ion A. From this, the most probable recoil angle between the two fragments can be obtained. The portion of kinetic energy of the total explosion partitioned into the ion of interest is related to the radial distribution of the covariance in the same way that kinetic energy and radius are related in VMI ion images.

Example recoil-frame Sij, SiSj, and covariance maps are given in Figure 2.13(a), (b), and (c), respectively. By subtracting (b) from (a), the recoil of I^+ ions relative to CH_2I^+, produced from XUV-ionisation of CH_2I_2 into $CH_2I_2{}^{2+}$, is obtained. The white arrow represents the direction of the trajectory of CH_2I^+ ions, and the areas of positive intensity represent the most probable recoil of I^+ ions relative to the reference. All atoms of the parent molecule are accounted for in this ion pair and they recoil in a back-to-back Coulomb explosion, with equal and opposite momenta. In the recoil-frame image, this is visualised by the 180° recoil feature, the radial distribution of which corresponds to the momentum partitioned into I^+ in such an explosion. A second example is given in Figure 2.14, showing the relative recoil of two I^{3+} products of $CH_2I_2{}^{Q\geq 6+}$. A back-to-back feature is observed, as in the previous example, which corresponds to a three-body fragmentation with

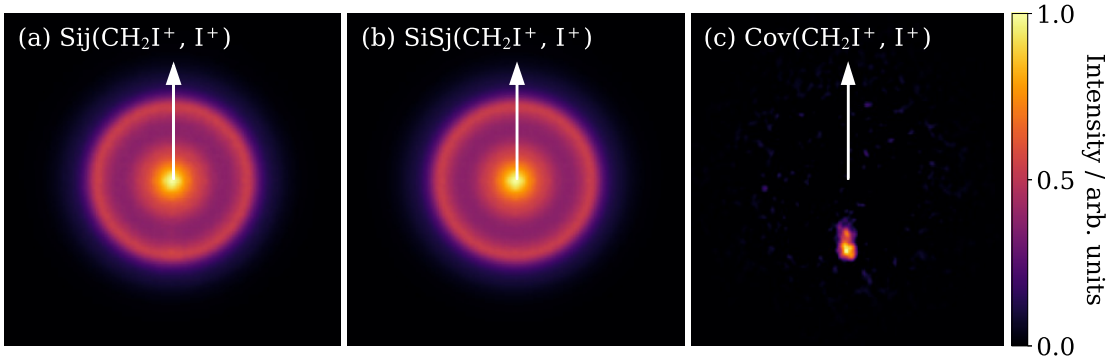

Figure 2.13: Sij (a), SiSj (b), and recoil-frame covariance (c) maps of the recoil of I^+ relative to CH_2I^+, produced in a two-body explosion of $CH_2I_2{}^{2+}$.

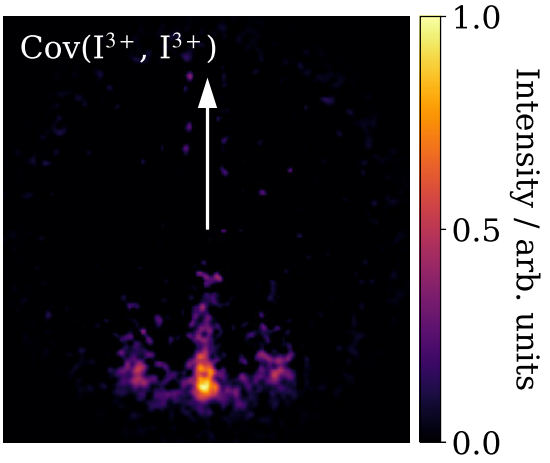

Figure 2.14: Recoil-frame covariance map showing the recoil of I^{3+} relative to a second I^{3+}, produced in a three-body fragmentation process of $CH_2I_2{}^{Q\geq 6+}$.

a neutral spectator co-fragment that is not involved in the Coulomb explosion. The mutual Coulombic repulsion between the two charged species determines their recoil trajectories. A second, off-180° feature is visible. For such a feature to arise, there must be a third charged fragment (in this case, it is $CH_x{}^+$, where x=0,1,2) that is involved in the Coulomb explosion.

Recoil-frame covariance can be implemented for both 3D and 2D data (where 3D refers to a great enough ToF resolution such that the momenta along the ToF axis can be retrieved, whereas this is not possible for 2D data) since it only depends on the x and y positions on the detector and not the momentum resolution along the ToF axis. As shown previously, it is advantageous to use narrow slices of the ion ToF peaks in the analysis of 2D data. The corresponding radial distribution

can be assumed to more closely reflect the correct distribution of ions with a given m/z and the kinetic energy distribution obtained from recoil-frame covariance analysis will be more accurate as a result.

2.3.4 Newton-frame Covariance Analysis

When the resolution along the ToF axis is great enough to retrieve 3D momentum distributions for each m/z, Newton-frame covariance techniques can be implemented (Appendix D), which yield more accurate energetic information since they do not suffer from using a 2D projection of the 3D Newton sphere. Momentum vectors are obtained for an ion of interest recoiling relative to a reference ion's trajectory. In a two-body explosion, the momentum vectors should be back-to-back due to conservation of momentum. In explosions producing more than two products, the momenta of the two ions used in the covariance calculation can be used to calculate the momentum of the remaining mass of the molecule under the assumption that the explosion is a three-body process so that the momenta in all three dimensions sum to zero. Therefore, the inferred momentum should be considered with caution if the missing mass is not a single atom, as a molecular fragment could potentially undergo further fragmentation.

An example Newton-frame covariance map is given in Figure 2.15, which shows the covariance between CH_3^+ and I^+, produced via XUV-ionisation of 2-iodopropane of the I 4d orbital, with the momenta of I^+ ions limited to within the range of 60-185 a.u (atomic units of momentum) for simplicity (the more complicated covariance map obtained when using the full I^+ momentum distribution is shown in Section 2.3.7). The momentum of I^+ is constrained to the positive x-direction, shown by the white arrow, which again represents the direction of the trajectory of the reference ion. The relative momentum of the ion of interest (CH_3^+) is given in the top half of the image, and through conservation of momentum, the predicted momentum of the remaining mass of the molecule is calculated and given in the bottom half of the covariance map. Two features are observed in this covariance map. The first is a low momentum feature appearing at 180° relative to the direction

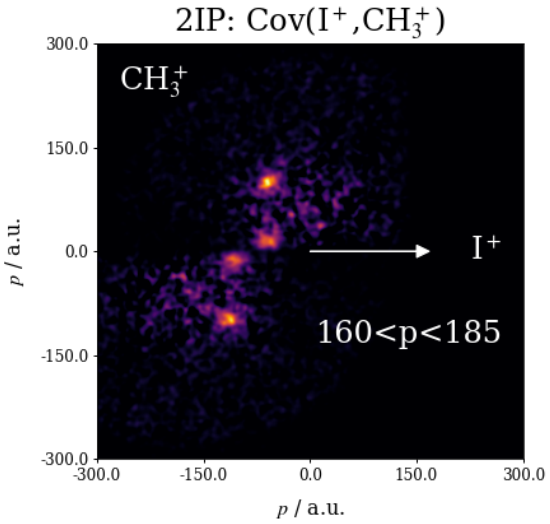

Figure 2.15: Newton-frame covariance map showing the momenta of CH_3^+ ions relative to I^+ ions, produced via XUV-ionisation of 2-iodopropane. Covariance has been calculated for I^+ ions with momenta (p) within a range of 160-185 a.u..

of the trajectory of the I^+. This corresponds to a fragmentation of $C_3H_7I^{2+}$ into the two charged products CH_3^+ and I^+. The remainder of the molecule remains neutral and any impulse from its dissociation from the charged fragments has a negligible effect on the recoil angle between two ions, which is determined by their mutual Coulombic repulsion. The second feature observed here is a higher momentum feature with a recoil angle off of 180°. For this feature to arise, at least one other ionic fragment is produced in the corresponding fragmentation mechanism, resulting in a higher energy Coulomb explosion and an off-180° recoil angle between the ion of reference and the ion of interest.

An alternative Newton-frame covariance representation (Appendix E) can also be used to deduce the relative momenta of a pair of ions as well as the expected relative momentum distribution of the remaining mass of the molecule. An example is given in Figure 2.16, which shows the covariance calculated for I^+ and $C_4H_2^+$ ions produced by XUV-ionisation of iodobenzene at the I 4d orbitals. The relative momenta of these two ions are shown in the top right and bottom right quadrants, respectively. The calculated expected momenta of the rest of the molecule is plotted in the left half of the image. The 180° recoil angle between I^+ and $C_4H_2^+$ is indicative of a Coulomb explosion of a molecular dication, and the remaining mass

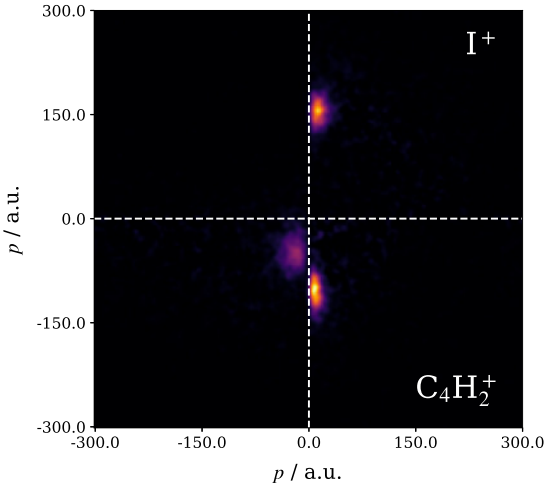

Figure 2.16: An alternative representation of Newton-frame covariance, showing the momenta of fragments produced by XUV-ionisation of iodobenzene. The reference ion (I^+) is plotted in the top right quadrant, the ion of interest ($C_4H_2{}^+$) is plotted in the bottom right quadrant, and the momenta of the remaining mass of the molecule–inferred through momenta conservation–is plotted on the left two quadrants.

of the molecule is neutral and gains less momenta from the fragmentation process than either of the cations used in the covariance calculation.

In both Newton-frame representations, the features 'at 180°' lie next to the x-axis but are not exactly *on* the axis. This is an artifact of the representations themselves. The features are expected to lie along the bisectors of the covariance maps, which correspond to the edge of a momentum bin. Therefore, intensity must appear either in the bin above or below the bisector. Furthermore, in a normally distributed momentum distribution, intensity is expected to spill over to either side of the bisector. However, in both representations, the momenta of the ion of interest is constrained either to a half or quadrant of the overall map. Therefore, intensity only appears on one side of the bisector, resulting in a distribution that has a maximum slightly off of the x-axis. Despite this, these features are considered effectively 180° to the trajectory of the reference ion.

2.3.5 Overlapping Newton Spheres

When Newton spheres of ions with different m/z are well separated by their times of flight, interpreting covariance maps is usually straightforward. For neighbouring

fragment masses differing by a single hydrogen, resolving their individual Newton spheres requires long ToFs, and the overlap of neighbouring Newton spheres becomes more pronounced as the mass of the molecule and its fragments increase because m/z is proportional to ToF^2. Long ToFs can be obtained by using either a physically longer ToF tube or by slowing all ions by altering the VMI conditions. However, obtaining long enough ToFs to resolve Newton spheres by numbers of hydrogen atoms is often not experimentally feasible: lengthening the ToF tube may be physically limited by the size and shape of its surroundings. A longer time of flight could also be achieved by using a lower VMI voltage. The increased ToFs would allow the Newton sphere to expand more before hitting the detector. However, as a result, the radius of the Newton sphere may be too large to be fully focused on the detector. Furthermore, decreasing the VMI voltages also decreases the velocity of the Newton sphere along the ToF axis and the impact of ions on the detector might become too low to be properly detected.

Figure 2.17 shows the effects of overlapping Newton spheres on covariance analysis and how to remove misleading signals. Covariance between $C_6H_2^+$ and I^+ (produced from XUV-ionisation of iodobenzene at the I 4d orbital) is used to illustrate this. In (a), the overlapping circles in the schematic represent $C_6H_x^+$ Newton spheres. Taking a broad ToF range (marked by the solid black lines) to capture the entire $C_6H_2^+$ Newton sphere results in a bright covariance signal at 180° relative to I^+, and another signal with a recoil angle off-180° relative to I^+. It is this latter signal that is 'false' and arises due to the $C_6H_2^+$ Newton sphere overlap with neighbouring $C_6H_x^+$ fragments. This overlap needs to be reduced to properly interpret the reaction dynamics producing the two ions of interest. The first step to do this is illustrated in (b): the ToF range selected for $C_6H_2^+$ is narrowed to reduce the number of ions from neighbouring Newton spheres used in the covariance calculation. The corresponding covariance map shows that the off-180° feature persists. To fully remove the signal arising from overlapping Newton spheres, the width of the I^+ ToF must also be considered, as shown in (c). By selecting a narrow I^+ ToF range, only ions generated approximately perpendicular to the ToF axis

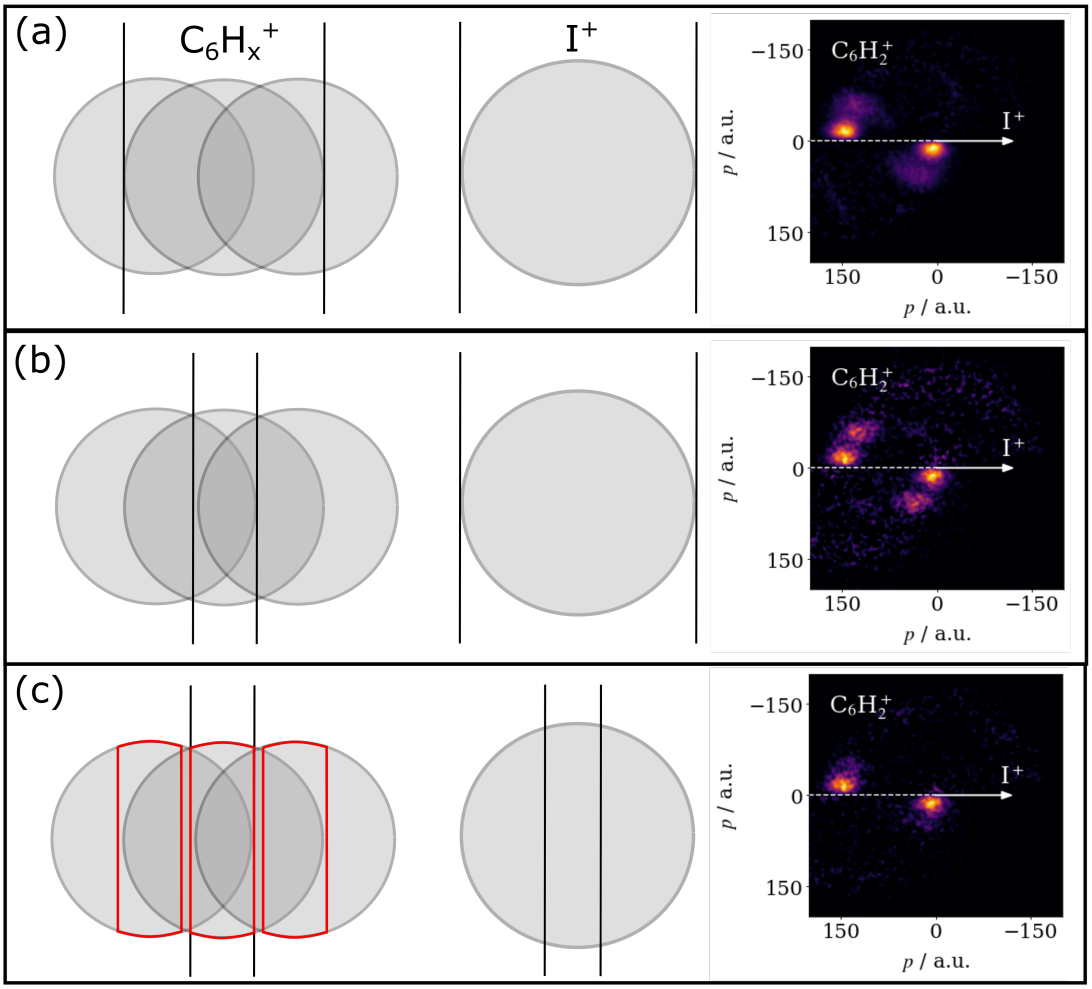

Figure 2.17: A depiction showing how the ToF region of ions used in Newton-frame covariance affects the appearance of covariance features, using covariance between I^+ and $C_6H_2^+$ produced via XUV-ionisation of iodobenzene. (a) Full ToF ranges are used for both ions. (b) A narrow ToF is selected for the $C_6H_2^+$ ion, and a full ToF range is used for I^+. (c) A narrow ToF range is used for both ions–restraining the ToF of I^+ consequently also restrains the $C_6H_2^+$ ions that could possibly be covariant with I^+ to the regions highlighted in red.

are selected and ions generated with momentum parallel or anti-parallel to the detector are ignored. As a result, this therefore also ignores any $C_6H_x^+$ fragments with momentum (anti-)parallel to the detector during the covariance calculations. The ToF limits imposed on the I^+ Newton sphere consequentially impose the same limits on the $C_6H_x^+$ Newton spheres, and the only ions that can be considered in the covariance calculation are highlighted in red in (c). When the I^+ ToF range is narrow enough, the imposed $C_6H_x^+$ ToF ranges that can be used in covariance

become discrete. The covariance map shows that such a procedure successfully reduces the intensity of the covariance with neighbouring fragments, leaving only the true feature that shows a 180° recoil angle between I^+ and $C_6H_2{}^+$.

2.3.6 Three-fold Covariance

Covariance analysis is not limited to two variables but can be extended to three using the following equation:[119, 120]

$$cov(A, B, C) = \langle (A - \langle A \rangle)(B - \langle B \rangle)(C - \langle C \rangle) \rangle \,. \tag{2.3.6.1}$$

For three random variables, if one of them is uncorrelated, their three-fold covariance is zero. Any uncertainty in the inferred momentum of a third fragment calculated in two-fold Newton-frame covariance is bypassed in three-fold covariance as the momentum of a third fragment comes directly from the experimentally obtained momentum information of the third fragment. This method can therefore separate three-fold covariances of n-body explosions (Appendix F). Furthermore, three-fold covariance can also aid in the assignment of covariance features obtained in two-fold calculations since features arising from three-body fragmentation processes into two charged fragments and neutral co-fragments will not show up in three-fold covariance. However, three-fold covariance is not without its own difficulties. The calculations take longer than two-fold covariance and the total covariance signal is reduced relative to two-fold covariance features because the product of the detection efficiency of three co-fragments is lower than that of only two co-fragments. This also means that the relative covariance intensities of different fragmentation pathways cannot be straightforwardly compared between two- and three-fold covariance.

The example three-fold Newton-frame covariance map given in Figure 2.18 can be interpreted in the same way as Figure 2.15. However, in this case, the lower half is not deduced by conservation of momentum but is the observed momenta of C^+ ions relative to C^{2+} and I^{2+} ions produced via XUV-ionisation of the I 4d orbitals of 2-iodopropane.

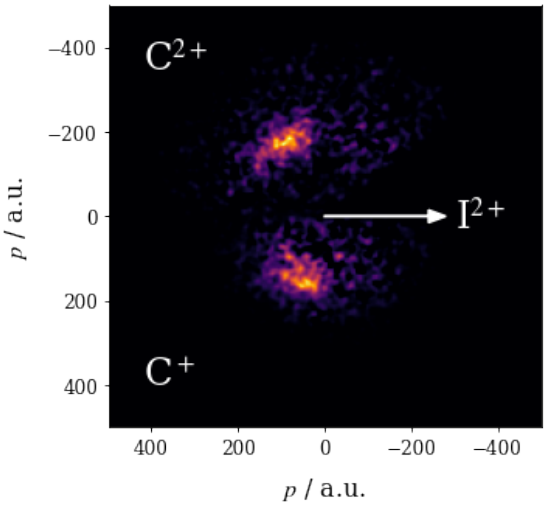

Figure 2.18: Three-fold covariance showing the recoil of C^{2+} and C^{+} relative to I^{2+}, generated by XUV-ionisation of 2-iodopropane at the I 4d orbitals.

2.3.7 Native-frame Covariance Analysis

For sequential fragmentation processes, where a fragment produced in the primary process is used as the ion of reference, and a fragment produced in the secondary process is the ion of interest, it can be helpful to present the Newton-frame covariance maps in the frame of reference of the intermediate fragment, i.e. its 'native-frame'.[59] As stated above, products of a primary two-body fragmentation process (ABC→A+BC) are generated with equal and opposite momentum. Then, when an intermediate (BC) fragments into secondary products, the secondary products contain momentum contributions from both the secondary fragmentation process and the primary fragmentation process. The momentum that the intermediate gained in the primary process is split between secondary products according to their mass ($m_{\mathrm{B}}/m_{\mathrm{BC}}$). This expected contribution can be subtracted from the products' observed momenta to deduce the momenta gained purely from the secondary process.[58, 59, 140] The secondary fragmentation step can then be analysed independently of the primary fragmentation process by performing native-frame analysis. Such procedures have been used previously in coincidence studies,[58, 59, 141] and these momentum considerations have been applied in this thesis to covariance analysis to determine in-depth descriptions of multi-

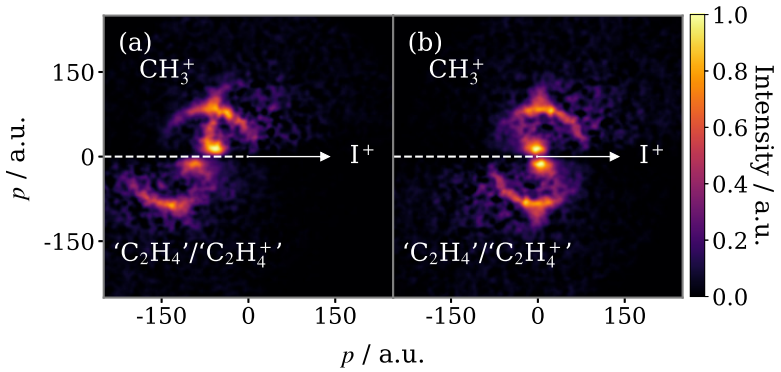

Figure 2.19: (a) The Newton-frame and (b) native-frame covariance representations showing the momenta of CH_3^+ ions relative to I^+ ions, produced from XUV-ionisation of 2-iodopropane at the I 4d orbitals.

step fragmentation processes when the 3D momenta of ions are retrievable from experiment (Appendix G). Figure 2.19 (a) is the Newton-frame representation of the momenta of CH_3^+ ions relative to I^+ ions, produced via XUV-induced ionisation of 2-iodopropane at the I 4d orbitals, and (b) is the same covariance map transformed into the native-frame of a $C_3H_7^{+/2+}$ intermediate.

2.3.8 Accounting for Experimental Fluctuations

Fluctuating experimental parameters that cause fluctuating event rates can lead to false covariance correlations. Such parameters include FEL pulse intensity, which varies on a shot-to-shot basis. One method that can be used to account for this is partial covariance, defined by the following equation:[130, 134]

$$pcov(A, B; I) = cov(A, B) - \frac{cov(A, I)cov(I, B)}{cov(I, I)} \qquad (2.3.8.1)$$

where I is a variable that accounts for varying experimental parameters (for example, the total ion count). However, if fluctuations are non-linear, partial covariance fails. Contingent covariance can instead be used, which calculates covariance for equal-sized subsets of the data that are filtered depending on the measured fluctuating parameter and averaged over the subsets. This process can be written as:

$$ccov(A, B) = \langle cov(A, B|P) \rangle = \frac{1}{K} \Sigma_{k=1}^{K} cov(A, B|P = P_k) \qquad (2.3.8.2)$$

where k is the number of normally distributed data subsets and is P_k assumed to be constant. This method gives the same result as partial covariance for processes with cross-sections linearly proportional to light intensity and is more versatile and easier to implement.[130]

Figure 2.20 shows the native-frame covariance calculated for CH_3^+ and I^+ (which was also given in Figure 2.19), calculated for different numbers of contingent bins (n). The number of bins used should be chosen so that noise is reduced without compromising the number of statistics within each bin. The contingent bins were filtered based on the fluctuating FEL pulse energy and contained equal numbers of laser shots. This selection process is demonstrated in Figure 2.21, which shows the attenuated pulse energy of the FEL recorded during the experiment investigating XUV-ionisation of 2-iodopropane at the I 4d orbitals. The dashed lines show how the data were split into 10 subsets with equal numbers of statistics based on this experimental fluctuating parameter. In Figure 2.20, when n=5, a high energy 'tail' is visible that disappears when a greater number of bins are used. The distributions obtained for n=10, 50, and 100 are very similar, and so n=10 was used for the analysis of this data set as it yielded the best signal-to-noise ratio without compromising the statistics used in each covariance calculation.

2.3.9 Integrated Intensities of Covariance Features

As mentioned, the intensity of covariance features observed between a pair of ions is indicative of their statistical contribution to the overall mass spectrum. By integrating the intensities of features obtained through recoil-frame or Newton-frame analysis, quantitative values can be assigned to observable fragmentation channels (assuming equal detection efficiencies of all ion species). Corresponding uncertainty values in integrated intensity can be retrieved for covariance features by a bootstrapping method: a dataset can be divided into many subsets comprising the same number of (randomly selected) laser shots, and covariance can be performed on each subset. Then, the feature of interest in each covariance map is integrated, plotted on a histogram, and fit with a Gaussian distribution. The centre of the

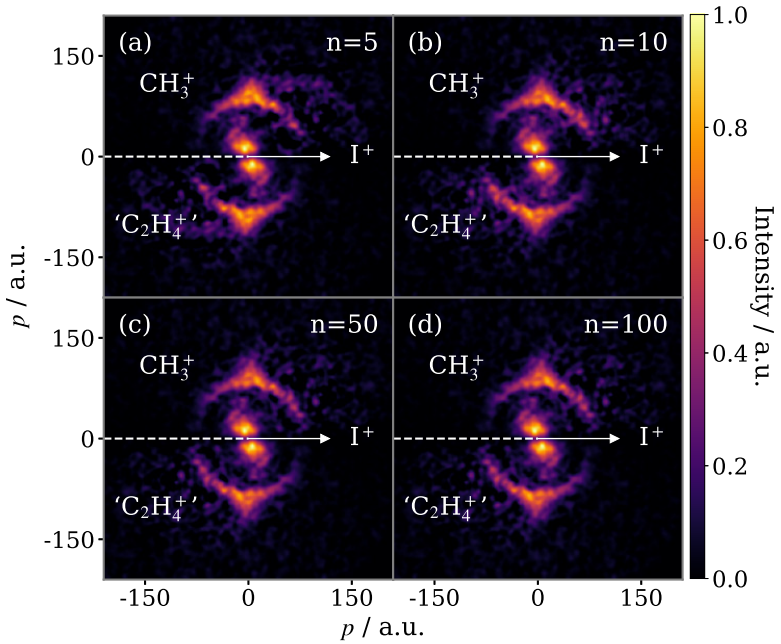

Figure 2.20: Native-frame covariance distributions of CH_3^+ relative to I^+ from 2-iodopropane, calculated using different numbers of contingent bins (n). The momenta of the remaining mass of the molecule is inferred using conservation of momentum.

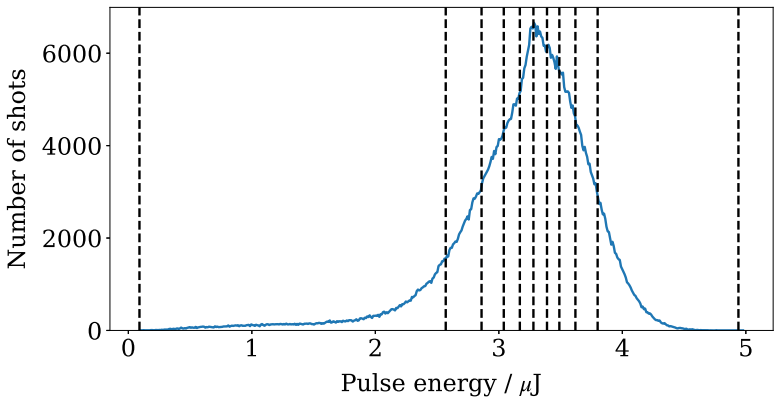

Figure 2.21: The attenuated XUV pulse energy distribution obtained from shot-to-shot measurements made for an experiment investigating the XUV-ionisation of 2-iodopropane at the I 4d orbitals. The ranges encapsulated by the dashed lines indicate the subsets of data used in contingent covariance with 10 bins.

Gaussian distribution retrieves the average integrated intensity of a covariance feature, and the width (σ) of the Gaussian distribution can be used as an uncertainty in the average value. An example of this method is given in Figure 2.22, which shows the approximately normally distributed histogram of intensities of features obtained from covariance calculated between I^+ and $C_6H_2^+$ ions–products of XUV-ionisation

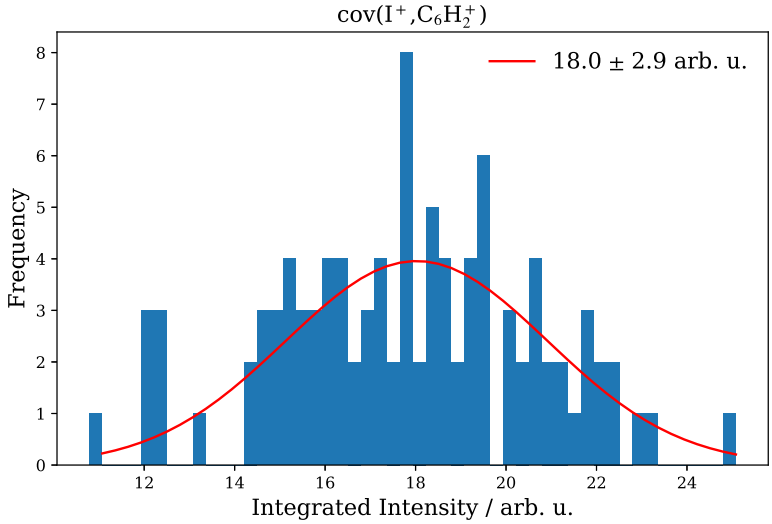

Figure 2.22: A histogram of integrated intensities of the covariance observed between I^+ and $C_6H_2{}^+$ products of iodobenzene, created by XUV-ionisation, obtained by a bootstrapping method where covariance was calculated for 100 subsets of the data, each comprising 50,000 laser shots.

of iodobenzene at the I 4d orbitals.

This bootstrapping method is used to acquire uncertainties in integrated covariance intensities in Chapter 4 and Chapter 5. For the sets of results presented in each of these chapters, the bootstrapping method used 100 subsets of the corresponding data, each made up of 50,000 laser shots.

2.4 Conclusion

This chapter has highlighted the main experimental methods used in the subsequent results chapters, as well as the theory of different analytical techniques and how to interpret their results. These analytical methods will be used in the following chapters to characterise correlated ion distributions of increasingly complex mass spectra. The abilities and limitations of both the experimental and analytical techniques to disentangle concurrent fragmentation channels will be discussed.

A little nervous breakdown can work wonders for a girl.

— Rory Gilmore, The Gilmore Girls

3

Photodissociation of CH_2I_2 at 202.5 nm

Contents

3.1 Introduction

In this chapter, pump-probe CEI techniques will be used to follow the fragmentation dynamics of CH_2I_2 initiated at 202.5 nm to show how fragmentation processes of relatively 'simple' molecules can be easily examined in time-resolved studies. In particular, the results presented will demonstrate how CEI and time-dependent covariance analysis can map nuclear motion along multiple degrees of freedom.

Halomethanes are the simplest of the halogenated hydrocarbons, and it is important to understand how they react following UV-photoabsorption due to their

participation in sea spray aerosol and particle formation and the catalysis of ozone depletion, contributing to climate change.[5, 142–151] The photodissociation of dihalogenated methanes (CH_2X_2) is more complex than the photodissociation of their monohalogenated counterparts (CH_3X), the latter of which can be modelled as an approximately linear process.[12, 20, 72, 152–154] Increasing the number of halogen substituents increases the number of photo-absorption sites and UV-accessible fragmentation and isomerisation pathways, leading to more complicated reaction dynamics. Dihalogenated methanes are, therefore, ideal targets for exploring the ability of CEI to map fragmentation channels along multiple degrees of freedom.

The UV-absorption spectrum (Figure 3.1) of CH_2I_2 consists of four broad distributions that correspond to transitions from the electronic ground state to at least five electronically excited states. The highest energy of the absorption bands shown, $2A_1$, is centred at 212 nm.[155–159] The photodynamics of the high energy shoulder of the $2A_1$ band are studied here using a 202.5 nm, 6.2 eV UV pump pulse and a 13.1 nm, 94.6 eV XUV probe pulse generated at the Free electron LASer in Hamburg (FLASH). At this wavelength, both the spin-orbit relaxed ($D_0^0 = 2.155\,\text{eV}$) and excited ($D_0^* = 3.098\,\text{eV}$) C-I (2.12 Å) dissociation pathways of CH_2I_2 are energetically accessible with one 202.5 nm pump pulse:[142, 160–163]

$$CH_2I_2 \rightarrow CH_2I + I^{0/*}. \tag{3.1.0.1}$$

In addition, one photon is also sufficient to induce a three-body dissociation where both C-I bonds break (i.e. the C-I bond in CH_2I breaks, $D_0^0 = 2.834\,\text{eV}$):[157]

$$CH_2I_2 \rightarrow CH_2 + 2I. \tag{3.1.0.2}$$

The XUV pulse energy used in this study was tuned to site-selectively ionise iodine at the I 4d orbitals, resulting in rapid charge build-up via AM decay and highly energetic Coulomb explosions.[67, 154, 164–166] The X-ray absorption cross-section of iodine for a photon of 94 eV is assumed to be equal to that of Xe^+ (27.7 Mb), which is isoelectric with iodine.[167–169] (By comparison, the absorption cross-section of hydrogen at 95 eV is on the order of 10^{-2} Mb, and those of the carbon

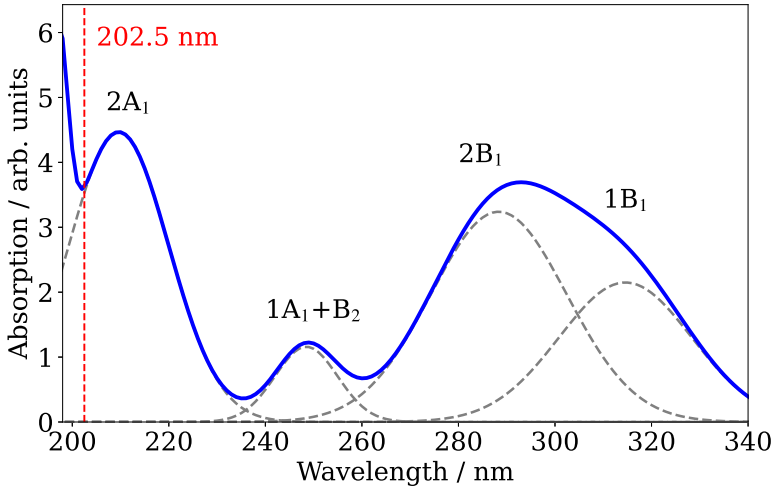

Figure 3.1: The combined and deconvoluted UV-absorption spectrum of CH_2I_2 (adapted from H. Xu *et al.*, J. Chem. Phys. 117(12), 2002) showing four Gaussian distributions centred at 312, 288, 249, and 212 nm. These correspond to transitions from the electronic ground state to at least five electronically excited states.[157–159]

2s and 2p orbitals are on the order of 10^{-1} Mb.)[170] The time taken for charge to build up on the molecule occurs on some finite (within ∼10 fs) timescale, and charge generated on multiply ionised iodine atoms can redistribute over the entire molecule before Coulomb explosions take place, as shown by XUV experiments carried out on CH_3I and CH_2I_2 by Fukuzawa and Ueda using the FEL at SACLA, Japan.[72]

The way charge redistributes across the molecule can be investigated as a function of time using pump-probe spectroscopy. Here, charge redistribution via 'charge transfer' during photodissociation is specifically of interest. These processes occur when an electron on a neutral co-fragment is donated to a highly ionised cation, provided that the potential energy barrier to charge transfer is less than the ionisation potential of the radical. Two cations are thus created, which repel, causing a Coulomb explosion.[171] The energy barrier to charge transfer is dependent on the separation between the electron and cation, and the distance where charge transfer becomes no longer energetically accessible is termed the critical distance (R_{crit}). For CH_3I, charge transfer can be considered an approximately linear mechanism as its centre of mass lies along the C-I bond and the Coulomb explosion between I^+ and CH_3^+ is approximately ballistic. Consequently, the charge transfer from CH_3 to iodine ions in high charge states (I^{q+}, $q \geq 2$) has been successfully predicted

using a classical over-the-barrier (COB) model, which depends on the charge on the cation (q) and the ionisation potential (IP) of the radical providing the electron via the following equation:[21, 172]

$$R_{\text{crit}}(q) = \frac{e^2}{4\pi\epsilon_0}\frac{1+2\sqrt{qe}}{\text{IP}} \tag{3.1.0.3}$$

where e is the charge of an electron, and ϵ_0 is the permittivity of vacuum.

Here, charge transfer reactions observed in CH_2I_2 at 202.5 nm are used in conjunction with time-dependent covariance analysis to identify and characterise the structural changes occurring during photodissociation. The dynamic change in the kinetic energy of correlated I^{q+} fragments, and onsets of dissociative features characteristic of charge transfer processes at positive pump-probe delays (where the pump pulse arrives before the probe pulse), indicate that CH_2I_2 undergoes concerted three-body fragmentation at 202.5 nm. The results presented demonstrate how CEI and covariance analysis can be used to simultaneously characterise nuclear motion along multiple degrees of freedom (here, the C-I and I-C-I coordinates).

3.2 Methods

3.2.1 Experimental

The experiment was carried out at BL1 at FLASH using the double-sided VMI mass spectrometer CAMP.[173, 174] A gaseous CH_2I_2 molecular beam was seeded in He gas and expanded into the VMI chamber as a continuous jet via two skimmers. The molecular beam was perpendicularly intersected by the pump and probe lasers in the reaction region. Both lasers were polarised parallel to the detection plane of the VMI spectrometer. Ions created in the interaction region were accelerated by the VMI voltages down the ToF tube onto a position-sensitive, dual-stacked MCP detector coupled to a P47 phosphor screen (Photonis). A PImMS camera, with a 324×324 pixel PImMS2 sensor, recorded the arrival times of ions hitting the detector (to a precision of 25 ns), as well as their x, y coordinates.

The wavelength of the XUV probe laser FLASH [λ_{probe} = 13.1 nm, bandwidth=0.1 nm (FWHM)] was selected to resonantly and site-selectively ionise the

iodine 4d orbitals. The un-attenuated pulse energies of each laser shot were recorded by the FLASH DAQ system. The laser passed through a combination of Nb 384 nm and Zr 202 nm filters, which have transmission coefficients of approximately 0.143 and 0.49, respectively.[175] The distribution of attenuated pulse energies is given in Figure 3.2. The average XUV pulse energy was found to be 1.8 ± 0.4 μJ via a Gaussian fit to this distribution. Based on previous experiments at this facility, the XUV pulse duration and focal size within the interaction region were estimated to be 50-60 fs and 8-10 μm.[174, 176] The assumed Gaussian intensity of the XUV laser at the interaction region was therefore approximately 8.5×10^{13} W cm^{-2}.

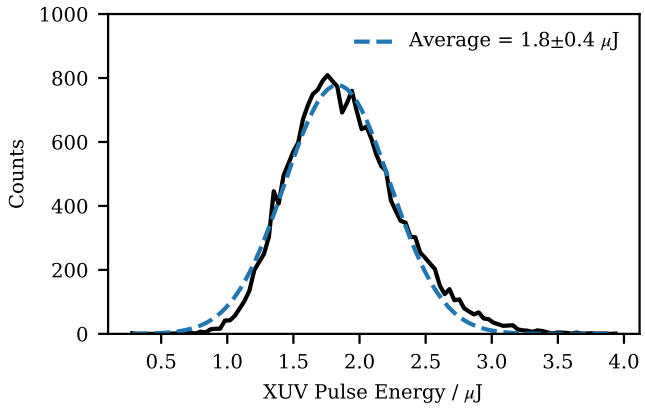

Figure 3.2: The attenuated XUV pulse energy distribution recorded for the UV+XUV experiment. The average pulse energy was found via a Gaussian fitting.

The UV pump wavelength [λ_{pump} = 202.5 nm, bandwidth=0.75 nm (FWHM)] was produced from the 810 nm output of the FLASH pump-probe laser system comprising of a Ti:sapphire oscillator (Quantum Gecco) and a 10 Hz chirped pulse amplifier (Coherent Hidra-25). The pulse energy and duration of the 810 nm pulses were 12 mJ and 57 ± 3 fs, respectively. Of this, 8 mJ was passed through a 50/50 beamsplitter. The reflected half of the beam was frequency tripled by a pair of β-BBO crystals and the fundamental frequency was separated by a series of dichroic mirrors. The transmitted half of the beam was split again with a second 50/50 beamsplitter. One half was retained for cross-correlations measurements, and the second half was recombined with the third harmonic using a BBO crystal to generate the fourth harmonic (202.5 nm) through sum-frequency generation.

A second set of dichroic mirrors separated the 202.5 nm from the fundamental and third harmonics. The approximate UV pulse energy obtained was 6 μJ, which was reduced to 2.7 according to the transmission of the beamline after the measurements were made ($\sim$45%). The pulse duration was determined from UV/IR cross-correlations of the fundamental and fourth harmonic pulses in Xe gas that produced a transient Xe^+ signal via two-colour multiphoton ionisation. The UV pulse duration was found to be 143 $\pm$ 15 fs, and the focal diameter (beam waist) was assumed to be 38 μJ. The Gaussian intensity of the pump pulse was, therefore, estimated to be 3.3 $\times$ 10^{12} W cm^{-2}.

The pump-probe delay between the UV and XUV arrival times at the interaction region was varied by a computer-controlled delay stage. In this work, positive delays correspond to the arrival of the UV pump pulse before the arrival of the XUV probe pulse. Zero pump-probe delay (t_0) is where the UV and XUV arrived at the interaction region at the same time. Since the UV was generated using IR laser pulses, the UV/XUV t_0 was determined using a two-step process using Xe gas: the results of UV/IR cross-correlation outlined above were considered with the delay-dependent Xe^{2+} ion yields (Figure 3.3), created by XUV Xe 4d ionisation and AM decay into Xe^{2+}, followed by IR ionisation to produce Xe^{3+}. From this, an IR/XUV t_0 could be obtained. The UV/XUV t_0 was determined by comparison of the IR/XUV t_0 and UV/IR t_0. Time-dependent IR/XUV data was obtained for Xe before and periodically throughout the experiment to ensure the UV/XUV t_0 remained consistent. Coulomb explosion data of CH_2I_2 was acquired in delay steps of 50 fs around the UV/XUV overlap time and in 200 fs from 3 ps onwards.

3.2.2 Data Analysis

For each laser shot, a unique shot identifier was recorded by the DAQ system at FLASH and by the PImMS camera. The DAQ system also recorded photon diagnostic information, whereas PImMS recorded ion arrival times and hit positions. Both recorded the pump-probe delay. The shot identifiers were used to correctly match information recorded by both systems. Due to the signal amplification that

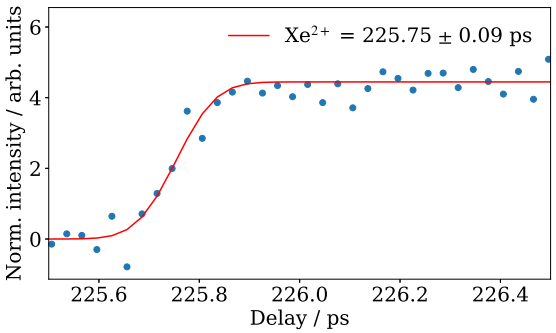

Figure 3.3: Time-dependent increase in yield of Xe^{2+} obtained via an IR-pump XUV-probe ionisation mechanism. A CDF function was fitted to obtain a time corresponding to the temporal overlap of the IR and XUV laser pulses, which is later defined as the IR/XUV t_0.

takes place when an ion is incident on the MCP detector, 2D Gaussian clusters were centroided across time and space via the nearest neighbour algorithm to improve the true count of ion hits (as described in Section 2.2.5). The radii of ions hitting the detector are non-linearly related to the ions' kinetic energy. Ion trajectory simulations using SIMION 8.1. were used to obtain a fifth-order polynomial relating radii and kinetic energy to calibrate for various fragment ion charge states. Average energy and momentum values were obtained using Gaussian fits implemented using the SciPy python package (`scipy.optimize.curve_fit`), along with the corresponding widths of the Gaussian distributions (σ) and uncertainties in the fits.[177]

Due to the limited ToF resolution of the PImMS2 camera, accurate 3D momentum information was not obtainable for each ion hit. Therefore, ion distributions shown here are obtained from the central slice of the respective ion's ToF peak and correlated ion pairs were analysed using recoil-frame covariance, described in Section 2.3.3.

3.3 Results and Discussion

3.3.1 Photofragments

The mass spectra obtained for XUV-only and UV/XUV interactions with CH_2I_2 are shown in Figure 3.4. For the XUV-only spectrum, I^+, CH_2I^+, $CH_2{}^+$, and

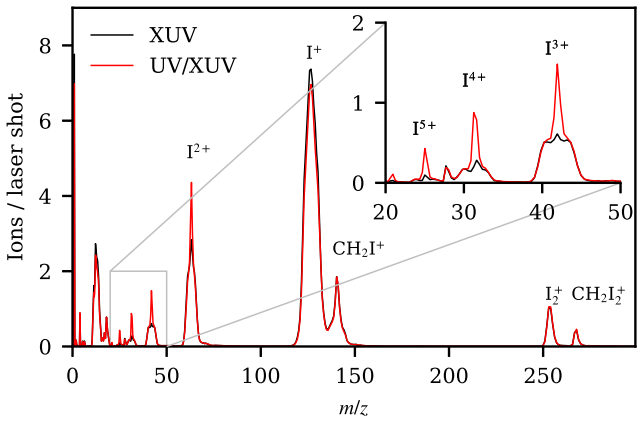

Figure 3.4: The VMI time-of-flight (ToF) mass spectra of CH_2I_2 produced in the XUV and UV/XUV experiments, normalised by the total number of laser shots recorded in each experiment.

the dihalogen I_2^+ are observable, as well as multiply charged I^{q+} cations, with $q = 2, 3, 4, 5$. These highly charged states are a result of the site-selective XUV-ionisation of the I 4d orbitals and subsequent AM decay. In comparison, the highest observed charged state of Xe, which is isoelectric with iodine, at this XUV energy was 3+, suggesting I^{q+} ions observed in this study could be created via one- or two-XUV-photon absorption at the iodine site. Iodine charge states greater than 5+ could not be individually distinguished due to overlapping peaks in the low m/z range. Two-colour enhancements are visible in the yield of I^{q+} fragments in the UV-XUV spectrum.

Central slices of individual m/z peaks were selected for detailed analysis. For ions within a certain m/z range, the distribution of x and y coordinates of ions hitting the detector could be used to extract radial distributions. Time-dependent momentum distributions were then obtained from the ion image radial distributions as a function of pump-probe delay and are displayed in Figure 3.5 for I^{q+} fragments. The ion yields are normalised by the number of shots in each delay bin as well as the sum of the XUV pulse energies recorded at each delay. The average momentum distributions of negative delays (i.e. where the probe arrives prior to the pump) are subtracted, resulting in visible enhancements and depletions of intensity at positive pump-probe delays.

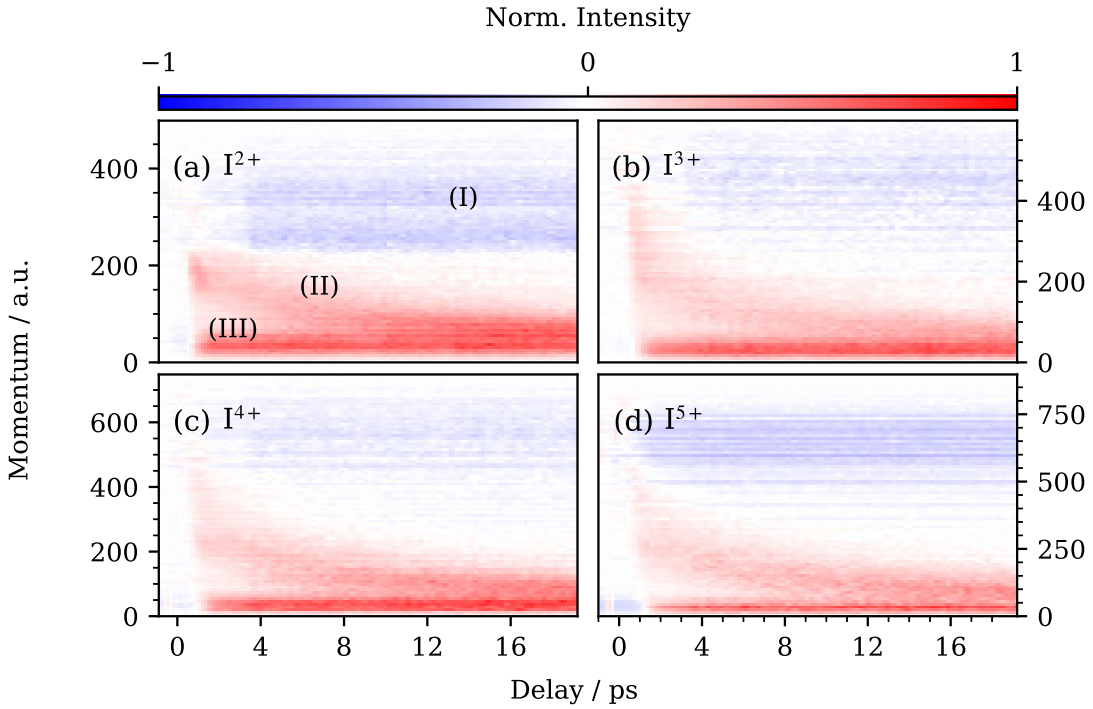

Figure 3.5: The delay-dependent momentum distributions of I^{q+} ions ($q = 2 - 5$) produced from CH_2I_2 (given in atomic units of momentum, a.u.). In each subfigure, and labelled in (a), an XUV-only feature at high momentum (I), a time-dependent Coulomb repulsion feature (II), and a low momentum feature with a delay onset (III) are visible.

Labelled in Fig 3.5(a), but also visible in the distributions for all I^{q+} ions, are three features. The first (I) is a high momentum channel that arises from XUV-only ionisation of at least two atomic sites of the ground state geometry of CH_2I_2, resulting in a Coulomb explosion. Because there is no interaction with the UV pump pulse, the molecule is ionised from its neutral ground state geometry and hence the momentum distribution of this feature is time-independent. At positive pump-probe delays, the UV pulse arrives before the XUV and photoexcites some of the sample. Therefore, the number of molecules in the ground-state geometry decreases, which leads to the observed depletion of (I) signal at positive delays. The second feature (II) is a time-dependent Coulomb repulsion feature that shows decreasing momentum as the delay increases. It is characteristic of a bond dissociation caused by the pump pulse, followed by ionisation of two atomic sites by the probe, which Coulomb explode with decreasing energy as internuclear distance increases. The final feature (III) appears at early, positive delays (~ 0.5 ps). This is

indicative of some photochemical process initiated by the pump pulse, followed by ionisation of only one atomic site. Rather than undergoing a Coulomb explosion, the molecule fragments via a dissociative pathway, and the observed fragment momenta corresponds to the velocity from neutral dissociation. The momenta of these features for each I^{q+} are approximately equal, suggesting (III) arises from the same reaction pathway and, in each case, is independent of charge state. The energy of this feature (averaged over all observable iodine charge states) is 0.074 ± 0.003 eV, with a σ of 0.035 eV. This energy corresponds to a dissociation velocity of 372 ± 13 $\mathrm{m\,s^{-1}}$.

The following sections discuss time-independent Coulomb explosions of the ground state parent molecule first, followed by the time-dependent dissociative processes.

3.3.2 Time-independent Coulomb Explosions

Figure 3.6 illustrates the momentum distributions of I^+ and CH_2I^+. The intensities of the features in these distributions show some slight enhancement at 0 ps but the momenta of the features are constant over all pump-probe delays. Whilst the features in both distributions are approximately equal in momentum, indicating a two-body fragmentation pathway where linear momentum is conserved, both distributions are broad as they also contain contributions from several other fragmentation channels producing fragments with overlapping momenta. To isolate the momenta of fragments generated in a two-body explosion of the ground-state parent geometry,

$$CH_2I_2^{2+} \rightarrow CH_2I^+ + I^+, \qquad (3.3.2.1)$$

covariance analysis is employed.

The recoil-frame covariance maps generated for pairs of ion species (cov(A, B)), calculated over all pump-probe delays, are given in Figure 3.7. These show the most probable radial distributions of the ion of interest (B) recoiling from the reference ion (A, whose trajectory is given by the white arrow). The results for Cov(I^+, CH_2I^+) and Cov(CH_2I^+, I^+) are straightforward to interpret. In these two covariances, the ion of interest recoils at an angle 180° from the reference

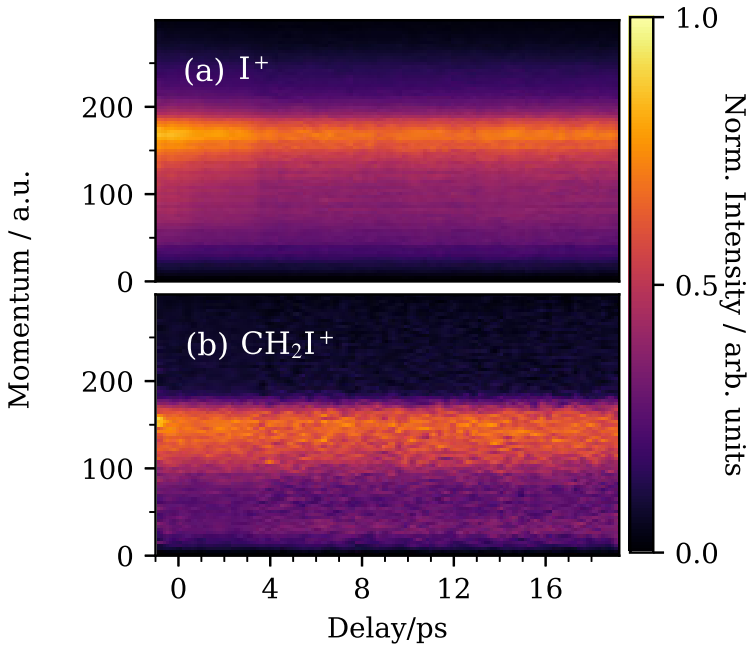

Figure 3.6: The delay-dependent momentum distributions of I^+ (a) and CH_2I^+ (b) produced following ionisation of CH_2I_2 (given in atomic units of momentum, a.u.).

ion, which is characteristic of an explosion between two charged fragments. These covariances are calculated using a central slice of each ion's TOF peak to recreate the central slice of the Newton sphere as best as possible. To achieve a good signal-to-noise ratio, the width of this bin was several PImMS time bins wide and therefore could not perfectly recreate the central slice of the Newton sphere. As a result, the energy distributions obtained from the back-to-back, two-body covariance features slightly underestimated the energies of the co-fragments by ∼10%. The total kinetic energy release (KER) of this fragmentation pathway obtained from recoil-frame covariance analysis was 3.2 ± 0.7 eV, whereas the KER obtained from the ion momentum distributions was 3.5 ± 0.3 eV

The total kinetic energy release (KER) of this fragmentation pathway, obtained from the ion momentum distributions, was used to predict whether the charge on the CH_2I^+ product was localised mainly on the carbon or iodine. This was done by comparing the experimentally observed KER to the KER expected from a Coulomb explosion of CH_2I_2 in its neutral ground state geometry, with the charge located on the carbon (6.8 eV) or the iodine (4.2 eV) of CH_2I^+. When the

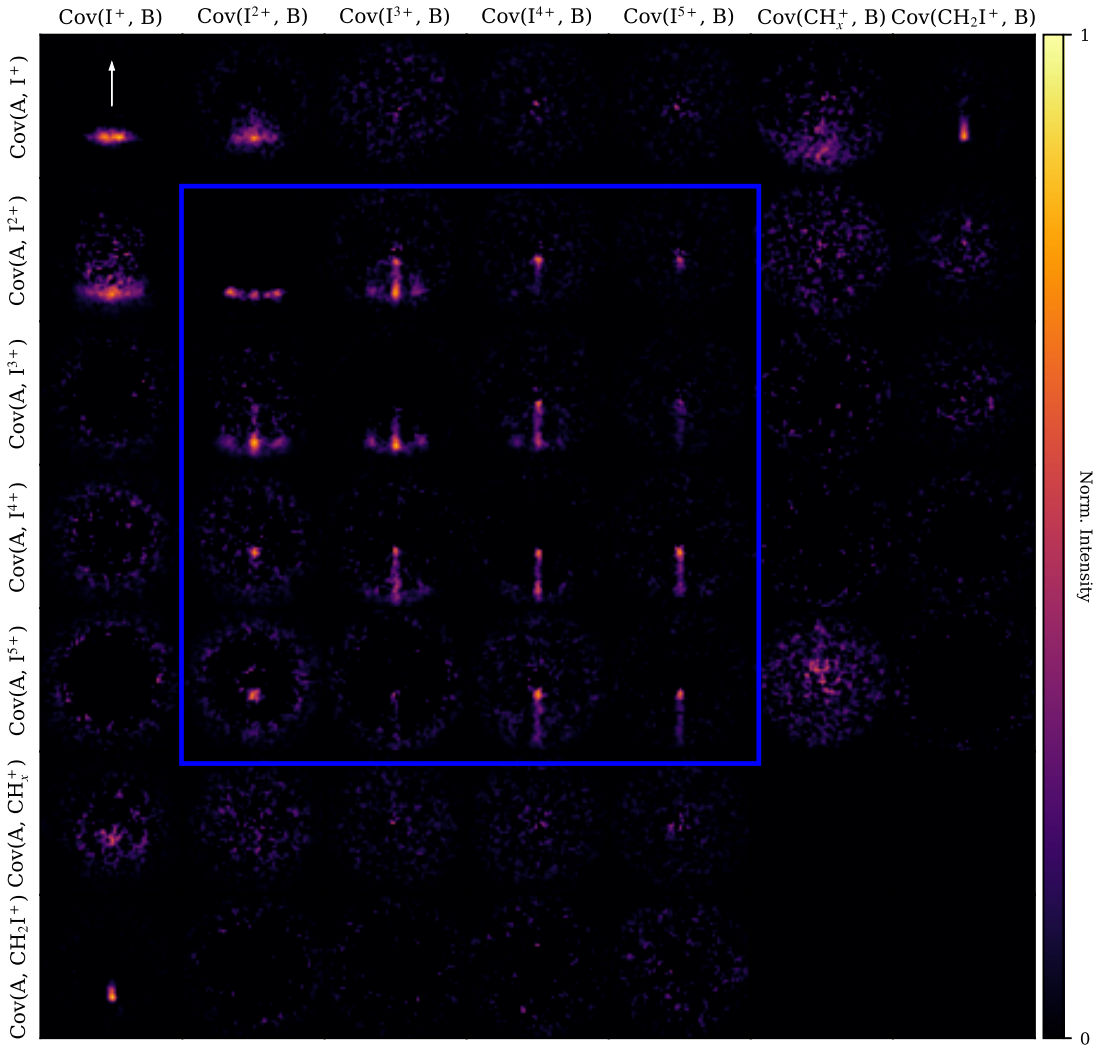

Figure 3.7: Recoil-frame covariance maps between ion pairs from CH_2I_2 calculated over all delays, all expressed on a normalised intensity scale. The white arrow depicts the trajectory of the reference ion, A, and the areas of positive intensity show the most probable distribution of the ions of interest, B, relative to A. Covariances obtained for two multiply charged iodine states are highlighted by the blue box. Negative covariances are set to 0 for simplicity.

charge is considered to be on the carbon, the experimental KER was 52.7 ± 7.8% of the KER calculated from Coulomb's law. Alternatively, when the charge is considered to be on the iodine, the experimental KER was 89.6 ± 13.3% of the predicted KER. It is therefore sensible to assume that the charge on CH_2I^+ is located on the iodine, and the decreased KER compared to the theoretical value is likely due to distortions in the internuclear coordinates of the parent molecule occurring during the AM charging process.

The time-independent momentum distributions of I^{q+} features (I) in Figure 3.5 were broad with many overlapping features arising from an amalgamation of concurrent Coulomb explosions with ions with different charge states and (likely) different spin-excited states. Recoil-frame covariance was used to identify the co-fragments leading to the features (I). Figure 3.7 shows that I^{q+} ($q = 2 - 5$) ions are covariant with all other I^{p+} ($p = 2 - 5$) ions. These covariance maps are highlighted by the blue box. For the majority of these ion pairs, two features are observed. The first feature is time-independent covariance at an off-180° recoil angle, which corresponds to a three-body Coulomb explosion of the ground state parent molecule, in a total cationic charge state Q, into two iodine ions (I^{q+} and I^{p+}) and a *cationic* $CH_2{}^+$ fragment.

$$CH_2I_2^{Q\geq 3+} \rightarrow CH_2^+ + I^{q\geq 1+} + I^{p\geq 1+} \tag{3.3.2.2}$$

Since this covariance is observed between two I^{5+} ions, XUV-only interactions with the parent molecule could generate molecular ions with Q up to at least 11+. The range of pairs of ions observed in the XUV mass spectrum and covariance analysis shows that as few as only one and as many as at least four XUV photons could be absorbed by a single molecule. In the regime where both iodine ions had a 5+ charge, both iodine atomic sites likely absorbed two XUV photons each.

The second covariance feature is a signal at a recoil angle of 180°. This feature, overall, is time-dependent and grows towards the centre of the image, corresponding to a photodissociation process. However, the higher energy edge of this feature corresponds to a time-independent Coulomb explosion between two I^{q+} ions when their internuclear distance is at a minimum, i.e. the geometry of the parent molecule, where the I-I internuclear distance is ~ 3.4 Å. This is a probe-only interaction that generates two iodine ions and a neutral CH_2 fragment.

$$CH_2I_2^{Q\geq 2+} \rightarrow CH_2 + I^{q\geq 1+} + I^{p\geq 1+} \tag{3.3.2.3}$$

Gaussian distributions were fitted to the radial and angular distributions of both features in each of the covariance images. The average values obtained from the

radial distributions were converted to kinetic energy and summed to provide average combined iodine kinetic energies (and the combined σs) and average recoil angles (and corresponding σs). The results for each charge pair are given in Table 3.1. These energy and angular distributions are also plotted as a function of the sum of the iodine charge states $(q + p)$ in Figure 3.8.

Table 3.1: The summed energy (KE) and average recoil angles (θ) for each pair of iodine charge states were obtained from Gaussian fits to the corresponding recoil-frame covariances in Figure 3.7, and are reported with corresponding σ for both three-body fragmentation channels with a neutral methylene (CH_2) and a cationic methylene (CH_2^+) fragment. Highly charged ion pairs (I^{q+}/I^{p+}) with $q,p \geq 4$ produced via the $I^{q+}/I^{p+}/CH_2^+$ channel were too energetic to be fully focused onto the detector and so corresponding KE and θ values could not be obtained.

		$I^{q+}/I^{p+}/CH_2$		$I^{q+}/I^{p+}/CH_2^+$	
I^{q+}	I^{p+}	KE $\pm$ σ (eV)	$\theta \pm \sigma$ (deg)	KE $\pm$ σ (eV)	θ $\pm$ σ (deg)
1	1	3.90 ± 0.70	168.93 ± 10.72	6.04 ± 0.50	144.40 ± 0.30
1	2	7.17 ± 1.72	179.95 ± 2.75	9.35 ± 1.23	149.85 ± 4.53
2	2	14.22 ± 1.78	180.77 ± 3.14	17.50 ± 2.04	154.84 ± 2.89
2	3	20.80 ± 4.21	181.39 ± 4.17	23.72 ± 2.64	154.96 ± 3.87
3	3	30.50 ± 2.66	181.28 ± 2.29	33.20 ± 1.84	156.20 ± 1.49
3	4	36.68 ± 4.06	181.52 ± 2.53	43.09 ± 3.30	154.43 ± 2.57
4	4	45.10 ± 8.58	181.24 ± 0.64	-	-
4	5	50.66 ± 9.87	180.90 ± 2.66	-	-
5	5	62.14 ± 2.62	181.08 ± 0.62	-	-

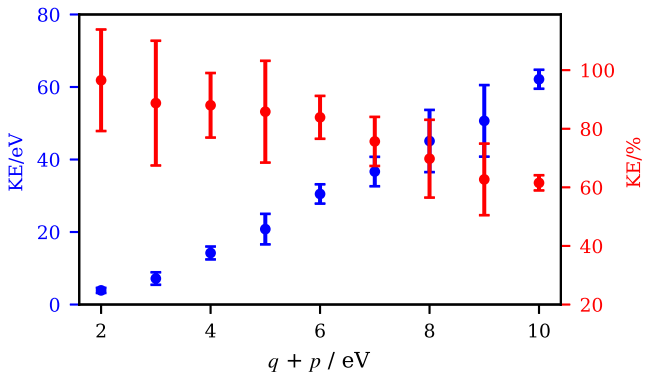

Figure 3.8: The KE (eV) values given in Table 3.1 for three-body Coulomb explosions between I^{q+} and I^{p+} ions and a neutral CH_2 are plotted as a function of total molecular charge. KE is also expressed as a percentage of the predicted KE for an explosion of a molecule in its neutral ground state geometry. The error bars correspond to the σ of the KE values given in Table 3.1.

For fragmentation with a neutral methylene, the summed KE of the (I^{q+}, I^{p+}) fragments increases with charge as expected according to Coulomb's law. In Figure 3.8, these KE values are also expressed as a percentage of the KE expected from explosions between (I^{q+}, I^{p+}) ions from CH_2I_2 in its neutral ground state geometry. This percentage decreases with the sum of the charge states, and could possibly be explained in two ways. Firstly, the ion yield of higher charged states ($q, p \geq 4$) was lower than for lower charge states, and the energies of these species corresponded to radii up to and beyond the edge of the detector, meaning that some higher energy ions might not have been detected and the KE values obtained from Gaussian fits to the ion distributions might be a lower estimate of the true KE distribution of these ions. Alternatively, the lower KE observed for increasing total charge may be due to distortions during the charging-up process. AM decay occurs over some 'charging up' time, which is fast but finite. As proposed by Takanashi *et al.*[72], the time taken to reach the molecular ions' final charge state increases with charge. The decreasing percentage of the expected KE seen here might be a consequence of greater molecular distortion occurring during the generation of higher charged parent molecules, such that higher charge states Coulomb explode from greater internuclear distances than those of the ground state neutral geometry.

The sum of the KE of the (I^{q+}, I^{p+}) ions produced in a three-body explosion with $CH_2{}^+$ also increases with the sum of iodine charge states, as expected by Coulomb's law. The KE and angular distributions for $q + p \geq 8$ were not obtainable as ions produced from such explosions were too energetic to be focused onto the detector. The KE values for a three-body explosion with three-charged fragments could not be expressed as a percentage of the total expected KE because the corresponding $CH_2{}^+$ ions were also too energetic to be focused onto the detector due to their relatively small mass compared to iodine. Therefore, no covariance was observed between I^{q+} ions and $CH_2{}^+$ and the obtainable KE information available for this type of three-body explosion was incomplete. Interestingly, the recoil angle between (I^{q+}, I^{p+}) ions produced in these three-body explosions remained approximately constant as the sum of charge states increased. The I-I recoil angle averaged over

all pairs of iodine charge states was 156 ± 7°. If the methylene was always singly charged for such three-body explosions, then the I^{q+}-I^{p+} repulsion is expected to become dominant in the Coulomb explosion as $q + p$, and the mutual repulsion between iodine atoms, increases, forcing the I-I recoil angle closer to 180°. The fact that the I-I recoil angle remained almost constant for all charge pairs is further evidence suggesting that the parent molecule undergoes some degree of deformation during the AM charging-up process, resulting in unexpected trends in the I-I recoil angle and decreasing energy partitioned into KE. The way the molecule distorts during the AM decay processes cannot be deduced from this data set as the VMI conditions were chosen to look at the decreasing KE of heavy iodine ions with pump-probe delay and, consequently, any $CH_2{}^+$ ions produced in a three-body Coulomb explosion were too energetic to be detected.

3.3.3 Photodissociation Processes

The time-dependent Coulomb repulsion features (II) visible in the ion momentum distributions in Figure 3.5, which contain contributions from explosions between several iodine charge states, are also visible in the Cov(I^{q+}, I^{p+}) distributions in Figure 3.7. The features at 180° that grow into the centre of the covariance images are a result of Coulomb explosions with decreasing KE as a function of pump-probe delay. These features are shown in more detail in Figure 3.9, which shows the KE (obtained through covariance analysis) of one iodine ion produced in a Coulomb explosion with a second as a function of pump-probe delay. A time-dependent Coulomb repulsion feature is visible for each pair of iodine charge states.

At long pump-probe delays, where charged fragments are far apart and Coulomb repulsion becomes negligible, the KE of fragments should reach an asymptotic value that reflects the dissociation energy of the reaction pathway, which is independent of charge. This value is therefore useful in discerning the corresponding fragmentation pathway. However, as shown in Figure 3.10, the KE observed between covariant I^{q+} ions at late pump-probe delays (18 ps) increased with the product of the two charges ($q \times p$). Therefore, within the range of pump-probe delays recorded in

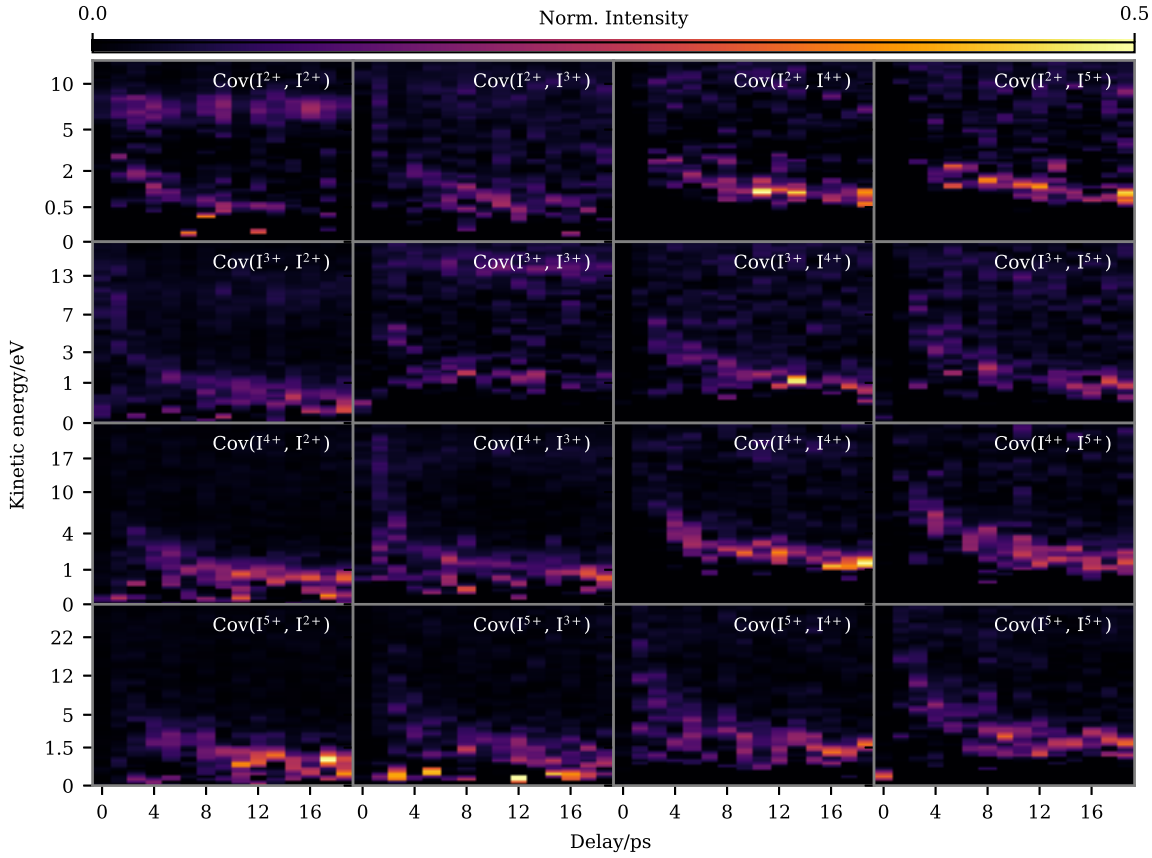

Figure 3.9: The time-dependent recoil-frame covariance obtained for each pair of I^{q+} charge states.

this experiment, photodissociated products ionised by the XUV probe were still close enough in proximity that they experienced mutual Coulombic repulsion and asymptotic energies were not reached.

Instead, to understand the nature of the dissociation process taking place, the appearances of the Coulomb repulsion features obtained via covariance were considered along with the low momentum features (III) seen in Figure 3.5. The momentum distributions of feature III were fitted with a single Gaussian distribution to obtain a neutral iodine dissociation velocity, which was independent of charge. The obtained velocity was equal to 372 ± 13 $\mathrm{m\,s^{-1}}$, which corresponds to a kinetic energy of 0.074 ± 0.003 eV. The kinetic energy obtained for this feature agrees closely with that expected for a concerted three-body dissociation,[178] where both C-I bonds break approximately simultaneously and the methylene group gains little

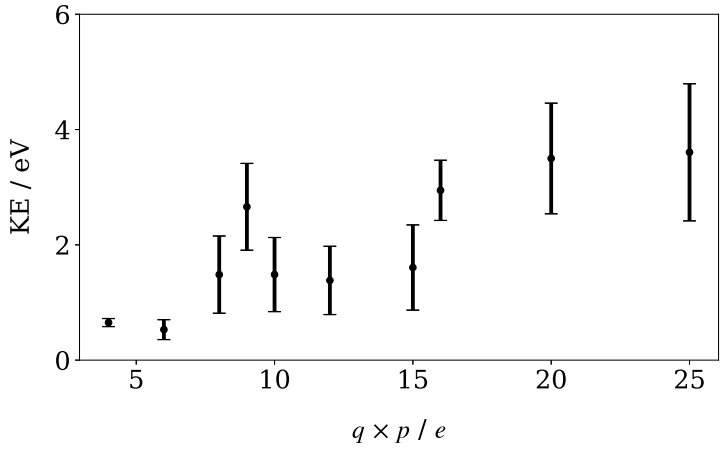

Figure 3.10: The summed KE of pairs of covariant iodine ions observed at 18 ps delay as a function of the product of their two charges ($q \times p$).

internal excitation (i.e. for energy and momentum to be conserved, $h\nu - 2D_0 \approx E_{kin}(\mathrm{CH_2}) + 2E_{kin}(\mathrm{I})$, where $h\nu$ is the photon energy and D_0 is the dissociation energy of the C-I bonds being broken). Furthermore, no covariance was observed for the (I^{q+}, $\mathrm{CH_2I}^+$) ion pairs, implying both C-I bonds were broken upon photoabsorption. If the bonds were broken sequentially, two iodine velocities would be expected. Since only one dissociation feature was observed, the velocity obtained is expected to be a good estimation of that of both iodine atoms produced in a concerted three-body dissociation due to its agreement with assignments in previous work.[178]

The expected asymptotic energy of the time-dependent Coulomb repulsion features is assumed to be equal to the kinetic energy observed in feature III, despite not being reached within the delays recorded in this experiment. At a given pump-probe delay, the kinetic energy observed in the time-dependent covariance contains contributions from the neutral dissociation process outlined above. The kinetic energy in excess of this is dependent on the energy of the 202.5 nm photon ($h\nu$ = 6.12 eV), the dissociation energies (D_0) of the bonds broken, the energy partitioned into internal modes (E^*_{int}), and the electrostatic potential energy between pairs of charged iodine ions I^{q+} and I^{p+}, separated by an internuclear distance r. This is expressed in the following equation, where k is the Coulomb constant:

$$T = h\nu - E^*_{\mathrm{int}} - \sum D_0 + \frac{kqp}{r^2} \qquad (3.3.3.1)$$

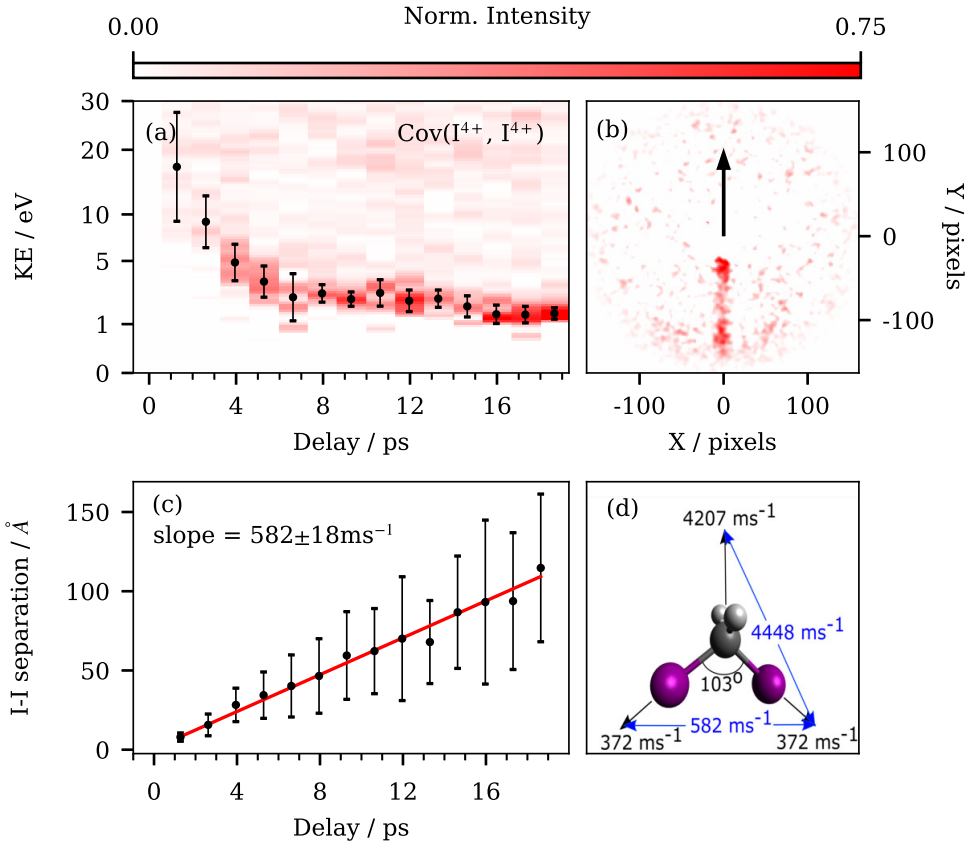

Figure 3.11: The time-dependent covariances of I^{4+} with I^{4+} is given in (a) with error bars corresponding to the standard deviation of the Gaussian energy distributions within each delay bin. The corresponding recoil-frame covariance map, calculated over all delays, is given in (b). (c) shows I-I internuclear separation as a function of time, obtained via fitting Gaussian distributions (as shown in (a)) to all time-dependent distributions given in Figure 3.9, converting the obtained energy distributions to internuclear distance via Coulomb's law, and averaging the results over all pairs of iodine charge states. The slope obtained from (c) and the neutral iodine dissociation velocity were used to calculate the corresponding CH_2 velocities and a geometry of the excited state, shown in (d). The numbers and arrows in black are the measured and inferred fragment velocities; the numbers and arrows in blue are fragment separation velocities.

Gaussian distributions were fit to covariant kinetic energy distributions for each pump-probe delay range as shown by the error bars in Figure 3.11(a) (the corresponding recoil-frame map is given in (b)). By assuming that both C-I bonds break concertedly and that products are not internally excited (i.e. E^*_{int}=0), these kinetic energy distributions can be used to extract the relationship between internuclear separation and time. Firstly, for all time-dependent covariant features observed for all pairs of iodine charge states, the kinetic energy associated with

the neutral dissociation velocity of the iodine fragment was subtracted. Secondly, the energy remaining from the UV photon after both C-I bonds are broken is considered and also subtracted from the energies obtained from covariance. The remaining energy corresponds to the energy gained from the Coulomb explosion. This was converted to internuclear separation via Coulomb's law. Averaging the results obtained for all pairs of iodine charge states yielded the approximately linear distribution given in Figure 3.11(c). Acceleration is expected to be negligible by the first timebin (200 fs). If acceleration is neglected, the gradient of this graph provides an estimate for the iodine-iodine separation velocity, which is approximately constant with time. This velocity was found to be 582 ± 18 $\mathrm{m\,s^{-1}}$ and when combined with the C-I bond dissociation velocity, the I-C-I angle can be calculated using trigonometry to yield a value of 102.9 ± 6.8°. All of these values combined allowed an I-CH_2 separation velocity of 4448 ± 2431 $\mathrm{m\,s^{-1}}$ to be obtained geometrically (Figure 3.11(d)). The obtained I-C-I angle is smaller than that of the neutral ground state geometry (116°) and is expected to be an average of many possible excited states since the UV photon energy used in this study can access a range of excited states and, due to the large density of states of iodine, after photoexcitation to a specific state, the population is expected to transfer to other states via avoided crossings.[179, 180]

To check the validity of these structural assignments, time-dependent momentum distributions were calculated for each pair of iodine charge states using the obtained neutral iodine dissociation velocity, the I-I separation velocity, and the I-C-I recoil angle. These are plotted in Figure 3.12. A good agreement is seen between the experimental time-dependent Coulomb repulsion features and the simulated distributions, which are calculated under the assumption that a three-body, concerted dissociation process is taking place. By combining time-dependent CEI and covariance analysis techniques, time-resolved structural changes to CH_2I_2 have been measured and, as a result, the multi-dimensional photodissociation mechanism has been characterised.

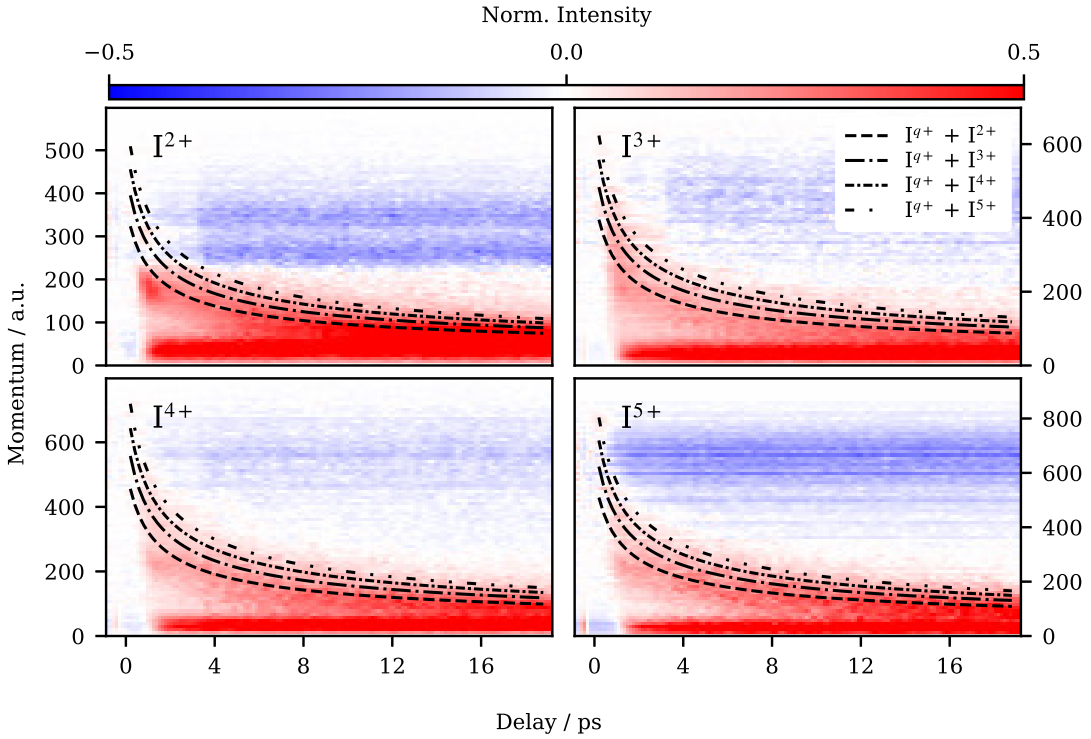

Figure 3.12: Simulated time-dependent Coulomb repulsion features, calculated under the assumption that three-body dissociation occurs via concerted C-I bond dissociation, using values obtained from features III and time-dependent covariance analysis.

3.3.4 Electron Charge Transfer

Next, the positive pump-probe delay onset of feature III in Figure 3.5 will be discussed. As described previously, feature III is indicative of photodissociation of CH_2I_2 and subsequent ionisation of only one fragment, so that the observed momenta are reflective of the neutral dissociation velocities of photofragments. At very early pump-probe delays, co-fragments are close in space. If the probe multiply ionises an iodine atom to a high charge state, an electron can transfer from a neutral moiety to the cation, creating a second cationic fragment. The mutual electrostatic repulsion between the two positively charged fragments causes an energetic Coulomb explosion, resulting in fragments with high momenta. As the pump-probe delay increases, the internuclear separations between fragments increase. The potential barrier to electron charge transfer also increases with internuclear separation and becomes energetically inaccessible at some critical distance, R_{crit}, such that the molecule

can only continue to dissociate via the low energy fragmentation pathway without electron transfer and Coulomb explosion. A pump-probe delay, t_{crit}, corresponding to R_{crit}, can be found by fitting a Gaussian cumulative distribution function (CDF) to the appearance time of the low momentum ion yields of features (III). This is shown for I^{3+} in Figure 3.13, where the onset of the low-momentum distribution is displayed in the top panel, and its corresponding integrated ion yield and CDF fit is given below. The error bar shown corresponds to the width (σ) of the Gaussian CDF. The delay-dependent ion yields and obtained t_{crit} values for all I^{q+} ions are also shown in Figure 3.14. The relatively large σ of each of the CDF fits for each ion correspond to a broad range of charge transfer onset times, which are linked to the broad momentum distribution observed for neutral iodine dissociation.

As expected, the obtained t_{crit} values generally increase with charge: the Coulombic attraction between an electron and cation increases with the cation's charge state and can overcome greater potential barriers to electron transfer.

To identify the neutral moiety involved in charge transfer, the experimentally determined fragment separation velocities shown in Figure 3.11(d) were considered. Theoretically, three neutral fragments could donate an electron to a highly charged iodine ion: CH_2I produced in a two-body dissociation, or CH_2 or I produced in a three-body dissociation. The possibility of a two-body dissociation has already been discussed and ruled out, and so the first of these fragments need not be considered. Charge transfer occurring from either the CH_2 or I can be confirmed by considering the COB model described in Equation 3.1.0.3.

The IP of CH_2 and atomic iodine are very similar (10.33 eV and 10.45 eV, respectively), and the COB model returns R_{crit} values of 5.27Å and 7.54Å for charge transfer with I^{2+} and I^{5+}, respectively. Corresponding t_{crit} values can be calculated by dividing these critical distances by the experimentally determined CH_2-I and I-I separation velocities presented in Figure 3.11(d). The I-CH_2 separation velocity of $5548 \pm 2615\ \text{m s}^{-1}$ yields t_{crit} values of 0.095 ± 0.045 ps and 0.14 ± 0.064 ps for I^{2+} and I^{5+}, respectively. This is a vast underestimate compared to the experimentally obtained t_{crit} values. When considering instead charge transfer from neutral I and

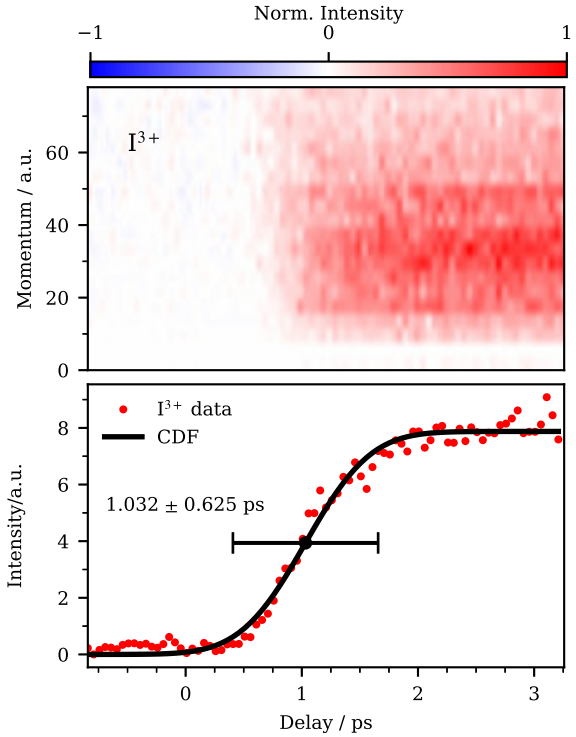

Figure 3.13: The time-dependent, momentum distribution of feature III in Fig 3.5(b), plotted on a magnified scale. The integrated ion yield for this feature is fitted with a Gaussian CDF to obtain the centre of the step function, t_{crit}, which is quoted with the corresponding Gaussian standard deviation.

the experimentally determined I-I separation velocity, the COB model predicts t_{crit} values of 0.91 ± 0.03 ps and 1.30 ± 0.04 ps for charge transfer to I^{2+} and I^{5+}, respectively. The experimental and COB t_{crit} and r_{crit} values obtained for all iodine charge states are given in Table 3.2. The close agreement between experimental and theoretical values strongly suggests the mechanism for charge transfer occurs via an electron being donated from a neutral, dissociated (but electron-rich) iodine atom to the second dissociated iodine substituent that has been highly charged by an XUV pulse.

3.4 Conclusion

In this chapter, CEI was coupled with pump-probe spectroscopy to investigate the photodissociation dynamics of CH_2I_2 at 202.5 nm. Recoil-frame covariance was used to find the time-dependent relative recoil distributions of pairs of highly

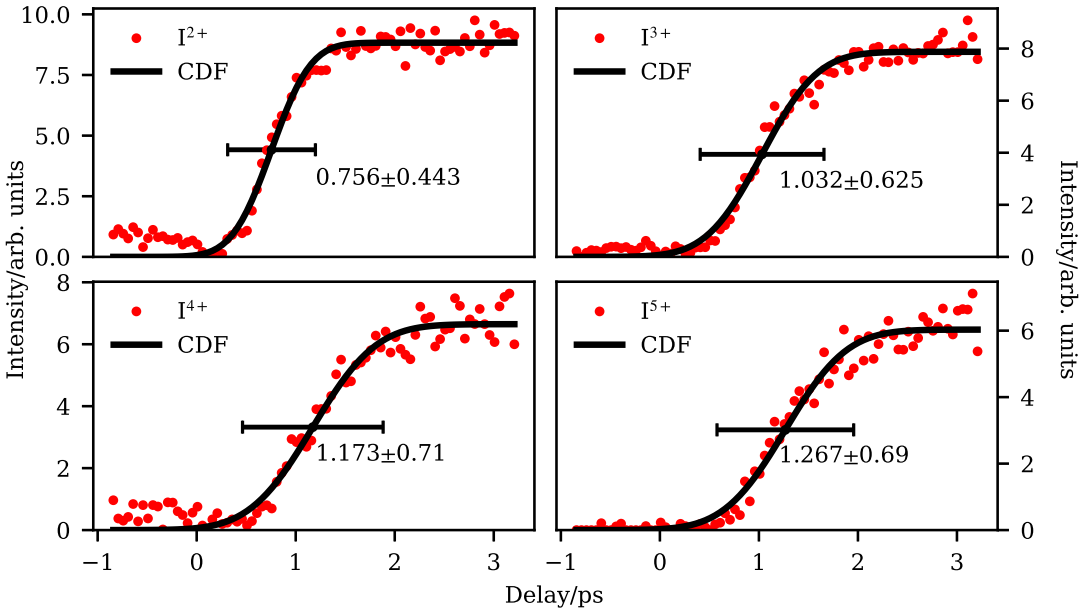

Figure 3.14: The time-dependent ion yields of features III seen in Fig 3.5 are shown here for each highly charged I^{q+} charge state. The distributions were fitted with a Gaussian CDF to obtain the centre of the step function t_{crit}, which are quoted with the corresponding Gaussian standard deviation.

Table 3.2: Observed and predicted parameters, using the classical over-the-barrier (COB) model,[172] for I-I^{q+} electron transfer following the photolysis of CH_2I_2 at 202.5 nm and the subsequent site-selective ionisation of iodine at 13.1 nm.

I^{q+}	Exp. t_{crit}(ps)	Exp. R_{crit}(Å)	COB t_{crit} (ps)	COB R_{crit} (Å)
I^{2+}	0.76 ± 0.015	4.42 ± 0.22	0.91 ± 0.03	5.28
I^{3+}	1.03 ± 0.015	5.99 ± 0.27	1.06 ± 0.03	6.15
I^{4+}	1.17 ± 0.026	6.81 ± 0.35	1.18 ± 0.04	6.89
I^{5+}	1.27 ± 0.022	7.39 ± 0.36	1.30 ± 0.04	7.54

charged iodine ions, produced via site-selective XUV-ionisation at the I 4d orbitals. These results, along with the onset times of the charge transfer channels, lead to the assignment of a three-body dissociation mechanism. Furthermore, parameters obtained from the time-dependent distributions were used to characterise geometry changes to the molecule after excitation. These results show the potential of CEI and covariance imaging to map structural evolution occurring over multiple degrees of freedom of a dissociating molecule.

Acknowledgments

I would like to acknowledge the collaboration of researchers who were involved in the beamtime, subsequent discussion of the results, and preparation of the publication manuscript: J. Unwin, F. Allum, S. Bari, R. Boll, K. Borne, M. Brouard, P. Bucksbaum, N. Ekanayake, B. Erk, R. Forbes, A. J. Howard, P. Eng-Johnsson, J. W. L. Lee, Z. Liu, B. Manschwetus, R. Mason, C. Passow, J. Peschel, D. Rivas, D. Rolles, A. Rörig, A. Rouzée, C. Vallance, F. Ziaee, and M. Burt. Furthermore, I thank DESY (Hamburg, Germany) for the provision of the experimental facilities and the scientific and technical teams at FLASH who made these experiments possible.

How do you feel about a little thing that I like to call... The IMAX Experience.

— Seth Cohen, The O.C.

4

Disentangling XUV-induced Fragmentation Mechanisms of Iodopropane Isomers Using 3D Covariance Analysis

Contents

4.1 Authorship Statement

The work presented in this chapter is based on two publications (McManus, Joseph W., *et al.* "Disentangling sequential and concerted fragmentations of molecular polycations with covariant native-frame analysis." *Physical Chemistry Chemical Physics* 24.37 (2022): 22699-22709, and Walmsley, Tiffany, *et al.* "The role of momentum partitioning in covariance ion imaging analysis." *The Journal of Physical Chemistry A: New Tools and Methods in Experiment and Theory*, 2024, 128, 22, 4548–4560). These publications were co-authored by the author of this thesis and another Doctoral student, Joseph W. McManus. Covariance analysis of the data presented in this chapter was jointly performed and interpreted by both students. Therefore, some of the results presented here may also be found in the Doctoral thesis of Joseph W. McManus, who equally contributed to this work.

4.2 Introduction

As demonstrated in Chapter 3, site-selective, XUV-ionisation to highly charged cationic states via AM decay processes can be used to probe the reaction dynamics of small molecules. However, as the size of a molecule increases, so too do the number and complexity of accessible fragmentation channels. The same sets of co-fragments can be generated via different, competing fragmentation pathways, which could complicate time-resolved spectra in pump-probe experiments. Furthermore, ionisation to lowly-charged states (e.g., 2+, 3+) may not lead to complete Coulomb explosions of the molecule and instead generate metastable products that decay over timescales longer than those of prompt Coulomb explosions. It is therefore important that analysis procedures can disentangle and separately analyse concurrent fragmentation mechanisms that yield the same sets of products with the same m/zs over different timescales. It is especially important to be able to disentangle sequential and concerted fragmentation pathways if CEI (which

relies on concerted processes to extract structural information) and pump-probe spectroscopy are to be extended to larger and more chemically relevant compounds.

Concerted and sequential three-body fragmentation was briefly introduced in Chapter 1. In a concerted regime, two bonds are broken on such a fast timescale that they cannot be distinguished as independent events (e.g., both bonds are broken within the approximate timescale of a single bond vibration). The following equation describes a general concerted fragmentation of a molecule ABC:

$$\mathrm{ABC} \rightarrow \mathrm{A{+}B{+}C}. \tag{4.2.0.1}$$

The trajectories of the three products are constrained to a plane, as shown in Figure 4.1. By considering the trajectory of A to be an axis of the plane, the momenta (p) of the three products within that plane can be expressed by the following equation:

$$p_{\mathrm{A}} + p_{\mathrm{B}}\cos\theta_{\mathrm{B}} + p_{\mathrm{C}}\cos\theta_{\mathrm{C}} = 0 \tag{4.2.0.2}$$

where $\theta_{\mathrm{B/C}}$ are the angles between $p_{\mathrm{B/C}}$ and the axis, p_{A}.[132]

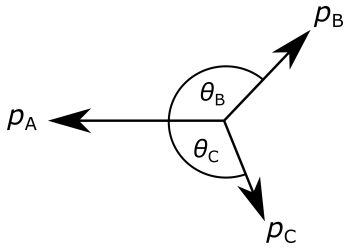

Figure 4.1: A schematic showing how the momenta of three products A, B, and C, produced in a concerted Coulomb explosion, are confined to a plane.

For a fully sequential fragmentation process, two bonds are broken on different timescales. For a general molecule ABC, the primary bond-breaking process generates one stable product (A) and one unstable intermediate (BC), which undergoes secondary fission into secondary products (B+C) sometime after the first bond-breaking event:

$$\mathrm{ABC} \rightarrow \mathrm{A} + \mathrm{BC} \rightarrow \mathrm{A} + \mathrm{B} + \mathrm{C}. \tag{4.2.0.3}$$

Depending on the geometry of the parent molecule (i.e. if it is non-linear), the primary process may exert a torque on the intermediate BC, which becomes rotationally excited about its centre of mass as a result. If the metastable lifetime of the intermediate is comparable to or longer than its rotational time period, then it can become randomly oriented relative to the primary bond-breaking vector before decaying into secondary products. The recoil angle of the secondary product relative to the primary product is dependent on how much the intermediate has rotated within its lifetime and, for fully sequential processes, the relative recoil angle between the vectors of primary and secondary fragmentation steps can be distributed over $0-180°$.[58, 59] However, as will be shown in this chapter, the recoil angle is dependent on the initial geometry of the molecule and the intermediate's axis of rotational excitation.

Sequential fragmentation of triatomic molecules has been successfully studied using coincidence methods in molecules such as CS_2, N_2O, and SO_2.[181, 182] In such molecules, the detection of only two products can yield the complete energetic information describing the fragmentation process. Sequential fragmentation is not limited to small molecules though, and has also been reported to occur in much larger systems.[41, 140, 183]

The individual steps of a sequential fragmentation mechanism can be studied independently by considering their own frame of reference, i.e. their native-frame (Chapter 2).[59] In a primary two-body explosion, the momenta of the products are equal and opposite. Then, after the intermediate fragments via a secondary process (which also produces fragments with equal and opposite momenta within its own frame of reference), the momenta of the secondary products have contributions from this primary process and the secondary process. Subtracting the contribution from the primary process allows the kinetics of the secondary process to be characterised independently of the primary process.[58, 59, 140]

The full 3D momentum information of ions is required to investigate correlated ion momenta in the native-frame. In the previous chapter, the resolution of ion momenta along the time of flight axis was not sufficient to obtain their 3D momentum

information and so the analysis was limited to 2D techniques. However, in this work, a much higher resolution along the time of flight axis was achieved (<1 ns), allowing 3D momentum information to be recovered for multiple ions hitting the detector per laser shot and, consequently, a much more advanced analysis to be carried out.

The results presented in this chapter were obtained at the Spring-8 Angstrom Compact free electron LAser (SACLA), Japan, under high event rate conditions, and, therefore, coincidence techniques are not appropriate for extracting correlated ion momenta. Here, 3D covariance analysis methods are used instead.[21] Newton-frame covariance techniques are used to disentangle concurrent fragmentation mechanisms of 1-iodopropane (1-IP) and 2-iodopropane (2-IP) cations, generated by site-selective XUV-ionisation at the I 4d subshell. In the first half of this chapter (specifically, sections 4.4.1, 4.4.2, and 4.4.3), modifications to the Newton-frame covariance analysis method, including the newly developed native-frame covariance analysis approach, are used to disentangle concerted and sequential fragmentation mechanisms of tricications of the iodopropane isomers. The nuclear dynamics of intermediates induced by primary Coulomb explosion processes are revealed to be sensitive to the molecular geometry of the parent molecule.

Products of XUV-ionisation are not solely determined by the site-selective primary ionisation processes and can be influenced by other electronic processes occurring on timescales competitive to Coulomb explosion. Therefore, site-selective ionisation does not necessarily lead to site-selective bond cleavage, and the fragments of XUV-ionisation depend more heavily on the final electronic states of the parent. Depending on the secondary and tertiary AM decay processes taking place after the initial core-shell ionisation, molecular ions can be generated in a range of excited states. Furthermore, charge redistribution across a molecule can result in a range of charge distributions and resultant Coulomb explosions into different products. These processes are dependent on many factors, such as the initial charge location and excited state of the molecule, bonding properties and ionisation potentials of molecular orbitals, and the shape and size of the molecule.[79, 83, 84, 184] In molecules with high densities of states (such as molecules containing heavy atoms

like iodine), electronic and nuclear motion can become coupled, facilitating the relaxation of highly excited electronic states via non-adiabatic conical intersections into low-lying electronic states, converting electronic excitation into vibrational excitation. Any structural change incurred by the molecule that competes with AM decay will influence the electronic density and internal energy redistribution processes and, therefore, the range of products generated by XUV-ionisation.[74, 76, 81, 86, 184] This is not an exhaustive description of processes that can occur competitively with Coulomb explosion but demonstrates how a large range of fragmentation processes can be accessed by site-selective ionisation regimes.

In the latter half of this chapter (specifically, Sections 4.4.4-4.4.10), the range of fragmentation processes accessed by XUV-ionisation of 1-IP and 2-IP are addressed. Modifications to the Newton-frame covariance analysis methods are used to deduce approximate branching ratios of different fragmentation channels and to characterise the nuclear motion of charged and neutral products induced by Coulomb explosions and photolytic processes. The methods presented allow processes that generate the same sets of ions with similar fragment momenta to be disentangled. Furthermore, these methods can also be used to interrogate the relationship between momenta and recoil angle within a single fragmentation mechanism that produces rotationally excited intermediates.

4.3 Methods

4.3.1 Experimental

XUV-ionisation of separate samples of 1-IP and 2-IP was carried out using the soft X-ray beamline BL1 at SACLA, which can produce photons with tunable energy in the range between 40-150 eV at a repetition rate of 60 Hz, with a bandwidth of 2% and a duration of 30 fs.[185] For this study, XUV photons of 95 eV–corresponding to a wavelength of 13.1 nm–were employed to site-selectively ionise iodine at the I 4d subshell.[186] The shot-to-shot XUV pulse energy was measured by a gas intensity monitor (GMT) and the average recorded energy was 33 μJ. This was attenuated by a Zr filter of thickness 0.6 μm, which allowed for 13% transmission. Combined

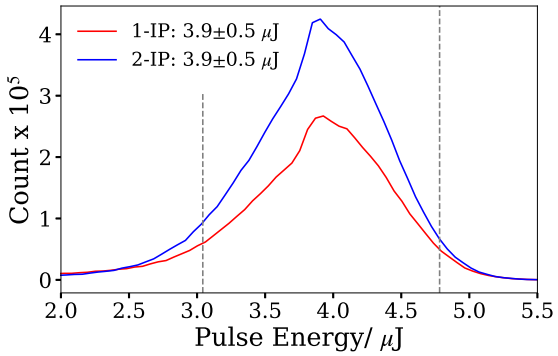

Figure 4.2: The attenuated XUV pulse energy distributions recorded for 1-IP and 2-IP, obtained from shot-to-shot measurements. The average pulse energies (and corresponding widths) were obtained by fitting a Gaussian distribution. The range encapsulated by the dashed lines indicates the range of pulse energies considered in contingent covariance calculations.

with the expected 90% transmission of the beamline,[185, 187] the mean XUV pulse energy at the interaction region was estimated to be 3.9 μJ for both isomer experiments. The attenuated XUV pulse energy distributions are given in Fig 4.2.

A schematic of the double-sided VMI spectrometer is given in Figure 4.3. In these experiments, only the ion imaging capability was used and electron data was not recorded. The FEL beam, which was horizontally polarised parallel to the detector plane, was focused into the spectrometer by a Kirkpartick-Baez (KB) mirror system (with minimal loss of intensity by reflecting the pulses at a grazing incidence angle off of a curved surface) to an approximate spot size of 10 μm ($1/e^2$), which had an approximate corresponding Gaussian intensity of 3.3 $\times$ 10^{14} W cm^{-2}. The XUV pulses intersected pulsed molecular beams of neat, unseeded, gaseous 1-IP and 2-IP in the centre of the VMI reaction chamber.[122, 129] The molecular samples were expanded into the chamber using a pulsed gas jet (General Valve) and passed through a skimmer. Around 70% of the XUV pulses were expected to be absorbed by the samples at the I 4d site.[52, 188] Resultant ions were accelerated down the ToF region via ion optics and velocity mapped onto a dual MCP detector equipped with a hexanode delay-line detector.[129] This recorded the x, y positions of individual ion hits on the detector, with a mean count rate of 12 ions per laser shot, and also recorded the arrival time of each ion at the

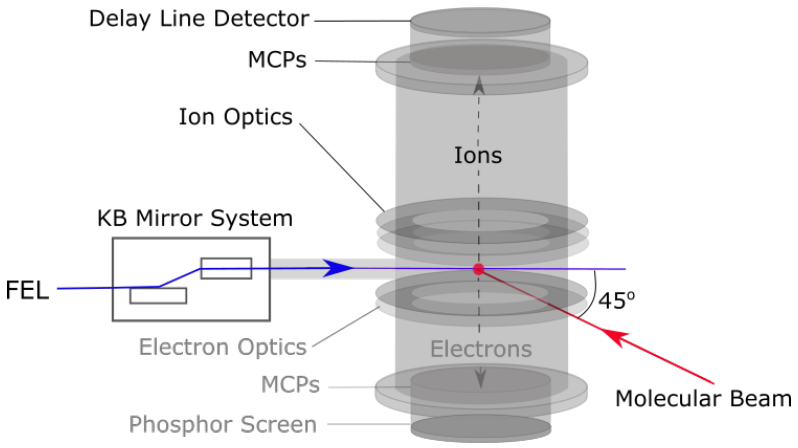

Figure 4.3: A schematic of the double-sided VMI spectrometer used at BL1 at SACLA, which is discussed in detail in the text.

detector relative to the 60 Hz trigger of the FEL.

4.3.2 Data Analysis

Due to the high time resolution of data recorded using a delay line hexanode detector (<1 ns), fragments differing in mass by a single hydrogen could be resolved in the mass spectra (Figure 4.4). This is even more evident in the ToF-ToF covariance maps (Figure 4.5). The narrow ToF-ToF covariance features allowed accurate ToF values, corresponding to the centre of each ion's Newton sphere, to be obtained for each ion species. Furthermore, the high ToF resolution allowed the momenta of ions along the ToF axis to be reconstructed so that 3D ion momentum information could be obtained for multiple ions hitting the detector per laser shot. The relative momenta of covariant ions are calculated in this chapter using the 3D momentum Newton-frame covariance techniques. All covariance maps are calculated contingently, splitting the data into 10 subsets with equal numbers of statistics (laser shots) based on the measured FEL pulse energy. Intensities of covariance features and their uncertainties are obtained via the bootstrapping method outlined in Section 2.3.9.

4.4 Results And Discussion

A range of cationic iodine and alkyl products generated by XUV-ionisation are observed in the mass spectrum obtained for each molecule (Figure 4.4). Subtle

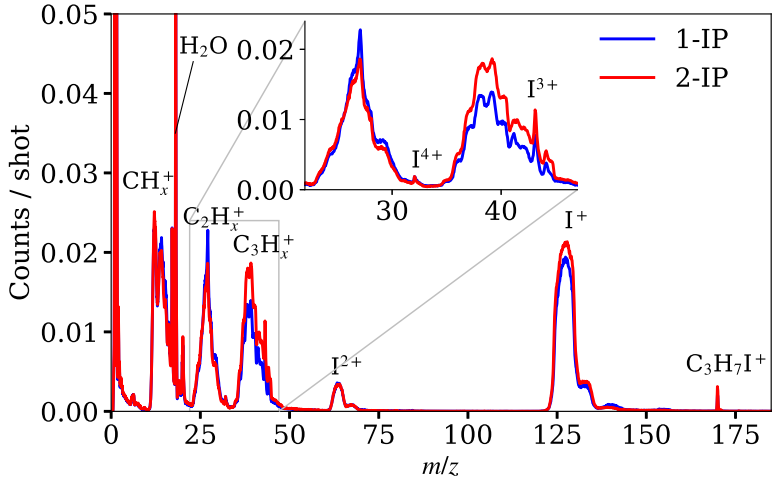

Figure 4.4: Mass spectra obtained from XUV-induced ionisation of 1-IP and 2-IP. Isomer-dependent fragment yields are visible in the spectra obtained for ethylene and propylene fragments.

differences between the relative yields of different ions can be seen for the two isomers, especially the yields of alkyl fragments. Iodine ions in charge states up to I^{4+} were detected, but from here on, only fragmentation channels producing neutral I or I^+ are discussed in detail.

The mass spectrum of 2-IP is provided again in Figure 4.5(a), and molecular diagrams are given for 2-IP and 1-IP in (b) and (c). The ToF-ToF covariance map for 2-IP is given in (d). A red box highlights covariances between I^+ and various alkyl cations, which are plotted on a magnified scale in (e). The corresponding region of the 1-IP ToF-ToF covariance map is given in (f). The full 1-IP ToF-ToF covariance map was given in Chapter 2. From these covariance maps, many pairs of ions generated via the same fragmentation channels can be identified. I^+ ions are covariant with various alkyl fragments with different numbers of carbon and hydrogen atoms. Covariance is also observed between carbon-containing fragments, most prominently between CH_x^+ and $C_2H_y^+$ fragments (where $x + y \leq 7$). The processes producing many of these pairs of ions will be discussed in more detail in the following sections using Newton-frame covariance analysis.

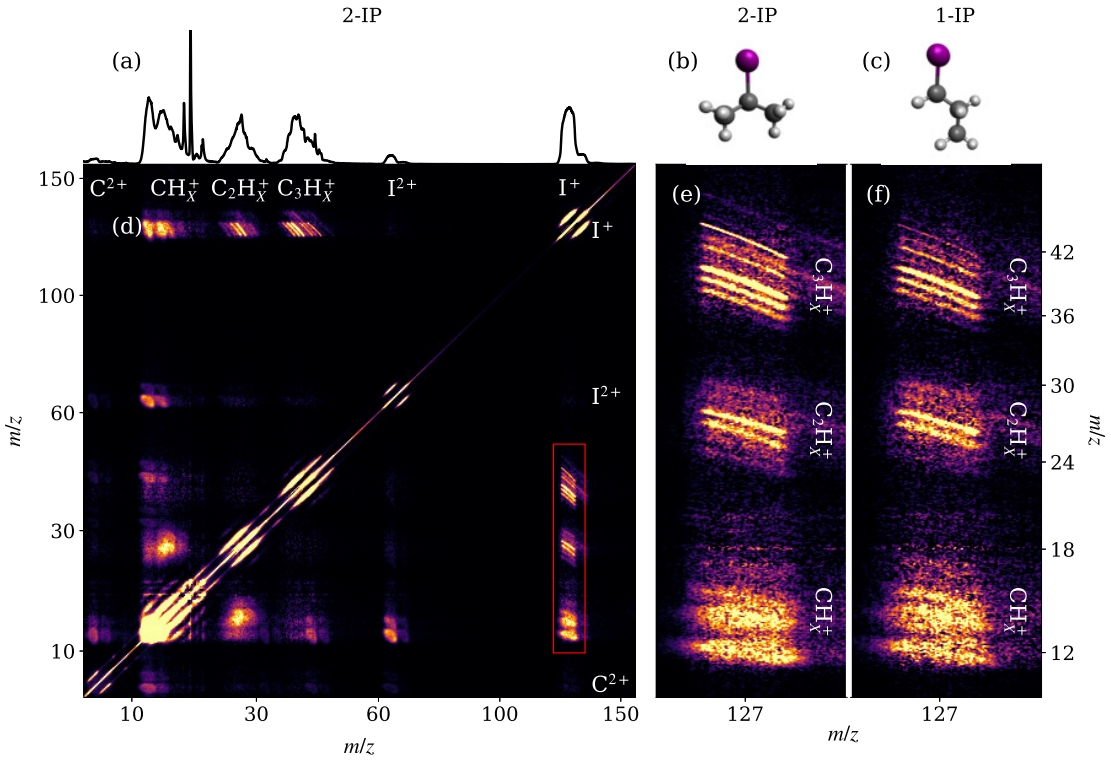

Figure 4.5: The mass spectrum of 2-IP is given in (a), and the structures of 2-IP and 1-IP in (b) and (c), respectively. In (d), the ToF-ToF covariance map (given in m/z) of 2-IP is shown, and the features enclosed in the red box are plotted on a larger scale in (e). The ToF-ToF covariance within the same region outlined by the red box is plotted for 1-IP in (f). Note that the m/z axes do not extend below 5 as no meaningful covariance was observable for lower values.

4.4.1 Manipulating Newton-frame Covariance Maps

The momentum distributions of CH_3^+ ions relative to I^+ ions obtained for both isomers are shown in the Newton-frame covariance maps in Figure 4.6. The I^+ momenta are constrained to the positive x-axes, the relative momenta of $CH_3{}^+$ ions are plotted in the top half of each map, and the inferred momenta of the remaining mass of the molecules ('$C_2H_4/C_2H_4{}^+$') are given in the bottom halves. Several features are observable. Firstly, a low momentum feature, close to the midpoint of the image, corresponds to fragmentation of the molecular dication into $CH_3{}^+$, I^+, and neutral co-fragments ('C_2H_4'). This fragmentation channel will be discussed in more detail in Section 4.4.5. The higher momentum features shown in Figure 4.6 correspond to three-body Coulomb explosions of the parent trication into

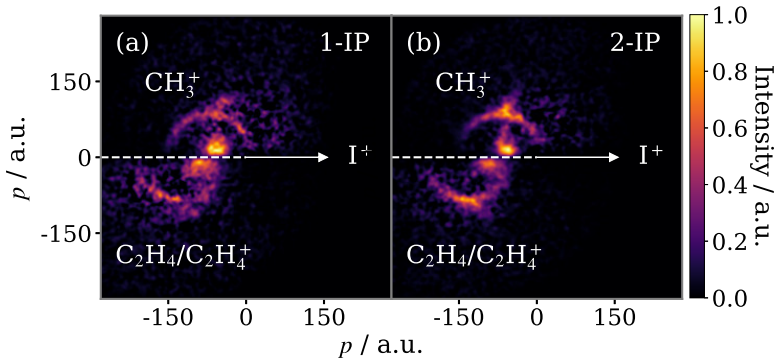

Figure 4.6: Newton-frame covariance maps showing the momenta of CH_3^+ relative to I^+ for 1-IP and 2-IP in (a) and (b), respectively. Each map is independently normalised.

three charged products. This feature is complicated by overlapping components corresponding to concerted and sequential fragmentation channels. These two contributions can be separated and more clearly discerned using modifications to the Newton-frame covariance calculation.

The momentum distribution of I^+ ions that are covariant with CH_3^+ are plotted in Figure 4.7(a) and (b) for 1-IP and 2-IP, respectively. Within these distributions, three features are observable (*I, II, III*). The Newton-frame covariance maps in Figure 4.6 can be separated into corresponding constituent features by filtering the covariance calculation on the I^+ momenta, as indicated in Figure 4.7. Feature *I* can be obtained by only considering I^+ ions with momenta above the dashed arcs in Figure 4.7(a) and (b). The results for both isomers are given in Figure 4.7(c) and (d). This feature corresponds to a sequential three-body fragmentation of the molecular trication, occurring via a primary Coulomb explosion that breaks the C-I bond and produces I^+ and a propyl dication intermediate, which undergoes a secondary Coulomb explosion into CH_3^+ and $C_2H_4^+$ after some metastable lifetime. This feature will be discussed in more specific detail in Section 4.4.3. Similarly, features *II* and *III* can be isolated by only including I^+ ions with momenta within the radii highlighted by the dashed arcs. These results are given in (e) and (f) for both isomers. Feature *II* corresponds to the concerted three-body fragmentation channel of the molecular trication, which will be discussed in more detail in Section 4.4.5.

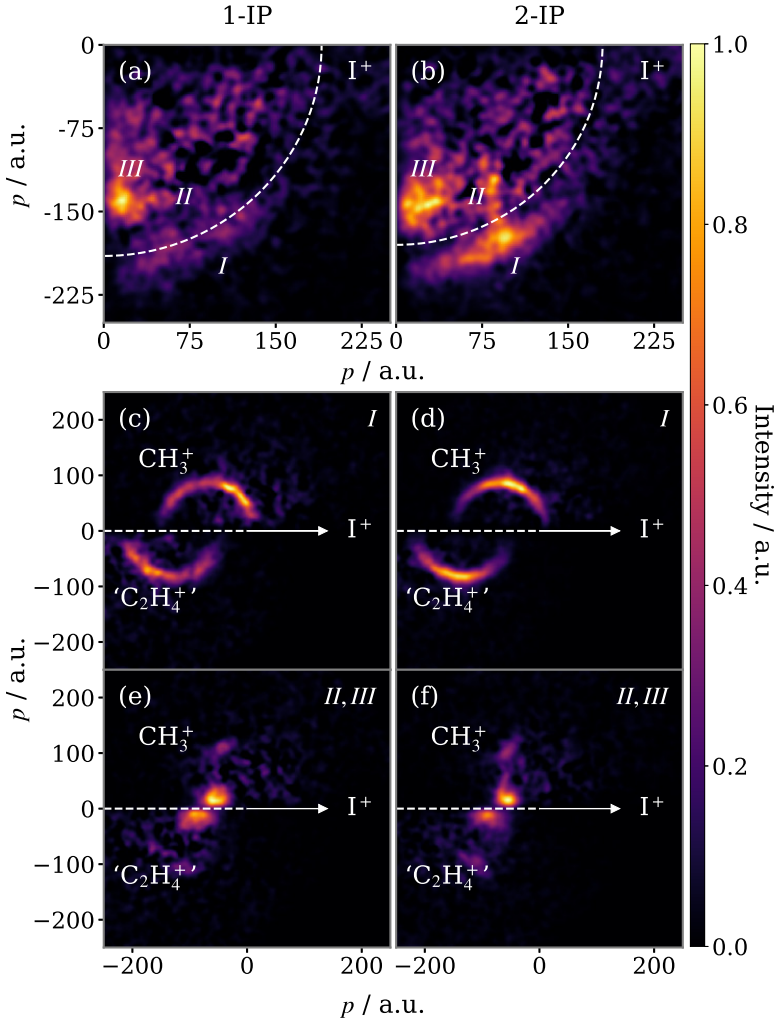

Figure 4.7: The momenta of I^+ ions covariant with $CH_3{}^+$ are given in (a) and (b) for 1-IP and 2-IP, respectively. Features *I, II, III*, described in the text are labelled. The momenta of CH_3^+ ions covariant with I^+ with momenta above the dashed lines in (a) and (b), corresponding to feature *I*, are plotted in (c) and (d) for 1-IP and 2-IP, respectively. The momenta of CH_3^+ ions covariant with I^+ with momenta below the dashed lines in (a) and (b), corresponding to features *II* and *III*, are plotted in (e) and (f) for 1-IP and 2-IP, respectively. The intensities of all panels are individually normalised to their corresponding maxima.

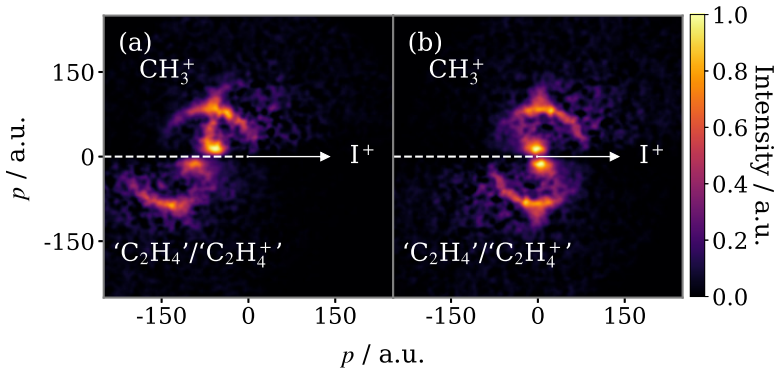

Figure 4.8: Covariance maps showing the momenta of CH_3^+ relative to I^+ for 1-IP in (a) the Newton-frame and in (b) the native-frame of a propyl intermediate.

Feature *III* corresponds to the fragmentation of the dication, which will be discussed in more detail in Section 4.4.5.

The Newton-frame covariance map of $CH_3{}^+$ momenta can be transformed into the native-frame of the propyl dication by subtracting the momentum contributions originating from the primary Coulomb explosion process with I^+, as shown in Figure 4.8 for 2-IP. The momentum distribution in the Newton-frame in (a) contains contributions from both the primary and secondary fragmentation processes, and removing the contribution from the primary process (which is encoded in the momentum of the reference ion I^+) allows the energetics of the secondary process to be analysed independently. In the native-frame (Figure 4.8(b)), the carbon-containing fragments recoil with equal and opposite momenta (are 'momentum matched'). As was done in Figure 4.7, by limiting the absolute momenta of I^+ ions used in the covariance analysis, the three fragmentation channels can also be disentangled in the native-frame. In Figure 4.9 (a) and (b), feature *I* is shown in the native-frame of the propyl intermediate for 1-IP and 2-IP, respectively. Likewise, in (c) and (d), features *II* and *III* have been separated and are shown in the native-frame for 1-IP and 2-IP, respectively.

The Newton- and native-frame covariance maps shown so far are calculated via two-fold covariance and the lower half of each covariance map is calculated using conservation of momentum, assuming fragmentation into only three products. The third fragment is assumed to be '$C_2H_4/C_2H_4{}^+$' but, based solely on these two-fold

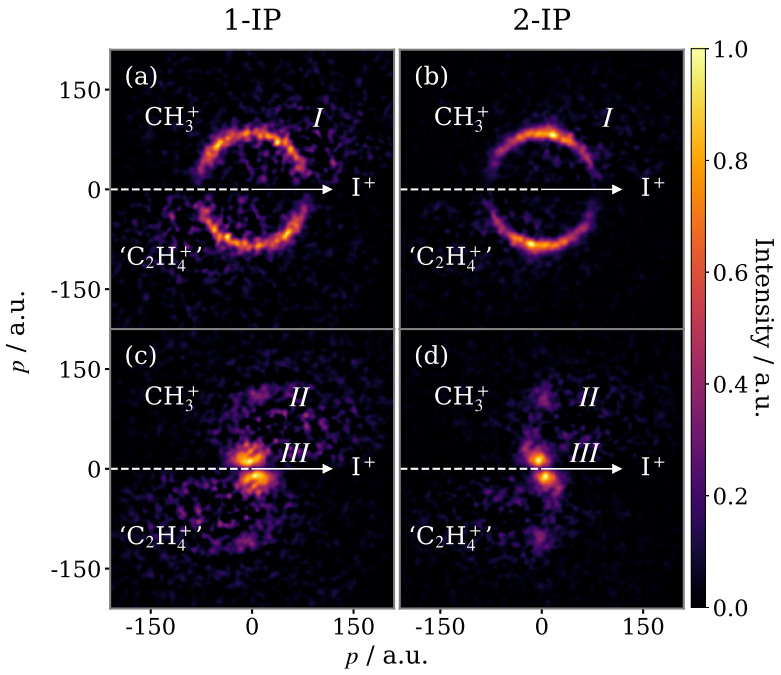

Figure 4.9: The momenta of CH_3^+ ions generated in a sequential three-body fragmentation process (feature *I*) are plotted in the covariance maps (a) and (b) relative to I^+ in the native-frame of a propyl intermediate for 1-IP and 2-IP, respectively. Likewise, the momenta of CH_3^+ ions generated in a concerted three-body fragmentation process (feature *II*) and via fragmentation of molecular dications (feature *III*) are plotted relative to I^+ in the native-frame covariance maps in (c) and (d) for 1-IP and 2-IP. All covariance maps are individually normalised.

maps, the form of the rest of the molecule is ambiguous and, theoretically, a greater number of products could be formed in the fragmentation processes producing I^+ and CH_3^+. Native-frame covariance maps can also be obtained for covariance between the (I^+, $C_2H_4^+$) ion pair. Feature *I* for the (I^+, CH_3^+) and (I^+, $C_2H_4^+$) ion pairs are given in the native-frame and compared in Figure 4.10(a) and (b), respectively, for 1-IP and in (c) and (d) for 2-IP. The distributions for the two ion pairs are equivalent (although the (I^+, $C_2H_4^+$) ion pair shows a noisier signal), strongly suggesting that feature *I* arises from sequential three-body fragmentation of the molecular trication into I^+, CH_3^+, and $C_2H_4^+$ in both cases. This is further confirmed in the Newton-frame covariance maps presented in Figure 4.11(a) and (b), which are the three-fold covariance maps between (I^+, CH_3^+, $C_2H_4^+$) produced from 1-IP and 2-IP, respectively. The same characteristic features are observed as in the two-fold covariance maps (Figure 4.7). These maps are also transformed to

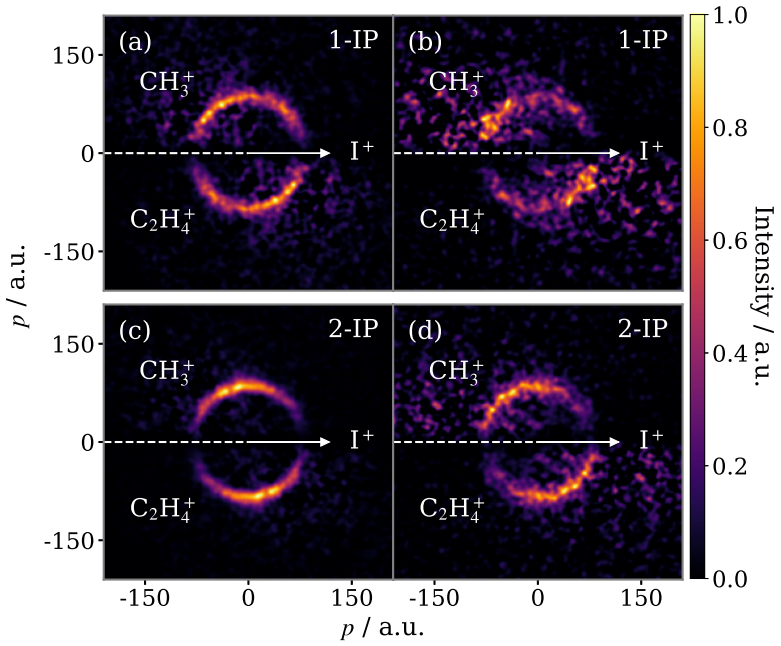

Figure 4.10: Native-frame covariance maps showing the momenta of CH_3^+ and $C_2H_4^+$, relative to I^+, produced via a sequential fragmentation process of the molecular trication by primary C-I fission into I^+ and $C_3H_7^{2+}$ (feature *I*). The maps for 1-IP are given in (a) and (b) and are calculated using the ion pairs (I^+, CH_3^+) and (I^+, $C_2H_4^+$), respectively. The corresponding plots for 2-IP are given in (c) and (d). Each map is normalised independently. In (a) and (c), CH_3^+ is the ion of interest used in the calculation, plotted in the top half of each map. In (b) and (d), $C_2H_4^+$ is the ion of interest used in the calculation, plotted in the bottom half of each map.

the native-frame in panels (c) and (d). Due to the lower intensity of the three-fold covariance features relative to those obtained by two-fold covariance, the data in the three-fold maps were binned more coarsely into fewer pixels so that the features could be seen more clearly.

4.4.2 Concerted Three-body Fragmentation of the Molecular Trication

Before discussing feature *I* in more detail, feature *II* will be characterised first due to its comparative simplicity.

Feature *II* in Figure 4.7(e) and (f) has a well-defined, narrowly distributed recoil angle. The recoil angle between CH_3^+ and I^+ was found to be $115 \pm 10°$ for 1-IP and $120 \pm 8°$ for 2-IP, and the momenta of CH_3^+ were measured to be 115 ± 10 a.u. for 1-IP and 116 ± 13 a.u. for 2-IP. The widths of these distributions are similar

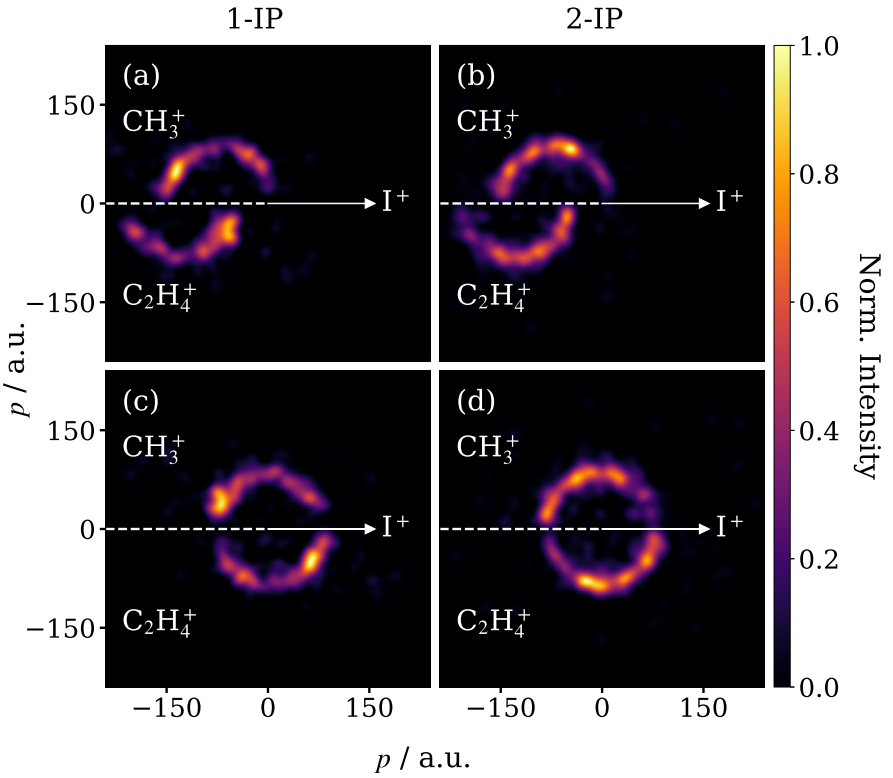

Figure 4.11: Newton-frame three-fold covariance map showing the momenta of CH_3^+ (top half) and $C_2H_4^+$ (bottom half) relative to I^+ for 1-IP (a) and 2-IP (b). These covariance maps are also given in the native frame of the propyl dication intermediates in (c) and (d), respectively. Each covariance map is independently normalised to its maximum intensity.

to the momentum resolution of the spectrometer at the applied VMI voltages (8 a.u.) but could imply some degree of asynchronicity or be intrinsic to Coulomb explosions arising from slightly varied charge separations/varied geometries, as well as from parent trications generated in different excited states with different internal energy distributions.

4.4.3 Sequential Three-body Fragmentation of the Molecular Trication

Contrary to feature *II*, feature *I* is characterised by a broad angular distribution. Following a primary Coulomb explosion into I^+ and $C_3H_7^{2+}$, the propyl intermediate is rotationally excited about its centre of mass so that, when the secondary fragmentation process takes place, the recoil of CH_3^+ sweeps out a wide angle

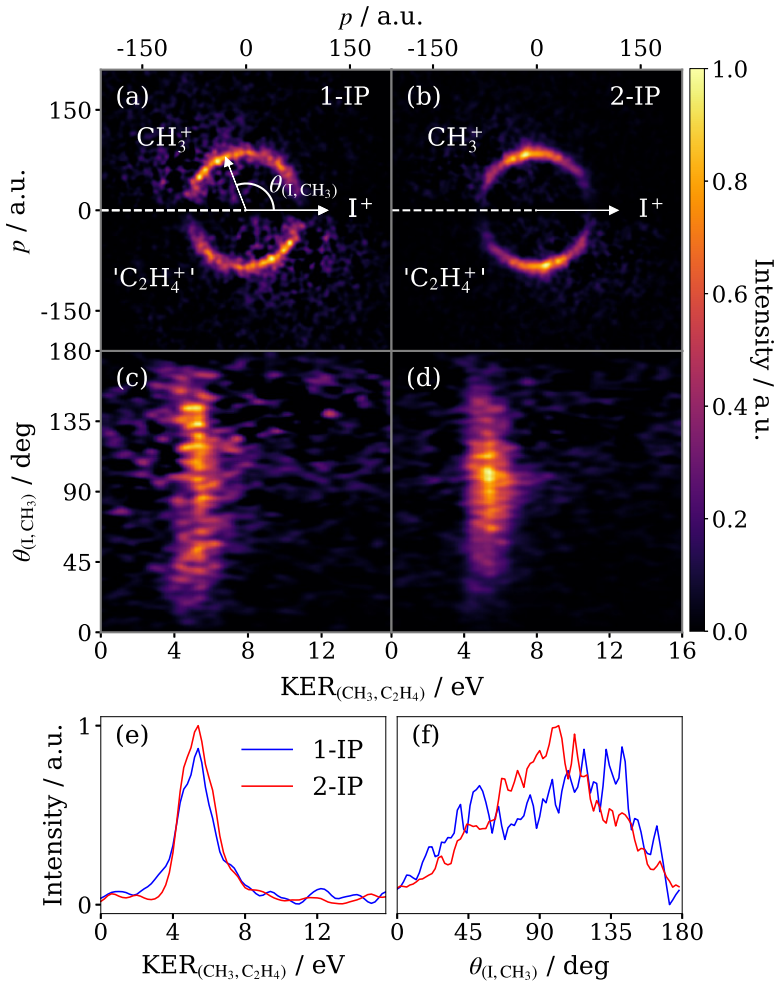

Figure 4.12: Native-frame covariance maps showing the momenta of CH_3^+ relative to I^+, in the native-frame of $C_3H_7^{2+}$, are given for 1-IP and 2-IP in (a) and (b), respectively, and are also given in a polar representation in (c) and (d), which show the KER of the secondary Coulomb explosion as a function of the I^+/CH_3^+ recoil angle in the native-frame. The integrated KER distributions are given in (e), and the integrated angular distributions are given in (f).

relative to the trajectory of the primary I^+ product. The native-frame covariance maps obtained for both isomers (Figure 4.12(a) and (b)) are converted to polar coordinates in Figure 4.12(c) and (d), allowing the recoil angle to be presented as a function of the kinetic energy release (KER) of the secondary fragmentation step. These polar distributions are integrated over their angular and KER coordinates, and the resulting KER and angular distributions are given for both isomers in (e) and (f), respectively.

For both isomers, the KER of the secondary process is independent of the recoil

angle and is not affected by the orientation of the intermediate relative to the I^+, indicating that the primary and secondary Coulomb explosion processes are well separated in time and can be considered independent events. The KER of the secondary explosion process is essentially equivalent for the two isomers, yielding in both cases (by a Gaussian fit) average KER values of 5.3±0.9 eV (where the error is the width of the Gaussian distribution, σ). This suggests that the initial charge separations on the propyl dication intermediates were similar for both isomers, despite being generated from different parent geometries. This KER corresponds to an effective charge separation on the intermediate of 2.96 Å, which is approximately double the C-C bond length in CH_3-C_2H_4 (∼1.52 Å in both 1-IP and 2-IP)[189, 190] and suggests that the two charges are located far away from each other on terminal carbons of the propyl (although this very simplistic picture only considers the charges to be point charges and neglects the possibility of diffuse and/or partial charges).

Although the energetics of the secondary Coulomb explosion are the same across both molecules, isomeric differences are apparent in the angular distributions shown in Figure 4.12(f). For 1-IP, the distribution is asymmetric with a maximum close to 180°. For 2-IP, the angular distribution has a maximum at ∼95°. These differences arise due to differences in the geometries of the isomers and the axes of rotation of the propyl intermediate induced by the torque from the primary Coulomb explosion. Figure 4.13 and Figure 4.14 depict this process for 1-IP and 2-IP, respectively.

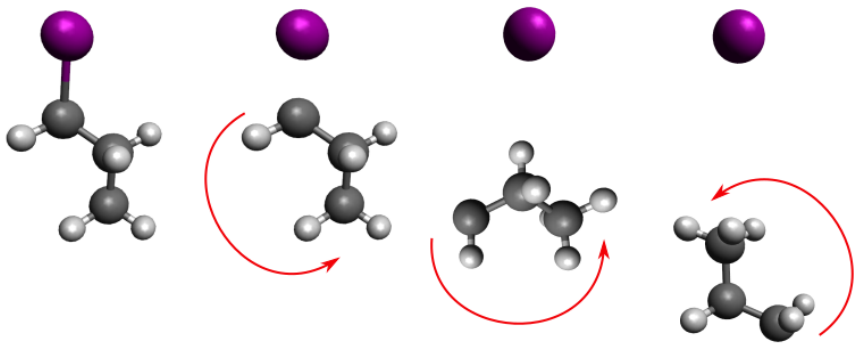

Figure 4.13: A schematic depicting the rotational excitation induced in a propyl dication intermediate following a Coulomb explosion of 1-IP^{3+} into I^+ and $C_3H_7{}^{2+}$.

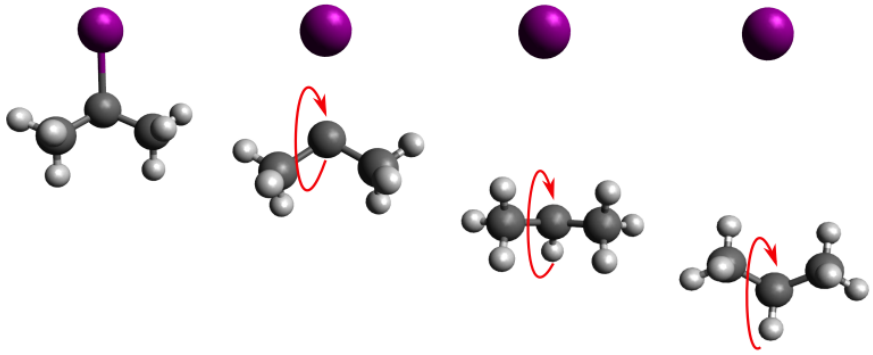

Figure 4.14: A schematic depicting the rotational excitation induced in a propyl dication intermediate following a Coulomb explosion of 2-IP^{3+} into I^+ and $C_3H_7{}^{2+}$.

For 1-IP, there is only one terminal CH_3 species and, prior to the primary Coulomb explosion event, it is at the opposite end of 1-IP to the iodine. The torque induced by the primary Coulomb explosion causes the propyl dication intermediate to rotate in such a way that, after approximately half a rotation, the CH_3 is directed towards the iodine, and after a full rotation, it again is directed away from the iodine. In 2-IP, there are two terminal CH_3 groups, which are approximately perpendicular (out of plane) to the C-I bond axis. Following the primary Coulomb explosion, the propyl dication intermediate rotates as depicted in Figure 4.14. In the neutral ground state geometry of 2-IP, both CH_3-I bond angles are approximately 109° and the C-C-C angle in the propyl is approximately 113°.[190] Assuming that the propyl dication intermediate is rigid and takes the form of the propyl in the neutral ground state geometry of 2-IP, the maximum and minimum values the CH_3-I recoil angle can take over the course of the rotation of the propyl dication intermediate are approximately ∼125° and ∼55°, respectively, and the recoil distribution is centred approximately around 90°. These expected recoil distributions agree well with the distribution given in Figure 4.12(f), although such a simplistic description does not capture the fine structure in the experimentally observed distribution.

The angular distributions observed for 1-IP and 2-IP are more complicated than those observed in previous studies of triatomics. Due to the geometries of the polyatomic and polycationic intermediates leading to these distributions, rotational excitation out of the planes described can also be induced by the primary Coulomb

explosion. Furthermore, depending on the internal excitation of the intermediate, its structure might not necessarily be rigid, and structural distortion occurring within the intermediate's lifetime (such as bond stretching and bending) can broaden the distributions observed for both recoil angle and KER.

Overlapping covariance features of concerted and sequential trication fragmentation pathways have been successfully disentangled by applying momentum constraints to the ions used in covariance analysis calculations and independently characterised using the native-frame representation. These methods have been used to infer the influence of the geometry of the parent molecule on the nuclear dynamics of long-lived intermediates. Next, these methods will be extended to study a wider range of fragmentation processes observed for both isomers, where two heavy cationic species are produced.

4.4.4 Assigning Fragmentation Channels Using ToF-ToF Covariance

The most intuitive fragmentation pathway generating two heavy cationic products is a two-body Coulomb explosion, where product ions recoil with equal and opposite momenta and anti-correlated ToFs. Two-body fragmentation into I^+ and $C_3H_7{}^+$ is observed for both isomers in the ToF-ToF covariance maps (Figure 4.5(e) and (f)). These features have a gradient of -1, showing that the ToFs of these ions are anti-correlated.

For both isomers, I^+ is covariant with a range of $C_3H_x{}^+$ products, where $x \leq 7$. The gradients of the corresponding features in Figure 4.5(e) and (f) are given in Table 4.1. The masses of the $C_3H_x{}^+$ fragment expressed as a fraction of the total mass of propyl are also listed in the table. For high values of x ($4 \leq x \leq 7$), the gradients obtained are close to -1, and are seemingly affected very little by H/H^+ loss. The identity of the hydrogen species lost is ambiguous since neutral H-atoms are not detected and charged H^+ species produced in these processes would be too energetic to be focused on the detector or observed in covariance. However, the gradients observed suggest that, since the mass of any H/H^+ lost is

Table 4.1: The ratios of the mass (m) of $C_3H_x^+$ ($x \leq 7$) fragments to the mass of propyl ($m_{C_3H_7}$) is given and compared to the gradients of the ToF-ToF covariance features observed for (I^+, $C_3H_x^+$) ion pairs.

$C_3H_x^+$	$m/m_{C_3H_7}$	gradient (1-IP)	gradient (2-IP)
$C_3H_7^+$	1	-1.00 ± 0.03	-1.00 ± 0.02
$C_3H_6^+$	0.98	-1.00 ± 0.01	-0.96 ± 0.03
$C_3H_5^+$	0.95	-1.03 ± 0.02	-0.99 ± 0.01
$C_3H_4^+$	0.93	-0.97 ± 0.01	-0.97 ± 0.02
$C_3H_3^+$	0.91	-0.96 ± 0.01	-0.90 ± 0.02
$C_3H_2^+$	0.88	-0.93 ± 0.02	-0.92 ± 0.01
C_3H^+	0.86	-0.89 ± 0.01	-0.95 ± 0.02
C_3^+	0.84	-0.84 ± 0.02	-0.84 ± 0.01

so small compared to that of the I^+ or $C_3H_x^+$, it would not significantly perturb the essentially back-to-back recoil angle between the I^+ and $C_3H_x^+$ products. For smaller values of x, the gradients of the ToF-ToF covariance features are shallower and their magnitudes more closely match the corresponding mass fraction given in Table 4.1. The loss of a greater number of H/H^+ begins to have some influence on the momenta of the cationic products and potentially indicates that not all H/H^+ species are lost at the same time. The loss of a 5^{th}, 6^{th}, and 7^{th} H/H^+ species could be delayed sufficiently enough from the first H/H^+ loss and C-I bond-breaking event to appear somewhat sequential.

The ToF-ToF covariance gradients that correspond to fragmentation channels that produce more than two heavy products, where only two are charged, may indicate whether fragments are generated concertedly or sequentially. The approximate gradients obtained for various (I^+, $C_nH_x^+$) features, where $n < 3$, are given in Table 4.2. These gradients are all shallower than -1, and suggest these co-fragments are primarily produced via a primary Coulomb explosion process followed by dissociation of a cationic intermediate into secondary products.

Sequential fragmentation occurring in IP^{2+} can be generalised to two processes. In the first case, the C-I bond breaks first due to a Coulomb explosion (depicted in Figures 4.15(a) and (b)), forming a propyl cation intermediate that further dissociates:

$$IP^{2+} \rightarrow I^+ + C_3H_7^+ \rightarrow I^+ + C_2H_4^{+/0} + CH_3^{0/+}. \qquad (4.4.4.1)$$

Table 4.2: The ratios of the mass (m) of $C_nH_x^+$ ($n \leq 3$) fragments to the mass of propyl ($m_{C_3H_7}$) is given and compared to the gradients of the ToF-ToF covariance features observed for (I^+, $C_nH_x^+$) ion pairs.

$C_nH_x^+$	$m/m_{C_3H_7}$	gradient (1-IP)	gradient (2-IP)
$C_2H_4^+$	0.65	-0.75 ± 0.02	-
$C_2H_3^+$	0.63	-0.69 ± 0.01	-0.69 ± 0.02
$C_2H_2^+$	0.61	-0.77 ± 0.02	-0.78 ± 0.01
CH_3^+	0.35	-0.72 ± 0.05	-0.68 ± 0.02

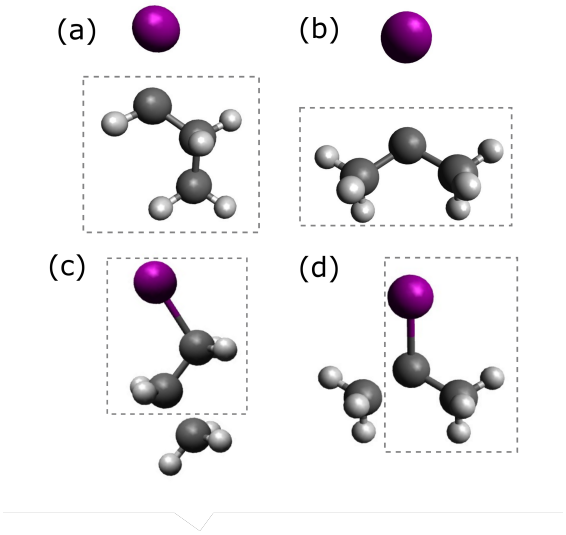

Figure 4.15: Schematics summarising the primary products formed in the Coulomb explosion steps that lead to the observed fragmentation channels that occur via a primary Coulomb explosion and secondary dissociation of an intermediate. (a) and (b) show primary C-I bond cleavage of 1-IP and 2-IP, respectively, into I^+ and a $C_3H_x^+$ intermediate. (c) and (d) show primary C-C bond cleavage of 1-IP and 2-IP, respectively, into CH_3^+ and a $C_2H_xI^+$ intermediate. Intermediate species are indicated by grey dashed boxes.

Either the ethylene or methylene secondary product can retain the charge. For both isomers, covariance was only observed with CH_3^+ and no CH_x^+ fragments where $x < 3$. If the possibility of H-migration is ignored, this implies the C-C bond originally furthest from the iodine breaks in such fragmentation processes.

The second type of sequential dication fragmentation process occurs via a primary Coulomb explosion that breaks a C-C bond (depicted in Figures 4.15(c) and (d)). In 2-IP, since both C-C bonds are equivalent, primary C-C bond fission can only break one type of bond:

$$IP^{2+} \rightarrow CH_3^+ + C_2H_4I^+. \qquad (4.4.4.2)$$

This process can also occur in 1-IP, but due to the increased number of unique carbon environments in 1-IP, the primary C-C bond fission process can also occur via the following pathway:

$$IP^{2+} \rightarrow C_2H_5^+ + CH_2I^+. \tag{4.4.4.3}$$

Secondary dissociation of the intermediate species can then occur, theoretically by either C-C dissociation or C-I dissociation. For both isomers, covariance between products formed from primary C-C bond fission was only observed for products formed via cleavage of the C-C bond furthest from the C-I bond (i.e. via equation 4.4.4.2) followed by secondary C-I dissociation, where either $C_2H_4{}^+$ or I^+ retains the charge:

$$IP^{2+} \rightarrow CH_3^+ + C_2H_4I^+ \rightarrow CH_3^+ + C_2H_4^{+/0} + I^{0/+}. \tag{4.4.4.4}$$

No covariance could be distinguished from the data sets for any other secondary processes following primary C-C bond fission. Therefore these other processes are considered to be of negligible frequency relative to other observed processes.

Given in Table 4.2 are the ratios of the masses of the charged carbon fragment and propyl. Comparing these ratios with the gradients observed for the ToF-ToF covariance features assumes that the KER of the secondary dissociation process is zero and that the C-I bond is broken in the primary process. However, these ratios do not all match the gradients obtained from the ToF-ToF covariance, which indicates that the KER of the secondary dissociation step is non-zero or that the primary bond-breaking process does not break the C-I bond, but indeed a C-C bond. Disagreement between values could also be due to the covariance features arising from a superposition of the same products being generated via different reaction pathways or from parent molecules in different charge states. Therefore, the fragmentation processes giving rise to the ToF-ToF covariance features cannot be unambiguously determined from the ToF-ToF covariance maps alone. As shown previously in this chapter, Newton-frame covariance maps can be much more informative.

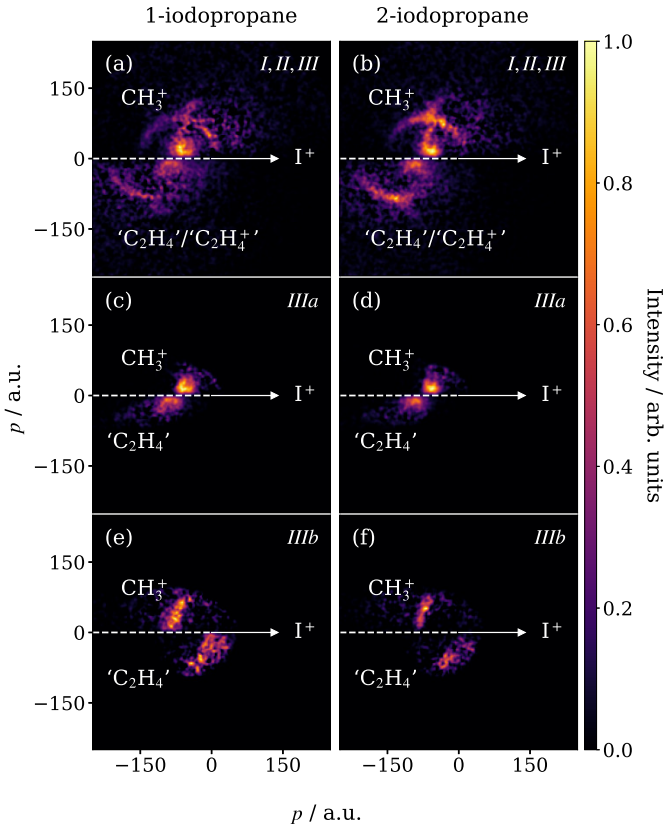

Figure 4.16: (a) and (b) are the Newton-frame covariance maps showing the momenta of CH_3^+ relative to I^+ for 1-IP and 2-IP, respectively. (c) and (d) show the covariance features arising from the primary Coulomb explosion of the molecular dication into I^+ and a $C_3H_7^+$ intermediate, followed by C-C dissociation of the intermediate. (e) and (f) show the covariance features arising from the primary Coulomb explosion of the molecular dication into CH_3^+ and a $C_2H_4I^+$ intermediate, followed by C-I dissociation of the intermediate.

4.4.5 Disentangling Fragmentation Processes Occurring via Sequential Coulomb Explosion and Dissociation

Both sequential fragmentation processes outlined in equation 4.4.4.1 and equation 4.4.4.4 can generate the (I^+, CH_3^+) ion pair. In this section, the different sequential fragmentation processes generating the same sets of products are disentangled. The total Newton-frame covariance maps for these ions are given again in Figure 4.16(a) and (b) for 1-IP and 2-IP, respectively. The lowest momenta feature, which corresponds to the fragmentation of the molecular dication into I^+, CH_3^+, and (assumedly) neutral C_2H_4, comprises components from both sequential fragmentation regimes.

To isolate these individual components, momentum conditions can be imposed on the Newton-frame covariance calculation. Equation 4.4.5.1 relates the momentum of a primary product (A) to the momenta of secondary products (B, C), assuming no kinetic energy is released in the secondary dissociation of an intermediate (BC).

$$p_{\mathrm{B}} = \frac{m_{\mathrm{B}}}{m_{\mathrm{BC}}} p_{\mathrm{BC}} = -\frac{m_{\mathrm{B}}}{m_{\mathrm{BC}}} p_{\mathrm{A}}. \tag{4.4.5.1}$$

The Newton-frame covariance calculation can be altered to only include pairs of ions whose momenta obey this ratio, within some momentum limit (termed ${}^{1}p_{lim}$) to account for non-zero KER of the secondary dissociation step. This condition is described by the following equation:

$$|p_{\mathrm{B}}| = \frac{m_{\mathrm{B}}}{m_{\mathrm{BC}}} |p_{\mathrm{A}}| \pm {}^{1}p_{lim}, \tag{4.4.5.2}$$

This filtering process is demonstrated for the (I^+, $CH_3{}^+$) ion pair generated from 1-IP, where I^+ is the primary product and $CH_3{}^+$ is the secondary product, in Figure 4.17. When ${}^{1}p_{lim}$ is high (e.g., 100 a.u.), the feature corresponding to the dication fragmentation process is not isolated from the trication features. Decreasing ${}^{1}p_{lim}$ to 5 a.u. selects only a narrow proportion of ions generated in this dication fragmentation process, but does not capture all of the feature and excludes ions with higher KER obtained in the secondary dissociation process. A ${}^{1}p_{lim}$ of 30 a.u. was found to exclude as much signal arising from other fragmentation channels as possible, whilst also capturing the entirety of the signal of interest. (A unique ${}^{1}p_{lim}$ was found for each ion pair in this way.) However, for this specific pair of ions, as can be seen in Figure 4.17(c), not all of the feature arising from the trication fragmentation could be removed using ${}^{1}p_{lim}$=30 a.u.. A second ${}^{2}p_{lim}$ was defined for this purpose. The sum of the momenta of the two secondary products should be equal and opposite to the momenta of the primary product, plus or minus the KER associated with the secondary dissociation step, which ${}^{2}p_{lim}$ should encapsulate:

$$|p(\mathrm{CH_3^+})| + |p(\mathrm{C_2H_4})| = |p(\mathrm{I^+})| \pm^2 p_{lim} \tag{4.4.5.3}$$

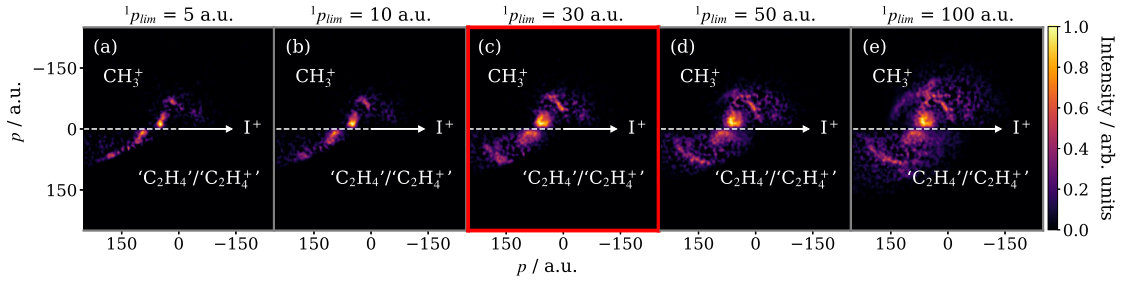

Figure 4.17: Newton-frame covariance maps showing the momenta of CH_3^+ relative to I^+, produced from 1-IP, calculated under the condition $|p_B| = m_B|p_A|/m_{BC} \pm^1 p_{lim}$, and shown as a function of $^1p_{lim}$. Outlined in red is the $^1p_{lim}$ selected for this channel.

A value for $^2p_{lim}$ was obtained using the native-frame representation (Figure 4.18(a)): the red dashed line upon the integrated radial distribution of the native-frame covariance map (b) indicates the appropriate $^2p_{lim}$ value (50 a.u.) for this specific pair of ions.

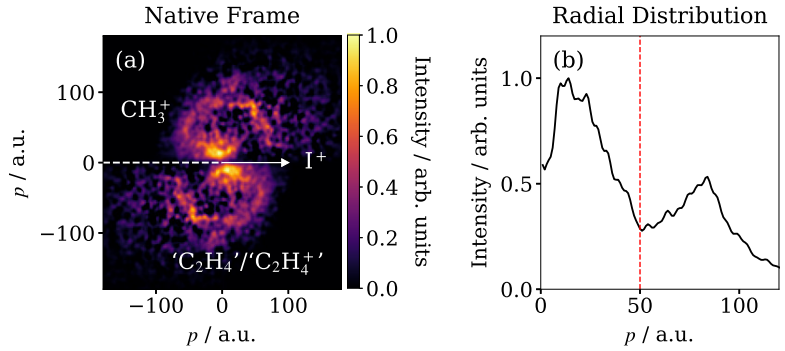

Figure 4.18: (a) The Newton-frame covariance map of the momenta of CH_3^+ relative to I^+, produced from 1-IP, displayed in the native-frame of the propyl intermediate. (b) the integrated radial distribution with the selected $^2p_{lim}$ for this specific channel indicated by a dashed red line.

Fig 4.16(c) and (d) show how applying both of these momentum constraints to the 1-IP and 2-IP data sets can successfully disentangle the correlated ion momenta arising from primary C-I bond fission and secondary C-C dissociation. The same process can also be applied to isolate the feature arising from primary C-C fission and secondary C-I dissociation, in which CH_3^+ is the primary product and I^+ is the secondary product. These results are given in Fig 4.16(e) and (f) for 1-IP and 2-IP, respectively. With careful consideration given to the expected momenta partitioning of a specific fragmentation channel, Newton-frame covariance

can successfully resolve overlapping momentum distributions of identical pairs of ions generated via different fragmentation channels.

In the following sections, Newton-frame covariance analysis and appropriate modifications are used to characterise a range of fragmentation channels producing two heavy cationic fragments.

4.4.6 Newton-frame Covariance Analysis of $I^+/C_3H_x^+$ Ions

Newton-frame covariance maps of the momenta of $C_3H_3^+$ ions relative to I^+ ions are provided for 1-IP and 2-IP in Figure 4.19(a) and (b), respectively. In both maps, the recoil angles between the momenta of the two charged fragments are back-to-back, negligibly affected by any H/H^+ loss. By integrating the corresponding covariance features obtained for all (I^+, $C_3H_x^+$) ion pairs, relative intensities can be obtained. These are given in (c) and (d), respectively, with error bars corresponding to uncertainties obtained via a bootstrapping method. The greatest intensity is observed for the (I^+, $C_3H_3^+$) ion pair, requiring the loss of four H/H^+ species. The loss of more than four H/H^+ species was also more frequent than the loss of less than four.

Figure 4.19(e) and (f) show the momenta of I^+ and $C_3H_x^+$ co-fragments as a function of x for 1-IP and 2-IP, respectively. The average momentum of each ion was obtained via Gaussian fitting to the distributions produced by Newton-frame covariance analysis, and the error bars shown correspond to the σ of the distribution. In both isomers, H/H^+ loss increases the standard deviation of the momentum distributions for both ions (approximately doubling between x=7 and x=0). The average $C_3H_x^+$ momenta remains effectively constant as a function of x for both isomers. In contrast, the I^+ momenta appears to increase as x decreases, increasing by approximately 10 a.u. between x=7 and x=0. These momentum dependencies may contain some information about the timescale of H/H^+ loss. If H/H^+ loss occurred prior to the (I^+, $C_3H_x^+$) Coulomb explosion, the products of the explosion should still be momentum matched and affected equally by H/H^+ loss. Instead, if H/H^+ loss occurred sequentially after the Coulomb explosion, the I^+ momenta

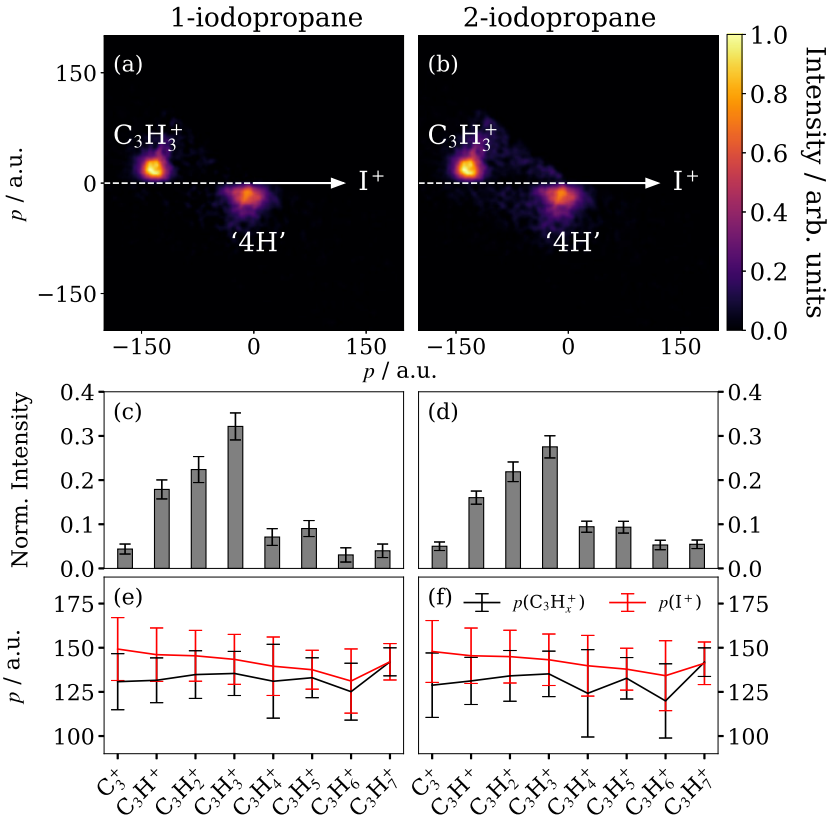

Figure 4.19: Newton-frame covariance maps of the momenta of $C_3H_3^+$ relative to I^+ are given for 1-IP and 2-IP in (a) and (b), respectively. The relative intensities of covariances observed between I^+ and all $C_3H_x^+$ fragments are given in (c) and (d) for 1-IP and 2-IP, respectively. In both cases, the intensities are normalised to the sum of all covariance intensities. The error bars were obtained via a bootstrapping method. The momentum distributions of $C_3H_x^+$ and I^+ ions, obtained from Newton-frame covariance distributions, are plotted in (e) and (f) for 1-IP and 2-IP, respectively, as a function of x. The error bars correspond to the widths of the approximately normally distributed momenta.

should remain constant, and the momenta of the $C_3H_x^+$ fragments could be expected to vary. Neither of these conditions are met, as it is the momenta of the $C_3H_x^+$ fragments that remain constant with x, and the I^+ momenta that increases with increased H/H^+ loss. This suggests that H/H^+ loss occurs on timescales competitive to the primary Coulomb explosion, imparting some momenta into I^+.

Interestingly, very similar distributions are observed for both isomers (both the range, corresponding relative intensities of fragmentation channels occurring, and relationships between fragment momenta and x). Despite having different geometries and, therefore, different shaped molecular orbitals and electronic density, the AM decay and charge redistribution processes populate distributions of electronic states

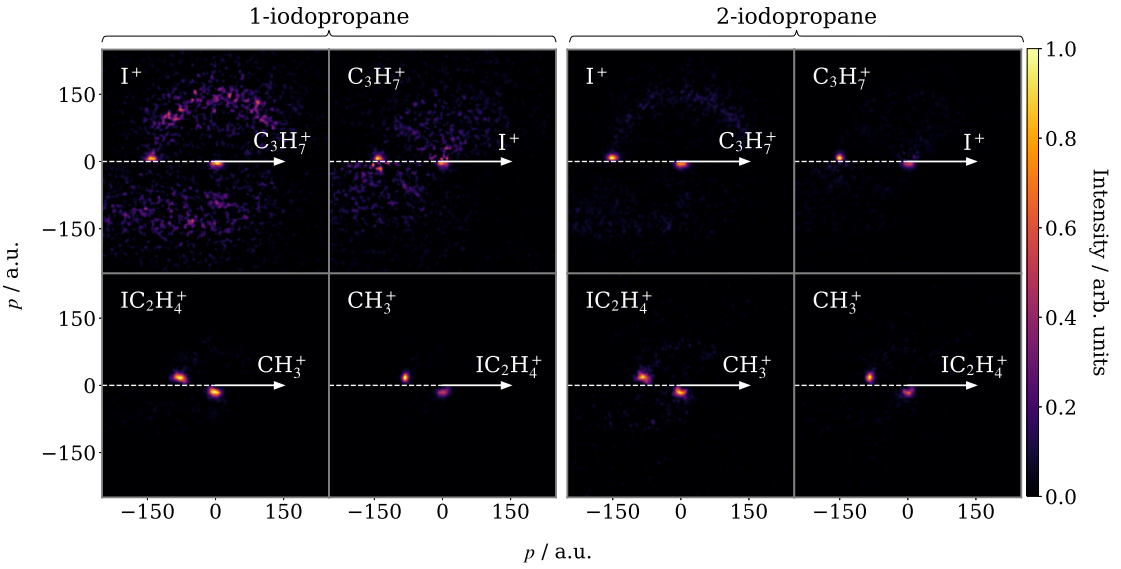

Figure 4.20: The Newton-frame covariance maps showing the relative momentum distributions of co-ions produced via two-body Coulomb explosions.

that evolve into seemingly similar sets of products.

Two-body Coulomb explosions can also occur via breaking a C-C bond. In 2-IP, this can generate the (CH_3^+, $C_2H_4I^+$) ion pair. These products can also be formed from 1-IP. However, due to the increased number of unique carbon environments, C-C fragmentation of 1-IP could also form ($C_2H_x^+$, CH_yI^+) ion pairs but no covariance was observed for these. The Newton-frame covariance maps obtained for all observable two-body fragmentation processes are given in Figure 4.20. By integrating the features in these covariance maps, relative intensities can be obtained for the different two-body fragmentation channels that can occur. This is plotted in Figure 4.21(a), where the error bars correspond to uncertainty values obtained via a bootstrapping method. For both isomers, two-body fragmentation occurs most predominantly via breaking the C-I bond, which is weaker than the C-C bonds.[191] Overall, two-body processes are less frequent than fragmentation channels occurring via primary Coulomb explosions and secondary dissociation (Figure 4.21(b) and (c)), which will be discussed in greater detail in the next sections.

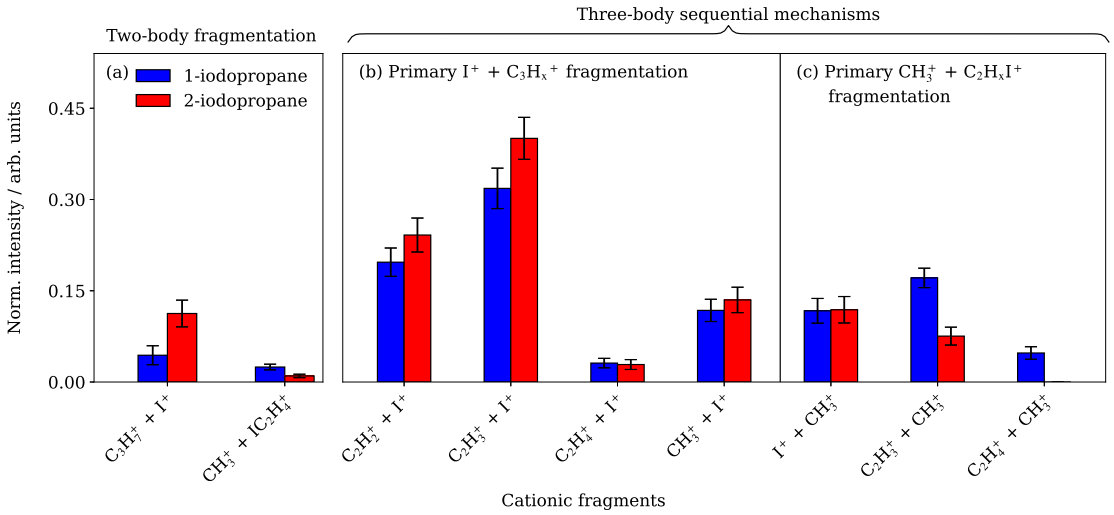

Figure 4.21: Integrated intensities of covariances between co-ions produced via two-body Coulomb explosion of the molecular dication (a), and sequential fragmentation processes occurring via primary C-I Coulomb explosions followed by secondary C-C dissociation (b) as well as primary C-C Coulomb explosions followed by secondary C-I dissociation (c). Intensities are normalised by the sum of all covariances. Error bars are obtained via bootstrapping.

4.4.7 Newton-frame Covariance Analysis of Sequential Coulomb Explosion and Dissociation Processes

Newton plots were obtained for all pairs of ions generated in sequential fragmentation processes where the primary process was a Coulomb explosion breaking the C-I bond and the secondary process was C-C dissociation. These are given in Figure 4.22. The integrated intensities of these features are given in Figure 4.21(b), with error bars corresponding to uncertainty obtained from a bootstrapping method. Newton plots were also obtained for all pairs of ions generated in sequential fragmentation processes where the primary process was C-C bond fission and the secondary process was C-I dissociation. These are given in Figure 4.23 The integrated intensities of these features are given in Figure 4.21(c).

When comparing Figure 4.21(b) and (c), in general, the relative intensities of different pairs of ions are broadly similar across the two isomers. Regimes following primary C-I bond fission are dominant over primary C-C bond fission. This is expected as the C-I bond in iodopropane is generally weaker than the C-C bonds.[191] However, one pathway in (c) stands out: the pathway producing primary CH_3^+,

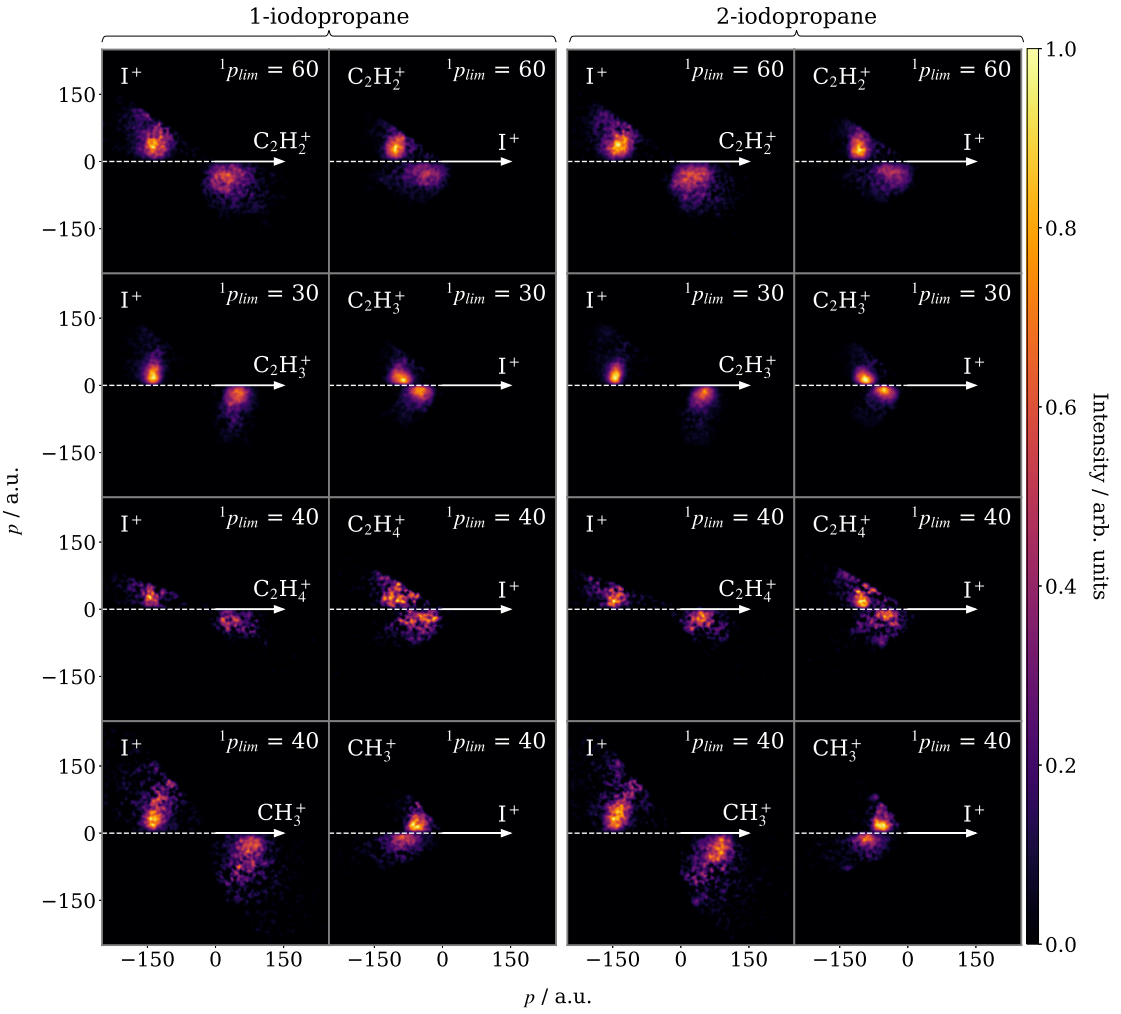

Figure 4.22: The Newton-frame covariance maps showing the relative momentum distributions of co-ions produced via primary Coulomb explosion into I^+ and a $C_3H_x{}^+$ intermediate, followed by secondary dissociation of the intermediate. Unique ${}^1p_{lim}$ values used to generate these covariance maps are given for each figure.

secondary $C_2H_3^+$ fragments. The iodine co-fragment is neutral, but the identity of the H/H^+ is ambiguous for the same reasons given previously. Neutral H would not be detected, and H^+ would be too energetic to be focused on the detector and found in covariance. However, as will be discussed, the fragmentation dynamics generating these products are almost exactly the same as those observed when all H atoms are accounted for: the loss of neutral H or H^+ does not affect the nuclear dynamics of this fragmentation channel, which behaves as expected for a molecular dication.

The significant intensity of this fragmentation channel is surprising considering that the experiment was carried out at a photon energy tuned to ionise the I

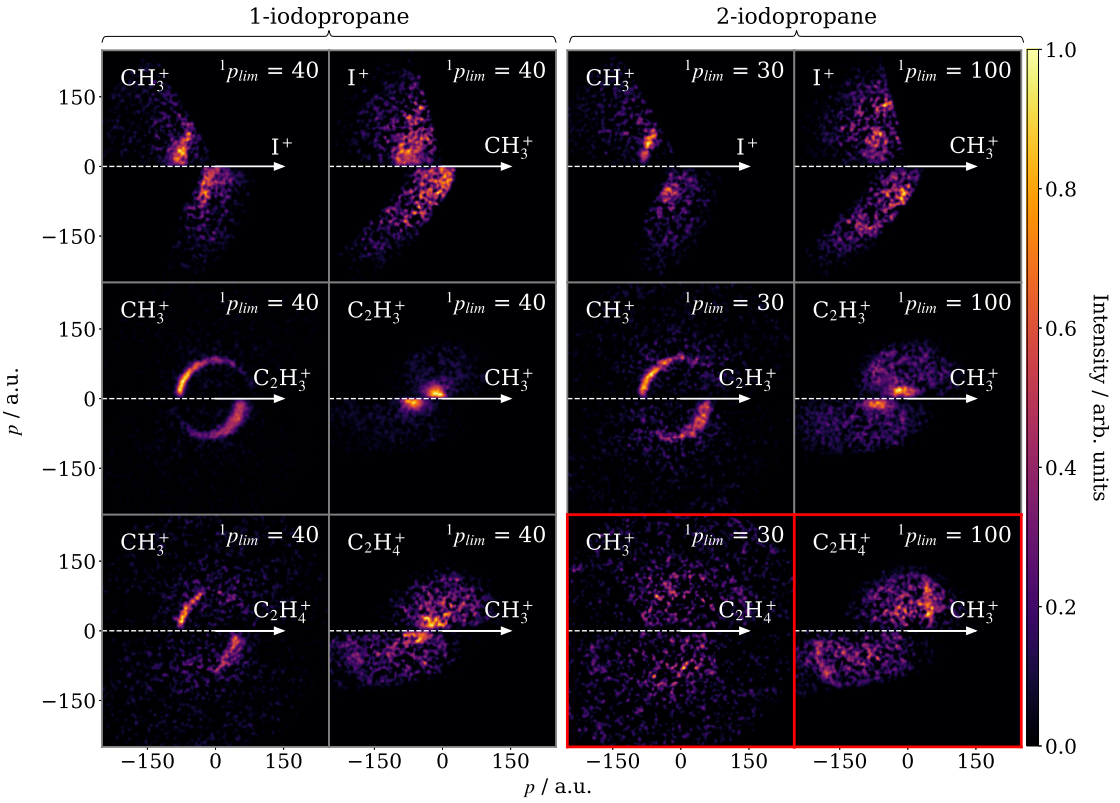

Figure 4.23: The Newton-frame covariance maps showing the relative momentum distributions of co-ions produced via primary Coulomb explosion into CH_3^+ and an I^+ and a $C_2H_4I^+$ intermediate, followed by secondary dissociation of the intermediate. Unique $^1p_{lim}$ values used to generate these covariance maps are given for each figure. Covariance between CH_3^+ and $C_2H_4^+$ was not observed for 2-IP and is highlighted in red.

4d orbital, yet the iodine remains neutral here. This could arise due to several possibilities. Firstly, despite the lower absorption cross section at the chosen XUV wavelength, it is possible that the carbon valence shell electrons could have been ionised in some instances rather than the I 4d electrons. Alternatively, following ionisation of the I 4d electrons and AM decay, it is possible that excited states were populated where the charge was localised on the carbon chain rather than on the iodine. The 3D ion information recorded in this experiment is sufficient to explain *how* fragments are generated (and will be discussed in more detail in the subsequent sections of this chapter) but, to understand *why* these fragmentation channels occur, more information is needed than can be obtained from the 3D ion momenta. Recording the photoelectrons in coincidence with the photoions would provide information about the ionisation events and possibly about the excited

states leading to these different fragmentation channels.

4.4.8 Primary C-I Fragmentation

In this section, the energetics of the sequential fragmentation processes occurring via primary C-I bond fission and secondary C-C dissociation are explored (i.e. the primary Coulomb explosion forming, and secondary dissociation of, the intermediates generated in the processes depicted in Figures 4.15(a) and (b)).

Firstly, the fragmentation channel producing the familiar ion pair (I^+, $CH_3{}^+$) will be discussed. The average momenta of the primary I^+ fragments were measured to be 144±20 a.u. and 148±18 a.u. for 1-IP and 2-IP, respectively. The neutral co-fragment in this instance is assumed to be C_2H_4. If the KER of the secondary dissociation step is assumed to be zero, the corresponding average momenta of $CH_3{}^+$ are expected to be 51 a.u. and 53 a.u. The measured average momenta of $CH_3{}^+$ were found to be 84±14 a.u. and 87±13 a.u., respectively, indicating that energy is released in the secondary dissociation step. To characterise the energetics of the secondary step, the corresponding Newton-frame covariance maps (Figure 4.24(a) and (b)) were transformed to the native-frame of the propyl cation intermediate (Figure 4.24 (c) and (d)). The momenta (and σ) of the Gaussian distribution of $CH_3{}^+$ in this frame are 17 ± 13 a.u. and 14 ± 12 a.u. for 1-IP and 2-IP, respectively, corresponding to a KER of 0.22 ± 0.08 eV and 0.15 ± 0.06 eV from the secondary dissociation step.

Figure 4.21(b) shows that the most common ion pair generated via primary C-I fragmentation and secondary C-C dissociation was the (I^+, $C_2H_3{}^+$) ion pair. The momenta of the I^+ ions were measured to be 144 ± 17 a.u. and 147 ± 15 a.u. for 1-IP and 2-IP, respectively, and are comparable to the I^+ momenta observed for the channel producing $CH_3{}^+$. This suggests that the initial charge distributions for these two fragmentation channels were similar, resulting in similar primary product momenta, but the initial excited state of the molecule and resulting charge on the intermediate may differ, leading to the generation of different secondary products. If the KER of the secondary dissociation step was zero, then the momenta of $C_2H_3^+$ are

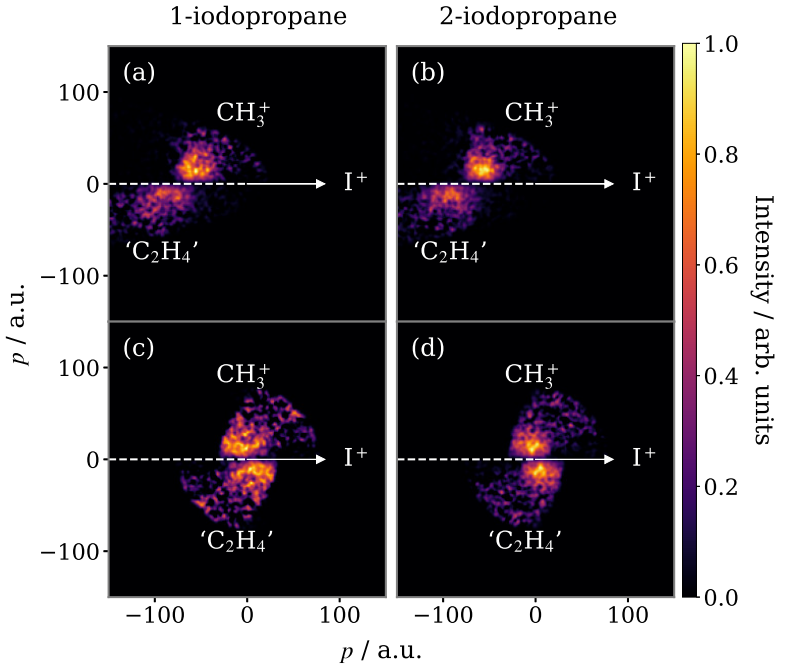

Figure 4.24: The Newton-frame covariance maps showing the momenta of CH_3^+, relative to I^+, produced via primary C-I bond fission of the molecular dication, and secondary C-C dissociation of the propyl intermediate, are given in (a) and (b) for 1-IP and 2-IP, respectively. The same distributions are given in the native-frame of the propyl intermediate in (c) and (d), respectively. All maps are normalised independently.

expected to be 93 a.u. and 95 a.u., but were found to be 111±21 a.u. and 114±20 a.u. for 1-IP and 2-IP, respectively. In the native-frame of the propyl intermediate, the average momenta (and σ) of the $C_2H_3^+$ momentum distribution was found to be 15 ± 14 a.u. and 14 ± 13 a.u., corresponding to a KER of 0.17 ± 0.07 eV and 0.15 ± 0.06 eV, respectively, for the secondary dissociation process.

To understand the discrepancy between the KER of the secondary dissociation process in the fragmentation channels producing (I^+, CH_3^+) and (I^+, $C_2H_3^+$) ion pairs, the covariance obtained for the (I^+, $C_2H_4^+$) ion pair from 1-IP is also considered. The I^+ momenta obtained from all three fragmentation channels are given in Table 4.3, as well as the KER of the secondary dissociation process, obtained via native-frame covariance analysis. The close agreement seen between the channels producing (I^+, $C_2H_3^+$) and (I^+, $C_2H_4^+$) ion pairs show that H/H^+ loss has a negligible effect on the energetics of the primary and secondary dissociation processes. Therefore, the difference in energetics observed for the (I^+, CH_3^+) and

(I^+, $C_2H_3^+$) ion pairs are likely not a result of H/H^+ loss, but could more likely be due to the propyl cation being in a different excited state, which would also allow for the different charge distributions. It is worth pointing out that, for the channel producing the (I^+, $C_2H_3^+$) ion pair, the CH_3 is neutral and therefore not detected. Similarly, the H/H^+ co-fragment would not be detected in either charge state. It cannot be said whether these two missing co-fragments are separate entities or a single moiety (CH_4) with the information obtained in this experiment.

Table 4.3: The momenta (p) of the primary I^+ fragments and KER of secondary dissociation of propyl intermediates obtained from covariance between ion pairs generated by sequential fragmentation occurring via a primary Coulomb explosion that breaks the C-I bond and a secondary C-C bond dissociation. The uncertainty in p corresponds to the σ of the approximately Gaussian momentum distribution, and the uncertainty in KER is derived from the momentum resolution of the detector at the applied VMI voltages (8 a.u.).

	1-IP		2-IP	
(I^+, $C_nH_x^+$)	$p(I^+)$ / a.u.	KER / eV	$p(I^+)$ / a.u.	KER / eV
CH_3^+	144 ± 20	0.22 ± 0.08	148 ± 18	0.15 ± 0.06
$C_2H_3^+$	144 ± 17	0.17 ± 0.07	147 ± 15	0.15 ± 0.06
$C_2H_4^+$	147 ± 15	0.20 ± 0.05	148 ± 17	0.13 ± 0.05

4.4.9 Primary C-C Fragmentation

In this section, the energetics of the sequential fragmentation processes occurring via primary C-C bond fission and secondary C-I dissociation are explored (i.e. the primary Coulomb explosion forming, and secondary dissociation of, the intermediates generated in the processes depicted in Figures 4.15(c) and (d)). Specifically, the (CH_3^+, $C_2H_3^+$) ion pair produced via primary C-C bond fission and secondary C-I dissociation is considered. The CH_3^+ momenta for this fragmentation channel was 82 ± 7 a.u. and 85 ± 9 a.u for 1-IP and 2-IP, respectively. The Newton-frame covariance maps showing the momenta of the secondary product $C_2H_3^+$ relative to the trajectory of the primary product CH_3^+ are given in Figure 4.25(a) and (b) for 1-IP and 2-IP, respectively. Based on the CH_3^+ momenta, at least 14 a.u. and 15 a.u. was expected to be partitioned into the corresponding $C_2H_3^+$ secondary products, with the iodine co-fragment retaining the largest fraction of primary momenta.

The experimentally observed $C_2H_3^+$ momenta were 26±14 a.u. and 27±13 a.u., indicating non-zero KER in the secondary dissociation step. By transforming the Newton-frame covariance maps into the native-frame of the $C_2H_4I^+$ intermediate (Figure 4.25(c) and (d)), the energetics of the secondary dissociation step can be directly interrogated. In this representation, the momenta of the $C_2H_3^+$ fragments were found to be 14 ± 11 a.u. and 18 ± 11 a.u. for 1-IP and 2-IP, respectively, corresponding to KER values of 0.07 ± 0.02 eV and 0.11 ± 0.02 eV, respectively, for the secondary dissociation step.

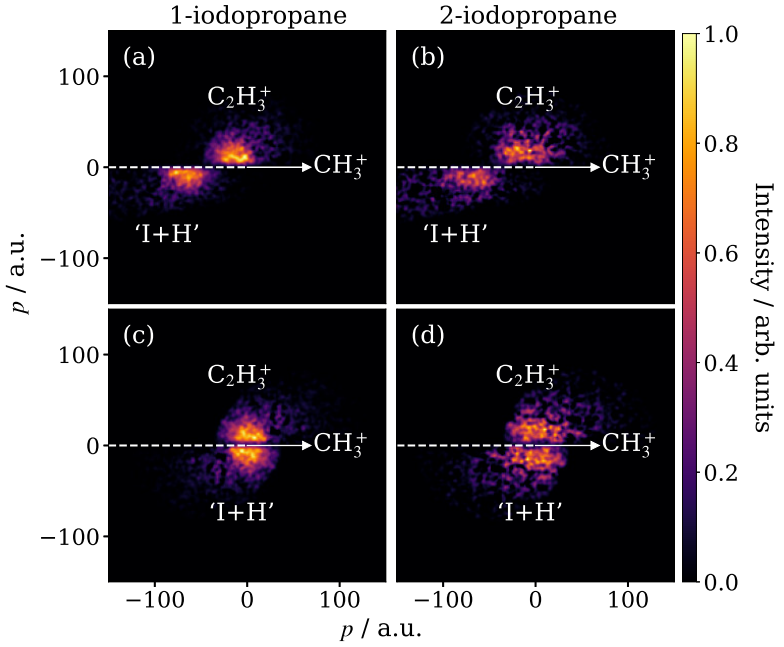

Figure 4.25: The Newton-frame covariance maps showing the momenta of CH_3^+, relative to I^+, produced via a primary Coulomb explosion breaking the C-C bond, and secondary C-I dissociation of the intermediate, are given in (a) and (b) for 1-IP and 2-IP, respectively. The same distributions are given in the native-frame of the propyl intermediate in (c) and (d), respectively. All maps are normalised independently.

Due to the relatively small mass of $C_2H_3^+$ relative to the neutral I co-fragment produced in the secondary dissociation step, the momenta of $C_2H_3^+$ in both the Newton and native-frame covariance maps are localised around the centre of the maps, with few pixels per unit radii. It is therefore challenging to resolve any angular information. By swapping the order of ions in the covariance calculation, the recoil of the primary product CH_3^+ relative to the secondary $C_2H_3^+$ is obtained.

This is shown in the Newton-frame covariance maps Figure 4.26(a) and (b) for 1-IP and 2-IP, respectively, and angular information can be characterised with greater clarity. The CH_3^+ feature has a constant radius, corresponding to the momenta gained in the primary Coulomb explosion. The relative recoil angle, however, sweeps out a broad distribution relative to $C_2H_3^+$. This is a result of the primary Coulomb explosion process rotationally exciting the $C_2H_4I^+$ intermediate about its centre of mass (approximately at the iodine atomic site). After some metastable lifetime, the intermediate dissociates and ejects a secondary $C_2H_3^+$ product in a broad range of angles relative to CH_3^+. The momenta gained by the iodine co-fragment in the secondary dissociation step is small compared to the fraction of momenta it retains from the primary process and therefore results in an essentially back-to-back recoil between CH_3^+ and I.

The integrated momenta of CH_3^+ and the iodine containing co-fragment ('I+H') are given in Figure 4.26(c) and (d) and the angular distributions in Figure 4.26(e) and (f). These distributions are broadly similar across the two isomers, despite the decreased intensity of this channel for 2-IP and the differing initial parent isomer geometries. CEI usually requires a prompt Coulomb explosion for structural determination, but these results show that this secondary dissociation process generating neutral co-products is essentially blind to the initial geometry of the molecule. Coupling this type of analysis with either an XUV-IR or XUV-XUV pump-probe experiment could allow the lifetime and dissociation of the intermediate to be characterised in more detail.

The channel yielding primary CH_3^+ and secondary $C_2H_3^+$ is more prominent than the channel yielding $C_2H_4^+$ for both isomers. Furthermore, this channel is much more significant in the mass spectrum of 1-IP than 2-IP. Since the neutral I and H/H^+ fragments could not be detected, and the photoelectron information was not recorded during these experiments, it is difficult to determine why the iodine remains neutral and whether it is free or exists as HI. However, it is possible to speculate that neutral free iodine could be stabilised by combining with neutral hydrogen, resulting in a preference for generating $C_2H_3^+$ over $C_2H_4^+$. If this is the

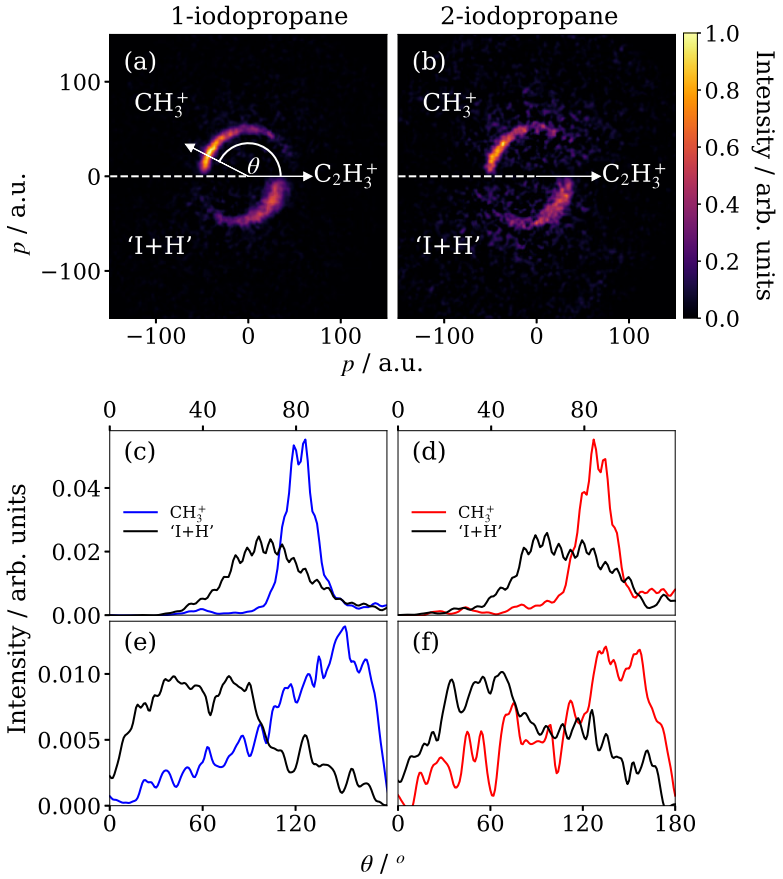

Figure 4.26: The Newton-frame covariance maps showing the momenta of primary CH_3^+ fragments relative to secondary $C_2H_3^+$ fragments, generated from the molecular dication, are given in (a) and (b) for 1-IP and 2-IP, respectively. The corresponding integrated momentum distributions for CH_3^+ and the neutral co-fragments are given in (c) and (d), and the integrated angular distributions in (e) and (f).

case, in 1-IP, the carbon directly attached to the iodine carries with it two hydrogen atoms. In 2-IP, the iodine atom is neighboured by a carbon atom bonded to only one hydrogen atom. The close proximity to double the number of H-atoms in 1-IP may be the cause of the increased prominence of this channel relative to 2-IP.

4.4.10 Sensitivity to Momentum Exchange Between Products

The methods presented so far in this chapter demonstrate how detailed and refined information describing relative momenta of co-fragments produced in *different* fragmentation mechanisms can be obtained. Now, sensitivity to the momenta of co-fragments generated within the *same* fragmentation mechanism will be demonstrated

by further extension of these methods.

In the examples given up to this point, covariance calculations were performed using momentum conditions and constraints according to the fragmentation channel of interest. For changes in momenta within a specific fragmentation channel, covariance can be further broken down and calculated as a function of the momenta of one of the ionic products. Covariance for the ($C_2H_3^+$, CH_3^+) ion pair is used as an example here. The angular distribution of primary CH_3^+ products relative to the secondary product $C_2H_3^+$ is calculated as a function of the momentum of the secondary fragment ($p(C_2H_3^+)$), which is plotted in Figure 4.27. This distribution visualises how the momentum of the secondary product is dependent on the orientation of the intermediate relative to the primary product. When the momentum of the secondary product is at its highest (∼50 a.u.), the angular distribution has a maximum near 180°, which corresponds to the intermediate being oriented in such a way that the $C_2H_3^+$ points away from the trajectory of the CH_3^+ and in the direction of the vector of the momentum gained by the intermediate in the primary process, as shown in the schematic Figure 4.28(a). The vector of the momenta gained by the $C_2H_3^+$ in the secondary process points in the same direction as its momenta retained from the primary process. The two vectors sum constructively, increasing the total $C_2H_3^+$ momenta, and the two cations recoil at approximately 180°. When $p(C_2H_3^+)$ is at its lowest in Figure 4.27 (∼10 a.u.), the relative recoil angle distribution is broad. The orientation of the intermediate giving rise to this distribution is depicted in the schematic Figure 4.28(b). The $C_2H_3^+$ component of the intermediate species points towards the trajectory of the CH_3^+ product and in the opposite direction to the primary momentum vector of the intermediate. The momentum vector of the secondary process acts in the opposite direction to the primary process, decreasing the total $C_2H_3^+$ momenta. Depending on the exact angle of orientation of the intermediate, a broad range of recoil angles is observed. These results demonstrate the sensitivity of 3D covariance analysis methods to small changes in the vector addition of two products, which depends on the lifetime and nuclear dynamics induced in the

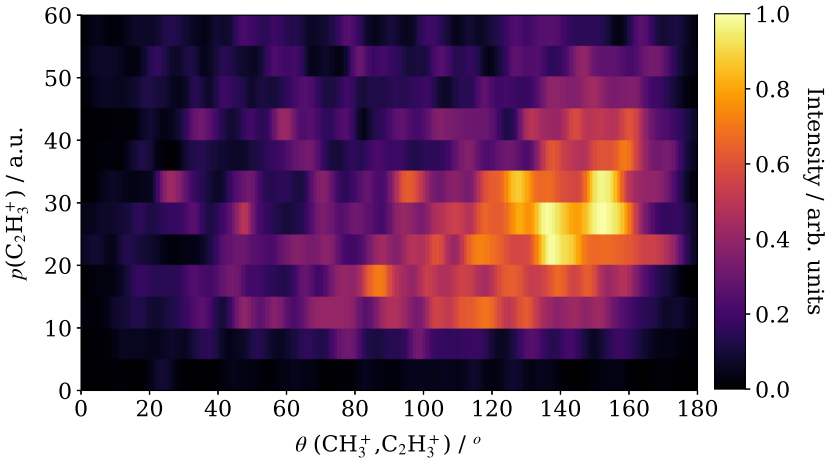

Figure 4.27: The angular distribution of primary CH_3^+ products relative to the secondary $C_2H_3^+$ products, calculated as a function of the momenta of the secondary product ($p(C_2H_3^+)$). The heat map is normalised to its maximum.

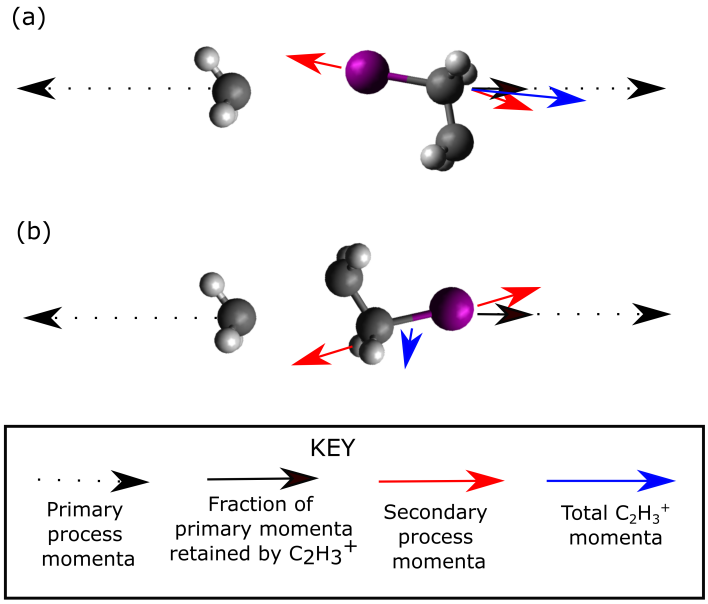

Figure 4.28: Schematics depicting the additive (a) and subtractive (b) primary and secondary momenta vectors of $C_2H_3^+$.

intermediate. Extending these techniques to time-resolved studies could provide highly detailed information describing small changes to the relative momenta and recoil of two ions to characterise multidimensional photo-dissociation dynamics.

4.5 Conclusions

In this chapter, 3D covariance analysis methods have been used to disentangle concurrent fragmentation channels occurring in molecular polycations of 1-IP and 2-IP. Different fragmentation channels generating the same pairs of co-ions with similar momenta can be resolved and independently analysed using carefully considered momentum constraints applied to the covariance calculations. This was demonstrated for fragmentation channels generating the (I^+, CH_3^+, $C_2H_4^+$) ion sets via concerted and sequential Coulomb explosions. Furthermore, the ability of native-frame covariance analysis to characterise the energetics of the individual steps of the sequential fragmentation process was demonstrated.

The methods presented in this chapter were also used to extract approximate branching ratios of competing fragmentation channels producing two heavy, charged fragments and allow detailed insights into how the geometry of a molecule and charge distribution affect the nuclear dynamics of metastable species. Furthermore, the relationship between product momenta and recoil angle can be related to the rotational nuclear dynamics of intermediate species. These analysis methods can extract highly detailed descriptions of the range of fragmentation mechanisms available to molecular polycations but rely on high ToF resolution to recreate the 3D momentum information for each ion hitting the detector. The results presented here indicate that 3D covariance analysis could be extended and applied to study more complicated experimental regimes such as pump-probe spectroscopy and fragmentation of larger complexes in lowly-charged cationic states generating long-lived polyatomic intermediates.

Acknowledgements

The experiment was performed at SACLA with the approval of JASRI and the program review committee (Proposal No. 2021A8038 Forbes). I would like to acknowledge J. W. McManus who equally contributed to the work presented in this chapter and co-authored the two corresponding papers. I would like to thank

the collaboration of researchers who were involved in the beamtime, subsequent discussion of results, and preparation of the two manuscripts: K. Nagaya, J. R. Harries, Y. Kumagai, H. Iwayama, M.N.R. Ashfold, M. Britton, P.H. Bucksbaum, B. Downes-Ward, T. Driver, D. Heathcote, P. Hockett, A.J. Howard, E. Kukk, J.W.L. Lee, Y. Liu, D. Milesevic, R.S. Minns, A. Niozu, J. Niskanen, A.J. Orr-Ewing, S. Owada, D. Rolles, P.A. Robertson, A. Rudenko, K. Ueda, J. Unwin, C. Vallance, M. Burt, M. Brouard, and I thank F. Allum and R. Forbes for arranging the beamtime. Furthermore, I thank SACLA for the provision of the experimental facilities and the scientific and technical teams who made these experiments possible.

So with the right attitude and a couple cocktails, it could be fun.

— Seth Cohen, The O.C.

5

Newton-Frame Covariance Analysis of Iodobenzene Fragmentation channels Induced by XUV-ionisation

Contents

5.1 Introduction

In Chapter 4, advanced covariance analysis methods were used to characterise concurrent fragmentation processes of molecular polycations produced from XUV-ionisation of iodopropane. Here, the applicability of these methods and techniques

to study the competing fragmentation pathways of more chemically complex compounds (comprising a larger number of atoms, resulting in more degrees of freedom) is demonstrated.

Aromatic compounds are characterised by high stability, low reactivity, non-polarity, and immiscibility. These properties are a result of their delocalised π-electron systems, making them widely useful in many areas of chemistry, biochemistry, and materials science. The chemistry of aromatic systems is determined by the energetics and PESs of the molecule, which often act to preserve aromaticity.[192–194] One specific branch of aromatics, polyaromatic hydrocarbons (PAHs), make up approximately 10-20% of the carbon in the Milky Way and a large fraction of carbon throughout the universe. When exposed to XUV light, they can become ionised and subsequently fragment and are, therefore, large contributors to the complex and evolutionary chemistry of the interstellar medium (ISM).[195–199] As such, there is broad interest in how polycationic aromatic compounds fragment and how their photochemistry is influenced by different ionisation and excitation regimes.

XUV-ionisation via AM decay can populate a broad range of excited states, each of which is characterised by its own fragmentation dynamics. In highly excited aromatic molecules, large numbers of nuclear and electronic degrees of freedom can become coupled, forming non-adiabatic conical intersections that facilitate and mediate rapid relaxation on femtosecond timescales from highly excited electronic states into ground electronic, but vibrationally hot, states.[199–203] The excess energy that is deposited into vibrational modes can induce structural distortion, isomerisation, and bond-cleavage via H-atom, H_2, and acetylene loss, in order of energetic accessibility.[192, 199, 204–208] Fragmentation becomes dominant as the internal energy of the system increases, although many structural changes induced by vibrational excitation can facilitate higher energy fragmentation pathways. For example, isomerisation can lower the energy barriers to fragmentation, and H-atom loss can also allow access to fast fragmentation into larger products.[194] These relaxation dynamics have been documented for many PAHs in monocationic and dicationic states, including naphthalene, anthracene, pyrene, phenanthrene, and

fluorene.[201, 208, 209] In terms of larger fragmentation processes, acetylene loss is the most commonly reported mechanism, but larger fragments may also be lost, usually containing even numbers of carbon atoms.[192, 204, 207, 209]

CEI and recoil-frame covariance analysis have been used successfully in previous studies to match pairs of ions generated from polycationic PAHs and extract the KER of their Coulomb explosions.[209] Unexpected pairs of co-fragments were detected, which suggested substantial molecular rearrangement of the carbon backbone before fragmentation. This can lead to complicated mass spectra since smaller fragments can be generated via a large number of associated pathways.[208, 209] However, the level of information available for describing a fragmentation channel can be limited when using recoil-frame covariance, as it only makes use of the 2D projection of an ion's Newton sphere on a detector and not 3D ion momenta. Chapter 4 showed that much more detailed information can be obtained when using more advanced, 3D covariance analysis techniques (such as Newton- and native-frame covariance coupled with momentum filtering techniques). These techniques can even disentangle concurrent fragmentation pathways that generate identical sets of ions with similar momenta. Here, these techniques will be applied to study the fragmentation of polycationic phenyl (Ph), the simplest aromatic molecule and a building block of PAHs, to demonstrate the applicability of these analysis techniques to study the photochemistry of larger compounds, such as the XUV chemistry of PAHs.

The excited-state photochemistry of Ph cations and polycations is very similar to that of PAHs. Following XUV-ionisation to a broad range of highly excited states, quick electronic relaxation ($\sim$100 fs) populates vibrationally hot excited states, which can then facilitate a large variety of possible structural changes, including isomerisation, H-atom loss, and fragmentation of the carbon chain.[200, 210, 211] Fragmentation into larger products generally requires more energy than H-atom loss and favours the formation of stable species, such as acetylene, but the energy barrier to these processes can be lowered by isomerisation, ring opening and closure, hydrogen transfer, and/or skeletal rearrangements.[194, 199, 200, 210, 212] For

Ph polycations, fragmentation can also produce two charged carbon species via a Coulomb explosion.[194, 199, 210, 212, 213]

In this chapter, site-selective ionisation of iodobenzene (IB) at the I 4d threshold was used to investigate the stability of Ph cations and polycations. The ensuing AM decay processes generated a range of stable and unstable cationic Ph states. Newton-frame covariance is used to map the momenta of carbon-containing cations relative to I^+ ions. These maps allow the nuclear dynamics of concurrent fragmentation mechanisms occurring in Ph cations to be characterised, as well as the timescales these processes occur on. The results demonstrate the potential of extending 3D covariance analysis techniques to study static and time-resolved photochemistry of larger molecules (such as PAHs) in high levels of detail and specifically highlight the capability of these methods to characterise fragmentation processes of lowly charged cations in long-lived excited states.

5.2 Methods

5.2.1 Experimental

Ion imaging was carried out at the Spring-8 Angstrom Compact free electron LAser (SACLA, Japan), using the soft X-ray beamline (BL1). More in-depth details of the experimental facility are given in Chapter 4. Briefly, the XUV photon energy used in this work was tuned to 120 eV to site-selectively ionise the sample at the high energy edge of the I 4d orbitals, which has an absorption cross-section of 1.4 Mb.[170, 214, 215] Pulses were generated with a repetition rate of 60 Hz, a bandwidth of 2%, and a 30 fs pulse duration. Shot-to-shot measurements of the pulse energies were made by a gas intensity monitor. The distribution of XUV pulse energies (Figure 5.1) was normally distributed throughout the experiment. The average unattenuated energy was found to be 11.37 ± 1.15 uJ. The pulse energy was attenuated by a 0.65 μm thick Zr filter with a transmission of 13%. Accounting for this and the transmission of the beamline (∼90%), the average XUV pulse energy at the interaction region of the VMI spectrometer (shown in Chapter 4 Figure 4.3) was expected to be approximately 1.33 ± 0.13 μJ. A KB mirror system was used

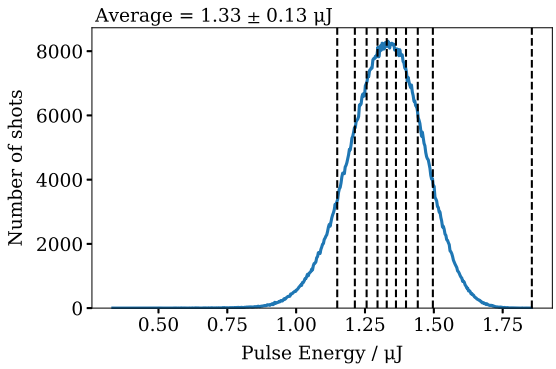

Figure 5.1: A histogram of the attenuated XUV pulse energies within the interaction region of the spectrometer. Dashed lines indicate how the data was split according to pulse energy into 10 subsets with equal numbers of laser shots for use in contingent covariance analysis.

to focus the XUV pulses to a spot size of approximately $\sim$10 μm ($1/e^2$) within the interaction region of the spectrometer. The approximate Gaussian intensity of the XUV beam at the focal spot was 1.1×10^{14} W cm^{-2}.

In this experiment, only photoions were recorded by the VMI spectrometer. A gaseous sample of iodobenzene was introduced to the reaction chamber via a pulsed gas jet (General Valve) and expanded via a skimmer to produce a pulsed molecular beam, which was then ionised by the XUV beam. Resultant ions were accelerated down a field-free ToF region and velocity mapped by ion optics onto a dual MCP detector, equipped with a hexanode delay line detector. The x, y, and ToF information were recorded for multiple ion hits on the detector per laser shot ($\sim$8 ions per shot, on average). The ToF information of each ion was accurately measured by the hexanode delay line detector relative to the electronic trigger of the 60 Hz repetition rate laser. The high ToF resolution of this detector ($<$1 ns) allowed for 3D momentum information to be recovered for multiple ion hits per laser shot.

5.2.2 Data Analysis

Since 3D momentum information was retrieved for each ion hit recorded at the detector, 3D covariance analysis methods could be employed to analyse the data. Relative ion momentum distributions are shown using the Newton-frame representation and, in some instances, covariances are also given in the native-frame of the intermediate

species. For cases where the same pairs of ionic products are produced via different fragmentation channels, corresponding covariance features are separated by filtering on the momenta of the reference ion used in the covariance calculations. Specific filtering parameters are discussed within the text as needed. All covariances were calculated contingently, as described in Section 2.3.8, by splitting the data into 10 subsets, each comprising the same number of laser shots, according to the XUV pulse energy. The dashed lines in Figure 5.1 show the XUV pulse energy ranges used to generate these subsets. Integrated intensities of covariance features, and corresponding uncertainty values, are calculated via the bootstrapping method also outlined in Section 2.3.9, using 100 subsets of the data comprising 50,000 randomly selected laser shots.

Classical point-charge simulations are used to model the effect of H^+ loss on co-product ion fragment momenta. Simulated concerted Coulomb explosions are initiated from the ground state geometry and lowest energy configuration of neutral IB. The charge on each fragment is assumed to be at the centre of mass of the fragment and to interact exclusively under Coulomb's law. Classical trajectories of the point charges are propagated to their asymptotic terminal velocities by solving Newton's equations (firstly, from 0-100 fs in 1 fs steps, and then from 100-1000 fs in 25 fs steps).

5.3 Results And discussion

The mass spectrum obtained following XUV-ionisation of IB is presented in Figure 5.2(a), along with the structure of the parent molecule (b). Each H-atom on the parent molecule is labelled according to the position of the carbon atom it is bonded to relative to the carbon bonded to the iodine, where 1 is the iodo-substituted carbon. The ToF-ToF covariance map is given in (c). The feature along the diagonal with the positive gradient is the autovariance signal, and correlated ion pairs are given by the off-diagonal features. A variety of ion pairs were detected and can be distinguished from the features in this spectrum, and the relative

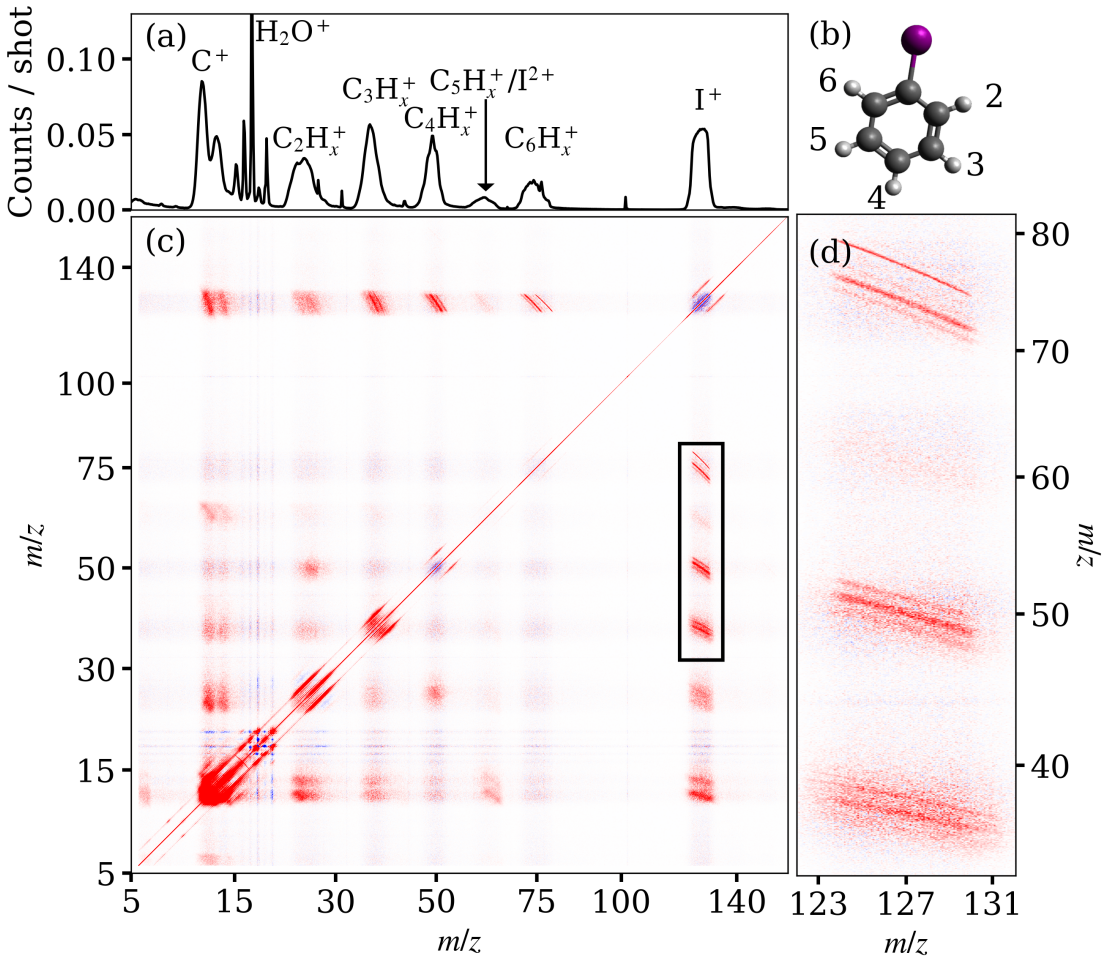

Figure 5.2: (a) The mass spectrum obtained following XUV-ionisation of IB. (b) Schematic of the structure of neutral ground state IB with each H atom labelled according to the carbon atom, where 1 is the iodo-substituted position. (c) The ToF-ToF covariance map. The region indicated by the black box is plotted in (d) on a magnified scale.

intensities of these features correspond to the statistical significance of each ion pair to the total mass spectrum.

Covariances between I^+ and $C_nH_x{}^+$ ($3 \leq n \leq 6$, $x \leq 5$) are highlighted by a black box in Figure 5.2(c) and shown on a magnified scale in (d). The ToF resolution of the hexanode delay line detector allows for fragments differing in mass by a single hydrogen atom to be resolved. The gradients of these features are indicative of the types of mechanisms producing these co-fragments. The gradients of several well-defined features are given in Table 5.1, along with the masses of the carbon-containing co-fragment expressed as a ratio of the mass of the

Table 5.1: Gradients obtained for several of the (I^+, $C_nH_x{}^+$) features observed in Figure 5.2(d), and the mass of the corresponding carbon fragment expressed as a ratio of the mass of Ph.

$C_nH_x{}^+$	gradient	$-m(C_nH_x{}^+)/m(C_6H_5{}^+)$
$C_6H_5{}^+$	-1.01 ± 0.02	-1
$C_6H_2{}^+$	-0.96 ± 0.03	-0.96
C_6H^+	-0.97 ± 0.04	-0.95
$C_4H_3{}^+$	-0.52 ± 0.07	-0.66
$C_4H_2{}^+$	-0.64 ± 0.04	-0.65

Ph. The ions produced in a two-body explosion (I^+ and $C_6H_5{}^+$) recoil with equal and opposite momenta. Therefore, the ToFs of these two ions are anti-correlated and have a gradient of approximately -1. The gradients obtained for other $C_6H_x{}^+$ fragments show that loss of H/H^+ has only a small effect on the relative recoil between the carbon-containing ion and I^+. Covariance features arising from many-body fragmentation channels, producing smaller carbon-containing fragments via fragmentation of the carbon ring (e.g., $I^+ + C_nH_x{}^+$, where $n < 3$), have gradients much shallower than -1. These indicate sequential fragmentation processes that occur via a primary Coulomb explosion into I^+ and a $C_6H_x{}^+$ intermediate that further decays in a secondary process into a charged and a neutral carbon-containing species. If the KER of the secondary dissociation step is zero, the slopes of the ToF-ToF covariance features are expected to be close in value to the ratio of the mass of the secondary product and intermediate (Equation 2.3.2.6).[132] The values for the examples given in Table 5.1 are generally in very close agreement, but disagreements between any of these values are likely because the corresponding covariance features can comprise contributions from different fragmentation pathways generating the same pairs of ions. Furthermore, the KER of the secondary dissociation steps are likely to be non-zero, even if they are small. Both of these factors also act to broaden the covariance features since the momenta of the secondary fragments have components acting out of the plane of the primary bond-breaking vector, rather than only along the bond-breaking vector.

The ToF spectrum suggests that iodine charge states greater than 1+ were generated by the XUV-ionisation process but the ToF-ToF covariance map shows

that only covariances with I^+ are significant and, henceforth, higher iodine charge states are not considered. ToF-ToF covariance is also observed between pairs of carbon-containing compounds, specifically $C_nH_x{}^+$ and $C_{6-n}H_y{}^+$ ($y \leq 5 - x$), and most prominently between ion pairs where $n = 2$ or $n = 3$. Very low-intensity covariance was also seen between $C_nH_x{}^+$ and $C_{6-n}H_yI^+$ ions pairs (∼100 times less intense than $C_nH_x{}^+/I^+$ covariance) with a gradient of -1, and indicate that only a relatively small amount of IB was ionised to excited states where fragmentation first occurs via C-C bond cleavage. However, these reactions are not the focus of this chapter, which aims to characterise the stability of Ph cations following C-I fragmentation.

The absolute momenta (p) of all detected I^+ ions are plotted in Figure 5.3. Two peaks are seen. The first corresponds to fragmentation channels producing I^+ and one carbon-containing monocation, with $p(I^+) = 153 \pm 18$ a.u. (where the error is the width, σ, of the Gaussian distribution). The second peak corresponds to fragmentation channels producing I^+ and either one carbon-containing dication or two carbon-containing monocations, with $p(I^+) = 213 \pm 25$ a.u. In the following sections, Newton-frame covariances corresponding to the processes constituting these two peaks will be separated by filtering on $p(I^+)$, as was done in Chapter 4. Here, fragmentation channels contributing to this lower momentum peak are isolated in covariance analysis using $p(I^+) \leq 200$ a.u., and the higher momentum peak using $p(I^+) \geq 200$ a.u., shown by the dashed line in Figure 5.3. This boundary was chosen as the lower momentum feature is more intense than the higher momentum feature, with the area under the former curve being approximately three times greater than that of the latter. Even though this boundary does not capture the whole of the higher momentum peak, it excludes as much of the covariance features corresponding to the more intense lower momentum peak as possible while still retaining sufficient statistics for the covariance calculation.

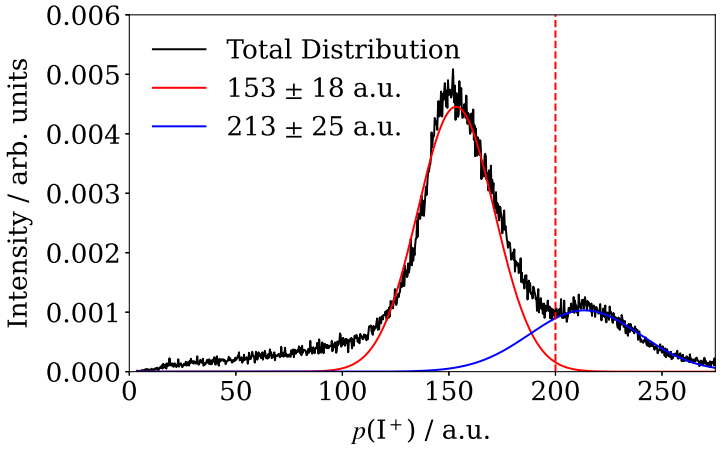

Figure 5.3: The momentum distribution of all detected I^+ species. Gaussian distributions were fitted to the two observable peaks, and the parameters obtained for both fits are discussed in the text. A dashed line indicates how covariance maps for the two momentum ranges were separated.

5.3.1 I^+ And $C_6H_x^+$ Ion Pairs

First, fragmentation processes producing I^+ and $C_6H_x^+$ are considered. In these processes, the Ph component of IB was stable or unstable with respect to H/H^+ loss, but the carbon chain remained intact.

Newton-frame covariance maps showing the momenta of $C_6H_5^+$ and $C_6H_2^+$ relative to I^+ are given in Figure 5.4(a) and (b), respectively. By integrating the covariance features obtained for all $I^+/C_6H_x^+$ co-fragments, relative intensities can be obtained. These are plotted in Figure 5.4(c), with error bars corresponding to uncertainties obtained via a bootstrapping method. The greatest intensity covariance is seen for $C_6H_2^+$, implying a preference for populating cationic excited states that lose at least 3 H/H^+ species, followed by $C_6H_5^+$. The Newton-frame covariance map Figure 5.4(b) shows that any impulse due to H/H^+ loss did not significantly perturb the recoil angle between the trajectories of the I^+ and $C_6H_x^+$ fragments, thus resulting in an essentially back-to-back recoil distribution.

The momenta of the I^+ and $C_6H_x^+$ fragments, obtained from Newton-frame covariance, are listed in Table 5.2 and are also plotted as a function of x in Figure 5.4(d). The momenta of the (I^+, $C_6H_5^+$) ion pair and Coulomb's law were used to obtain an effective intercharge separation on the molecular dication

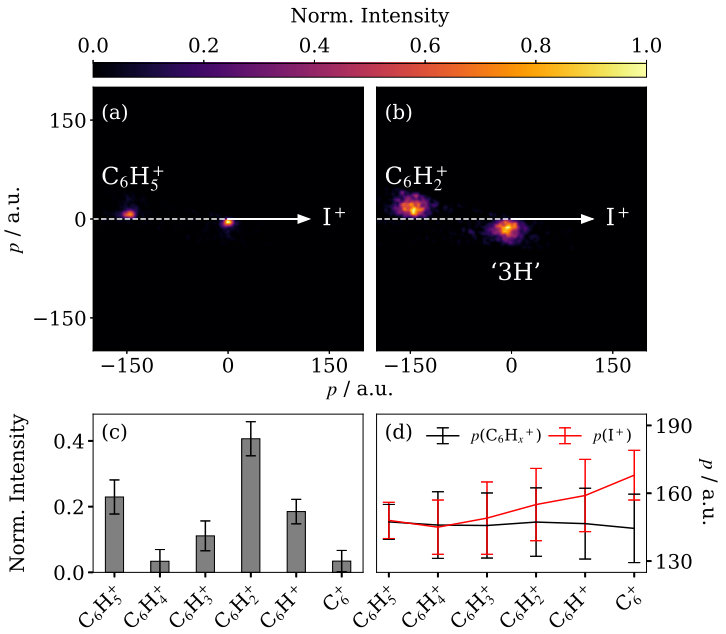

Figure 5.4: The Newton-frame covariance maps of the momenta of $C_6H_5^+$ (a) and $C_6H_2^+$ (b) relative to I^+. The integrated intensity of covariance features observed for all (I^+, $C_6H_x^+$) ion pairs are given in (c), with error bars obtained via a bootstrapping method. The momenta (p) of $C_6H_x^+$ and I^+ fragments, obtained from Gaussian fits to the Newton-frame covariance maps, are plotted in (d) as a function of x, with error bars corresponding to the σ of the Gaussian distributions.

leading to two-body Coulomb explosion. This was found to be 4.33 ± 0.06 Å, which is approximately the internuclear distance between iodine and a carbon atom in the meta position of the neutral ground state parent geometry (∼4.34 Å) and suggests that the charge on the Ph component of IB is most likely distributed about its π-system (for comparison, the internuclear distance between the iodine and carbon in the para-position is ∼4.87 Å). This is depicted in Figure 5.5: a red arc overlies a schematic of IB and indicates the most likely location of the charge on the Ph component of IB prior to the Coulomb explosion with I^+, according to the effective intercharge separation calculated from the fragment momenta. The origin of the arc is at the iodine atom and its radius is equal to the internuclear distance between the iodine and the carbon atom in the meta position.

The error bars shown in Figure 5.4(d) correspond to the σ of the approximately Gaussian features in the Newton-frame covariance maps. As x decreases, σ increases for both ion types. However, the average momenta of the $C_6H_x^+$ ions are

Table 5.2: The average momenta (p) of covariant $C_6H_x^+$ and I^+ fragments, obtained via Gaussian fits to the Newton-frame covariance features, quoted with the σ of the Gaussian distributions.

$C_nH_x^+$	$p(C_6H_x^+) \pm \sigma$ (a.u.)	$p(I^+) \pm \sigma$ (a.u.)
$C_6H_5^+$	147 ± 8	148 ± 8
$C_6H_4^+$	145 ± 15	145 ± 12
$C_6H_3^+$	146 ± 15	149 ± 16
$C_6H_2^+$	147 ± 15	155 ± 16
C_6H^+	147 ± 16	159 ± 16
C_6^+	145 ± 16	168 ± 11

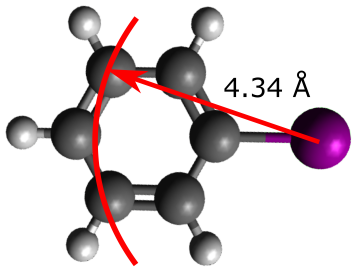

Figure 5.5: A schematic showing the effective intercharge separation between I^+ and $C_6H_5^+$. The red arc has an origin at the iodine atom and a radius equal to the internuclear distance between the iodine and the carbon atom in the meta position, which is also shown by the red arrow.

approximately independent of x and remain constant, whereas $p(I^+)$ increases with decreasing x, as was observed in Chapter 4 for 1- and 2-iodopropane. As x decreases from $x = 5$ to $x = 0$, $p(I^+)$ increases by approximately 20 a.u., corresponding to a decrease in effective intercharge separation of $\sim$1 Å. These x-dependencies reveal potential characteristics of the H/H^+ loss processes.

If H/H^+ loss occurred before the C-I Coulomb explosion, then the momenta of both I^+ and $C_6H_x^+$ species should be affected, and repel with equal and opposite momenta in the ensuing Coulomb explosion. However, the experimentally observed ion pairs become less momentum-matched as x decreases. If, instead, H/H^+ loss occurred after the C-I Coulomb explosion, $p(I^+)$ should remain constant and $p(C_6H_x^+)$ should vary with x, but this is opposite to the trends observed. Therefore, H/H^+ loss may occur either concertedly or on very similar timescales to the C-I

Coulomb explosion process. Similar mismatches in product momenta have been reported in other studies, where CH_3I was ionised to very high charge states (e.g., up to 22+). This phenomenon was assigned to small kinematic contributions from the H-atom or H^+ emission processes.[154, 216] It is interesting that, despite the much lower iodine charge states generated here, similar momenta mismatches are also observable. Neutral H-atoms were not detected in this experiment, and any H^+ ions generated in such processes would have been too energetic to be focused onto the detector, and, therefore, no covariance with H^+ was obtainable. Therefore, the charge state of the hydrogen species lost in these fragmentation channels is ambiguous.

Simplistic, classical point charge simulations (described in Section 5.2.2) were carried out to investigate the effect of H^+ loss on $p(I^+)$ and $p(C_6H_x{}^+)$. Concerted Coulomb explosions were simulated between I^+, $C_6H_x{}^+$, and (5-x)H^+ fragments, originating from the ground state geometry of iodobenzene, with point charges placed at the centre of mass of each fragment. All combinations of H^+ loss from different carbon positions were considered, including degenerate combinations of positions. The simulated momenta of the I^+ and $C_6H_x{}^+$ fragments are listed in Table 5.3 and are plotted in Figure 5.6 for comparison with the experimentally observed fragment momenta. The trends in experimental and simulated $p(I^+)$ agree very well, with both momenta increasing with increasing H^+ loss. However, while the experimentally observed $p(C_6H_x{}^+)$ remains approximately constant for all x, the simulated $p(C_6H_x{}^+)$ decreases with x. These results suggest that it is plausible the H-species lost are H^+, but the timescales of these processes are not necessarily all concerted. The simple classical simulations neglect any possibility of diffuse and partial charge distributions and do not consider different timescales of the different H^+ loss processes or that the geometry of the parent polycation is not necessarily in its neutral ground state configuration. A more thorough simulation could be carried out to investigate these relationships further, accounting for varying timescales of each bond-breaking process, the geometry of the iodobenzene polycation, and to include neutral H-atom loss. Higher levels of theory than these very basic simulations may also be beneficial in understanding the effect of H/H^+ loss on

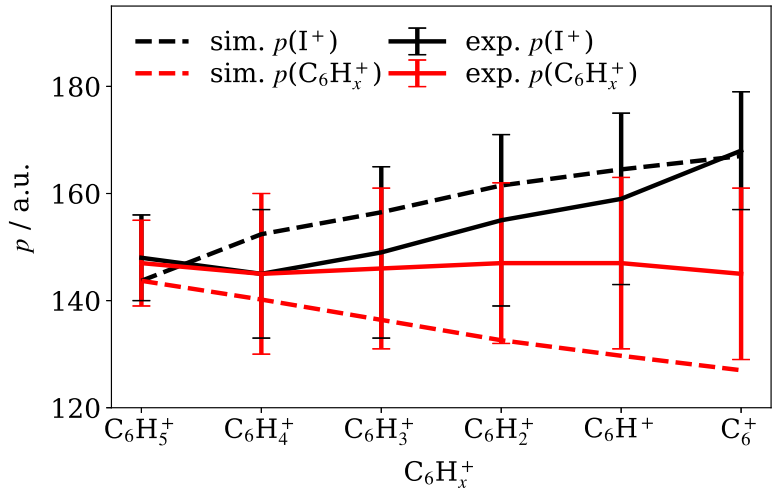

Figure 5.6: The average I^+ ($p(I^+)$) and $C_6H_x{}^+$ ($p(C_6H_x{}^+)$) fragment momenta, obtained from classical Coulomb explosion simulations and plotted as a function of x ('sim.'). Also plotted are the experimentally obtained momentum distributions for both ions ('exp.'), with error bars corresponding to the σ of the respective Gaussian momentum distributions.

fragment momenta. However, the information gained from such simulations may not provide much more clarity to the processes observed in this experiment. In-depth simulated studies have previously been carried out on the energetics of H/H^+ loss processes occurring in PAHs, which showed very similar energetics for processing generating either a neutral H-atom or H^+ species from different combinations of initial H-atom positions on the PAH.[209] Considering this, and the broad Gaussian momentum distributions observed here, many combinations of parameters and fragmentation processes could give rise to similar outcomes and lead to fragment momenta within the ranges measured here that cannot be differentiated within the momentum resolution of the spectrometer.

5.3.2 I^+ And $C_nH_x{}^+$ Ion Pairs Produced With Neutral $C_{6-n}H_y$ Co-fragments

Next, the fragmentation processes producing I^+ and $C_nH_x{}^+$ ions pairs and a neutral carbon-containing co-fragment are considered. In these cases, the parent molecules were unstable with respect to fragmentation of the carbon ring, but H/H^+ loss could also occur. Newton-frame covariance maps of the products of such

Table 5.3: Simulated concerted Coulomb explosions were carried out to investigate the effect of H^+ loss on $p(I^+)$ and $p(C_6H_x{}^+)$, which are listed in this table for all variations of H^+ loss from different carbon atom locations. The carbon atom locations (2, 3, 4, 5, 6) correspond to the positions labelled in Figure 5.2(b). Average momenta of I^+ and $C_6H_x{}^+$ were obtained for each number of H^+ loss and plotted in Figure 5.6.

$C_6H_x{}^+$	H^+ loss	$p(I^+)$ / a.u.	$p(C_nH_x{}^+)$ / a.u.
$C_6H_5{}^+$		143.7	143.7
$C_6H_4{}^+$	6	144.3	146.4
	5	154.9	138.2
	4	163.8	131.7
	3	154.9	138.2
	2	144.3	146.4
$C_6H_3{}^+$	5, 6	150.9	142.6
	4, 6	160.2	134.0
	4, 5	168.3	130.0
	3, 6	154.5	135.9
	3, 5	165.1	129.8
	3, 4	167.7	130.2
	2, 6	144.3	142.5
	2, 5	154.8	135.8
	2, 4	159.9	134.1
	2, 3	150.5	143.0
$C_6H_2{}^+$	4, 5, 6	163.4	134.3
	3, 5, 6	161.2	132.1
	3, 4, 6	165.9	128.9
	3, 4, 5	174.3	125.3
	2, 5, 6	151.3	138.1
	2, 4, 6	158.2	132.9
	2, 4, 5	166.0	128.8
	2, 3, 6	151.0	138.3
	2, 3, 5	161.1	132.2
	2, 3, 4	162.8	134.7
C_6H^+	3, 4, 5, 6	170.4	127.2
	2, 4, 5, 6	162.2	130.6
	2, 3, 5, 6	158.1	132.3
	2, 3, 4, 6	161.9	130.8
	2, 3, 4, 5	170.1	127.4
$C_6{}^+$	2, 3, 4, 5, 6	166.9	127.0

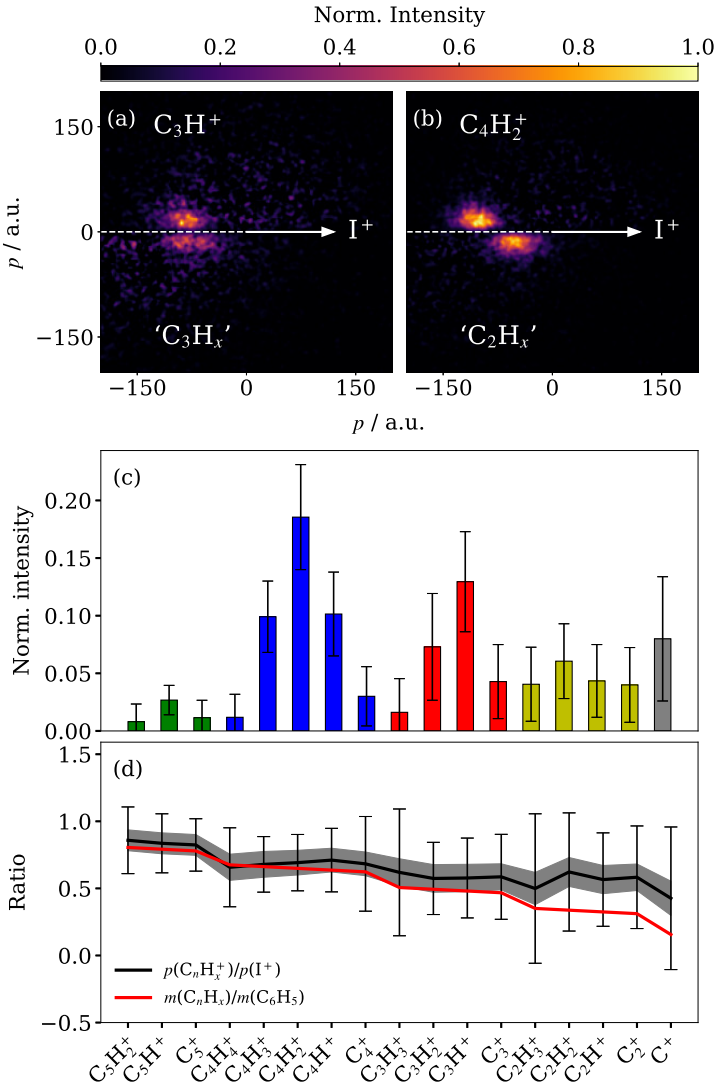

Figure 5.7: Newton-frame covariance maps showing the momenta of C_3H^+ (a) and $C_4H_2^+$ (b) relative to I^+, produced with a neutral carbon-containing co-fragment. The integrated intensity of covariance features observed for all (I^+, $C_nH_x^+$) ion pairs are given in (c), with error bars obtained via a bootstrapping method. The ratio of the momenta (p) of all ion pairs is plotted in (d). The grey shaded region is related to the momentum resolution of the detector at the applied VMI voltages (8 a.u.) and the error bars correspond to the sum of the σ of the Gaussian momentum distributions of both ions in each ion pair. Also shown is the mass (m) of the $C_nH_x^+$ fragment, expressed as a fraction of the mass of Ph.

fragmentation channels are isolated by only considering I^+ ions with $p(I^+) \leq 200$ a.u. in the covariance calculation.

Newton-frame covariance maps showing the momenta of C_3H^+ and $C_4H_2^+$ ions relative to I^+ ions are given in Figure 5.7(a) and (b), respectively. The relative recoil

angle in both cases is effectively back-to-back, indicating that these fragments are generated with a neutral co-fragment in a process that does not significantly alter the relative recoil between the I^+ and $C_nH_x{}^+$ co-fragments, which is determined mostly by their mutual Coulombic repulsion.

The relative intensities of the covariance features observed for all $C_nH_x{}^+$ fragments are plotted in Figure 5.7(c). It can be seen that the most favourable fragmentation pathway generates $C_4H_x{}^+$ products, likely with a neutral C_2H_y co-fragment such as acetylene. The momenta of both charged fragments are given in Table 5.4 and, by examining the ratio of the momenta of the $C_nH_x{}^+$ and I^+ products, further insights into the fragmentation pathway can be deduced. This ratio is plotted in Figure 5.7(d), along with the mass of the $C_nH_x{}^+$ products expressed as a fraction of the mass of Ph. The grey shaded region is the uncertainty derived from the momentum resolution of the detector at these VMI voltages (8 a.u.), and the error bars are derived from the sum of the σ of the momentum distributions of the covariance features for both ions.

Consider a sequential fragmentation process occurring via a primary two-body Coulomb explosion and secondary dissociation of a metastable intermediate species. Assuming that the secondary products gain no KER from the secondary dissociation process, the momenta of the intermediate is partitioned between the secondary products according to their mass (Equation 2.3.2.6). The momenta and mass ratios plotted in Figure 5.7(d) are in good agreement for the largest $C_nH_x{}^+$ fragments ($n = 4, 5$), and strongly suggest that the corresponding fragmentation mechanism is sequential via a primary Coulomb explosion into I^+ and a $C_6H_x{}^+$ intermediate, which dissociates into two carbon-containing species (ignoring H/H^+ loss processes). The metastable lifetime of the intermediate must be long enough that these two fragmentation steps are independent. As n decreases, the ratios plotted in (d) increasingly deviate, with the momenta of the carbon-containing fragment being increasingly more than expected for a fully sequential fragmentation process. This could be due to several reasons. Firstly, if the metastable intermediate is short-lived, the two fragmentation steps might not be fully sequential but occur on a

Table 5.4: The $C_nH_x^+$ fragment masses (m), given as a fraction of the mass of Ph and compared to the ratio of the momenta (p) of the $C_nH_x^+$ and I^+ fragments. The momenta recorded for each ion is quoted with the width of the corresponding Gaussian distribution (σ).

$C_nH_x^+$	$\frac{m(C_nH_x^+)}{m(Ph^+)}$	$p(C_nH_x^+) \pm \sigma$ (a.u.)	$p(I^+) \pm \sigma$ (a.u.)	$\frac{p(C_nH_x^+)}{p(I^+)}$
$C_5H_2^+$	0.81	136 ± 27	158 ± 24	0.859
C_5H^+	0.79	134 ± 25	160 ± 18	0.835
C_5^+	0.78	134 ± 17	163 ± 25	0.824
$C_4H_4^+$	0.68	98 ± 25	149 ± 22	0.658
$C_4H_3^+$	0.66	101 ± 18	148 ± 15	0.679
$C_4H_2^+$	0.65	106 ± 19	153 ± 18	0.692
C_4H^+	0.64	111 ± 22	156 ± 21	0.709
C_4^+	0.62	110 ± 35	161 ± 25	0.683
$C_3H_3^+$	0.51	93 ± 39	150 ± 33	0.622
$C_3H_2^+$	0.49	90 ± 21	156 ± 22	0.573
C_3H^+	0.48	91 ± 24	157 ± 21	0.579
C_3^+	0.47	96 ± 27	163 ± 24	0.587
$C_2H_3^+$	0.35	74 ± 39	150 ± 26	0.512
$C_2H_2^+$	0.34	88 ± 30	141 ± 39	0.623
C_2H^+	0.32	87 ± 24	154 ± 32	0.568
C_2^+	0.31	94 ± 34	161 ± 27	0.586
C^+	0.16	68 ± 33	160 ± 27	0.425

faster, but asynchronous, timescale where they cannot be considered independent events. Secondly, the increased momenta could result from greater KER in the secondary dissociation step. Furthermore, smaller fragments can be produced in a greater number of ways. For example, the $C_6H_x^+$ intermediate could break down to form C_2H_2 and a $C_4H_x^+$ secondary intermediate, which may further decay into $C_2H_2^+ + C_2H_{x-2}$ tertiary products. These smaller products could also be formed in 'many-body' dissociation processes where the $C_6H_x^+$ intermediate concertedly breaks down into more than two products (e.g., $C_2H_x^+ + 2C_2H_2$). Each different fragmentation channel generating the same charged products will have its own characteristic KER. As n decreases, the uncertainties associated with the ratios of the momenta of the two charged products also increase, which is expected if smaller fragments are generated via a greater number of fragmentation pathways from multiple sites on the $C_6H_x^+$ intermediate. The deviation between the two ratios plotted in Figure 5.7(d) is captured by the averages of the momentum values and in

the error associated with the detector, but these ratios agree within the very broad error bars associated with the large σ of the Gaussian momentum distributions.

The widths plotted in Figure 5.7(d) and of the ion momenta given in Table 5.4 show no clear dependence on x, but are generally much broader than those observed in the covariances between I^+ and $C_6H_x{}^+$ co-ions (Table 5.2 and Figure 5.4). This implies that any broadening of the momentum distributions due to H/H^+ loss, as seen in the previous section, is masked by a greater blurring effect from breaking the carbon ring. Here, both $p(I^+)$ and $p(C_nH_x{}^+)$ $(n < 6)$ increase as x decreases. This is in contrast to the previous section, where $p(C_6H_x{}^+)$ was constant with respect to x. Secondary fragments of $C_6H_x{}^+$ intermediates that have undergone greater amounts of H/H^+ loss (lower x) will gain a larger proportion of the momentum of the intermediate than fragments of $C_6H_x{}^+$ intermediates with higher x. This may be the cause of the increasing $p(C_nH_x{}^+)$ with decreasing x, although this assumes H/H^+ loss occurs prior to the carbon-chain fragmentation of the intermediate.

5.3.3 Overview of Fragmentation Channels Producing I^+ and One Cationic Carbon-containing Product

The relative integrated intensities of the covariance features obtained for (I^+, $C_nH_x{}^+$) ion pairs ($n \leq 6$) are given in Table 5.5 as a percentage of all observed fragmentation pathways yielding I^+ and only one cationic carbon-containing co-fragment. Of all fragmentation channels yielding $C_6H_x{}^+$ products, ∼20% are formed following H/H^+ loss. Fragments generated by the breakup of the carbon chain make up ∼74% of all covariances observed between I^+ and $C_nH_x{}^+$ products. Regimes yielding $C_4H_x{}^+$ fragments are the most common, followed by $C_6H_x{}^+$ and $C_3H_x{}^+$. The most prominent products are $C_4H_2{}^+$, $C_6H_2{}^+$, and C_3H^+. The broad range of products observed is a consequence of AM processes populating a range of excited states, each with its own lifetime and decay pathways. For fragmentation channels occurring via the production of an intermediate, the corresponding metastable lifetime could be long enough that structural distortions could occur before secondary fragmentation and any secondary products cannot be assumed to be in their ground-state energy

Table 5.5: The integrated intensities of the (I^+, $C_nH_x{}^+$) covariance features, expressed as a percentage of all observed fragmentation pathways yielding I^+ and only one cationic carbon-containing co-fragment.

$C_nH_x{}^+$	Intensity %	Total Intensity %
$C_6H_5{}^+$	7 ± 2	27 ± 10
$C_6H_4{}^+$	1 ± 2	
$C_6H_3{}^+$	3 ± 2	
$C_6H_2{}^+$	10 ± 2	
C_6H^+	5 ± 1	
$C_6{}^+$	1 ± 1	
$C_5H_2{}^+$	1 ± 1	4 ± 3
C_5H^+	2 ± 1	
$C_5{}^+$	1 ± 1	
$C_4H_4{}^+$	1 ± 1	32 ± 9
$C_4H_3{}^+$	7 ± 2	
$C_4H_2{}^+$	14 ± 3	
C_4H^+	8 ± 2	
$C_4{}^+$	2 ± 1	
$C_3H_3{}^+$	1 ± 3	19 ± 12
$C_3H_2{}^+$	5 ± 3	
C_3H^+	10 ± 3	
$C_3{}^+$	3 ± 3	
$C_2H_3{}^+$	3 ± 2	13 ± 10
$C_2H_2{}^+$	4 ± 3	
C_2H^+	3 ± 3	
$C_2{}^+$	3 ± 2	
C^+	6 ± 4	6 ± 4

configurations. This is perhaps suggested by the broad ion momentum distributions observed in covariance analysis, which could arise from a broad range of populated excited states generating the same ionic products.

5.3.4 I^+ and $C_6H_x{}^{2+}$ Ion Pairs

Next, fragmentation channels, stable and unstable with respect to H/H^+ loss, producing I^+ and $C_6H_x{}^{2+}$ fragments will be considered. Newton-frame covariance maps showing the momenta of $C_6H_5{}^{2+}$ and $C_6H_2{}^{2+}$ relative to I^+ are given in Figure 5.8(a) and (b). These plots are less well-resolved than those presented in Section 5.3.1 (Figure 5.4). However, characteristic back-to-back features are still observed, showing that any H/H^+ loss does not significantly perturb the relative

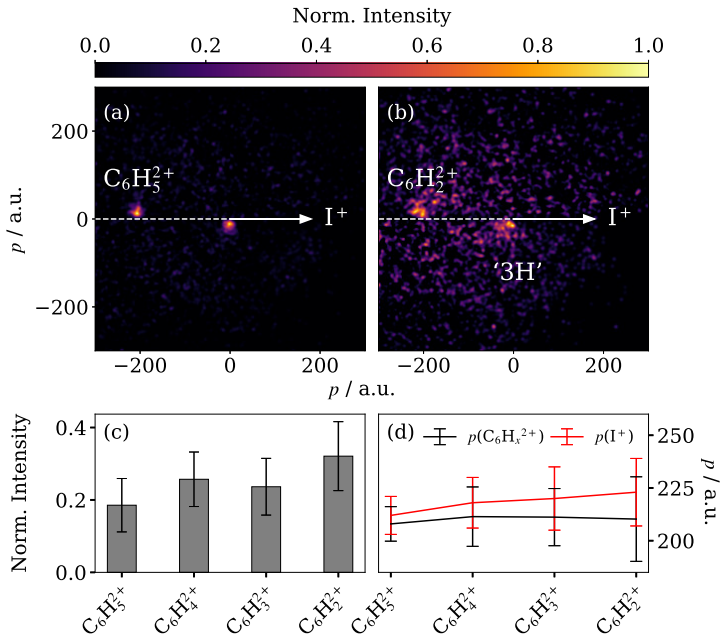

Figure 5.8: Newton-frame covariance maps of the momenta of $C_6H_5^{2+}$ (a) and $C_6H_2^{2+}$ (b) relative to I^+. The integrated intensity of all (I^+, $C_6H_x^{2+}$) covariance features are plotted in (c), with error bars obtained via a bootstrapping method. The momenta (p) of all $C_6H_x^{2+}$ and I^+ ions obtained from Gaussian fits to the Newton-frame covariance maps are plotted in (d) as a function of x, with error bars corresponding to the σ of the Gaussian distributions.

recoil angle between I^+ and $C_6H_x^{2+}$ co-ions. The integrated intensities of covariance features obtained for all ion pairs are plotted in Figure 5.8(c), with error bars obtained via a bootstrapping method. No discernible covariance was observed for $x = 0, 1$. Once again, a preference is seen for generating fragments where $x < 5$. The greatest intensity is observed for $C_6H_2^{2+}$, which is similar to results obtained for the $C_6H_x^+$ products (Figure 5.4(c)), where the greatest intensity was observed for $C_6H_2^+$. In contrast, the $C_6H_x^{2+}$ product with the lowest intensity (but still discernible in covariance analysis) was $C_6H_5^{2+}$, which differs from the results obtained for the $C_6H_x^+$ products. However, the disparity in intensity between different $C_6H_x^{2+}$ species is less pronounced than observed for $C_6H_x^+$ species. Interestingly, previous studies on dicationic benzene observed long-lived doubly charged states of $C_6H_x^{2+}$ with greater intensity for even values of x.[193] This is also suggested in the results presented in Figure 5.8(c), although it should be cautioned that the parent polycation charge state generating $C_6H_x^{2+}$ products where $x < 5$ is ambiguous since the charge

states of any lost H/H^+ species cannot be exactly determined from this data set.

The average momenta of I^+ and $C_6H_x{}^{2+}$ ions were obtained via Gaussian fits to the Newton-frame covariance distributions and are plotted in (d) as a function of x. The error bars correspond to the widths (σ) of the Gaussian distributions. The $p(I^+)$ measured for each ion pair is also given in Table 5.6. The relationship between an ion's momentum (arising from a Coulomb explosion with a second ion) and its charge separation (r) with a partner ion can be expressed using Coulomb's law:

$$\frac{(m_1+m_2)p^2}{2m_1m_2} = \frac{kq_1q_2}{r} \rightarrow p \propto \sqrt{\frac{q_1q_2}{r}}, \tag{5.3.4.1}$$

where k is the Coulomb constant, and q_1, q_2 and m_1, m_2 are the charges and masses of the two co-ions, respectively. The ratios of $p(I^+)$ obtained from Coulomb explosions producing $C_6H_x{}^+$ monocations (p_{mono}) or $C_6H_x{}^{2+}$ dications (p_{di}) can be compared via the following equation:

$$\frac{p_{di}}{p_{mono}} = \frac{\sqrt{\frac{2}{r_{di}}}}{\sqrt{\frac{1}{r_{mono}}}} = \sqrt{\frac{2r_{mono}}{r_{di}}}. \tag{5.3.4.2}$$

These ratios are compared in Table 5.7, and show that the effective intercharge separations between I^+ and both $C_6H_x{}^+$ and $C_6H_x{}^{2+}$ co-ions are approximately equal, suggesting that the cationic charge on the $C_6H_x{}^+$ and dicationic charge on the $C_6H_x{}^{2+}$ ions are both distributed about their π-systems. If all H-species are lost as neutral H-atoms, then the rate and behaviour of H-atom loss are expected to be independent of the Ph charge state since such processes involve cleavage of C-H σ-type bonds but the charges on the $C_6H_x{}^+$ and $C_6H_x{}^{2+}$ ions are expected to be on the π-system. Figure 5.8(d) shows that $p(C_6H_x{}^{2+})$ is not dependent on x but, as x decreases, $p(I^+)$ increases, as was seen in Figure 5.7(d). From x=5 to x=2, $p(I^+)$ increases by ∼10 a.u., which corresponds to a decrease in the effective intercharge separation of approximately ∼0.5 Å. This is very close to the change observed between the (I^+, $C_6H_5{}^+$) and (I^+, $C_6H_2{}^+$) ion pairs.

Table 5.6: The momenta of I^+ ions, $p(I^+)$, produced in fragmentation processes generating $C_6H_x{}^{2+}$ co-products, obtained from Newton-frame covariance.

$C_6H_x{}^{2+}$	$p(I^+) \pm \sigma$
$C_6H_5{}^{2+}$	212 ± 9
$C_6H_4{}^{2+}$	218 ± 12
$C_6H_3{}^{2+}$	220 ± 15
$C_6H_2{}^{2+}$	223 ± 16

Table 5.7: Table comparing ratios of $p(I^+)$ and intercharge separations obtained for covariances with $C_6H_x{}^{2+}$ (*di*) and $C_6H_x{}^{+}$ (*mono*).

$C_nH_x{}^{+/2+}$	$p(I^+)_{di}/p(I^+)_{mono}$	r_{mono}/r_{di}
C_6H_5	1.43	1.02
C_6H_4	1.49	1.12
C_6H_3	1.47	1.08
C_6H_2	1.44	1.04

5.3.5 I^+ and $C_nH_x{}^+$ Ion Pairs Produced with a $C_{6-n}H_y{}^+$ Co-ion

Next, fragmentation channels producing I^+ and two cationic carbon-containing co-fragments will be discussed. In these cases, the IB polycation is unstable with respect to fragmentation of the carbon ring, and in some instances also to H/H^+ loss.

The Newton-frame covariance map of the momenta of $C_2H_2{}^+$ ions relative to I^+ ions is given in Figure 5.9(a). This covariance was isolated by only considering I^+ ions with $p(I^+) \geq 200$ a.u. in the covariance calculation. The feature observed has a broad angular distribution, characteristic of a sequential Coulomb explosion process. Ignoring any H/H^+ loss, a primary Coulomb explosion produces I^+ and a rotationally excited $C_6H_x{}^{2+}$ intermediate, which exists long enough that it is randomly oriented relative to the trajectory of I^+ before it undergoes a secondary Coulomb explosion into $C_2H_2{}^+$ and, presumably, $C_4H_y{}^+$ fragments (where $x+y \leq 5$). The Newton-frame covariance map obtained for two secondary carbon-containing products is given in (b), which shows that the two secondary products recoil with an approximately back-to-back 180° angle.

The Newton-frame covariance map in (a) is transformed into the native-frame of a $C_6H_x{}^{2+}$ intermediate in (c) to characterise the energetics of the secondary

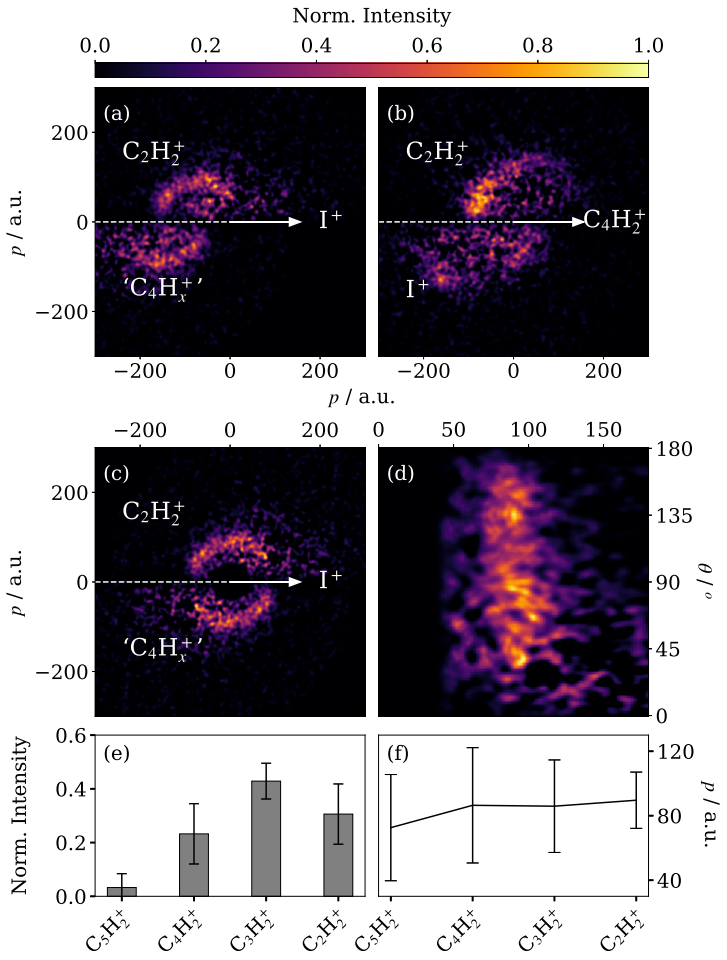

Figure 5.9: The Newton-frame covariance maps of the momenta of $C_2H_2^+$ relative to I^+ (a) and $C_4H_2^+$ (b), produced by fragmentation processes generating I^+ and two charged carbon-containing co-fragments. (c) is the distribution given in (a) transformed into the native-frame of a $C_6H_x^{2+}$ intermediate. This native-frame distribution is also given in a polar representation in (d). Relative integrated intensities of covariances obtained for several $C_nH_x^+$ fragments with I^+ are plotted in (e), with error bars obtained via a bootstrapping method. The KER of the secondary Coulomb explosion steps generating the fragments in (e) are plotted in (f), with error bars derived from the σ of the fragments' momenta.

Coulomb explosion process independently of the primary Coulomb explosion. In this frame, the secondary products are momentum-matched. The momenta of $C_2H_2^+$ in the native-frame is also shown in a polar representation in (d). This distribution is characterised by a broad angular distribution, indicating that the lifetime of the intermediate surpasses its rotational period. The feature has constant momentum across all recoil angles, corresponding to the momentum gained in the secondary Coulomb explosion process. However, the momentum distribution is broad

(σ=18 a.u.). This suggests that the intermediate is completely randomly rotated in all three dimensions relative to the trajectory of I^+ before the secondary Coulomb explosion takes place, which blurs out the momentum distribution. Additionally, the momentum distribution is broad as the feature likely contains components arising from Coulomb explosions between $C_2H_2{}^+$ and $C_4H_y{}^+$ fragments with varying y due to H/H^+-loss processes. Similar distributions were observed for a range of $C_nH_x{}^+$ fragments. For each value of n, the relative intensity of one of these features is plotted in Figure 5.9(e). The greatest intensity is observed for the fragmentation channels yielding $C_3H_x{}^+$+$C_3H_y{}^+$ and $C_2H_x{}^+$+$C_4H_y{}^+$ ($x + y \leq 5$) co-fragments.

The $p(I^+)$ values obtained for all fragmentation channels producing I^+ and $C_6H_x{}^{2+}$ or two carbon-containing cations are given in Table 5.8. The values reported are similar across all fragmentation channels, which suggests that the C-I Coulomb explosion step occurs from similar initial geometries and intercharge separations, regardless of whether the $C_6H_x{}^{2+}$ ion produced is stable or unstable.

The momenta of fragments, obtained from polar momentum distributions such as Figure 5.9(d), were used to calculate the approximate KER of each of the secondary Coulomb explosion processes. These are plotted in Figure 5.9(f). It is noted that the yields of these fragmentation channels were very low and three-fold covariance could only be obtained for the (I^+, $C_2H_2{}^+$, $C_4H_3{}^+$) and (I^+, $C_2H_2{}^+$, $C_4H_2{}^+$) sets of ions (Figure 5.10). The KER of the secondary step of the fragmentation channel producing (I^+, $C_2H_2{}^+$, $C_4H_3{}^+$) was found to be 3.77 ± 0.05 eV, and for (I^+, $C_2H_2{}^+$, $C_4H_2{}^+$), the corresponding KER was found to be 3.79 ± 0.08 eV. These values are also listed in Table 5.9(i) and show that the small difference in mass due to H/H^+ loss has an insignificant effect on the secondary KER.

For fragmentation channels where n=1, 3, or 5, the identity of the corresponding co-fragments ($C_{6-n}H_y{}^+$) could not be exactly known since three-fold covariance was not obtainable. Although the $C_{6-n}H_y{}^+$ co-fragments could contain differing numbers of H-atoms, approximate KER values were calculated from two-fold native-frame covariance maps (e.g., Figure 5.9(c)) under the assumption that H/H^+ loss has

Table 5.8: The momenta of I^+ ions observed in covariance with various $C_6H_x{}^{2+}$ fragments and $C_nH_x{}^+$ fragments produced with a second charged carbon-containing co-fragment, obtained via a Gaussian fit and reported with the corresponding σ of the distribution.

$C_6H_x{}^{2+}/C_nH_x{}^+$	$p(I^+) \pm \sigma$
$C_6H_5{}^{2+}$	212 ± 9
$C_6H_4{}^{2+}$	218 ± 12
$C_6H_3{}^{2+}$	220 ± 15
$C_6H_2{}^{2+}$	223 ± 16
$C_5H_2{}^+$	221 ± 19
C_5H^+	221 ± 16
$C_5{}^+$	217 ± 17
$C_4H_4{}^+$	224 ± 20
$C_4H_3{}^+$	222 ± 20
$C_4H_2{}^+$	224 ± 18
C_4H^+	225 ± 21
$C_4{}^+$	227 ± 23
$C_3H_3{}^+$	220 ± 17
$C_3H_2{}^+$	220 ± 17
C_3H^+	225 ± 21
$C_3{}^+$	221 ± 18
$C_2H_3{}^+$	227 ± 23
$C_2H_2{}^+$	225 ± 20
C_2H^+	225 ± 22
$C_2{}^+$	222 ± 21

a negligible effect on the secondary KER and that $y = (6 - n) - 1$, i.e. the co-fragment has one less hydrogen atom than carbon atoms. Therefore, the KER values are estimates and approximate but can be used to make qualitative conclusions (neglecting any impulse from H/H^+ loss). For $C_5H_2{}^+$, $C_4H_2{}^+$, $C_3H_2{}^+$, and $C_2H_2{}^+$, the KER values obtained from two-fold covariance for the secondary Coulomb explosion processes were 3.9 ± 1.6 eV, 3.3 ± 1.1 eV, 2.9 ± 0.6 eV, and 3.5 ± 0.3 eV, respectively (listed in Table 5.9(ii)). The larger uncertainties in these values compared to those obtained from three-fold covariance, derived from the σ of the momentum distributions, are likely because the momentum distributions comprise contributions from different fragmentation channels with varying numbers of H/H^+ loss. For comparison, Richardson, Eland, and Lablanquie obtained the following KER values for pairs of products of doubly charged benzene, generated by irradiation with He(II) 40.8 eV light: $C_5H_2{}^+ + CH_3{}^+ + H = 3.0 \pm 1.7$ eV; $C_4H_3{}^+ + C_2H_2{}^+ + H = 3.8 \pm 1.0$ eV;

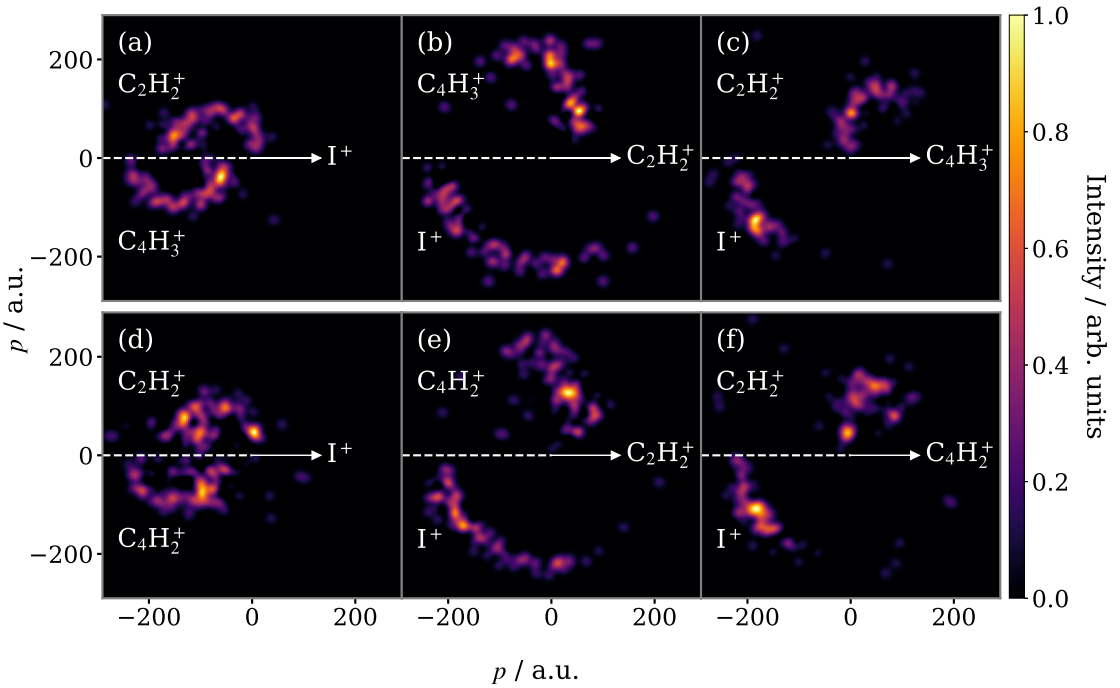

Figure 5.10: Three-fold covariance obtained for the fragmentation channels producing (a-c) (I^+, $C_2H_2^+$, $C_4H_3^+$) and (d-f) (I^+, $C_2H_2^+$, $C_4H_2^+$). Within each set of three ions, each ion was used as the reference ion in the three-fold covariance calculation, i.e. I^+, $C_2H_2^+$, and $C_4H_3^+$ were the reference ions used in (a), (b), and (c), respectively.

Table 5.9: The KER values obtained for secondary Coulomb explosion processes forming $C_nH_x^+ + C_{6-n}H_y^+$ ion pairs (where $x + y \leq 5$). (i) are obtained from three-fold covariances, (ii) are approximate values derived from two-fold covariances, assuming $y = (6 - n) - 1$. For both, expected approximate intercharge separations (r) are given.

	$C_nH_x^+ + C_{6-n}H_y^+$	KER $\pm\,\sigma$ (eV)	r (Å)
(i)	$C_2H_2^+ + C_4H_2^+$	3.8 ± 0.1	3.8
	$C_2H_2^+ + C_4H_3^+$	3.8 ± 0.1	3.8
(ii)	$C_2H_2^+ + C_4H_{y=3}^+$	3.5 ± 0.3	4.1
	$C_3H_2^+ + C_3H_{y=2}^+$	2.9 ± 0.6	5.0
	$C_4H_2^+ + C_2H_{y=1}^+$	3.3 ± 1.1	4.4
	$C_5H_2^+ + CH_{y=0}^+$	3.9 ± 1.6	3.7

$C_3H_2^+ + C_3H_3^+ + H = 4.2$ eV.[193] There is some level of agreement between this prior work on benzene dications and the energetic results obtained here (despite the low intensity of these covariance features and resultant poor signal-to-noise ratio), especially with the KER values obtained via three-fold covariance. This suggests that the $C_6H_x^{2+}$ intermediates that led to the fragmentation channels observed in this study might have similar structures to those proposed for benzene dications.

The most stable geometries of dicationic benzene are expected to be either close in geometry to the neutral Ph or linear ring-opened isomers.[194, 210, 212, 213] The lowest energy configuration is expected to be a chair conformer, followed by two planar conformers 0.39 eV and 0.52 eV higher in energy. Higher energy states are expected to be slightly distorted from the planar geometry of the neutral Ph due to first and second-order Jahn-Teller distortions arising from additional charge in the π-system.[210, 213] In IB, any small out-of-plane distortion in any bond would be sufficient enough distortion that a Coulomb explosion generating I^+ exerts a torque and induces rotational excitation in the $C_6H_x{}^{2+}$ intermediate. The rotational lifetime of the intermediate must be shorter than its metastable lifetime for momentum distributions such as those presented in Figure 5.9(c) and (d) to be observed. For intermediates with very long-lived metastable states (relative to the rotational lifetime), extensive geometrical rearrangement could potentially occur before the secondary Coulomb explosion takes place.

Anand *et al.* proposed various potential energy surfaces and transition states for fragmentation channels of dicationic benzene into two charged carbon-containing fragments, in a range of linear and ringed conformations.[210] The potential energy surfaces of $C_6H_x{}^{2+}$ intermediates produced from iodobenzene will likely be different to those of benzene due to the addition of the heavy iodine substituent that brings with it a high density of states and spin-orbit coupling. However, the transition structures proposed by Anand *et al.* can be used to approximately infer possible structures of the $C_6H_x{}^{2+}$ intermediates expected here as well as the extent of atom rearrangement that can occur within their metastable lifetimes. The KER values plotted in Figure 5.9(f) and listed in Table 5.9(ii) were used to extract effective intercharge separations on the $C_6H_x{}^{2+}$ intermediates (also listed in Table 5.9(ii)). The experimentally obtained KER values should only ever be equal to or less than the KER expected from theoretical structures. Therefore, the intercharge separations obtained from experimental KER values can be considered 'maximum' expected intercharge separations. Examples of theoretical structures of transition states of benzene dications generating two $C_3H_3{}^+$ products, proposed

by Anand *et al.*, are plotted in Figure 5.11.[210] Assuming that the two charges are located at carbon atomic sites, only carbon-carbon internuclear distances less than that listed in Table 5.9(ii) (5.0 Å) could give the experimentally observed KER. Distances greater than 5.0 Å would yield too low a KER compared to the experimentally observed KER. For each transition structure, the greatest carbon-carbon internuclear distance less than the experimentally predicted intercharge separation is given. The internuclear distance given for Transition state 4 (TS4) is the closest to the expected intercharge separation and yields two linear products. By further comparisons made with the theoretical transition structures proposed for fragmentation pathways generating the ($C_2H_x^+$, $C_4H_x^+$) and (CH_x^+, $C_5H_x^+$) ion pairs, the most likely intermediate geometries are close to ringed structures and form linear products. However, structures formed through greater distortion cannot be ruled out for certain with the momentum resolution of this experiment and the broad ion momentum distributions observed.

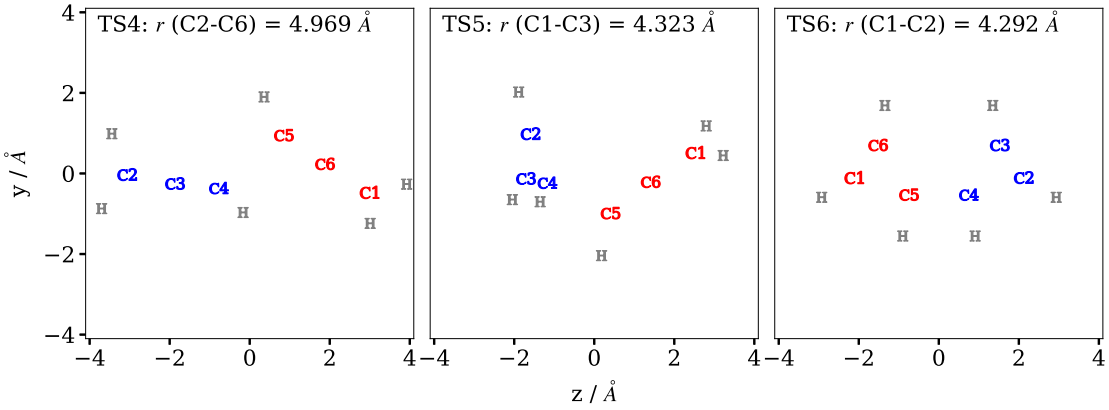

Figure 5.11: Transition state structures forming two $C_3H_3^+$ fragments (shown in red and blue) from dicationic benzene, as proposed by Anand *et al.* (S. Anand *et al.*, J. Phys. Chem. A, 109.50 (2005): 11551-11559.). The maximum carbon-carbon internuclear distances (r) less than the expected intercharge separation obtained in this work (5.0 Å, as in Table 5.9(ii)) are given.

5.4 Conclusion

Site-selective XUV-ionisation of iodobenzene at the I 4d ionisation threshold initiated various AM decay processes, which generated IB polycations that fragmented to

produce a range of stable and unstable carbon-containing cations. An initial Coulomb explosion that broke the C-I bond and produced I^+ was used as a reference fragmentation process to examine the nuclear dynamics and lifetimes of the sequential breakup of the $C_6H_x{}^+$ and $C_6H_x{}^{2+}$ intermediates. The modified covariance analysis techniques demonstrated in Chapter 4 were applied here to characterise the many concurrent fragmentation processes occurring in a larger polyatomic polycation. The results presented here demonstrate the potential of extending these techniques to study the photochemistry of larger molecules of interest in detail, such as the XUV photochemistry of PAHs. For example, the likelihood of H/H^+ loss and the loss of larger products such as C_2H_2 from different excited states of PAHs can be investigated and the most probable charge distributions of parent ions can be deduced using these techniques. Furthermore, the lifetime of a rotationally excited intermediate species relative to its rotational period can be characterised.

These techniques are demonstrably useful for identifying and disentangling fragmentation processes that result from metastable states. For structural determination applications, CEI generally makes use of prompt fragmentation processes to take instantaneous 'snapshots' of molecular geometries. However, fragmentation processes generating metastable intermediates, which can lose all memory of the parent molecule within their lifetime, could complicate the spectra obtained in time-resolved studies, and it is important to be able to recognise their corresponding features when using CEI for structural determination.

The momentum resolution of this experiment was sensitive to the many fragmentation regimes induced by XUV-ionisation, allowing them to be disentangled via covariance analysis. However, to understand *why* these fragmentation channels occur, photoelectron information is required to know more about the ionisation processes causing each fragmentation channel.

Acknowledgements

The experiment was performed at SACLA with the approval of JASRI and the program review committee (Proposal No. 2022B8048 Warne). I would like to thank

the collaboration of researchers who were involved in the beamtime, subsequent discussion of results, and preparation of a manuscript: F. Allum, M. Britton, M. Brouard, P. H. Bucksbaum, M. Fushitani, I. Gabalski, T. Gejo, J. Harries, P. Hockett, A. J. Howard, H. Iwayama, Y. Kumagai, E. Kukk, C.-s. Lam, S. Lim, R. S. Minns, J. W. McManus, K. Nagaya, S. Nishimuro, J. Niskanen, A. Niozu, S. Owada, W. O. Razmus, D. Rolles, J. Somper, K. Ueda, J. Unwin, S.-i. Wada, J. Woodhouse, R. Forbes, E. M. Warne, and M. Burt. Furthermore, I thank SACLA for the provision of the experimental facilities and the scientific and technical teams who made these experiments possible.

Who cares if I'm pretty if I fail my finals?

— Rory Gilmore, The Gilmore Girls

6

Recoil-frame Covariance Analysis of Iodobenzene Fragmentation Channels Induced by IR-ionisation

Contents

6.1 Introduction

Coulomb explosion fragments and their internal energy distributions depend on charge generation and redistribution processes. The previous two chapters have demonstrated that XUV-ionisation generates molecular polycations in a broad range

of excited states with different internal energy distributions. As a result, many competing fragmentation pathways are observed, complicating the mass spectra. Fragmentation processes induced by XUV inner-shell ionisation differ from those induced by valence-shell ionisation, which can operate under strong-field or MPI regimes.[89, 91–94] As a result, there is much less atomic site selectivity and, usually, the electrons with the lowest binding energy (e.g., the HOMO or valence electrons) are removed, potentially allowing charge to be generated on a greater number of atomic sites, depending on the geometries of the molecular orbitals. However, ionisation probability and subsequent fragmentation can also be influenced by a range of other field-induced processes, such as the alignment of the molecular orbitals with the electric field, distortion of the molecular energy levels and nuclear dynamics, and vibrational excitation.[109, 217–219] Subsequently, inner-shell ionisation and valence-shell ionisation processes generating the same polycationic charge states can lead to different sets of fragments, or the same sets of products via different pathways, including from different initial excited states and internal energy distributions.

In this chapter, the distribution of products obtained in the XUV-ionisation study of iodobenzene (IB) is compared to ionisation using IR pulses acting in a mixed strong-field tunnelling and multi-photon ionisation regime. Polycations of IB are generated in the same charge states, but the range of fragmentation channels observable in each ionisation regime suggests a dependence on the primary ionisation and ensuing internal energy redistribution processes. Furthermore, fragmentation channels unique to IR-ionisation show that the site or non-site selectivity of an ionisation regime can influence the range of accessible fragmentation pathways.

6.2 Methods

6.2.1 Experimental

CEI of IB was carried out using the in-house IR laser system and VMI mass spectrometer. A schematic of these systems is given in Figure 6.1. A gaseous sample of IB was generated by evaporating a liquid sample under vacuum conditions and

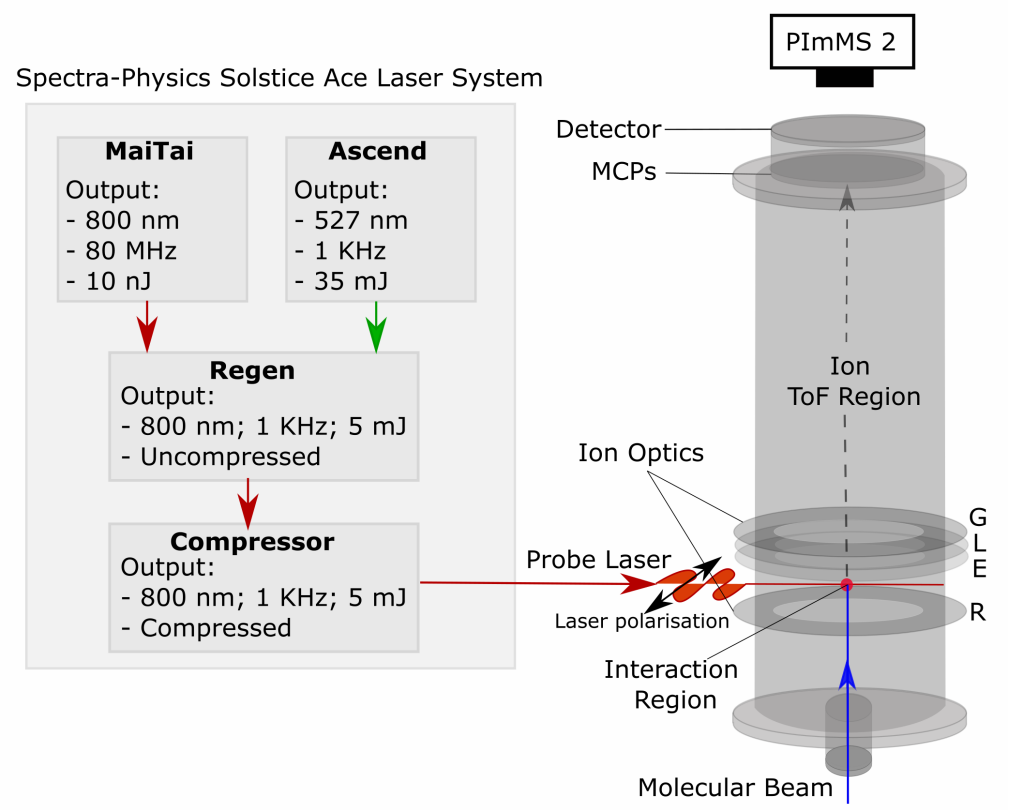

Figure 6.1: A schematic of the in-house laser system and spectrometer, which is discussed in detail in the text. (Ion optics RELG = repeller, extractor, lens, ground)

was mixed with He carrier gas. The sample was introduced to the spectrometer via a pulsed valve and skimmer, producing a pulsed molecular beam.

IR pulses were produced using the Spectra-Physics Solstice Ace laser system, which comprises several parts that are shown in the schematic in Figure 6.1. Firstly, broadband 800 nm pulses (80 MHz, 10 μJ) were generated via mode-locking within the Ti:Sapphire MaiTai oscillator. The output of the MaiTai was amplified by a second laser (Ascend), which is a four-level, Nd:YLF, Diode-Pumped Solid State (DPSS) laser. The Ascend produces laser emission at 1053 nm, which is frequency (ω) doubled via second harmonic generation (SHG; $\omega+\omega=2\omega$) to 527 nm (1 KHz, 35 mJ). These pulses are the pump pulses used for chirped-pulse amplification, which takes place in the regenerative amplifier ('Regen'). Firstly, the initially short pulses are stretched in time so that their intensities can safely be amplified without destroying the amplifying optics. After amplification within the Regen, uncompressed 800 nm

pulses (1 KHz, 5mJ) are produced. A grating compressor takes this output and compresses it, reversing the earlier stretching, to generate 800 nm, 1 KHz, 5 mJ compressed laser pulses. Overall, according to its specifications, the Solstice can output laser pulses with a central wavelength of 800 nm, a bandwidth of 60 nm, a pulse duration of 35 fs, an average power of 5 W, and a repetition rate of 1 kHz.

The experiment was conducted twice at two different pulse intensities. The power of the IR beam before the spectrometer was controlled by a waveplate followed by a polarising beamsplitter, which attenuated the pulse power to 130 mW and 260 mW for the 'low' and 'high' intensity regimes, respectively. These powers were measured prior to the lens (with a focal length of 35 cm) and the spectrometer window (UV fused silica). The beam diameter measured directly before the lens was 7 mm, corresponding to a $1/e^2$ width of $\sim$6 mm. The beam quality M^2 could not be measured but calculations characterising the beam were performed assuming that M^2=1. The spot size was therefore assumed to be focused to $\sim$60 μm within the chamber of the spectrometer.

The IR pulse duration was measured using an autocorrelator. Firstly, the attenuation and pulse-stretching of the lens and spectrometer window were mimicked by passing the IR pulse through two fused silica windows of equivalent thickness. A beam splitter separated the 800 nm pulse into two halves. One half was directed onto a delay stage and then recombined with the other half of the beam within a non-linear β-BBO crystal for SHG of 400 nm. By varying the position of the delay stage, the temporal overlap of the two halves of the 800 nm pulse within the SHG crystal could be varied, and the intensity of the 400 nm output could be measured as a function of the time between the two pulse halves arriving at the SHG crystal. This measurement is shown in Figure 6.2. The full-width half-maximum (FWHM) of the cross-correlated intensity peak (66 fs) is used to extract an approximate expected pulse duration within the spectrometer, which was determined to be 47 ± 2 fs.

From the assumed spot size and pulse duration within the spectrometer, an approximate, upper estimate can be found for the Gaussian intensity of the 800 nm laser beam. For the 'low' intensity regime (130 mW), the upper bound on the

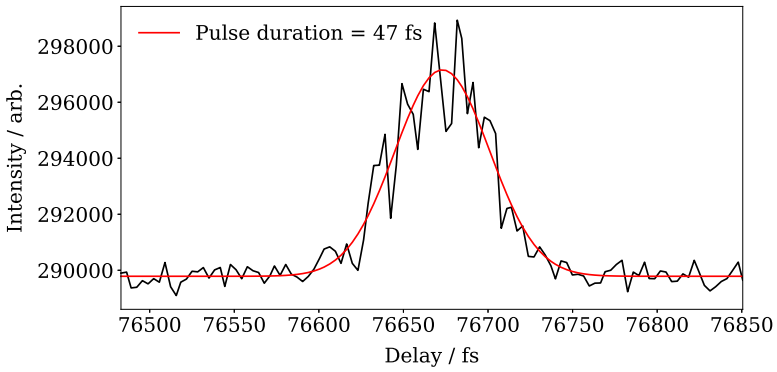

Figure 6.2: The delay-dependent intensity of 400 nm light generated by SHG of 800 nm pulses within an autocorrelator, used to calculate the pulse duration of the fundamental 800 nm laser. A Gaussian fit (overlaid) was used to obtain the pulse duration.

Gaussian intensity was $1.9\times10^{14}\,\mathrm{W\,cm^{-2}}$. This corresponded to 0.13 mJ per pulse. The Keldysh parameter for this regime was 0.62, corresponding to a ponderomotive energy (U_p) of 11.35 eV. For the 'high' intensity regime (260 mW), the Gaussian intensity was $3.9\times10^{14}\,\mathrm{W\,cm^{-2}}$ and the energy per pulse was 0.26 mJ. The Keldysh parameter for this regime was 0.44, which corresponds to a U_p of 23.07 eV. For both intensity regimes, the Keldysh parameters obtained likely correspond to a mixed ATI and tunnelling ionisation regime.

The laser was polarised parallel to the detector plane and perpendicular to the axis of the ToF tube and perpendicularly intersected the molecular beam within the interaction region of the velocity map imaging spectrometer, as shown in Figure 6.1. Resultant ion fragments were accelerated down a field-free drift region, separated by ToF, and velocity mapped onto a position-sensitive detector comprising a dual MCP detector and a phosphor (P47) screen. The ToF and x and y positions of multiple ions hitting the detector per laser shot were measured using the resultant fluorescence of the P47 screen, which was recorded by a Pixel Imaging Mass Spectrometry (PImMS) camera installed with a 324 × 324 pixel PImMS2 sensor with 25 ns timing precision. The laser and gas pulse repetition rates used in this experiment were limited to the repetition rate of the PImMS2 camera, which was 20 Hz.

To improve the detection efficiency of higher m/z fragments of interest, the voltages applied to the MCP detector were pulsed and delayed relative to the trigger

of the laser pulses so that only ions with an m/z greater than that of H_2O^+ (18) were detected. This removed the majority of contamination contributing to the background noise of the experiment, mostly consisting of H_2O^+ and fragments of H_2O^{n+}. As a result, the camera was less saturated with signal arising from water hitting the detector, allowing more sample to be used, leading to greater sample signal detected per laser shot.

6.2.2 Data Analysis

For a single ion hit on the detector, multiple photons could be generated from the P47 screen by the signal amplification of the MCPs and multiple PImMS2 pixels could be activated over several time registers by one single photon. Therefore, a centroiding algorithm (Section 2.2.5) was implemented to improve the x, y, and ToF assignments of the ion hits recorded by PImMS2. Due to the low ToF resolution of the PImMS2 camera, the ionic fragment momenta could only be calculated using their 2D spatial positions on the detector. A radius-to-momentum calibration was obtained by modelling ion trajectories within the spectrometer using the simulation software SIMION 8.1.[121]

A histogram of the number of ion hits detected per laser shot is given for the high intensity data set in Figure 6.3. The average number of hits per laser shot was found via a Gaussian fitting to be 115. This is more than ten times greater than the hit rate used in the XUV study in Chapter 5. The data obtained for the low IR laser intensity was collected on a different day to the high intensity data. An example of the histogram of ion hits per laser shot obtained for one file of the low intensity data is given in Figure 6.4. Two approximately normally distributed peaks are seen, which is a result of sensitivity to fluctuations in the exact timing of the gas pulse relative to the laser timing trigger used on that day. The total histogram of ion hits per laser shot for the entire low intensity data set is given in Figure 6.5. As a consequence of each individual file containing two normally distributed peaks and potential drift in the laser power and gas intensity throughout the experiment, the total distribution is not normally distributed as

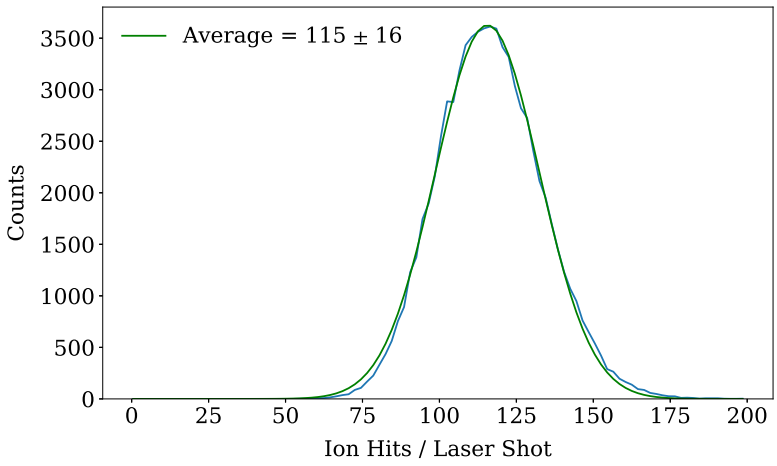

Figure 6.3: Ion hits detected per laser shot for the high intensity ($3.9\times10^{14}\,\mathrm{W\,cm^{-2}}$) data set. The average number of ions detected was found via a Gaussian fit, which is overlaid.

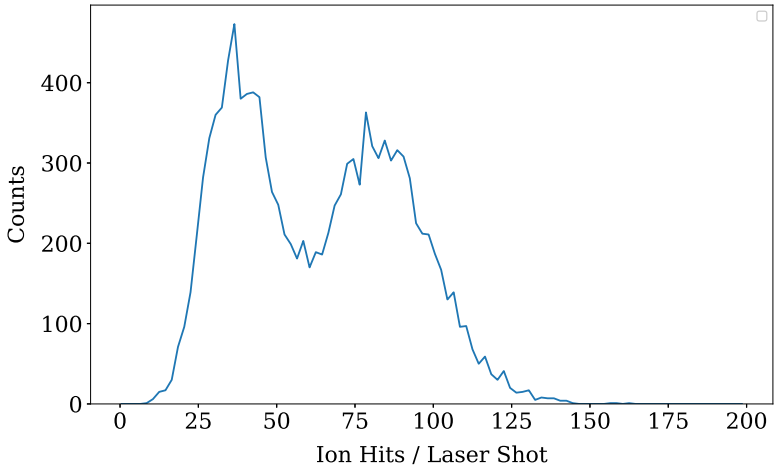

Figure 6.4: Ion hits detected per laser shot for one example file of the low intensity ($1.9\times10^{14}\,\mathrm{W\,cm^{-2}}$) data set.

it should be. However, the energetics of fragmentation processes accessed via this laser intensity are not affected by fluctuating ions detected per laser shot. Therefore, only laser shots where more than 55 ions were detected are considered (marked by the red dashed line in Figure 6.5) to be as consistent as possible when comparing distributions with the high intensity data set.

Since 3D ion momenta were not obtainable for this dataset, covariances in this chapter are calculated using the recoil-frame representation, which retrieves relative 2D radial distributions of ions on the detector. Narrow m/z ranges were used in

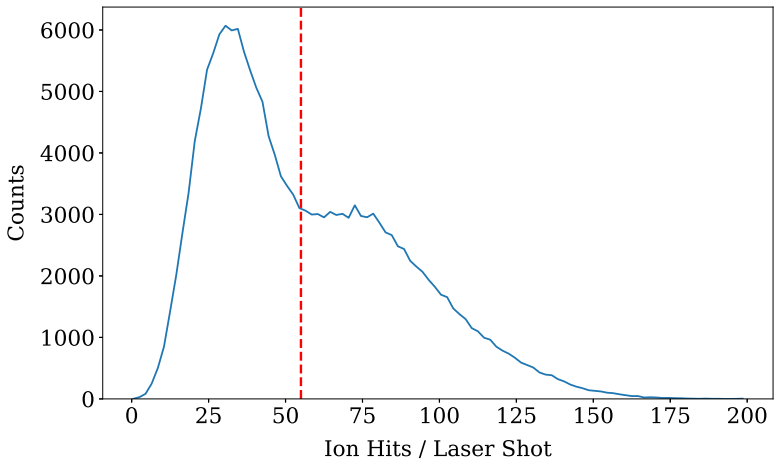

Figure 6.5: Ion hits detected per laser shot for the entire low intensity ($1.9\times10^{14}\,\mathrm{W\,cm^{-2}}$) data set. Due to the non-Gaussian profile of this distribution, only laser shots where more than 55 ions were detected (indicated by the dashed red line) are used when comparing distributions to the high intensity data set.

covariance calculations, rather than entire ion ToF peaks, to effectively select ions making up the central slice of the corresponding Newton sphere, but wide enough to retain sufficient statistics to extract meaningful distributions.

6.3 Results And Discussion

The mass spectrum of IB generated via ionisation by the 130 mW IR pulse is given in Figure 6.6(a). The lowest m/z products of IB observed were $C_2H_x^+$. CH_x^+ products and products with smaller m/z (e.g., C^{2+}) were not recorded due to the water gating. These low m/z products made up only a small fraction of the data recorded in the XUV study (e.g., fragmentation channels generating I^+, C^+, and a neutral carbon-containing co-fragment made up only ~6% of the fragmentation channels presented in Table 5.5). Therefore, although these low m/z fragments are excluded in this study by the water gating, comparisons between XUV- and IR-ionisation regimes can still be made for fragmentation channels generating the most prominent products detected in the XUV study (i.e. fragments with m/z greater than that of water cations). Within the resolution of the ToF, neighbouring fragments differing by single hydrogen atoms could not be distinguished and are considered as groups from here on (e.g., $C_2H_x^+$). The ToF-ToF covariance map

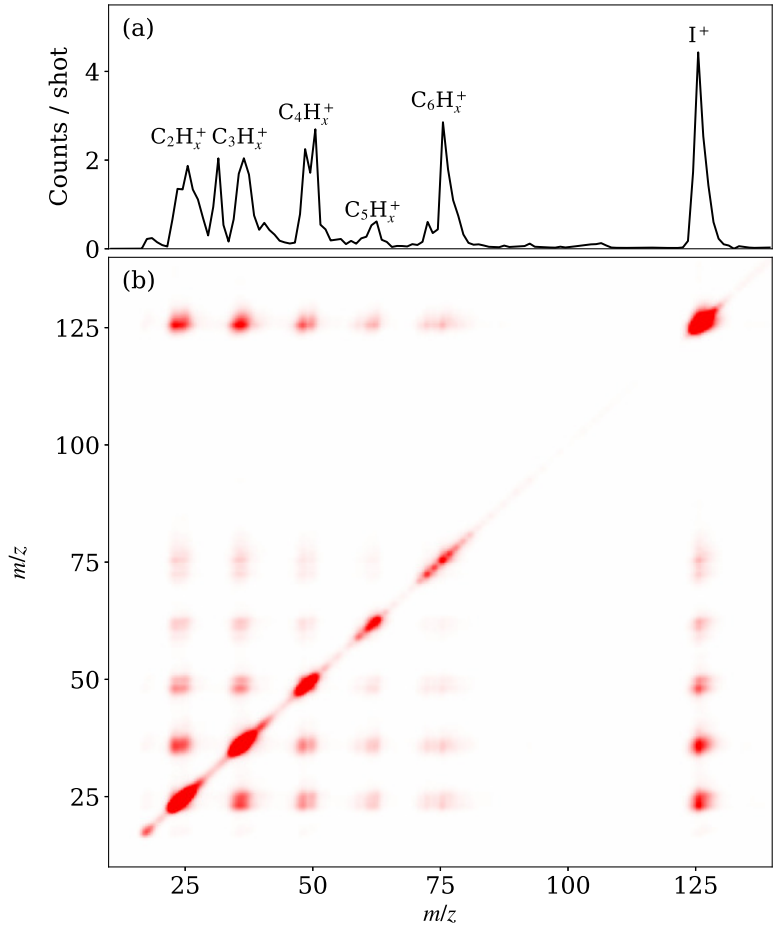

Figure 6.6: (a) The mass spectrum recorded for IR-ionisation of IB, and (b) the corresponding ToF-ToF covariance map measured at $1.9\times10^{14}\,\mathrm{W\,cm^{-2}}$.

is given in Figure 6.6(b). Covariance observed between I^+ and carbon-containing cations indicates that products of parent molecular charge states of at least 2+ could be generated by the IR and detected in covariance.

As in the XUV ToF-ToF covariance map (Figure 5.2), correlations between I^+ and all carbon-containing cations are observed. In Figure 6.7, the integrated ToF-ToF covariance observed between I^+ and all $C_nH_x{}^+$ fragments ($2 \leq n \leq 6$) are plotted for both the XUV and IR generated spectra. Both spectra are normalised to their respective maxima, which coincides with the $C_3H_x{}^+/C_6H_x{}^{2+}$ fragments in each case. Overall, the integrated intensities are similar for both ionisation regimes, despite the poorer m/z resolution of the IR spectrum compared to that of the XUV spectrum. The intensity of the peak corresponding to $C_2H_x{}^+$ is increased

for IR-ionisation relative to XUV-ionisation, whereas the intensity of the $C_4H_x^+$ peak is decreased. $C_2H_x^+$ can be formed from unstable $C_4H_x^+$, which might be the cause of the corresponding increase and decrease in these ion yields.

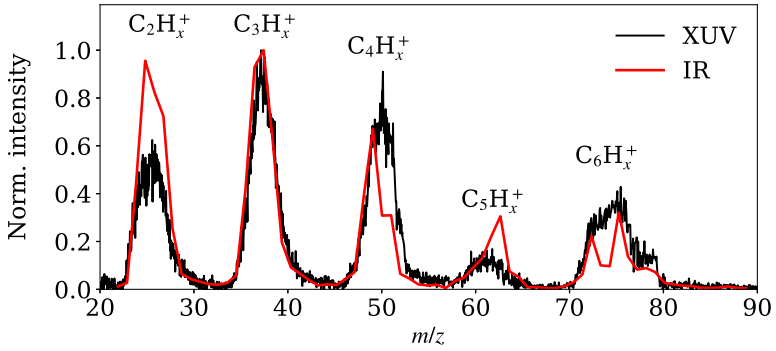

Figure 6.7: A comparison of the integrated ToF-ToF covariance observed between I^+ and $C_nH_x^+$ fragments generated by XUV ionisation and IR ionisation at the low IR intensity ($1.9\times10^{14}\,\mathrm{W\,cm^{-2}}$).

The mass spectra (normalised by number of laser shots) obtained under the two IR intensity regimes are both plotted in Figure 6.8. These data sets were taken on different days and so the experimental conditions cannot be exactly compared (for example, the average densities of the pulsed molecular beams were likely different across both days). However, it can be seen from the obtained mass spectra that the relative yields of carbon-containing cations (with $m/z <\sim 80$) were generally increased for the higher intensity regime compared to the yield of I^+ ($m/z = 127$).

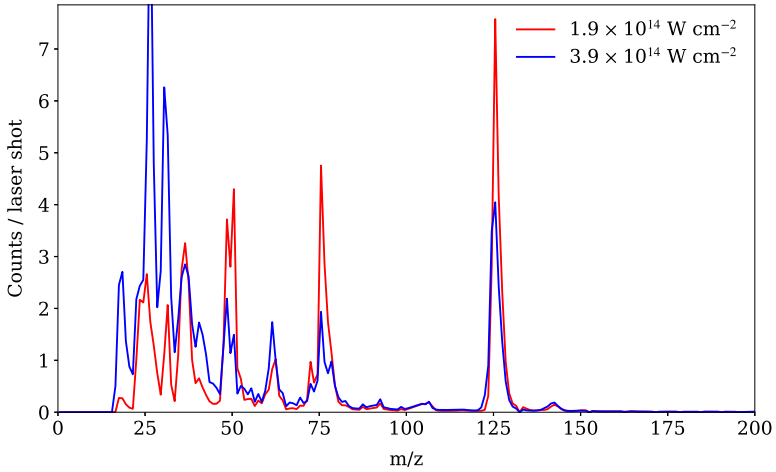

Figure 6.8: A comparison of the mass spectra obtained for the low ($1.9\times10^{14}\,\mathrm{W\,cm^{-2}}$, red) and high ($3.9\times10^{14}\,\mathrm{W\,cm^{-2}}$, blue) IR intensity regimes.

6.3.1 Ion Momentum Distributions

The ion image of $C_6H_x^+$ fragments recorded by PImMS2 at the low IR intensity is given in Figure 6.9(a). The two visible features (one condensed around the origin of the image and one with a larger radius) correspond to the peaks labelled $C_6H_x^+$ + I and $C_6H_x^+$ + I^+, respectively, in the integrated momentum distribution in Figure 6.10(b). It is worth noting that any H/H^+ loss could not be resolved in this experiment and the exact charge state of the parent ions generating these fragments is ambiguous. Therefore, the charge states of the parent molecules producing $C_6H_x^+$ fragments (where $x < 5$) may be greater than 2+. However, for simplicity, since H/H^+ loss cannot be observed here, it is ignored from here on. As implied by the labels in Figure 6.10(b), the lower momentum feature corresponds to the ionisation and subsequent dissociation of the molecular cation into $C_6H_x^+$ and neutral I co-fragments (ignoring H/H^+ loss). The momentum distribution of this feature was characterised by a Gaussian fitting, with an average value (and σ) of 17 ± 7 a.u.. This momentum corresponds to a KER of approximately $\sim$0.05 eV for the dissociative ionisation process. The higher momentum feature in Figure 6.10(b) arises from ionisation to form a parent cation in at least a dicationic state, which Coulomb explodes into I^+ and $C_6H_x^+$ co-fragments (ignoring H/H^+ loss). The average momentum of this feature is 161 ± 12 a.u., and the specific energetics of these processes will be discussed in more detail later on in this chapter.

The ion image of I^+ recorded by PImMS2 at 130 mW is given in Figure 6.10(a). Increased intensity is generated along the laser polarisation axis, showing preferential IR-ionisation of molecules whose C-I bond is aligned with the polarisation vector of the laser field. Five radial features are observed and are labelled in the momentum distribution in Figure 6.10(b).

Features A and B are lowest in momenta, and are generated in a dissociative ionisation regime, where IB^+ dissociates into I^+ and neutral carbon-containing fragments. Peak A has a momentum distribution of 8 ± 5 a.u., and Peak B has a momentum distribution centred around 36 ± 4 a.u.. The difference in KER of these two channels is 0.18 eV. Combined with the single dissociative ionisation

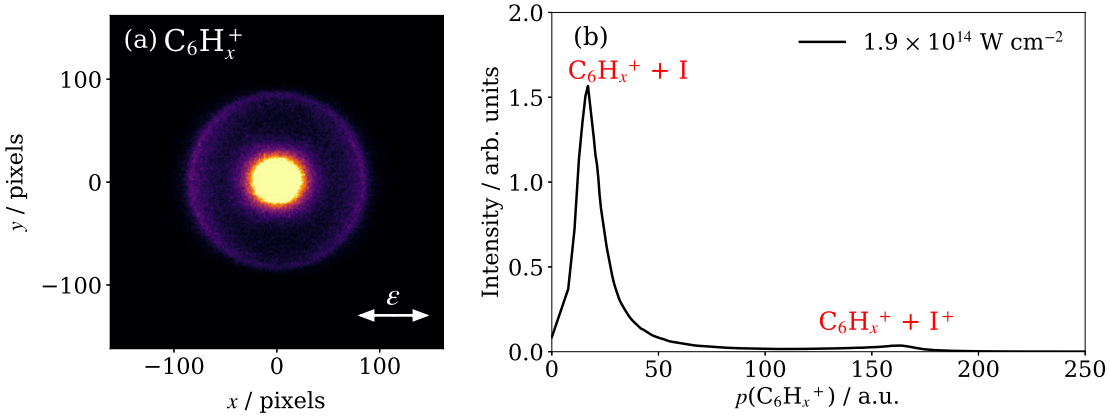

Figure 6.9: (a) The $C_6H_x^+$ ion image obtained at the low IR intensity ($1.9 \times 10^{14}\,\mathrm{W\,cm^{-2}}$), with the laser polarisation ε marked on, and (b) the corresponding momentum distribution, normalised by number of laser shots, and showing two peaks that arise from fragmentation into $C_6H_x^+$ and a neutral I or I^+.

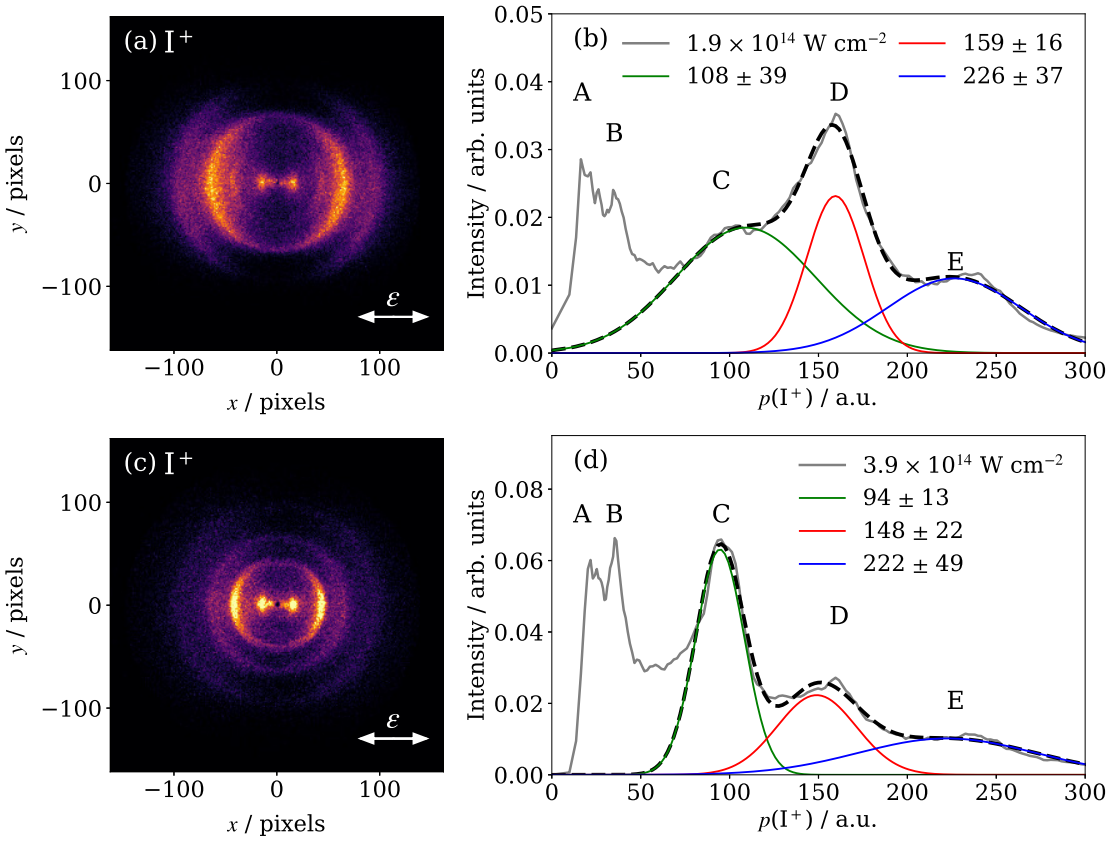

Figure 6.10: (a) The I^+ ion image obtained at the low IR laser intensity ($1.9 \times 10^{14}\,\mathrm{W\,cm^{-2}}$), with the laser polarisation ε shown, and (b) the corresponding momentum distribution, normalised by the number of laser shots, showing five peaks that are discussed in the text. The latter three peaks have been fitted with Gaussian distributions, and the corresponding centres and widths (in a.u.) are given in the legend. Corresponding plots of the I^+ ion image and momentum distribution obtained at the high IR laser intensity ($3.9 \times 10^{14}\,\mathrm{W\,cm^{-2}}$) are given in (c) and (d).

peak observed in the $C_6H_x{}^+$ momentum distribution (Figure 6.9(b)), at least three different dissociative ionisation regimes are distinguished in this data set, although the two observed in the I^+ momentum distribution Figure 6.10(b) are within error of that of $C_6H_x{}^+$. These different features may be a result of single ionisation of different molecular orbitals, although the difference in ionisation energy of the HOMO and HOMO-1 is $\sim$0.73 eV,[220] which is greater than the difference in KER observed for the two channels generating I^+. It is also noted that absorption of three 800 nm photons would be sufficient to excite IB to its bound $\pi/\pi*$-state. Intersystem crossing via a conical intersection to a repulsive $n\sigma*$-state (expected to occur within 20-700 fs) could form free I and C_6H_5, which could then be independently ionised by the laser field, potentially within the duration of one laser pulse.[220] From this data set, the exact mechanism forming these features cannot be known. Photoelectron information or a time-resolved study may reveal more insights. However, since these peaks come from molecular monocations, no covariance with a second cationic fragment is obtainable, and therefore they are not the focus of this chapter.

Peaks C and D in Figure 6.10(b) correspond to a Coulomb explosion of IB^{2+} into I^+ and a charged carbon-containing fragment (ignoring H/H^+ loss). The momentum distributions of these two channels correspond to Coulomb explosions with average KER values of 1.9 ± 0.2 eV and 4.1 ± 0.1 eV, respectively. Assuming a purely Coulombic process, these KER values correspond to intercharge separations of 7.6 ± 1 Å, and 3.5 ± 0.04 Å, respectively. Peak E corresponds to a Coulomb explosion of IB^{3+} into I^+ and either $C_6H_x{}^{2+}$ or two charged carbon-containing fragments (ignoring H/H^+ loss). The average momenta of this peak corresponds to a KER of 8.3 ± 0.2 eV and an effective intercharge separation of 3.5 ± 0.1 Å (assuming the co-product is $C_6H_x{}^{2+}$). All three of these fragmentation channels (C, D, E) were confirmed through covariance analysis (Section 6.3.2).

The effective intercharge separations obtained for peaks D and E imply similar molecular geometries at the time of the Coulomb explosion. The distances extracted imply that the charge on the Ph component of IB is distributed about its π-system in both instances, much like the XUV-ionisation fragmentation regimes

suggested in Chapter 5 (Figure 5.5). The comparatively large charge separation extracted from peak C is interesting. This fragmentation channel is unique to the IR-ionisation regime and demonstrates how different ionisation regimes can generate different fragmentation processes. The maximum distance between two atoms in the ground state neutral configuration of IB (the distance between I and the H at the para position) is approximately 5.95 Å. If the charges were located on these two atoms, the intercharge distance would be too small to give the observed $p(I^+)$ distribution. To generate the observed $p(I^+)$ distribution, either the charge distribution on the molecular dication would have to be very diffuse, or the molecule is not in its ground state geometry.

Why is this fragmentation channel present for the IR-ionisation regime and not observed following XUV-ionisation? In the latter case, ionisation was predominantly site-selective at the I 4d orbitals, and the charge generation and redistribution processes resulted in prompt Coulomb explosions into I^+ and $C_6H_x{}^{+/2+}$ co-fragments. It is assumed that the I^+ was charged directly from the primary ionisation process. In IR-ionisation regimes, primary ionisation can occur across the whole molecule rather than just at the iodine atomic site. This is because the electron density of the molecular orbitals with the lowest ionisation potentials are distributed over many atomic sites, which can be seen in the first three HOMOs of IB (see Figure 6.11). Three example ionisation regimes are considered. Firstly, double IR-ionisation at the iodine atomic site might lead to charge redistribution and Coulomb explosion, as observed in the XUV-ionisation regime, producing peaks D/E. Secondly, direct single ionisation of both the Ph and the iodine could also lead to a Coulomb explosion producing peaks D/E. However, there is a third ionisation regime accessible to IR-ionisation that is much less probable via XUV-ionisation: direct double ionisation of the Ph component of IB. The C-I bond might not necessarily break immediately and the internal energy of the dication might be sufficient to induce structural distortion, such as isomerisation or ring-opening during some metastable lifetime before the charge redistributes so that one charge is on the iodine and induces a Coulomb explosion to form I^+. For example, in a ring-opened configuration, if one

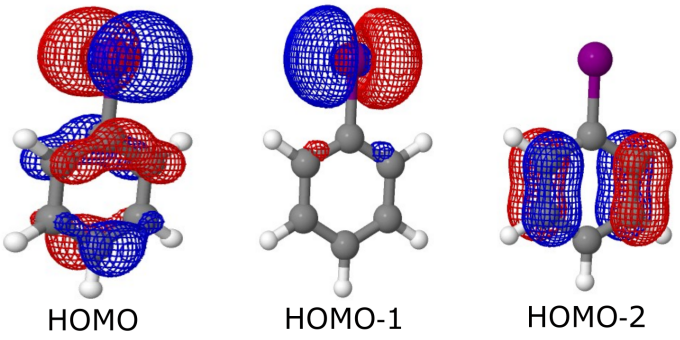

Figure 6.11: Highest occupied molecular orbital (HOMO) diagrams for the first three HOMOs of iodobenzene, generated using the application Molcalc.[221]

charge is located on the iodine and one on the carbon furthest from the iodine, the intercharge distance could be much closer to 7.6 Å, leading to a lower KER and $p(I^+)$, as seen in peak C. However, the exact mechanism causing peak C can not be precisely determined from this ion imaging data alone. Recording the photoelectrons in coincidence with photoions would be very beneficial in understanding how each of these channels relates to specific ionisation processes and an IR-pump-XUV-probe experiment may reveal more insights into the geometry of the fragment before the Coulomb explosion occurs. Even though peak C requires a Coulomb explosion into I^+ and a carbon-containing cation, a corresponding peak was not distinguishable in the $C_6H_x{}^+$ ion momentum distribution. However, this fragmentation channel was discernible using covariance analysis, as will be discussed in Section 6.3.2.

For comparison, the I^+ ion image and $p(I^+)$ distribution obtained at a higher IR intensity are given in Figure 6.10(c) and (d), respectively. The mean momenta of the peaks are consistent (within error) across both IR laser intensities. The relative intensities of peaks A, B, and C are increased compared to those obtained at a lower intensity (Figure 6.10(b)). Peak D decreased, and E remained approximately the same. The Keldysh parameters for these two laser intensities (given in Section 6.2.1) suggest ionisation via a mixed regime. The slightly lower Keldysh parameter at a higher laser intensity might suggest that more tunnelling ionisation can occur than at a lower laser intensity, and perhaps the change in relative peak intensities, especially of peaks C and D, is a result of different ionisation mechanisms being

accessed more efficiently. Further experiments could be carried out at higher and lower field intensities than presented here to investigate these intensity-dependent characteristics in more detail.

6.3.2 Recoil-frame Covariance Analysis

Next, the co-products of the different Coulomb explosion processes will be examined in more detail. Firstly, recoil-frame covariance analysis and momentum distributions of ions produced via channels C, D, and E will be analysed. Secondly, the distributions obtained for channels D and E will be compared to the XUV-ionisation results presented in Chapter 5.

Covariance features of peaks C, D, and E in Figure 6.10(b), obtained at the lower IR intensity, were isolated by performing covariance calculations that considered only I^+ ions with momenta within each of the corresponding peak ranges. Covariances for ions generated via channel C were isolated from D and E by only considering I^+ ions with $p(I^+) \leq \sim 130$ a.u.. Resultant recoil-frame covariance maps showing the recoil of $C_6H_x{}^+$ and $C_4H_x{}^+$ ions relative to I^+ ions are given in Figure 6.12(a) and (b), respectively. The integrated momentum distributions for these two maps are given in (c) and (d), respectively. Overlaid are the Gaussian fits showing the average momenta of the $C_nH_x{}^+$ fragments, quoted with the widths of the Gaussian distributions.

Given in Table 6.1 are the momenta of all $C_nH_x{}^+$ fragments obtained via covariance with I^+ produced via channel C in the low-intensity experiment. These values are also expressed as a ratio of the I^+ momenta and compared to the mass of the carbon fragment expressed as a fraction of the mass of Ph. Overall, there is good agreement between these two ratios (excluding those obtained for $C_5H_x{}^+$, which was a very low yield fragment and yielded very noisy covariance maps).

For $n < 6$, this agreement suggests that the fragments are produced in sequential mechanisms occurring via a primary Coulomb explosion that breaks the C-I bond and produces I^+ and a $C_6H_x{}^+$ intermediate species, which undergoes a secondary dissociation step after some metastable lifetime into secondary carbon-containing products. Considering the relative intensities of these covariance features (also given

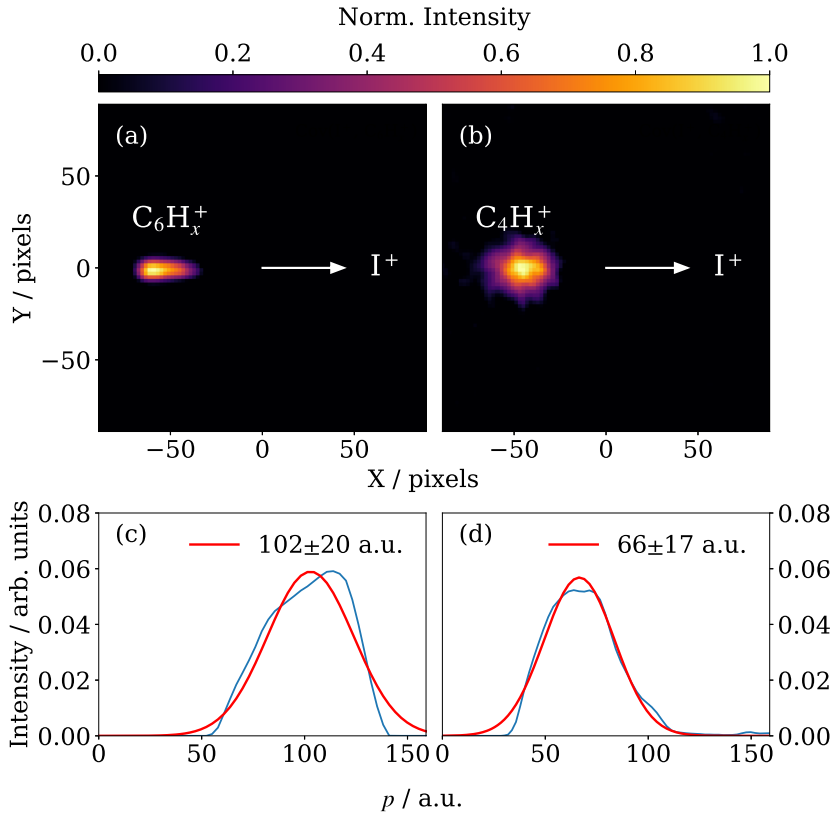

Figure 6.12: Recoil-frame covariance maps obtained for the lower IR intensity data ($1.9 \times 10^{14}\,\mathrm{W\,cm^{-2}}$) showing the recoil of $C_6H_x^+$ (a) and $C_4H_x^+$ (b) relative to I^+ ions, with $p(I^+)\leq 130$ a.u. (channel C). The corresponding integrated momentum distributions are shown in (c) and (d), and approximate centres are found via Gaussian fits, which are overlain.

in Table 6.1), and that no CH_x^+ fragments were detected in this experiment due to the MCP gating, it can be estimated that 80% of all $C_6H_x^+$ produced via channel C were metastable and decayed into secondary products, with a maximum of 20% forming stable $C_6H_x^+$ (with respect to C-C bond breakage, and ignoring H/H^+ loss).

Recoil-frame covariance maps are given in Figure 6.13 for fragmentation channels similar to those observed in the XUV-ionisation regime, pertaining to channels D and E. The momentum distributions of the features obtained are comparable for both IR laser intensities, but a better signal-to-noise ratio was obtained for the lower IR intensity, hence only covariances obtained at $1.9 \times 10^{14}\,\mathrm{W\,cm^{-2}}$ are shown. Covariance corresponding to two-body Coulomb explosions of the molecular dication is seen in Figure 6.13(a) and defined by the following equation (ignoring H/H^+ loss):

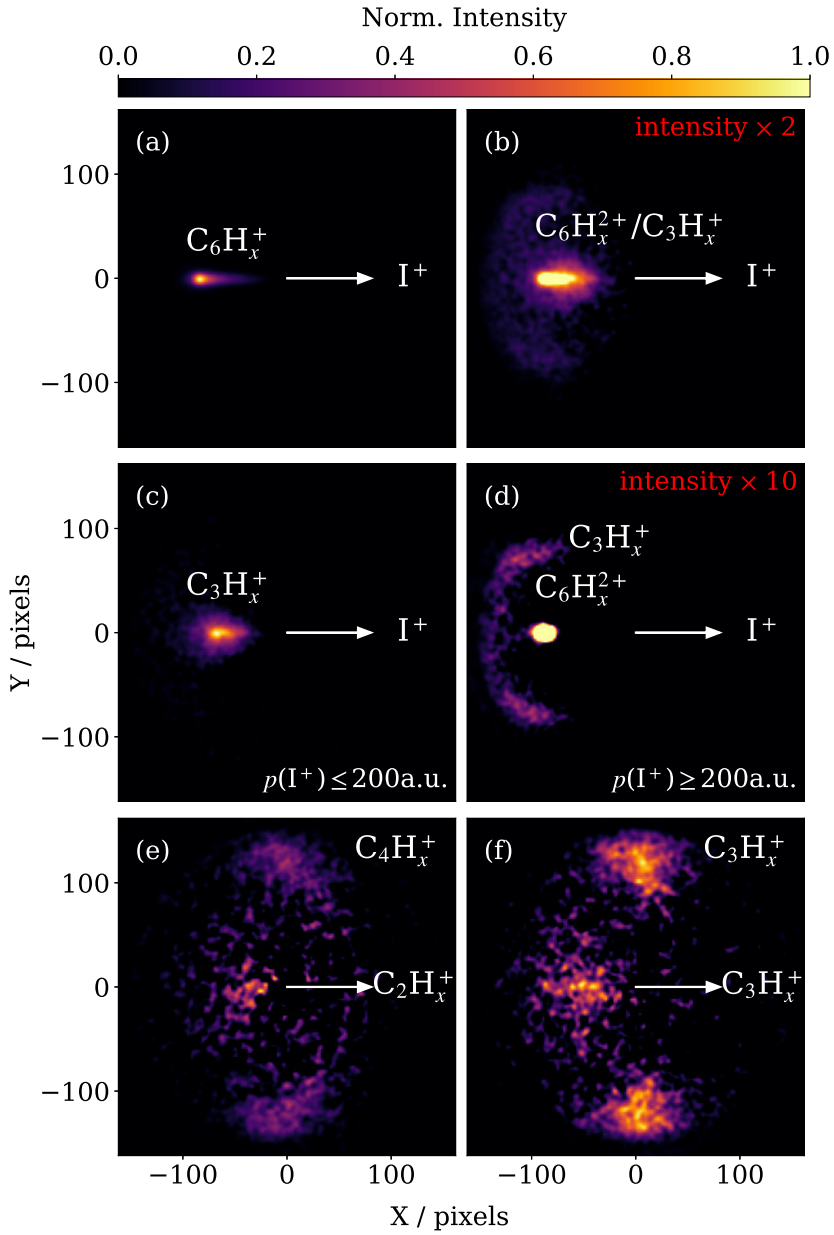

Figure 6.13: Recoil-frame covariance maps for ion pairs generated by IR-ionisation of IB at a low IR laser intensity (1.9×10^{14} W cm^{-2}), each normalised independently. The direction of the ion of reference is restrained along the direction of the white arrow, and positive intensity corresponds to the relative recoil of the ion of interest in each case. The intensities in (b) and (d) have been multiplied by ×2 and ×10, respectively, to better visualise weaker intensity features. (a) and (b) were calculated using the full $p(I^+)$ range. (c) and (d) were calculated by filtering on the I^+ radii, corresponding to momenta of ≤ 200 and ≥ 200, respectively.

Table 6.1: The momenta of $C_nH_x{}^+$ fragments found via recoil-frame covariance with I^+, where $p(I^+) \leq 130$ a.u., observed using the low IR laser intensity (1.9×10^{14} W cm^{-2}). These values are also expressed as a fraction of the I^+ momenta in peak C and compared to the mass of the carbon-containing fragments expressed as a fraction of the mass of Ph. The ranges given for the mass fractions relate to the potential variation in x in each of the $C_nH_x{}^+$ fragments that this experiment was not sensitive to. Also given is the relative intensity of covariance features of all ions corresponding to channel C.

$C_nH_x{}^+$	$p(C_nH_x{}^+) \pm \sigma$ (a.u.)	$\frac{p(C_nH_x^+)}{p(I^+)}$	$\frac{m(C_nH_x^+)}{m(Ph^+)}$	Intensity %
$C_6H_x{}^+$	102 ± 20	0.99	0.93-1.00	20.0
$C_5H_x{}^+$	96 ± 37	0.93	0.78-0.84	8.7
$C_4H_x{}^+$	66 ± 17	0.64	0.62-0.68	21.2
$C_3H_x{}^+$	50 ± 20	0.49	0.47-0.51	19.6
$C_2H_x{}^+$	40 ± 16	0.39	0.31-0.35	30.5

$$IB^{2+} \rightarrow I^+ + C_6H_x^+. \tag{6.3.2.1}$$

In (b), three features are visible and overlap. These can be distinguished by filtering the covariance calculation on the momentum of the reference I^+ ion ((c) and (d)). For $p(I^+) \leq 200$ a.u., a feature arising from three-body fragmentation of the molecular dication is visible in (c) (ignoring H/H^+ loss):

$$IB^{2+} \rightarrow I^+ + C_nH_x^+ + C_{6-n}H_y, \tag{6.3.2.2}$$

where $x + y \leq 5$. For $p(I^+) \geq 200$ a.u., two features are observed in (d): the first is a bright feature at 180° to the I^+ trajectory and corresponds to a two-body Coulomb explosion of the molecular trication (ignoring H/H^+ loss):

$$IB^{3+} \rightarrow I^+ + C_6H_x^{2+}, \tag{6.3.2.3}$$

and the second feature is an off-180° feature that corresponds to three-body fragmentation of the molecular trication into I^+ and two charged carbon-containing fragments:

$$IB^{3+} \rightarrow I^+ + C_nH_x^+ + C_{6-n}H_y^+. \tag{6.3.2.4}$$

This mechanism is also confirmed by the covariance maps in (e) and (f), which show covariance between two charged carbon-containing fragments at an off-180° recoil angle, implying a third charged fragment, I^+.

In (e) and (f), back-to-back covariance is also observed between the two carbon-containing features, suggesting they are produced from the molecular dication with a neutral I co-fragment. From the feature in (e), the momenta of the $C_2H_x{}^+$ and $C_4H_x{}^+$ ions were determined to be 62 ± 31 a.u. and 82 ± 44 a.u., respectively. Despite being very broad and with a poor signal-to-noise ratio, the relative recoil of these two ions implies that the C-I bond was broken either concertedly or before the break-up of the carbon ring. If the C-I bond was broken in a secondary process, the two carbon-containing cations might be expected to have a broader recoil distribution, as was seen in Section 4.4.9 of Chapter 4, but an essentially 180° feature is observed. Furthermore, a greater mismatch between the momenta of the two carbon-containing fragments would be expected. If, for example, the primary process produced $C_2H_x{}^+$ and a $C_4H_xI^+$ intermediate species, which could decay into a $C_4H_x{}^+$ and a neutral I product, then the neutral I product would retain the majority of the intermediate's momentum over $C_4H_x{}^+$, resulting in a large disparity between the $C_2H_x{}^+$ and $C_4H_x{}^+$ momenta. However, the momenta measured for these two fragments are within error of each other, supporting the assumption that the C-I bond cleaves before or concertedly with the fragmentation of the carbon ring. This is further supported by the distribution observed in the $C_3H_x{}^+/C_3H_x{}^+$ covariance map (Figure 6.13(f)): the feature with a recoil angle of 180° has only one maximum, with momenta equal to 67 ± 25 a.u., implying two $C_3H_x{}^+$ fragments have approximately equal and opposite momenta.

In the next sections, the momenta of ions observed from covariance with I^+ ions in peak D and E will be discussed in turn and compared to those obtained in the corresponding XUV-ionisation regime.

6.3.3 IR Versus XUV: Fragmentation Channels Producing I^+ and One Carbon-containing Cation

In this section, fragmentation channels generating I^+ and only one carbon-containing cation are discussed. Firstly, Coulomb explosion process generating $C_6H_x{}^+$ fragments that are stable with respect to C-C bond breakage are considered. However, due to the ToF resolution of the spectrometer and the PImMS ion imaging camera, fragments differing by a single H-atom could not be distinguished, and so any instability with respect to C-H bond breakage cannot be confirmed for this data set as it was in the XUV data set.

The radius of the recoil-frame covariance features in Figure 6.13(a) can be used to extract fragment momenta, and the momenta of features observed in the recoil-frame covariance maps for the (I^+, $C_nH_x{}^+$) ion pairs ($n < 6$), produced from the molecular dication, are given in Table 6.2 for comparison with those obtained for the (I^+, $C_6H_x{}^+$) ion pair. Firstly, the extracted $p(I^+)$ distributions are similar and within error across all n, including n=6, implying that the intercharge separation before the C-I bond-breaking process was equivalent for each fragmentation pathway. In each case, $p(I^+)$ is greater than the momenta observed from the XUV-ionisation process. The intercharge separation for the IR-ionisation process was found to be 3.5 Å, whereas, for the XUV data, it was measured to be 4.3 Å. This intercharge separation is smaller than expected and might suggest that IR-ionisation populates cationic states with different charge distributions than the XUV, or that IR-ionisation might initiate a more prompt Coulomb explosion, where the C-I bond has less time to potentially elongate before breaking.

The $p(C_nH_x{}^+)$ values in Table 6.2 decrease with decreasing n. These momenta are also expressed as a fraction of $p(I^+)$ in Table 6.2, and can be compared to the mass of the $C_nH_x{}^+$ fragment expressed as a fraction of the mass of Ph. Excellent agreement can be seen between these two ratios (better agreement than was observed for the corresponding channels observed following XUV-ionisation), implying that the $C_nH_x{}^+$ ($n < 6$) fragments are produced in a sequential fragmentation process

Table 6.2: The momenta of $C_nH_x^+$ and I^+ ions produced in fragmentation channels producing only one carbon-containing cation, obtained via recoil-frame covariance analysis of the low IR laser intensity data set ($1.9 \times 10^{14}\,\mathrm{W\,cm^{-2}}$). The ratios of these momenta are also given and compared to the mass of the carbon-containing fraction expressed as a fraction of the mass of Ph. The ranges given for the mass fractions relate to the potential variation in x in each of the $C_nH_x^+$ fragments that this experiment was not sensitive to. Also given is the relative intensity of covariance observed for each ion pair, expressed as a percentage of all covariances listed in the table. Note: these are upper estimates as covariance with CH_x^+ was not recorded.

$C_nH_x^+$	$p(C_nH_x^+) \pm \sigma$ (a.u.)	$p(I^+) \pm \sigma$ (a.u.)	$\frac{p(C_nH_x^+)}{p(I^+)}$	$\frac{m(C_nH_x^+)}{m(Ph^+)}$	Intensity %
$C_6H_x^+$	164 ± 14	164 ± 15	1.00	0.93-1.00	25.8 ± 0.2
$C_5H_x^+$	143 ± 47	172 ± 33	0.83	0.78-0.84	10.1 ± 0.2
$C_4H_x^+$	99 ± 32	160 ± 24	0.62	0.62-0.68	27.5 ± 0.2
$C_3H_x^+$	96 ± 34	180 ± 45	0.53	0.47-0.51	19.4 ± 0.3
$C_2H_x^+$	68 ± 25	170 ± 50	0.40	0.31-0.35	17.2 ± 0.2

that occurs via a primary Coulomb explosion that breaks the C-I bond and generates a metastable $C_6H_x^+$ fragment that dissociates into secondary products.

The relative intensities of these covariance features, expressed as a percentage of all processes generating I^+ ions with momenta within peak D, are also given in Table 6.2. Since no CH_x^+ fragments were detected due to the MCP gating and, therefore, no (I^+, CH_x^+) covariance was obtained, these percentages are upper estimates. Despite this, similar trends and relative intensities are observed between the IR data presented here and the XUV data presented in the previous chapter. The fragmentation channel with the highest yield produced $C_4H_x^+$ fragments with neutral C_2H_x, followed by $C_6H_x^+$, and the lowest yield was observed for $C_5H_x^+$ fragments.

The similarities observed between the IR and XUV data sets raise some interesting questions about how the range of fragmentation channels observed depends on the ionisation pathway. In either ionisation regime, the relative product momenta indicate sequential processes occurring via the generation of an intermediate in a metastable state. Despite each ionisation regime populating different *initial* cationic excited states, the similar momentum distributions and relative yields of the range of products observed in either case suggest that the *final* excited states that become populated through energy redistribution processes might have similar properties that result in similar sets of products. In the case of

XUV-ionisation, highly excited states are expected to decay to low electronic but vibrationally excited states that facilitate fragmentation.[199–203] IR-ionisation, on the other hand, populates lowly excited electronic cationic states, which–if similarly vibrationally excited–could facilitate fragmentation into products similar to those observed in the XUV study.

6.3.4 IR Versus XUV: Fragmentation Producing I^+ and Either $C_6H_x{}^{2+}$ or Two Carbon-containing Cations

As described previously, recoil-frame covariance of fragmentation channels producing I^+ and either $C_6H_x{}^{2+}$ or two carbon-containing cations (e.g., Figure 6.13(d-f)) were independently mapped by only considering I^+ ions with $p(I^+)$ within the range of peak E in Figure 6.10(b). The $p(I^+)$ distributions obtained from covariance between all ion pairs are given in Table 6.3. These values are similar across all fragmentation channels, implying that the Coulomb explosion process breaking the C-I bond was equivalent in each regime. These $p(I^+)$ values are all greater than those observed for the corresponding XUV-ionisation fragmentation channels.

Table 6.3: I^+ momenta, generated via fragmentation processes producing either $C_6H_x{}^{2+}$ or two carbon-containing cations ($C_nH_x{}^+$+$C_{6-n}H_y{}^+$), obtained from recoil-frame covariance.

$C_nH_x^+$	$p(I^+) \pm \sigma$ a.u.
$C_6H_x^{2+}$	238 ± 28
$C_5H_x{}^+$	234 ± 30
$C_4H_x{}^+$	236 ± 24
$C_3H_x{}^+$	239 ± 27
$C_2H_x{}^+$	235 ± 39

In the XUV-ionisation data presented in Chapter 5, the momentum distributions of $C_nH_x{}^+$ ions relative to I^+ (produced with a second carbon-containing cation) swept out a broad angular distribution relative to the trajectory of a primary I^+ fragment and were characteristic of a sequential fragmentation occurring via a primary Coulomb explosion breaking the C-I bond and a secondary Coulomb explosion of a $C_6H_x{}^{2+}$ intermediate. However, here in Figure 6.13(d), the relative recoil between I^+ and $C_3H_x{}^+$, for example, is more narrowly confined to some

off-180° angle, characteristic of a more prompt three-body fragmentation process, where the process breaking the carbon ring is not entirely independent of the C-I bond-breaking process. This can also be seen in (e) and (f), where a feature with an off-180° recoil angle is observed between two carbon-containing fragments. The recoil angles extracted from each of these distributions are given in Table 6.4 for various pairs of ions. The sums of these sets of recoil angles are within error of 360°.

From the data presented in Chapter 5, XUV-ionisation is suspected to generate $C_6H_x{}^{2+}$ ions in metastable, electronically excited states, which persist long enough for the intermediate to fully rotate in space relative to the trajectory of a primary I^+ fragment before relaxing into vibrationally hot states that facilitate secondary fragmentation. Such processes were identified by covariance features with broad angular distributions. In contrast, the covariance features seen in the IR data set have a much narrower angular distribution, which is characteristic of a more prompt fragmentation mechanism. This suggests that the IR-ionisation regime accesses excited states defined by a more prompt fragmentation into I^+ and two smaller charged carbon-containing fragments.

Table 6.4: The relative recoil angles between pairs of ions produced in fragmentation processes generating I^+ and two carbon-containing cations, obtained via recoil-frame covariance.

A	B	$\angle AB \pm \sigma/°$
I^+	$C_2H_x{}^+$	139 ± 20
I^+	$C_4H_x{}^+$	152 ± 10
$C_4H_x{}^+$	$C_2H_x{}^+$	90 ± 16
I^+	$C_3H_x{}^+$	145 ± 15
$C_3H_x{}^+$	$C_3H_x{}^+$	88 ± 9

6.4 Conclusions

CEI of IB was carried out using ultrafast and intense IR probe pulses that operated in a mixed strong-field and multiphoton regime. Resultant molecular polycations fragmented into a range of carbon-containing products (but any H/H^+ loss could not be resolved within this data set due to the limited ToF resolution of the

spectrometer and PImMS2 camera). The results obtained here were compared to those presented in the XUV study in Chapter 5. The IR-ionisation was not atomic-site-selective, whereas XUV-ionisation was primarily at the I 4d edge. As a result, fragmentation channels unique to the IR-ionisation regime were observed, and could potentially have resulted from ionisation of molecular orbitals and generation of two cationic charges at the Ph component of IB rather than primary ionisation at the iodine site. Laser intensity-dependent changes were observed in the relative yield of I^+ ions produced via different fragmentation channels. This is potentially due to either a strong-field or multiphoton ionisation regime being accessed more efficiently at different laser intensities. Extending this work to higher and lower laser intensities may provide more clarity on how different fragmentation channels can be accessed via different IR-ionisation regimes.

Fragmentation channels that occurred via a prompt Coulomb explosion that initially broke the C-I bond were observed in both the XUV- and IR-ionisation experiments. The similarities and differences between the timescales of subsequent fragmentation processes of carbon-containing primary products, induced by either regime, demonstrate how ionisation, excitation, and relaxation processes influence the range of final excited states (and products) accessible to a single ionisation regime. To understand more about how ionisation regimes influence the observed fragmentation channels, it would be useful to record photoelectrons in coincidence with the ions, to reveal information about ionisation sites and properties of excited states. Furthermore, an XUV-IR pump-probe experiment may yield interesting insights into the geometries of intermediates and the time frames that they persist over. By comparing the quality of the results obtained in both experiments, it is clear that more sophisticated experimental and analytical approaches yield more accurate and detailed insights into the range of fragmentation channels occurring. The high ToF resolution achieved by the spectrometer used in the XUV-ionisation experiment allowed for full 3D momentum information to be retrieved for multiple ions hitting the detector per laser shot and fragments differing by single numbers of

hydrogen atoms to be resolved. This ability is paramount for resolving concurrent fragmentation channels in as much detail as possible.

Acknowledgements

I would like to thank S. Lim, J. Unwin, E. Warne, and M. Burt for their support of this project. Furthermore, I would like to acknowledge S. Lim, J. Unwin, and E. Warne for collecting the data presented in this chapter.

I have to go.

— Serena van der Woodsen, Gossip Girl

7

Conclusions and Future work

In this thesis, CEI and covariance analysis have been used to study the reaction and nuclear dynamics of concurrent fragmentation pathways occurring along multiple degrees of freedom.

In Chapter 3, the photodissociation dynamics of CH_2I_2 at 202.5 nm was investigated by a UV-pump XUV-probe experiment. Time-dependent recoil-frame covariance analysis was used to separately characterise the energetics of Coulomb explosions generating pairs of iodine ions in different charge states. These were considered alongside values obtained from charge transfer features to simultaneously map out the structural changes occurring along the I-C and I-C-I coordinates during the three-body dissociation of the parent molecule. These results demonstrated the potential of CEI to map PESs of the structural evolution of an initially neutral molecule over multiple degrees of freedom. Since this analysis was carried out assuming that co-ions were point charges operating exclusively under Coulomb's law, future work should aim to further validate results obtained from time-dependent CEI and covariance analysis with theoretical simulations using high levels of theory. CH_2I_2 is expected to have a high density of excited states due to having two heavy iodine substituents, and so the results observed here likely comprise components corresponding to products produced from a range of excited states. It would

be beneficial to simulate the expected geometries of a range of excited states to compare with the total experimentally observed distributions.

The resolution of the results presented in Chapter 3 was limited as ion 3D momentum information could not be obtained from the data. When 3D momenta can be obtained from an experiment, more advanced covariance analysis procedures can be carried out that provide more sophisticated insights into the processes generating fragment ions. For example, Newton-frame covariance analysis can be adapted to disentangle fragmentation mechanisms that generate the same sets of ionic products. Since the momenta of ionic products are dependent on their causal fragmentation pathways, covariance signals corresponding to different fragmentation mechanisms can be isolated by constraining the covariance calculation to only consider reference ions with momenta within a given range. This was demonstrated in Chapter 4 using $I^+/CH_3{}^+$ ion pairs (produced with $C_2H_4{}^+$) that were generated from 1- and 2-IP following XUV-ionisation at the I 4d orbitals. By filtering on the momentum of reference ion (I^+), the relative momenta of $CH_3{}^+$ ions produced in concerted and sequential Coulomb explosions of the molecular trication could be disentangled. Furthermore, by carefully considering how momentum is partitioned between products, the individual steps of the same multi-step fragmentation process can be analysed independently using native-frame covariance analysis. This was also demonstrated using $I^+/CH_3{}^+$ ion pairs that were produced in the sequential fragmentation of the molecular trication, occurring via a primary Coulomb explosion into I^+ and a propyl dication intermediate, which fragmented via a secondary Coulomb explosion into $CH_3{}^+$ and $C_2H_4{}^+$. The momenta of the secondary products contain contributions from both the primary and the secondary Coulomb explosion processes. The primary momentum contribution is also encoded in the momenta of the I^+ ions, which can be subtracted from the momenta of the secondary products in the covariance calculation. This transforms the covariance into the native-frame of the intermediate, which allows the energetics of the secondary Coulomb explosion to be analysed independently of the primary process.

These 3D covariance analysis techniques were used to characterise a broad range of fragmentation channels producing two cationic products occurring for the two isomers of iodopropane following XUV-ionisation. The results showed that, for spectrometers that are highly sensitive to ion momenta (such as the spectrometer used at SACLA, equipped with a hexanode delay line detector), the relationship between the geometry of the parent molecule, nuclear dynamics, and momentum interchange between fragments can be interrogated in great detail, even between products generated by the same reaction mechanism.

The ability of these 3D covariance analysis techniques to follow the fragmentation dynamics of larger, more complicated molecules was demonstrated in Chapter 5, where the fragmentation of IB polycations, generated via XUV-ionisation at the I 4d orbitals, was studied. Primary Coulomb explosions of IB polycations producing I^+ and $C_6H_x{}^{+/2+}$ co-ions were used to study the (in)stability of the latter species and any ensuing excited-state chemistry producing carbon-containing co-fragments. Many different fragmentation channels were observed, which is a result of ionisation and charge redistribution processes that populate a broad range of excited cationic states and internal energy distributions. A large amount of information can be extracted using 3D covariance analysis that describes *how* a molecule fragments via simultaneously occurring processes. However, to understand the reasons *why* a certain fragmentation channel is observed, more information is required than just the ion spectra. By recording photoelectrons in coincidence with photoions, fragmentation channels could be linked to particular ionisation regimes and populated excited states.

When extending CEI and covariance analysis to time-resolved studies of larger molecules, it is important to consider that the probe laser pulse itself can induce many fragmentation channels, including channels generating metastable intermediates (as seen in Chapter 4 and Chapter 5) that can complicate both the appearance and the analysis of time-resolved spectra. It is important to be able to characterise the range of different features within probe-only spectra so that such signals can be accounted for in time-dependent pump-probe data. However, the products of probe-only

interactions are also interesting in and of themselves as they are strongly dependent on the specific ionisation and charge redistribution regimes that produce them. The results obtained via XUV-ionisation of IB in Chapter 5 were compared to results obtained via IR-ionisation of IB in Chapter 6. Several fragmentation channels unique to the IR-ionisation regime were observed, demonstrating how different charge generation and redistribution processes can access different fragmentation pathways. Several fragmentation channels were also observed in both ionisation regimes that yielded similar sets of products. However, the timescales of the corresponding fragmentation channels differed between the two studies: the XUV-study suggested that carbon-containing co-ions (e.g., $C_2H_2^+$+$C_4H_3^+$) were generated via ionisation to excited states that produced $C_6H_x^{2+}$ intermediates that underwent secondary Coulomb explosions after some metastable lifetime. However, in the IR-study, the timescales of fragmentation channels producing carbon-containing co-ions were seemingly much faster than a sequential process. The similarities and differences between fragmentation channels observed in these two studies indicate a dependence on the time taken for internal energy to redistribute, which is dependent on the initial ionisation processes.

Achieving higher time resolution in pump-probe experiments is an ongoing goal for the ultrafast scientific community, and has consequently catalysed improvements to experimental capabilities. Whilst photodissociation can be studied with femtosecond laser pulses, applying attosecond pulse generation in XUV-IR pump-probe spectroscopy could reveal deeper insights into the charge generation processes that occur before fragmentation and on faster timescales than nuclear dynamics, as well as how these processes influence the range of products observed. However, extending CEI experiments (operating under high count rates) to larger molecules calls for analytical methods that can calculate higher-order ion correlations than the two- and three-fold covariance techniques used here. For four-fold correlations and above, covariance becomes contaminated by the pairwise correlations between uncorrelated events. Therefore, covariance analysis methods need to be extended to cumulant mapping, which can also be used for higher n-fold correlations than just four.[222,

223] However, this problem is circumvented when operating under coincidence conditions, where all detected fragments can be assumed to originate from the same fragmentation event. Combining experiments that exploit both photoelectron and photoion capabilities, that use detectors with ToF resolution great enough to reconstruct 3D momentum information for multiple particles hitting the detector per laser shot, and that operate under coincidence conditions or 'covariance' conditions that employ cumulant mapping techniques would yield incredibly detailed insights into the mechanisms of concurrent fragmentation channels and why they occur. Furthermore, experiments are becoming highly sensitive to changes in correlated ion fragment momenta, even within the same reaction mechanism. The advances in analysis techniques required to visualise such detailed data may lead to methods that can be extended beyond the gas-phase photochemistry of single molecules to other areas in the field of reaction dynamics such as clusters, aerosols, secondary ion mass spectrometry, or surface mapping.

Appendices

A
Centroiding Code

The Python function below, `centroid_shots`, is used to centroid the data retrieved from a PImMS camera. The function takes the following variables: `input_array`, which is an array of x, y, ToF, and shot identifier; `time_win` is the maximum number of time windows considered for a cluster; `min_shot` is the first shot identifier considered in the function and `max_shot` is the final shot identifier considered; `min_t` and `max_t` are the minimum and maximum ToFs considered in the algorithm; `min_cluster_size` and `max_cluster_size` are the minimum and maximum limits on cluster sizes considered by the algorithm. The function returns an array containing centroided data. The code was adapted by F. Allum, M. Burt, and J. W. McManus based on Fortran code from C. S. Slater and I. J. Bush.

```
from numba import jit

@jit(nopython = True)
def centroid_shots(input_array, time_win, min_shot, max_shot, min_t,
    ↪  max_t, min_cluster_size, max_cluster_size):

    start_shot = 0
    total_hits = (input_array.shape)[0]
    max_events = int(total_hits/min_cluster_size)

    event_no = 0
    event_counter = 0
```

```
image = np.zeros((324,324), dtype = np.int32) # used to keep
    ↪ track of where the hits for on each shot
cluster_array = np.zeros((max_t, 3), dtype = np.int32)
event_array = np.zeros((max_events, 6), dtype = np.int32)

for shot in range(min_shot, max_shot):
    # Search through all events until the first event of the
        ↪ shot is found
    for test in range(start_shot, total_hits):
        if (input_array[test, 3] == shot):
            start_shot = test #save the first event of the shot
            break

    # Starting from the first event of the shot search until the
        ↪  first event of the next shot is found
    for test in range(start_shot, total_hits):
        if input_array[test, 3] > shot:
            end_shot = test - 1 #save the last event of the shot
            break

    # Search events in shot to find an uncounted hit
    for i in range(start_shot, end_shot):
        if (input_array[i, 4] == 0): # search final column of
            ↪ input array, within which 0 -> uncounted, 1 ->
            ↪ counted

            # Check event is in time range specified
            i_t = input_array[i, 2]
            if min_t <= i_t <= max_t:

                cluster_array = np.zeros((1300, 3), dtype = np.
                    ↪ int32)
                size = 1 # reset cluster size
                event_no += 1
                input_array[i, 4] = 1 # mark hit as found
                i_row = input_array[i, 0] # x coordinate
                i_col = input_array[i, 1] # y coordinate
                cluster_array[size - 1, 0] = i_row # Add hit to
                    ↪ cluster array
                cluster_array[size - 1, 1] = i_col
                cluster_array[size - 1, 2] = i_t
                min_t_event = i_t
                max_t_event = i_t + time_win
                image[i_row, i_col] = event_no # mark where the
                    ↪ hit was in the image
```

```
# Search for connected hits
found_neighbour = True
for p in range(max_cluster_size + 10): # search
    ↪ for a maximum of (max_cluster_size + 10)
    ↪ additional hits
    if found_neighbour:
        found_neighbour = False

        for j in range(i, end_shot):
            found_j = False
            if input_array[j, 4] == 0:

                # Check hit j is within the time
                    ↪ window of the initial hit i
                j_t = input_array[j, 2]
                if min_t_event <= j_t <=
                    ↪ max_t_event:

                    j_row = input_array[j, 0]
                    j_col = input_array[j, 1]

                    # Check the found hit j is close
                        ↪  to the cluster in the
                        ↪ image
                    for j_row2 in range(j_row - 1,
                        ↪ j_row + 2):
                        if found_j == False:
                            for j_col2 in range(
                                ↪ j_col - 1, j_col +
                                ↪  2 ):
                                if image[j_row2,
                                    ↪ j_col2] ==
                                    ↪ event_no:

                                    input_array[j, 4]
                                        ↪  = 1 # mark
                                        ↪  event as
                                        ↪ found
                                    size += 1 #
                                        ↪ increment
                                        ↪ cluster
                                        ↪ size
                                    image[j_row,
                                        ↪ j_col] =
```

```
                                                    ↪ event_no #
                                                    ↪ mark new
                                                    ↪ hit in the
                                                    ↪ image
                                                cluster_array[
                                                    ↪ size - 1,
                                                    ↪ 0] = j_row
                                                    ↪ # Add hit
                                                    ↪ to cluster
                                                    ↪ array
                                                cluster_array[
                                                    ↪ size - 1,
                                                    ↪ 1] = j_col
                                                cluster_array[
                                                    ↪ size - 1,
                                                    ↪ 2] = j_t

                                                # Reset these
                                                    ↪ variables
                                                    ↪ if a
                                                    ↪ neighbouring
                                                    ↪  hit was
                                                    ↪ found to
                                                    ↪ keep on
                                                    ↪ searching
                                                    ↪ for more
                                                found_neighbour =
                                                    ↪  True
                                                found_j = True
                                                break

                    # Convert cluster into an event by applying
                        ↪ equation to find cluster centre
                    if min_cluster_size <= size <= max_cluster_size: #
                        ↪  check cluster size is within bounds

                        x_sum = 0
                        y_sum = 0
                        t_sum = 0

                        # Cluster_array isn't reintialised, new data
                            ↪ overwrites old, so only read out data in
                            ↪  the array
                        # saved for the current cluster
                        for k in range(size):
```

```
                        cx = cluster_array[k, 0]
                        cy = cluster_array[k, 1]
                        ct = cluster_array[k, 2]
                        time = ct - i_t + 1
                        x_sum += cx/time
                        y_sum += cy/time
                        t_sum += 1/time

                    t_spread = np.max(cluster_array[:size, 2]) -
                        ↪ np.min(cluster_array[:size, 2]) + 1

                    event_array[event_counter, 0] = int(x_sum/
                        ↪ t_sum + 0.5)
                    event_array[event_counter, 1] = int(y_sum/
                        ↪ t_sum + 0.5)
                    event_array[event_counter, 2] = i_t # cluster
                        ↪ time = time of earliest event in the
                        ↪ cluster
                    event_array[event_counter, 3] = shot
                    event_array[event_counter, 4] = size
                    event_array[event_counter, 5] = t_spread
                    event_counter += 1

    return(event_array[0:event_counter,:]) # only return the section
        ↪  of the array which has logged events
```

B

ToF-ToF Covariance Code

The Python function below calculates the ToF-ToF covariance using the following variables: a numpy array of the dataset (`frame_array_A`, comprising one column for ToF and a second column for shot identifier), an array of unique shot identifiers (`shot_array`), the integer number of ToF bins (`n_bins`), and the integer size of each ToF bin (`bin_fac`). The function returns the Sij, SiSj, and covariance terms. The code has been contributed to by F. Allum and J. W. McManus.

```
import numpy as np
from numba import njit
@njit

def calc_covar(frame_array_A, shot_array, n_bins, bin_fac):

    Sij = np.zeros((n_bins,n_bins))
    mean_tof = np.zeros((n_bins))
    nshotsA=0
    no_A=np.shape(frame_array_A)[0]
    nendA=0
    number_of_shots = len(shot_array)
    for shot in shot_array:
        for test in range(nshotsA, no_A):
            if (frame_array_A[test,1] == shot):
                nshotsA = test
                break
        for test in range(nshotsA, no_A):
            if frame_array_A[test,1] > shot:
```

```
            nendA = test
            break

    for i in range(nshotsA, nendA):
        A_tof = int(frame_array_A[i,0]/bin_fac+0.5)
        if A_tof<n_bins:
            mean_tof[A_tof]+=1
            for j in range(nshotsA,nendA):
                B_tof = int(frame_array_A[j,0]/bin_fac+0.5)
                if B_tof<n_bins:
                    Sij[A_tof,B_tof]+=1
SiSj=np.outer(mean_tof,mean_tof)/number_of_shots**2
Sij=Sij/number_of_shots
covar=Sij-SiSj
return((Sij,SiSj,covar))
```

C
Recoil-frame Covariance Code

The Python function below calculates recoil-frame covariance between two ions (A, the reference ion and B, the ion of interest).

The function `two_fold_recoil_frame_covariance` takes the following variables: `df_A` and `df_B` are dataframes containing the information for ion A and ion B, respectively; `shot_list`, which is an array containing unique shot identifiers; and `pixels`, which is number of pixels to bin the image into. The function uses the other functions `recoil_frame_Sij_1` (or `recoil_frame_Sij_2`) `recoil_frame_SiSj` to calculate and return the Sij and SiSj terms. The latter is subtracted from the prior of these terms to calculate the recoil-frame covariance map. The code has been contributed to by F. Allum and J. W. McManus, based on Fortran code.

```
import numpy as np
# 2D recoil-frame covariance function

from numba import jit

@jit(nopython = True)
def recoil_frame_Sij_1(array_A, array_B, shot_array, pixels):

    Sij_array = np.zeros((pixels, pixels), dtype = np.int64)

    no_A = array_A.shape[0]
    no_B = array_B.shape[0]
```

```
nshotsA, nshotsB = 0, 0
nendA, nendB = 0, 0

for shot in shot_array:

    A_in_shot, B_in_shot = False, False

    for test in range(nshotsA, no_A):
        if (array_A[test, 2] == shot):
            nshotsA = test
            A_in_shot = True
            break

    if A_in_shot:
        for test in range(nshotsA, no_A):
            if array_A[test, 2] > shot:
                nendA = test
                break

        for test in range(nshotsB, no_B):
            if (array_B[test, 2] == shot):
                nshotsB = test
                B_in_shot = True
                break

    if B_in_shot:
        for test in range(nshotsB, no_B):
            if array_B[test, 2] > shot:
                nendB = test
                break

    if A_in_shot & B_in_shot:

        for i in range(nshotsA, nendA):
            rad_A = array_A[i, 0]
            theta_A = array_A[i, 1]

            for j in range(nshotsB, nendB):
                rad_B = array_B[j, 0]
                theta_B = array_B[j, 1]

                theta_rel = theta_B - theta_A

                if theta_rel>2*np.pi:
                    theta_rel=theta_rel-2*np.pi
```

```
                elif theta_rel<0:
                    theta_rel=theta_rel+2*np.pi

                x = int(round(rad_B*np.cos(theta_rel) + pixels/2))
                y = int(round(rad_B*np.sin(theta_rel) + pixels/2))

                if (0 < x < pixels) and (0 < y < pixels): # if hit
                ↪  is within the image array
                    Sij_array[y-1, x-1] += int(1)

    return(Sij_array)

@jit(nopython = True)
def recoil_frame_Sij_2(array_A, array_B, shot_array, pixels, mean_A)
    ↪ :

    Sij_array = np.zeros((pixels, pixels), dtype = np.float64)

    no_A = array_A.shape[0]
    no_B = array_B.shape[0]

    nshotsA, nshotsB = 0, 0
    nendA, nendB = 0, 0

    for shot in shot_array:

        A_in_shot, B_in_shot = False, False

        for test in range(nshotsA, no_A):
            if (array_A[test, 2] == shot):
                nshotsA = test
                A_in_shot = True
                break

        if A_in_shot:
            for test in range(nshotsA, no_A):
                if array_A[test, 2] > shot:
                    nendA = test
                    break

            for test in range(nshotsB, no_B):
                if (array_B[test, 2] == shot):
                    nshotsB = test
                    B_in_shot = True
                    break
```

```
        if B_in_shot:
            for test in range(nshotsB, no_B):
                if array_B[test, 2] > shot:
                    nendB = test
                    break

        if A_in_shot & B_in_shot:

            n_A_ions = (nendA - nshotsA)
            for i in range(nshotsA, nendA):
                rad_A = array_A[i, 0]
                theta_A = array_A[i, 1]

                for j in range(nshotsB, nendB):
                    rad_B = array_B[j, 0]
                    theta_B = array_B[j, 1]

                    theta_rel = theta_B - theta_A

                    if theta_rel>2*np.pi:
                        theta_rel=theta_rel-2*np.pi
                    elif theta_rel<0:
                        theta_rel=theta_rel+2*np.pi

                    x = int(round(rad_B*np.cos(theta_rel) + pixels/2))
                    y = int(round(rad_B*np.sin(theta_rel) + pixels/2))

                    if (0 < x < pixels) and (0 < y < pixels): # if hit
                        ↪ is within the image array
                        Sij_array[y-1, x-1] += mean_A/n_A_ions

    return(Sij_array)


@jit(nopython = True)
def recoil_frame_SiSj(reduced_array_A, reduced_array_B, pixels):

    SiSj_array = np.zeros((pixels, pixels), dtype = np.int64)

    no_A = reduced_array_A.shape[0]
    no_B = reduced_array_B.shape[0]

    for i in range(no_A):
        rad_A = reduced_array_A[i, 0]
```

```
        theta_A = reduced_array_A[i, 1]
        count_A = reduced_array_A[i, 2]

        for j in range(no_B):
            rad_B = reduced_array_B[j, 0]
            theta_B = reduced_array_B[j, 1]
            count_B = reduced_array_B[j, 2]

# if rad_A and rad_B:
            if 3:

                theta_rel = theta_B - theta_A
                if theta_rel > 2*np.pi:
                    theta_rel = theta_rel - 2*np.pi
                elif theta_rel < 0:
                    theta_rel = theta_rel + 2*np.pi

                x = int(round(rad_B*np.cos(theta_rel) + pixels/2))
                y = int(round(rad_B*np.sin(theta_rel) + pixels/2))

                if (0 < x < pixels) and (0 < y < pixels): # if hit is
                    ↪  within the image array
                    SiSj_array[y-1, x-1] += int(count_A*count_B)

    return(SiSj_array)


def two_fold_recoil_frame_covariance(df_A, df_B, shot_list, pixels,
    ↪ norm = False):

    n_shots = len(shot_list)

    # Sij = <xy>

    start_time = time.time()

    A_array = df_A[['r', 'theta', 'shot']].values
    B_array = df_B[['r', 'theta', 'shot']].values

    shot_array_A = np.unique(df_A.shot)
    shot_array_B = np.unique(df_B.shot)

    shot_array = np.intersect1d(shot_array_A, shot_array_B)
    shot_array = shot_array.astype('int64')
```

```
    if norm:
        mean_A = len(df_A)/n_shots
        Sij = recoil_frame_Sij_2(A_array, B_array, shot_array,
            ↪ pixels, mean_A)
        Sij /= float(n_shots)

    else:
        Sij = recoil_frame_Sij_1(A_array, B_array, shot_array,
            ↪ pixels)
        Sij = Sij.astype('float64')
        Sij /= float(n_shots)

    print("Calculating Sij took %s seconds" % round((time.time() -
        ↪ start_time), 1))

    # SiSj = <x><y>

    start_time = time.time()

    df_A_count_series = df_A.groupby(['r', 'theta']).size()
    df_A_count_df_SiSj = df_A_count_series.to_frame(name = 'size').
        ↪ reset_index()

    df_B_count_series = df_B.groupby(['r', 'theta']).size()
    df_B_count_df_SiSj = df_B_count_series.to_frame(name = 'size').
        ↪ reset_index()

    A_array_SiSj = df_A_count_df_SiSj[['r', 'theta', 'size']].values
    B_array_SiSj = df_B_count_df_SiSj[['r', 'theta', 'size']].values

    SiSj = recoil_frame_SiSj(A_array_SiSj, B_array_SiSj, pixels)
    SiSj = SiSj.astype('float64')
    SiSj /= n_shots**2

    print("Calculating SiSj took %s seconds" % round((time.time()-
        ↪ start_time),1))

    return(Sij, SiSj)
```

D

Newton-frame Covariance Code

The Python function below calculates Newton-frame covariance between two ions (A, the reference ion and B, the ion of interest). It returns the momentum distribution of B relative to A, and also calculates the momentum distribution of the remaining unaccounted-for mass of the molecule, C, through conservation of momentum. The function `cov_2fold_3D_Newton_plot` takes the following variables: `A_array` and `B_array` are numpy arrays containing the information for ion A and ion B, respectively; `shot_array` is an array containing unique shot identifiers; `n_SiSj` is the number of times the SiSj term is calculated (to be averaged); `bin_size` is how many atomic units each pixel of the covariance map corresponds to; `pixels` is the number of pixels to bin the image into. The function uses the `cov_2fold_term_3D_Newton_plot` function to calculate the Sij and SiSj terms. The latter is subtracted from the prior of these terms to calculate the covariance map. The code has been contributed to by F. Allum and J. W. McManus.

```
import numpy as np

@njit()
def cov_2fold_term_3D_Newton_plot(A_array, B_array, shot_array,
    ↪ shift_no, bin_size, pixels):

    term = np.zeros((pixels, pixels))
```

```
A_total = A_array.shape[0]
B_total = B_array.shape[0]

A_start, B_start = 0, 0
A_end, B_end = 0, 0

shot_array_2 = np.roll(shot_array, -shift_no)

prev_shot_2 = 0

for shot_1, shot_2 in zip(shot_array, shot_array_2):

    A_in_shot, B_in_shot = False, False

    # Find if A is in this shot
    for test in range(A_start, A_total):
        if A_array[test, 0] == shot_1:
            A_start = test
            A_in_shot = True
            break

    # Find end point of A in this shot
    if A_in_shot:
        for test in range(A_start, A_total):
            if A_array[test, 0] > shot_1:
                A_end = test
                break

        if prev_shot_2 > shot_2:
            B_start = 0
        prev_shot_2 = shot_2

        # Find if B is in this shot
        for test in range(B_start, B_total):
            if B_array[test, 0] == shot_2:
                B_start = test
                B_in_shot = True
                break

        # Find end point of B in this shot
        if B_in_shot:
            for test in range(B_start, B_total):
                if B_array[test, 0] > shot_2:
                    B_end = test
                    break
```

```
        if A_in_shot & B_in_shot:

            # For each A ion in this shot
            for i in range(A_start, A_end):
                A_x = A_array[i, 1]
                A_y = A_array[i, 2]
                A_z = A_array[i, 3]
                A_mag = A_array[i, 4]

                # For each B ion in this shot
                for j in range(B_start, B_end):
                    B_x = B_array[j, 1]
                    B_y = B_array[j, 2]
                    B_z = B_array[j, 3]
                    B_mag = B_array[j, 4]

                    C_x = -(A_x + B_x)
                    C_y = -(A_y + B_y)
                    C_z = -(A_z + B_z)
                    C_mag = np.sqrt(C_x**2 + C_y**2 + C_z**2)

                    # Prevents autovariance
                    if abs(A_mag - B_mag) < 0.1:
                        continue

                    cos_AB_theta_rel = (A_x*B_x + A_y*B_y + A_z*
                        ↪ B_z)/(A_mag*B_mag)
                    cos_AC_theta_rel = (A_x*C_x + A_y*C_y + A_z*
                        ↪ C_z)/(A_mag*C_mag)

                    Bproj_par = B_mag*cos_AB_theta_rel
                    Bproj_perp = B_mag*np.sqrt(1 -
                        ↪ cos_AB_theta_rel**2)
                    Cproj_par = C_mag*cos_AC_theta_rel
                    Cproj_perp = -C_mag*np.sqrt(1 -
                        ↪ cos_AC_theta_rel**2)
                    Aproj_par = A_mag
                    Aproj_perp = 0

                    Aproj_par = int(Aproj_par/bin_size + 0.5 +
                        ↪ pixels/2)
                    Bproj_par = int(Bproj_par/bin_size + 0.5 +
                        ↪ pixels/2)
                    Bproj_perp = int(Bproj_perp/bin_size + 0.5 +
```

```
                        ↪ pixels/2)
                    Cproj_par = int(Cproj_par/bin_size + 0.5 +
                        ↪ pixels/2)
                    Cproj_perp = int(Cproj_perp/bin_size + 0.5 +
                        ↪ pixels/2)

                    B_out = (Bproj_par, Bproj_perp)
                    C_out = (Cproj_par, Cproj_perp)

                    for x_out, y_out in [B_out, C_out]:
                        if 0 <= x_out < pixels:
                            if 0 <= y_out < pixels:
                                    term[x_out, y_out] += 1

    return(term)

def cov_2fold_3D_Newton_plot(A_array, B_array, shot_array, n_SiSj,
    ↪ bin_size, pixels):


    shot_array_A, shot_array_B = A_array[:, 0], B_array[:, 0]
    shot_array_Sij = np.intersect1d(shot_array_A, shot_array_B).
        ↪ astype('int32')
    shot_array_SiSj = np.unique(np.append(shot_array_A, shot_array_B
        ↪ )).astype('int32')
    ratio = len(shot_array)/len(shot_array_SiSj)

    Sij = cov_2fold_term_3D_Newton_plot(A_array, B_array,
        ↪ shot_array_Sij, 0, bin_size, pixels)

    SiSj_list = []
    for n in range(n_SiSj):

        shift_no = np.random.choice(np.arange(len(shot_array_SiSj)))
        SiSj = cov_2fold_term_3D_Newton_plot(A_array, B_array,
            ↪ shot_array_SiSj, shift_no, bin_size, pixels)
        SiSj_list.append(SiSj)

    SiSj = sum(SiSj_list)/(n_SiSj*ratio)

    cov = Sij - SiSj

    return(Sij, SiSj, cov)
```

E

Alternative Newton-frame Covariance Code

The Python function below calculates Newton-frame covariance between two ions (A, the reference ion and B, the ion of interest) and provides it in the alternative representation discussed in the main text. It returns the momentum distribution of B relative to A, and also calculates the momentum distribution of the remaining unaccounted-for mass of the molecule, C, through conservation of momentum. The function `calc_2fold_alt_Newton_plot` takes the following variables: `df_A` and `df_B` are dataframes containing the information for ion A and ion B, respectively; `bin_size` is how many atomic units each pixel of the covariance map corresponds to; `shot_list` is an array containing unique shot identifiers; `pixels` is the number of pixels to bin the image into; `n_SiSj` is the number of times the SiSj term is calculated (to be averaged); `n_SiSj_shots` is the number of laser shots to use in the SiSj calculation. The function uses the `calc_Sij_alt_Newton_plot` and `calc_SiSj_alt_Newton_plot` functions to calculate the Sij and SiSj terms, respectively. The latter is subtracted from the prior of these terms to calculate the covariance map. The code has been contributed to by F. Allum and J. W. McManus.

```
import numpy as np

from numba import jit
```

```
@jit(nopython = True)
def calc_SiSj_alt_Newton_plot(SiSj, reduced_frame_array_A,
    ↪ reduced_frame_array_B, bin_factor, pixels):

    hlf_pxl = int(pixels/2)

    no_A = reduced_frame_array_A.shape[0]
    no_B = reduced_frame_array_B.shape[0]

    for i in range(no_A):
        A_vec = np.ascontiguousarray(reduced_frame_array_A[i,:3])
        A_mag = reduced_frame_array_A[i, 4]

        for j in range(no_B):
            B_vec = np.ascontiguousarray(reduced_frame_array_B[j,:3])
            B_mag = reduced_frame_array_B[j, 4]

            if A_mag and B_mag:
                if np.dot(A_vec, B_vec) <= (A_mag*B_mag):

                    C_vec = -(A_vec + B_vec)

                    mol_plane_norm = np.cross(A_vec, B_vec/A_mag)
                    para_bisector = A_mag*B_vec + B_mag*A_vec
                    perp_bisector = np.cross(mol_plane_norm,
                        ↪ para_bisector)
                    para_bisector /= np.sqrt(para_bisector[0]**2 +
                        ↪ para_bisector[1]**2 + para_bisector[2]**2)
                    perp_bisector /= np.sqrt(perp_bisector[0]**2 +
                        ↪ perp_bisector[1]**2 + perp_bisector[2]**2)

                    A_para = np.dot(A_vec, para_bisector)
                    A_perp = np.dot(A_vec, perp_bisector)
                    B_para = np.dot(B_vec, para_bisector)
                    B_perp = np.dot(B_vec, perp_bisector)
                    C_para = np.dot(C_vec, para_bisector)
                    C_perp = np.dot(C_vec, perp_bisector)

                    A_para = int(A_para/bin_factor + hlf_pxl + 0.5)
                    A_perp = int(A_perp/bin_factor + hlf_pxl + 0.5)
                    B_para = int(B_para/bin_factor + hlf_pxl + 0.5)
                    B_perp = int(B_perp/bin_factor + hlf_pxl + 0.5)
                    C_para = int(C_para/bin_factor + hlf_pxl + 0.5)
                    C_perp = int(C_perp/bin_factor + hlf_pxl + 0.5)
```

```
                    if (A_para < pixels) and (A_perp < pixels) and (
                        ↪ B_para < pixels) and (B_perp < pixels) \
                    and (C_para < pixels) and (C_perp < pixels):
                        SiSj[A_para, A_perp] += 1
                        SiSj[B_para, B_perp] += 1
                        SiSj[C_para, C_perp] += 1

    return(SiSj)

@jit(nopython = True)
def calc_Sij_alt_Newton_plot(Sij, frame_array_A, frame_array_B,
    ↪ shot_array, bin_factor, pixels):

    hlf_pxl = int(pixels/2)

    no_A = frame_array_A.shape[0]
    no_B = frame_array_B.shape[0]

    nshotsA, nshotsB = 0, 0
    nendA, nendB = 0, 0

    for shot in shot_array:

        A_in_shot, B_in_shot = False, False

        for test in range(nshotsA, no_A):
            if (frame_array_A[test, 3] == shot):
                nshotsA = test
                A_in_shot = True
                break

        if A_in_shot:
            for test in range(nshotsA, no_A):
                if frame_array_A[test, 3] > shot:
                    nendA = test
                    break

            for test in range(nshotsB, no_B):
                if (frame_array_B[test, 3] == shot):
                    nshotsB = test
                    B_in_shot = True
                    break

        if B_in_shot:
```

```
            for test in range(nshotsB, no_B):
                if frame_array_B[test, 3] > shot:
                    nendB = test
                    break

        if A_in_shot & B_in_shot:
            for i in range(nshotsA, nendA):

                A_vec = np.ascontiguousarray(frame_array_A[i,:3])
                A_mag = frame_array_A[i, 4]

                # For each 'B' ion in this shot
                for j in range(nshotsB, nendB):
                    B_vec = np.ascontiguousarray(frame_array_B[j,:3])
                    B_mag = frame_array_B[j, 4]

                    if A_mag and B_mag:
                        if np.dot(A_vec, B_vec) <= (A_mag*B_mag):

                            C_vec = -(A_vec + B_vec)

                            mol_plane_norm = np.cross(A_vec, B_vec/
                                ↪ A_mag)
                            para_bisector = A_mag*B_vec + B_mag*A_vec
                            perp_bisector = np.cross(mol_plane_norm,
                                ↪ para_bisector)
                            para_bisector /= np.sqrt(para_bisector
                                ↪ [0]**2 + para_bisector[1]**2 +
                                ↪ para_bisector[2]**2)
                            perp_bisector /= np.sqrt(perp_bisector
                                ↪ [0]**2 + perp_bisector[1]**2 +
                                ↪ perp_bisector[2]**2)

                            A_para = np.dot(A_vec, para_bisector)
                            A_perp = np.dot(A_vec, perp_bisector)
                            B_para = np.dot(B_vec, para_bisector)
                            B_perp = np.dot(B_vec, perp_bisector)
                            C_para = np.dot(C_vec, para_bisector)
                            C_perp = np.dot(C_vec, perp_bisector)

                            A_para = int(A_para/bin_factor + hlf_pxl +
                                ↪  0.5)
                            A_perp = int(A_perp/bin_factor + hlf_pxl +
                                ↪  0.5)
                            B_para = int(B_para/bin_factor + hlf_pxl +
```

```
                            ↪ 0.5)
                        B_perp = int(B_perp/bin_factor + hlf_pxl +
                            ↪ 0.5)
                        C_para = int(C_para/bin_factor + hlf_pxl +
                            ↪ 0.5)
                        C_perp = int(C_perp/bin_factor + hlf_pxl +
                            ↪ 0.5)

                        if (A_para < pixels) and (A_perp < pixels)
                            ↪ and (B_para < pixels) and (B_perp <
                            ↪ pixels) \
                        and (C_para < pixels) and (C_perp < pixels)
                            ↪ :
                            Sij[A_para, A_perp] += 1
                            Sij[B_para, B_perp] += 1
                            Sij[C_para, C_perp] += 1

    return(Sij)

def calc_2fold_alt_Newton_plot(df_A, df_B, bin_size, shot_list,
    ↪ pixels, n_SiSj, n_SiSj_shots):

    start_time = time.time()

    n_shots = len(shot_list)
    A_arr = df_A[['px_AU', 'py_AU', 'pz_AU', 'tag_ID', 'pmag_AU']].
        ↪ values
    B_arr = df_B[['px_AU', 'py_AU', 'pz_AU', 'tag_ID', 'pmag_AU']].
        ↪ values

    # Sij = <xy>

    shot_array_A = np.unique(df_A.tag_ID)
    shot_array_B = np.unique(df_B.tag_ID)
    shot_array_comb = np.intersect1d(shot_array_A, shot_array_B)
    shot_array = shot_array_comb.astype('int64')

    Sij = np.zeros((pixels, pixels), dtype = np.float64)
    Sij = calc_Sij_alt_Newton_plot(Sij, A_arr, B_arr, shot_array,
        ↪ bin_size, pixels)
    Sij /= n_shots

    # SiSj = <x><y>

    SiSj_list = []
```

```
    for n in range(n_SiSj):

        SiSj_shot_list = np.random.choice(shot_list, n_SiSj_shots,
            ↪ replace = False)

        df_A_SiSj = df_A[df_A['tag_ID'].isin(SiSj_shot_list)]
        df_B_SiSj = df_B[df_B['tag_ID'].isin(SiSj_shot_list)]

        A_arr_SiSj = df_A_SiSj[['px_AU', 'py_AU', 'pz_AU', 'tag_ID',
            ↪  'pmag_AU']].values
        B_arr_SiSj = df_B_SiSj[['px_AU', 'py_AU', 'pz_AU', 'tag_ID',
            ↪  'pmag_AU']].values

        SiSj = np.zeros((pixels, pixels), dtype = np.float64)
        SiSj = calc_SiSj_alt_Newton_plot(SiSj, A_arr_SiSj,
            ↪ B_arr_SiSj, bin_size, pixels)
        SiSj = SiSj/(n_SiSj_shots**2)
        SiSj_list.append(SiSj)

    SiSj = sum(SiSj_list)/n_SiSj

    covar = Sij - SiSj

    print("2-fold covariance calculation took %s seconds" % round((
        ↪ time.time() - start_time),1))

    return((Sij, SiSj, covar))
```

F

Three-fold Newton-frame Covariance Code

The Python function below calculates three-fold Newton-frame covariance between three ions (A, the reference ion and B and C, the two ions of interest). It returns the momentum distribution of B and C relative to A. The function `cov_3fold_3D_Newton_plot` takes the following variables: `A_array`, `B_array`, and `C_array` are numpy arrays containing the information for ion A, ion B, and ion C, respectively; `shot_array` is an array containing unique shot identifiers; `n_SiSjSk` is the number of times the SijSk/SikSj/SjkSi/SiSjSk terms are calculated (to be averaged); `bin_size` is how many atomic units each pixel of the covariance map corresponds to; `pixels` is the number of pixels to bin the image into. The function also takes the variable `plim`, which is a momentum constraint applied that enforces that the momenta of all three ions must add to 0±`plim` in all three dimensions. This is only valid when the entire molecule is accounted for (i.e. the three ions used in the calculation constitute a three-body explosion). The function uses the `cov_3fold_term_3D_Newton_plot` function to calculate the individual terms of the calculation. The code has been contributed to by F. Allum and J. W. McManus.

```
import numpy as np

# Newton plot covariance function

@njit()
```

```
def cov_3fold_term_3D_Newton_plot(A_array, B_array, C_array,
    ↪ shot_array, shift_no_1, shift_no_2, bin_size, pixels,plim):

    term = np.zeros((pixels, pixels))

    A_total = A_array.shape[0]
    B_total = B_array.shape[0]
    C_total = C_array.shape[0]

    A_start, B_start, C_start = 0, 0, 0
    A_end, B_end, C_end = 0, 0, 0

    shot_array_2 = np.roll(shot_array, -shift_no_1)
    shot_array_3 = np.roll(shot_array, -shift_no_2)

    prev_shot_2 = 0
    prev_shot_3 = 0

    for shot_1, shot_2, shot_3 in zip(shot_array, shot_array_2,
        ↪ shot_array_3):

        A_in_shot, B_in_shot, C_in_shot = False, False, False

        # Find if A is in this shot
        for test in range(A_start, A_total):
            if A_array[test, 0] == shot_1:
                A_start = test
                A_in_shot = True
                break

        # Find end point of A in this shot
        if A_in_shot:
            for test in range(A_start, A_total):
                if A_array[test, 0] > shot_1:
                    A_end = test
                    break

            if prev_shot_2 > shot_2:
                B_start = 0
            prev_shot_2 = shot_2

            # Find if B is in this shot
            for test in range(B_start, B_total):
                if B_array[test, 0] == shot_2:
                    B_start = test
```

```
            B_in_shot = True
            break

    # Find end point of B in this shot
    if B_in_shot:
        for test in range(B_start, B_total):
            if B_array[test, 0] > shot_2:
                B_end = test
                break

        if prev_shot_3 > shot_3:
            C_start = 0
        prev_shot_3 = shot_3

        # Find if C is in this shot
        for test in range(C_start, C_total):
            if C_array[test, 0] == shot_3:
                C_start = test
                C_in_shot = True
                break

        # Find end point of C in this shot
        if C_in_shot:
            for test in range(C_start, C_total):
                if C_array[test, 0] > shot_3:
                    C_end = test
                    break

    if A_in_shot & B_in_shot & C_in_shot:

        # For each A ion in this shot
        for i in range(A_start, A_end):
            for j in range(B_start, B_end):
                for k in range(C_start, C_end):
                    A_x = A_array[i, 1]
                    B_x = B_array[j, 1]
                    C_x = C_array[k, 1]

                    if A_x + B_x + C_x <-plim:
                        continue
                    if A_x + B_x + C_x >plim:
                        continue

                    A_y = A_array[i, 2]
                    B_y = B_array[j, 2]
```

```
C_y = C_array[k, 2]

if A_y + B_y + C_y <-plim:
    continue
if A_y + B_y + C_y >plim:
    continue

A_z = A_array[i, 3]
B_z = B_array[j, 3]
C_z = C_array[k, 3]

if A_z + B_z + C_z <-plim:
    continue
if A_z + B_z + C_z >plim:
    continue

A_mag = A_array[i, 4]
B_mag = B_array[j, 4]
C_mag = C_array[k, 4]

# Prevents autovariance
if abs(A_mag - B_mag) < 0.1:
    continue


cos_AB_theta_rel = (A_x*B_x + A_y*B_y +
    ↪ A_z*B_z)/(A_mag*B_mag)

# Filter auto-covariance artefact from hit
    ↪  reconstruction
if cos_AB_theta_rel > 0.77:
    continue

cos_AC_theta_rel = (A_x*C_x + A_y*C_y +
    ↪ A_z*C_z)/(A_mag*C_mag)

Bproj_par = B_mag*cos_AB_theta_rel
Bproj_perp = B_mag*np.sqrt(1 -
    ↪ cos_AB_theta_rel**2)
Cproj_par = C_mag*cos_AC_theta_rel
Cproj_perp = -C_mag*np.sqrt(1 -
    ↪ cos_AC_theta_rel**2)
Aproj_par = A_mag
Aproj_perp = 0
```

```
                        Aproj_par = int(Aproj_par/bin_size + 0.5 +
                            ↪ pixels/2)
                        Bproj_par = int(Bproj_par/bin_size + 0.5 +
                            ↪ pixels/2)
                        Bproj_perp = int(Bproj_perp/bin_size + 0.5
                            ↪ + pixels/2)
                        Cproj_par = int(Cproj_par/bin_size + 0.5 +
                            ↪ pixels/2)
                        Cproj_perp = int(Cproj_perp/bin_size + 0.5
                            ↪ + pixels/2)

                        B_out = (Bproj_par, Bproj_perp)
                        C_out = (Cproj_par, Cproj_perp)

                        for x_out, y_out in [B_out, C_out]:
                            if 0 <= x_out < pixels:
                                if 0 <= y_out < pixels:
                                        term[x_out, y_out] += 1

    return(term)


def cov_3fold_3D_Newton_plot_timekeeping(A_array, B_array, C_array,
    ↪ shot_array, n_SiSjSk, bin_size, pixels,plim):

    start_time = time.time()

    shot_array_A, shot_array_B, shot_array_C = A_array[:, 0],
        ↪ B_array[:, 0], C_array[:, 0]
    shot_array_Sijk = np.intersect1d(np.intersect1d(shot_array_A,
        ↪ shot_array_B), shot_array_C).astype('int64')
    shot_array_SiSjSk = np.unique(np.append(np.append(shot_array_A,
        ↪ shot_array_B), shot_array_C)).astype('int64')
    ratio = len(shot_array)/len(shot_array_SiSjSk)

    Sijk = cov_3fold_term_3D_Newton_plot(A_array, B_array, C_array,
        ↪ shot_array_Sijk, 0, 0, bin_size, pixels)
    print('Calculated Sijk at %s seconds' % round(time.time() -
        ↪ start_time, 1))

    SijSk_list, SikSj_list, SjkSi_list, SiSjSk_list = [], [], [], []
    for n in range(n_SiSjSk):

        shift_no_1, shift_no_2 = np.random.choice(np.arange(len(
            ↪ shot_array_SiSjSk)), size = 2, replace = False)
```

```
        SijSk = cov_3fold_term_3D_Newton_plot(A_array, B_array,
            ↪ C_array, shot_array_SiSjSk, 0, shift_no_1, bin_size,
            ↪ pixels,plim)
        print('Calculated SijSk %s of %s at %s seconds' % (n + 1,
            ↪ n_SiSjSk, round(time.time() - start_time, 1)))
        SijSk_list.append(SijSk)
        SikSj = cov_3fold_term_3D_Newton_plot(A_array, B_array,
            ↪ C_array, shot_array_SiSjSk, shift_no_1, 0, bin_size,
            ↪ pixels,plim)
        print('Calculated SikSj %s of %s at %s seconds' % (n + 1,
            ↪ n_SiSjSk, round(time.time() - start_time, 1)))
        SikSj_list.append(SikSj)
        SjkSi = cov_3fold_term_3D_Newton_plot(A_array, B_array,
            ↪ C_array, shot_array_SiSjSk, shift_no_1, shift_no_1,
            ↪ bin_size, pixels,plim)
        print('Calculated SjkSi %s of %s at %s seconds' % (n + 1,
            ↪ n_SiSjSk, round(time.time() - start_time, 1)))
        SjkSi_list.append(SjkSi)
        SiSjSk = cov_3fold_term_3D_Newton_plot(A_array, B_array,
            ↪ C_array, shot_array_SiSjSk, shift_no_1, shift_no_2,
            ↪ bin_size, pixels,plim)
        print('Calculated SiSjSk %s of %s at %s seconds' % (n + 1,
            ↪ n_SiSjSk, round(time.time() - start_time, 1)))
        SiSjSk_list.append(SiSjSk)

    SijSk = sum(SijSk_list)/(n_SiSjSk*ratio)
    SikSj = sum(SikSj_list)/(n_SiSjSk*ratio)
    SjkSi = sum(SjkSi_list)/(n_SiSjSk*ratio)
    SiSjSk = sum(SiSjSk_list)/(n_SiSjSk*ratio*ratio)

    cov = Sijk - SijSk - SikSj - SjkSi + 2*SiSjSk

    return(Sijk, SijSk, SikSj, SjkSi, SiSjSk, cov)


def cov_3fold_3D_Newton_plot(A_array, B_array, C_array, shot_array,
    ↪ n_SiSjSk, bin_size, pixels,plim):

    shot_array_A, shot_array_B, shot_array_C = A_array[:, 0],
        ↪ B_array[:, 0], C_array[:, 0]
    shot_array_Sijk = np.intersect1d(np.intersect1d(shot_array_A,
        ↪ shot_array_B), shot_array_C).astype('int64')
    shot_array_SiSjSk = np.unique(np.append(np.append(shot_array_A,
        ↪ shot_array_B), shot_array_C)).astype('int64')
    ratio = len(shot_array)/len(shot_array_SiSjSk)
```

```
Sijk = cov_3fold_term_3D_Newton_plot(A_array, B_array, C_array,
    ↪ shot_array_Sijk, 0, 0, bin_size, pixels,plim)

SijSk_list, SikSj_list, SjkSi_list, SiSjSk_list = [], [], [], []
for n in range(n_SiSjSk):

    shift_no_1, shift_no_2 = np.random.choice(np.arange(len(
        ↪ shot_array_SiSjSk)), size = 2, replace = False)
    SijSk = cov_3fold_term_3D_Newton_plot(A_array, B_array,
        ↪ C_array, shot_array_SiSjSk, 0, shift_no_1, bin_size,
        ↪ pixels,plim)
    SijSk_list.append(SijSk)
    SikSj = cov_3fold_term_3D_Newton_plot(A_array, B_array,
        ↪ C_array, shot_array_SiSjSk, shift_no_1, 0, bin_size,
        ↪ pixels,plim)
    SikSj_list.append(SikSj)
    SjkSi = cov_3fold_term_3D_Newton_plot(A_array, B_array,
        ↪ C_array, shot_array_SiSjSk, shift_no_1, shift_no_1,
        ↪ bin_size, pixels,plim)
    SjkSi_list.append(SjkSi)
    SiSjSk = cov_3fold_term_3D_Newton_plot(A_array, B_array,
        ↪ C_array, shot_array_SiSjSk, shift_no_1, shift_no_2,
        ↪ bin_size, pixels,plim)
    SiSjSk_list.append(SiSjSk)

SijSk = sum(SijSk_list)/(n_SiSjSk*ratio)
SikSj = sum(SikSj_list)/(n_SiSjSk*ratio)
SjkSi = sum(SjkSi_list)/(n_SiSjSk*ratio)
SiSjSk = sum(SiSjSk_list)/(n_SiSjSk*ratio*ratio)

cov = Sijk - SijSk - SikSj - SjkSi + 2*SiSjSk

return(Sijk, SijSk, SikSj, SjkSi, SiSjSk, cov)
```

G

Native-frame Covariance Code

The Python function below is a variation of the Newton-frame covariance code, which calculates the covariance between two ions (A, the reference ion and B, the ion of interest) from the native-frame of an intermediate (BC). It returns the momentum distribution of B relative to A in the native-frame of BC, and also calculates the momentum distribution of the remaining unaccounted-for mass of the molecule, C, through conservation of momentum. The function `cov_2fold_3D_NF_plot` takes the following variables: `A_array` and `B_array` are numpy arrays containing the information for ion A and ion B, respectively; `B_mass` and `C_mass` are the masses (in atomic units) of fragments B and C; `shot_array` is an array containing unique shot identifiers; `n_SiSj` is the number of times the SiSj term is calculated (to be averaged); `bin_size` is how many atomic units each pixel of the covariance map corresponds to; `pixels` is the number of pixels to bin the image into. The function uses the `cov_2fold_term_3D_NF_plot` function to calculate the Sij and SiSj terms. The latter is subtracted from the prior of these terms to calculate the covariance map. The Newton-frame covariance code has been contributed to by F. Allum and J. W. McManus and adapted into the native-frame by J. W. McManus.

```
import numpy as np

@njit()
```

```
def cov_2fold_term_3D_NF_plot(A_array, B_array, B_mass, C_mass,
    ↪ shot_array, shift_no, bin_size, pixels,plim):

    term = np.zeros((pixels, pixels))

    A_total = A_array.shape[0]
    B_total = B_array.shape[0]

    BC_mass = B_mass+C_mass
    B_frac = B_mass/BC_mass
    C_frac = C_mass/BC_mass

    A_start, B_start = 0, 0
    A_end, B_end = 0, 0

    shot_array_2 = np.roll(shot_array, -shift_no)

    prev_shot_2 = 0

    for shot_1, shot_2 in zip(shot_array, shot_array_2):

        A_in_shot, B_in_shot = False, False

        # Find if A is in this shot
        for test in range(A_start, A_total):
            if A_array[test, 0] == shot_1:
                A_start = test
                A_in_shot = True
                break

        # Find end point of A in this shot
        if A_in_shot:
            for test in range(A_start, A_total):
                if A_array[test, 0] > shot_1:
                    A_end = test
                    break

            if prev_shot_2 > shot_2:
                B_start = 0
            prev_shot_2 = shot_2

            # Find if B is in this shot
            for test in range(B_start, B_total):
                if B_array[test, 0] == shot_2:
                    B_start = test
```

```
            B_in_shot = True
            break

    # Find end point of B in this shot
    if B_in_shot:
        for test in range(B_start, B_total):
            if B_array[test, 0] > shot_2:
                B_end = test
                break

    if A_in_shot & B_in_shot:

        # For each A ion in this shot
        for i in range(A_start, A_end):
            A_x = A_array[i, 1]
            A_y = A_array[i, 2]
            A_z = A_array[i, 3]
            A_vec = np.ascontiguousarray(A_array[i,1:4])
            A_mag = A_array[i, 4]

            BC_vec=-A_vec

            # For each B ion in this shot
            for j in range(B_start, B_end):
                B_x = B_array[j, 1]
                B_y = B_array[j, 2]
                B_z = B_array[j, 3]
                B_vec = np.ascontiguousarray(B_array[j,1:4])
                B_mag = B_array[j, 4]

                if A_mag and B_mag:
                    if np.dot(A_vec, B_vec) <= (A_mag*B_mag):

                        C_vec = -(A_vec + B_vec)

                        B_vec -= BC_vec * B_frac
                        B_mag = np.sqrt(B_vec[0]**2 + B_vec
                            ↪ [1]**2 + B_vec[2]**2)
                        C_vec -= BC_vec * C_frac
                        C_mag = np.sqrt(C_vec[0]**2 + C_vec
                            ↪ [1]**2 + C_vec[2]**2)


                        if abs((B_mag+C_mag)) < plim:
                            continue
```

```
                                theta_BC_B = np.arccos(np.dot(B_vec,
                                    ↪ BC_vec)/(B_mag*A_mag))
                                theta_BC_C = np.arccos(np.dot(C_vec,
                                    ↪ BC_vec)/(C_mag*A_mag))

                                Bx = int(B_mag*np.cos(theta_BC_B)/
                                    ↪ bin_size + hlf_pxl + 0.5)
                                By = int(B_mag*np.sin(theta_BC_B)/
                                    ↪ bin_size + hlf_pxl + 0.5)
                                Cx = int(C_mag*np.cos(-theta_BC_C)/
                                    ↪ bin_size + hlf_pxl + 0.5)
                                Cy = int(C_mag*np.sin(-theta_BC_C)/
                                    ↪ bin_size + hlf_pxl + 0.5)

                                if (0 < Bx < pixels) and (0 < By <
                                    ↪ pixels) and (0 < Cx < pixels) and
                                    ↪  (0 < Cy < pixels):
                                    term[Bx, -By] += 1
                                    term[Cx, -Cy] += 1

    return(term)

def cov_2fold_3D_NF_plot(A_array, B_array, B_mass, C_mass,
    ↪ shot_array, n_SiSj, bin_size, pixels,plim):


    shot_array_A, shot_array_B = A_array[:, 0], B_array[:, 0]
    shot_array_Sij = np.intersect1d(shot_array_A, shot_array_B).
        ↪ astype('int32')
    shot_array_SiSj = np.unique(np.append(shot_array_A, shot_array_B
        ↪ )).astype('int32')
    ratio = len(shot_array)/len(shot_array_SiSj)

    Sij = cov_2fold_term_3D_NF_plot(A_array, B_array, B_mass, C_mass,
        ↪  shot_array_Sij, 0, bin_size, pixels,plim)

    SiSj_list = []
    for n in range(n_SiSj):

        shift_no = np.random.choice(np.arange(len(shot_array_SiSj)))
        SiSj = cov_2fold_term_3D_NF_plot(A_array, B_array, B_mass,
            ↪ C_mass, shot_array_SiSj, shift_no, bin_size, pixels,
            ↪ plim)
        SiSj_list.append(SiSj)
```

```
    SiSj = sum(SiSj_list)/(n_SiSj*ratio)

    cov = Sij - SiSj

    return(Sij, SiSj, cov)
```

References

[1] G Kelfkens et al. *Ozone layer-climate change interactions Influence on UV levels and UV related effects*. NOP, 2002.

[2] Katie A Read, Anoop S Mahajan, Lucy J Carpenter, Mathew J Evans, Bruno V E Faria, Dwayne E Heard, James R Hopkins, James D Lee, Sarah J Moller, Alastair C Lewis, et al. "Extensive halogen-mediated ozone destruction over the tropical Atlantic Ocean". In: *Nature* 453.7199 (2008), pp. 1232–1235.

[3] R Von Glasow, R Von Kuhlmann, M G Lawrence, U Platt, and P J Crutzen. "Impact of reactive bromine chemistry in the troposphere". In: *Atmospheric Chemistry and Physics* 4.11/12 (2004), pp. 2481–2497.

[4] Maria A Navarro, Elliot L Atlas, Alfonso Saiz-Lopez, Xavier Rodriguez-Lloveras, Douglas E Kinnison, Jean-Francois Lamarque, Simone Tilmes, Michal Filus, Neil RP Harris, Elena Meneguz, et al. "Airborne measurements of organic bromine compounds in the Pacific tropical tropopause layer". In: *Proceedings of the National Academy of Sciences* 112.45 (2015), pp. 13789–13793.

[5] King-Chuen Lin and Po-Yu Tsai. "Molecular halogen elimination from halogen-containing compounds in the atmosphere". In: *Physical Chemistry Chemical Physics* 16.16 (2014), pp. 7184–7198.

[6] Thomas Gustavsson, Roberto Improta, and Dimitra Markovitsi. "DNA/RNA: building blocks of life under UV irradiation". In: *The Journal of Physical Chemistry Letters* 1.13 (2010), pp. 2025–2030.

[7] Benoıt Richard, Julia M Schäfer, Zoltan Jurek, Robin Santra, and Ludger Inhester. "Statistical analysis of correlations in the X-ray induced Coulomb explosion of iodopyridine". In: *Journal of Physics B: Atomic, Molecular and Optical Physics* 54.19 (2021), p. 194001.

[8] Stuart W Crane, Lingfeng Ge, Graham A Cooper, Ben P Carwithen, Matthew Bain, James A Smith, Christopher S Hansen, and Michael N R Ashfold. "Nonadiabatic Coupling Effects in the 800 nm Strong-Field Ionization-Induced Coulomb Explosion of Methyl Iodide Revealed by Multimass Velocity Map Imaging and Ab Initio Simulation Studies". In: *The Journal of Physical Chemistry A* 125.44 (2021), pp. 9594–9608.

[9] I V Hertel and W Radloff. "Ultrafast dynamics in isolated molecules and molecular clusters". In: *Reports on Progress in Physics* 69.6 (2006), p. 1897.

[10] Ahmed H Zewail. "Femtochemistry: Atomic-scale dynamics of the chemical bond". In: *The Journal of Physical Chemistry A* 104.24 (2000), pp. 5660–5694.

[11] J W G Mastenbroek, C A Taatjes, K Nauta, M H M Janssen, and S Stolte. "Two-dimensional imaging of the photolysis of oriented molecules". In: *The Journal of Physical Chemistry* 99.13 (1995), pp. 4360–4363.

[12] M E Corrales, J González-Vázquez, R de Nalda, and L Bañares. "Coulomb explosion imaging for the visualization of a conical intersection". In: *The Journal of Physical Chemistry Letters* 10.2 (2018), pp. 138–143.

[13] B Abel, H Hippler, N Lange, J Schuppe, and J Troe. "Competition between unimolecular C–Br–bond fission and Br_2 elimination in vibrationally highly excited CF_2Br_2". In: *The Journal of Chemical Physics* 101.11 (1994), pp. 9681–9690.

[14] Jakob Juul Larsen, Nils Jakob Mo/rkbak, Johannes Olesen, Nis Bjerre, Mette Machholm, So/ren Rud Keiding, and Henrik Stapelfeldt. "Femtosecond photodissociation dynamics of I_2 studied by ion imaging". In: *The Journal of Chemical Physics* 109.20 (1998), pp. 8857–8863.

[15] Farzaneh Ziaee, Kurtis Borne, Ruaridh Forbes, Yubaraj Malakar, Balram Kaderiya, Travis Severt, Itzik Ben-Itzhak, Artem Rudenko, Daniel Rolles, et al. "Single-and multi-photon-induced ultraviolet excitation and photodissociation of CH_3I probed by coincident ion momentum imaging". In: *Physical Chemistry Chemical Physics* 25.14 (2023), pp. 9999–10010.

[16] I A Bocharova, A S Alnaser, U Thumm, Th Niederhausen, D Ray, Charles L Cocke, and I V Litvinyuk. "Time-resolved Coulomb-explosion imaging of nuclear wave-packet dynamics induced in diatomic molecules by intense few-cycle laser pulses". In: *Physical Review A* 83.1 (2011), p. 013417.

[17] Ch Ellert, H Stapelfeldt, E Constant, H Sakai, J Wright, D M Rayner, and P B Corkum. "Observing molecular dynamics with timed Coulomb explosion imaging". In: *Philosophical Transactions of the Royal Society of London. Series A: Mathematical, Physical and Engineering Sciences* 356.1736 (1998), pp. 329–344.

[18] Th Ergler, A Rudenko, B Feuerstein, K Zrost, C D Schröter, R Moshammer, and J Ullrich. "Ultrafast mapping of H_2^+ (D_2^+) nuclear wave packets using time-resolved Coulomb explosion imaging". In: *Journal of Physics B: Atomic, Molecular and Optical Physics* 39.13 (2006), S493.

[19] Henrik Stapelfeldt, Eric Constant, Hirofumi Sakai, and Paul B Corkum. "Time-resolved Coulomb explosion imaging: A method to measure structure and dynamics of molecular nuclear wave packets". In: *Physical Review A* 58.1 (1998), p. 426.

[20] Felix Allum, Michael Burt, Kasra Amini, Rebecca Boll, Hansjochen Köckert, Pavel K Olshin, Sadia Bari, Cédric Bomme, Felix Braußе, Barbara Cunha de Miranda, et al. "Coulomb explosion imaging of CH_3I and CH_2ClI photodissociation dynamics". In: *The Journal of Chemical Physics* 149.20 (2018), p. 204313.

[21] Felix Allum, Nils Anders, Mark Brouard, Philip Bucksbaum, Michael Burt, Briony Downes-Ward, Sven Grundmann, James Harries, Yudai Ishimura, Hiroshi Iwayama, et al. "Multi-channel photodissociation and XUV-induced charge transfer dynamics in strong-field-ionized methyl iodide studied with time-resolved recoil-frame covariance imaging". In: *Faraday Discussions* 228 (2021), pp. 571–596. URL: http://dx.doi.org/10.1039/D0FD00115E.

[22] Ruaridh Forbes, Felix Allum, Sadia Bari, Rebecca Boll, Kurtis Borne, Mark Brouard, Philip H Bucksbaum, Nagitha Ekanayake, Benjamin Erk, Andrew J Howard, et al. "Time-resolved site-selective imaging of predissociation and charge transfer dynamics: the CH_3I B-band". In: *Journal of Physics B: Atomic, Molecular and Optical Physics* 53.22 (2020), p. 224001.

[23] Y Malakar, W L Pearson, M Zohrabi, B Kaderiya, F Ziaee, S Xue, A T Le, I Ben-Itzhak, D Rolles, A Rudenko, et al. "Time-resolved imaging of bound and dissociating nuclear wave packets in strong-field ionized iodomethane". In: *Physical Chemistry Chemical Physics* 21.26 (2019), pp. 14090–14102.

[24] Ya-Rong Lee, Cheng-Chu Chen, and Shen-Maw Lin. "Photodissociation of CH_2Br_2, 1,1- and 1,2-$C_2H_4Br_2$ at 248 nm: A simple C–Br bond fission versus a concerted three-body formation". In: *The Journal of Chemical Physics* 118.23 (2003), pp. 10494–10501.

[25] Marcos Dantus, Mark J Rosker, and Ahmed H Zewail. "Real-time femtosecond probing of "transition states" in chemical reactions". In: *The Journal of Chemical Physics* 87.4 (1987), pp. 2395–2397.

[26] Todd S Rose, Mark J Rosker, and Ahmed H Zewail. "Femtosecond real-time observation of wave packet oscillations (resonance) in dissociation reactions". In: *The Journal of Chemical Physics* 88.10 (1988), pp. 6672–6673.

[27] Richard N Zare and Paul J Dagdigian. "Tunable Laser Fluorescence Method for Product State Analysis: Laser-induced fluorescence is used as a detector of collisionally unrelaxed products of chemical reactions." In: *Science* 185.4153 (1974), pp. 739–747.

[28] Paul R Stannard and William M Gelbart. "Intramolecular vibrational energy redistribution". In: *The Journal of Physical Chemistry* 85.24 (1981), pp. 3592–3599.

[29] David J Nesbitt and Robert W Field. "Vibrational energy flow in highly excited molecules: Role of intramolecular vibrational redistribution". In: *The Journal of Physical Chemistry* 100.31 (1996), pp. 12735–12756.

[30] Johann from Neumann and Eugene P Wigner. "On the behavior of eigenvalues in adiabatic processes". In: *The Collected Works of Eugene Paul Wigner*. Springer, 1993, pp. 294–297.

[31] Friedrich Hund. "On the interpretation of molecular spectra. I". In: *Quantum Chemistry: Classic Scientific Papers*. World Scientific, 2000, pp. 214–234.

[32] D S N Parker, R S Minns, T J Penfold, G A Worth, and H H Fielding. "Ultrafast dynamics of the S1 excited state of benzene". In: *Chemical Physics Letters* 469.1-3 (2009), pp. 43–47.

[33] R S Minns, D S N Parker, T J Penfold, G A Worth, and H H Fielding. "Competing ultrafast intersystem crossing and internal conversion in the "channel 3" region of benzene". In: *Physical Chemistry Chemical Physics* 12.48 (2010), pp. 15607–15615.

[34] Rashid R Valiev, Victor N Cherepanov, Gleb V Baryshnikov, and Dage Sundholm. "First-principles method for calculating the rate constants of internal-conversion and intersystem-crossing transitions". In: *Physical Chemistry Chemical Physics* 20.9 (2018), pp. 6121–6133.

[35] Maria E Corrales, Vincent Loriot, Garikoitz Balerdi, Jesús González-Vázquez, Rebeca de Nalda, Luis Banares, and Ahmed H Zewail. "Structural dynamics effects on the ultrafast chemical bond cleavage of a photodissociation reaction". In: *Physical Chemistry Chemical Physics* 16.19 (2014), pp. 8812–8818.

[36] L J Frasinski, K Codling, P Hatherly, J Barr, I N Ross, and W T Toner. "Femtosecond dynamics of multielectron dissociative ionization by use of a picosecond laser". In: *Physical Review Letters* 58.23 (1987), p. 2424.

[37] C Cornaggia, J Lavancier, D Normand, J Morellec, P Agostini, J P Chambaret, and A Antonetti. "Multielectron dissociative ionization of diatomic molecules in an intense femtosecond laser field". In: *Physical Review A* 44.7 (1991), p. 4499.

[38] D T Strickland, Y Beaudoin, P Dietrich, and P B Corkum. "Optical studies of inertially confined molecular iodine ions". In: *Physical Review Letters* 68.18 (1992), p. 2755.

[39] J H Posthumus. "The dynamics of small molecules in intense laser fields". In: *Reports on Progress in Physics* 67.5 (2004), p. 623.

[40] Utuq Ablikim, Cédric Bomme, Hui Xiong, Evgeny Savelyev, Razib Obaid, Balram Kaderiya, Sven Augustin, Kirsten Schnorr, Ileana Dumitriu, Timur Osipov, et al. "Identification of absolute geometries of cis and trans molecular isomers by Coulomb Explosion Imaging". In: *Scientific Reports* 6.1 (2016), pp. 1–8.

[41] Utuq Ablikim, Cédric Bomme, Evgeny Savelyev, Hui Xiong, Rajesh Kushawaha, Rebecca Boll, Kasra Amini, Timur Osipov, David Kilcoyne, Artem Rudenko, et al. "Isomer-dependent fragmentation dynamics of inner-shell photoionized difluoroiodobenzene". In: *Physical Chemistry Chemical Physics* 19.21 (2017), pp. 13419–13431.

[42] Michael Burt, Kasra Amini, Jason W L Lee, Lars Christiansen, Rasmus R Johansen, Yuki Kobayashi, James D Pickering, Claire Vallance, Mark Brouard, and Henrik Stapelfeldt. "Communication: Gas-phase structural isomer identification by Coulomb explosion of aligned molecules". In: *The Journal of Chemical Physics* 148.9 (2018).

[43] Martin Pitzer, Maksim Kunitski, Allan S Johnson, Till Jahnke, Hendrik Sann, Felix Sturm, Lothar Ph H Schmidt, Horst Schmidt-Böcking, Reinhard Dörner, Jürgen Stohner, et al. "Direct determination of absolute molecular stereochemistry in gas phase by Coulomb explosion imaging". In: *Science* 341.6150 (2013), pp. 1096–1100.

[44] Philipp Herwig, Kerstin Zawatzky, Manfred Grieser, Oded Heber, Brandon Jordon-Thaden, Claude Krantz, Oldřich Novotnỳ, Roland Repnow, Volker Schurig, Dirk Schwalm, et al. "Imaging the absolute configuration of a chiral epoxide in the gas phase". In: *Science* 342.6162 (2013), pp. 1084–1086.

[45] Jakob Juul Larsen, Hirofumi Sakai, C P Safvan, Ida Wendt-Larsen, and Henrik Stapelfeldt. "Aligning molecules with intense nonresonant laser fields". In: *The Journal of chemical physics* 111.17 (1999), pp. 7774–7781.

[46] F Rosca-Pruna and MJJ Vrakking. "Experimental observation of revival structures in picosecond laser-induced alignment of I_2". In: *Physical Review Letters* 87.15 (2001), p. 153902.

[47] Edward Hamilton, Tamar Seideman, Tine Ejdrup, Mikael D Poulsen, Christer Z Bisgaard, Simon S Viftrup, and Henrik Stapelfeldt. "Alignment of symmetric top molecules by short laser pulses". In: *Physical Review A* 72.4 (2005), p. 043402.

[48] James D Pickering, Benjamin Shepperson, Lars Christiansen, and Henrik Stapelfeldt. "Alignment of the CS_2 dimer embedded in helium droplets induced by a circularly polarized laser pulse". In: *Physical Review A* 99.4 (2019), p. 043403.

[49] Dominik Pentlehner, Jens H Nielsen, Alkwin Slenczka, Klaus Mølmer, and Henrik Stapelfeldt. "Impulsive laser induced alignment of molecules dissolved in helium nanodroplets". In: *Physical review letters* 110.9 (2013), p. 093002.

[50] F Légaré, Kevin F Lee, I V Litvinyuk, P W Dooley, A D Bandrauk, D M Villeneuve, and P B Corkum. "Imaging the time-dependent structure of a molecule as it undergoes dynamics". In: *Physical Review A* 72.5 (2005), p. 052717.

[51] Michael Burt, Rebecca Boll, Jason W L Lee, Kasra Amini, Hansjochen Köckert, Claire Vallance, Alexander S Gentleman, Stuart R Mackenzie, Sadia Bari, Cédric Bomme, et al. "Coulomb-explosion imaging of concurrent CH_2BrI photodissociation dynamics". In: *Physical Review A* 96.4 (2017), p. 043415.

[52] K Amini, S Blake, M Brouard, M Burt, E Halford, A Lauer, C S Slater, J W L Lee, and C Vallance. "Three-dimensional imaging of carbonyl sulfide and ethyl iodide photodissociation using the pixel imaging mass spectrometry camera". In: *Review of Scientific Instruments* 86.10 (2015).

[53] T Walmsley, J Unwin, F Allum, S Bari, Rebecca Boll, K Borne, M Brouard, P Bucksbaum, N Ekanayake, B Erk, et al. "Characterizing the multi-dimensional reaction dynamics of dihalomethanes using XUV-induced Coulomb explosion imaging". In: *The Journal of Chemical Physics* 159.14 (2023).

[54] James Unwin, Felix Allum, Mathew Britton, Ian Gabalski, Hubertus Bromberger, Mark Brouard, Philip H Bucksbaum, Taran Driver, Nagitha Ekanayake, Diksha Garg, et al. "X-ray induced Coulomb explosion imaging of transient excited-state structural rearrangements in CS_2". In: *Communications Physics* 6.1 (2023), p. 309.

[55] Tomoyuki Endo, Simon P Neville, Vincent Wanie, Samuel Beaulieu, Chen Qu, Jude Deschamps, Philippe Lassonde, Bruno E Schmidt, Hikaru Fujise, Mizuho Fushitani, et al. "Capturing roaming molecular fragments in real time". In: *Science* 370.6520 (2020), pp. 1072–1077.

[56] Heide Ibrahim, Benji Wales, Samuel Beaulieu, Bruno E Schmidt, Nicolas Thiré, Emmanuel P Fowe, Éric Bisson, Christoph T Hebeisen, Vincent Wanie, Mathieu Giguére, et al. "Tabletop imaging of structural evolutions in chemical reactions demonstrated for the acetylene cation". In: *Nature communications* 5.1 (2014), p. 4422.

[57] Hansjochen Köckert, Jason W L Lee, Felix Allum, Kasra Amini, Sadia Bari, Cédric Bomme, Felix Braußе, Mark Brouard, Michael Burt, Barbara Cunha De Miranda, et al. "UV-induced dissociation of CH_2BrI probed by intense femtosecond XUV pulses". In: *J. Phys. B* 55.1 (2022), p. 014001.

[58] Jyoti Rajput, Herendra Kumar, Pragya Bhatt, and CP Safvan. "A new technique for measurement of subrotational lifetime of molecular ions". In: *Scientific Reports* 10.1 (2020), pp. 1–8.

[59] Jyoti Rajput, T Severt, Ben Berry, Bethany Jochim, Peyman Feizollah, Balram Kaderiya, M Zohrabi, U Ablikim, Farzaneh Ziaee, D Rolles, et al. "Native frames: Disentangling sequential from concerted three-body fragmentation". In: *Physical Review Letters* 120.10 (2018), p. 103001.

[60] Rebecca A Ingle, Christopher S Hansen, Emma Elsdon, Matthew Bain, Simon J King, Jason W L Lee, Mark Brouard, Claire Vallance, Renato Turchetta, and Michael N R Ashfold. "Ultraviolet photochemistry of 2-bromothiophene explored using universal ionization detection and multi-mass velocity-map imaging with a PImMS2 sensor". In: *The Journal of Chemical Physics* 147.1 (2017), p. 013914.

[61] Eero Itälä, Dang Trinh Ha, Kuno Kooser, Elisabeth Rachlew, Michael A Huels, and Edwin Kukk. "Fragmentation patterns of core-ionized thymine and 5-bromouracil". In: *The Journal of Chemical Physics* 133.15 (2010), 10B614.

[62] Heide Ibrahim, Catherine Lefebvre, André D Bandrauk, André Staudte, and François Légaré. "H_2: the benchmark molecule for ultrafast science and technologies". In: *Journal of Physics B: Atomic, Molecular and Optical Physics* 51.042002 (2018), 29pp.

[63] Simon Brennecke. "Electron Momentum Distributions from Strong-Field-Induced Ionization of Atoms and Molecules". PhD thesis. Hannover: Institutionelles Repositorium der Leibniz Universität Hannover, 2023.

[64] E Irani, R Sadighi-Bonabi, and A Anvari. "Investigation of intense femto-second laser ionization and dissociation of methane with time-dependent density-functional approach". In: *Chemical Physics Letters* 604 (2014), pp. 60–67.

[65] Zhifeng Wu, Chengyin Wu, Qingqing Liang, Sufan Wang, Min Liu, Yongkai Deng, and Qihuang Gong. "Fragmentation dynamics of methane by few-cycle femtosecond laser pulses". In: *The Journal of Chemical Physics* 126.7 (2007), p. 074311.

[66] Brian W J McNeil and Neil R Thompson. "X-ray free-electron lasers". In: *Nature photonics* 4.12 (2010), pp. 814–821.

[67] Evgeny Savelyev, Rebecca Boll, Cédric Bomme, Nora Schirmel, Harald Redlin, Benjamin Erk, Stefan Düsterer, Erland Müller, Hauke Höppner, Sven Toleikis, et al. "Jitter-correction for IR/UV-XUV pump-probe experiments at the FLASH free-electron laser". In: *New Journal of Physics* 19.4 (2017), p. 043009.

[68] Paul Emma, R Akre, J Arthur, R Bionta, C Bostedt, J Bozek, A Brachmann, P Bucksbaum, Ryan Coffee, F-J Decker, et al. "First lasing and operation of an ångstrom-wavelength free-electron laser". In: *nature photonics* 4.9 (2010), pp. 641–647.

[69] Katja Honkavaara, Bart Faatz, Josef Feldhaus, S Schreiber, Rolf Treusch, and M Vogt. "Status of the soft x-ray user facility FLASH". In: *Proceedings of FEL2015, Daejeon, Korea* (2015).

[70] Ichiro Inoue, Taito Osaka, Toru Hara, Takashi Tanaka, Takahiro Inagaki, Toru Fukui, Shunji Goto, Yuichi Inubushi, Hiroaki Kimura, Ryota Kinjo, et al. "Generation of narrow-band X-ray free-electron laser via reflection self-seeding". In: *Nature Photonics* 13.5 (2019), pp. 319–322.

[71] Ichiro Inoue, Yuichi Inubushi, Takahiro Sato, Kensuke Tono, Tetsuo Katayama, Takashi Kameshima, Kanade Ogawa, Tadashi Togashi, Shigeki Owada, Yoshiyuki Amemiya, et al. "Observation of femtosecond X-ray interactions with matter using an X-ray–X-ray pump–probe scheme". In: *Proceedings of the National Academy of Sciences* 113.6 (2016), pp. 1492–1497.

[72] Tsukasa Takanashi, Kosuke Nakamura, Edwin Kukk, Koji Motomura, Hironobu Fukuzawa, Kiyonobu Nagaya, Shin-Ichi Wada, Yoshiaki Kumagai, Denys Iablonskyi, Yuta Ito, et al. "Ultrafast Coulomb explosion of a diiodomethane molecule induced by an X-ray free-electron laser pulse". In: *Physical Chemistry Chemical Physics* 19.30 (2017), pp. 19707–19721.

[73] John W Cooper and Steven T Manson. "Photo-ionization in the soft X-ray range: angular distributions of photoelectrons and interpretation in terms of subshell structure". In: *Physical Review* 177.1 (1969), p. 157.

[74] Ludger Inhester, Bart Oostenrijk, Minna Patanen, Esko Kokkonen, Stephen H Southworth, Christoph Bostedt, Oksana Travnikova, Tatiana Marchenko, Sang-Kil Son, Robin Santra, et al. "Chemical understanding of the limited site-specificity in molecular inner-shell photofragmentation". In: *The Journal of Physical Chemistry Letters* 9.5 (2018), pp. 1156–1163.

[75] Ying-Chih Chiang, Selma Engin, Peng Bao, Frank Otto, Přemysl Kolorenč, Petra Votavová, Tsveta Miteva, Jiali Gao, and Nicolas Sisourat. "Molecular-bond breaking induced by interatomic decay processes". In: *Physical Review A* 100.5 (2019), p. 052701.

[76] V Morcelle, A Medina, L C Ribeiro, I Prazeres, R R T Marinho, M S Arruda, L A V Mendes, M J Santos, B N C Tenório, A B Rocha, et al. "Fragmentation of valence and carbon core excited and ionized CH_2FCF_3 molecule". In: *The Journal of Physical Chemistry A* 122.51 (2018), pp. 9755–9760.

[77] Bruno Nunes Cabral Tenorio, Ricardo R Oliveira, and Sonia Coriani. "Insights on the site-selective fragmentation of CF_2Cl_2 and CH_2Cl_2 at the chlorine K-edge from ab initio calculations". In: *Chemical Physics* 548 (2021), p. 111226.

[78] Yao-Te Wang, Yu-Ju Chiang, and Chen-Lin Liu. "Resolved specific dissociation channel of a core-excited peptide model molecule". In: *Chemical Physics Letters* 759 (2020), p. 137967.

[79] Helena Levola, Eero Itälä, Kim Schlesier, Kuno Kooser, Sanna Laine, Joakim Laksman, Dang Trinh Ha, Elisabeth Rachlew, Marta Tarkanovskaja, Katrin Tanzer, et al. "Ionization-site effects on the photofragmentation of chloro-and bromoacetic acid molecules". In: *Physical Review A* 92.6 (2015), p. 063409.

[80] Abdul Rahman Abid, Eetu Pelimanni, Maximilian Reinhardt, Nacer Boudjemia, Antti Kivimäki, Marko Huttula, Olle Björneholm, and Minna Patanen. "Electron–ion coincidence spectroscopy of a large organic molecule: photofragmentation of avobenzone after valence and core ionisation". In: *Journal of Physics B: Atomic, Molecular and Optical Physics* 53.24 (2020), p. 244001.

[81] Shin-ichi Nagaoka, Osamu Takahashi, and Yasumasa Hikosaka. "Site-specificity reduction during Auger decay following Si: 2p photoionization in $Cl_3SiSi(CH_3)_3$ vapor: An interatomic-Coulombic-decay-like process". In: *Chemical Physics* 534 (2020), p. 110756.

[82] Hiroshi Iwayama and James R Harries. "Resonant-Auger-state-selected dissociation dynamics and dissociation limits of N 1s$\rightarrow \pi^*$ core excited N_2 molecules studied using a two-dimensional Auger-electron-photoion coincidence method". In: *Journal of Electron Spectroscopy and Related Phenomena* 232 (2019), pp. 40–44.

[83] Shabnam Oghbaiee, Mathieu Gisselbrecht, Noelle Walsh, Bart Oostenrijk, Joakim Laksman, Erik P Månsson, Anna Sankari, John H D Eland, and Stacey L Sorensen. "Site-dependent nuclear dynamics in core-excited butadiene". In: *Physical Chemistry Chemical Physics* 24.47 (2022), pp. 28825–28830.

[84] Peter Salén, Luca Schio, Robert Richter, Michele Alagia, Stefano Stranges, Stefano Falcinelli, and Vitali Zhaunerchyk. "Electronic state influence on selective bond breaking of core-excited nitrosyl chloride (ClNO)". In: *The Journal of Chemical Physics* 157.12 (2022), p. 124306.

[85] W Eberhardt, T K Sham, R Carr, S Krummacher, M Strongin, S L Weng, and D Wesner. "Site-specific fragmentation of small molecules following soft-X-ray excitation". In: *Physical Review Letters* 50.14 (1983), p. 1038.

[86] J Laksman, K Kooser, H Levola, E Itala, D T Ha, Elisabeth Rachlew, and E Kukk. "Dissociation pathways in the cysteine dication after site-selective core ionization". In: *The Journal of Physical Chemistry B* 118.40 (2014), pp. 11688–11695.

[87] K Kooser, D T Ha, S Granroth, E Itälä, L Partanen, E Nõmmiste, H Aksela, and E Kukk. "Resonant Auger electron–photoion coincidence study of the fragmentation dynamics of an acrylonitrile molecule". In: *Journal of Physics B: Atomic, Molecular and Optical Physics* 43.23 (2010), p. 235103.

[88] A Picón, CS Lehmann, C Bostedt, Artem Rudenko, A Marinelli, T Osipov, Daniel Rolles, N Berrah, C Bomme, M Bucher, et al. "Hetero-site-specific X-ray pump-probe spectroscopy for femtosecond intramolecular dynamics". In: *Nature communications* 7.1 (2016), p. 11652.

[89] D Mathur and F A Rajgara. "Nonadiabatic response of molecules to strong fields of picosecond, femtosecond, and subfemtosecond duration: An experimental study of the methane dication". In: *The Journal of Chemical Physics* 124.19 (2006), p. 194308.

[90] James David Pickering. *Ultrafast Lasers and Optics for Experimentalists*. IOP Publishing, 2021.

[91] H R Reiss. "Limits on tunneling theories of strong-field ionization". In: *Physical Review Letters* 101.4 (2008), p. 043002.

[92] Misha Yu Ivanov, Michael Spanner, and Olga Smirnova. "Anatomy of strong field ionization". In: *Journal of Modern Optics* 52.2-3 (2005), pp. 165–184.

[93] N Boroumand, A Thorpe, A M Parks, and T Brabec. "Keldysh ionization theory of atoms: mathematical details". In: *Journal of Physics B: Atomic, Molecular and Optical Physics* 55.21 (2022), p. 213001.

[94] L V Keldysh et al. "Ionization in the field of a strong electromagnetic wave". In: *Sov. Phys. JETP* 20.5 (1965), pp. 1307–1314.

[95] Junliang Xu, Cosmin I Blaga, Pierre Agostini, and Louis F DiMauro. "Time-resolved molecular imaging". In: *Journal of Physics B: Atomic, Molecular and Optical Physics* 49.11 (2016), p. 112001.

[96] Kasra Amini, Jens Biegert, Francesca Calegari, Alexis Chacón, Marcelo F Ciappina, Alexandre Dauphin, Dmitry K Efimov, Carla Figueira de Morisson Faria, Krzysztof Giergiel, Piotr Gniewek, et al. "Symphony on strong field approximation". In: *Reports on Progress in Physics* 82.11 (2019), p. 116001.

[97] Michael Klaiber and John S Briggs. "Crossover from tunneling to multiphoton ionization of atoms". In: *Physical Review A* 94.5 (2016), p. 053405.

[98] Vincent Wanie, Heide Ibrahim, Samuel Beaulieu, Nicolas Thiré, Bruno E Schmidt, Yunpei Deng, Ali S Alnaser, Igor V Litvinyuk, Xiao-Min Tong, and François Légaré. "Coherent control of D_2/H_2 dissociative ionization by a mid-infrared two-color laser field". In: *Journal of Physics B: Atomic, Molecular and Optical Physics* 49.2 (2015), p. 025601.

[99] Tomoyuki Endo, Hikaru Fujise, Yuuna Kawachi, Ayaka Ishihara, Akitaka Matsuda, Mizuho Fushitani, Hirohiko Kono, and Akiyoshi Hishikawa. "Selective bond breaking of CO_2 in phase-locked two-color intense laser fields: laser field intensity dependence". In: *Physical Chemistry Chemical Physics* 19.5 (2017), pp. 3550–3556.

[100] Annick Giusti-Suzor, Frederic H Mies, Louis F DiMauro, Eric Charron, and Baorui Yang. "Dynamics of H_2^+ in intense laser fields". In: *Journal of Physics B: Atomic, Molecular and Optical Physics* 28.3 (1995), p. 309.

[101] Andrius Baltuška, Th Udem, M Uiberacker, M Hentschel, Eleftherios Goulielmakis, Ch Gohle, Ronald Holzwarth, V S Yakovlev, A Scrinzi, Th W Hänsch, et al. "Attosecond control of electronic processes by intense light fields". In: *Nature* 421.6923 (2003), pp. 611–615.

[102] Sufan Wang, Xiaoping Tang, Lirong Gao, Mohamed E Elshakre, and Fanao Kong. "Dissociation of methane in intense laser fields". In: *The Journal of Physical Chemistry A* 107.32 (2003), pp. 6123–6129.

[103] Jeffrey L Krause, Kenneth J Schafer, and Kenneth C Kulander. "High-order harmonic generation from atoms and ions in the high intensity regime". In: *Physical Review Letters* 68.24 (1992), p. 3535.

[104] David N Fittinghoff, Paul R Bolton, Britton Chang, and Kenneth C Kulander. "Observation of nonsequential double ionization of helium with optical tunneling". In: *Physical Review Letters* 69.18 (1992), p. 2642.

[105] Th Weber, Harald Giessen, Matthias Weckenbrock, Gunter Urbasch, Andre Staudte, Lutz Spielberger, Ottmar Jagutzki, Volker Mergel, Martin Vollmer, and Reinhard Dörner. "Correlated electron emission in multiphoton double ionization". In: *Nature* 405.6787 (2000), pp. 658–661.

[106] Manfred Lein, Eberhard K U Gross, and Volker Engel. "Intense-field double ionization of helium: identifying the mechanism". In: *Physical Review Letters* 85.22 (2000), p. 4707.

[107] Igor V Litvinyuk, Kevin F Lee, Patrick W Dooley, David M Rayner, David M Villeneuve, and Paul B Corkum. "Alignment-dependent strong field ionization of molecules". In: *Physical review letters* 90.23 (2003), p. 233003.

[108] Xiao-Min Tong, Z X Zhao, and Chii-Dong Lin. "Theory of molecular tunneling ionization". In: *Physical Review A* 66.3 (2002), p. 033402.

[109] Hiroka Hasegawa, Tiffany Walmsley, Akitaka Matsuda, Toru Morishita, Lars Bojer Madsen, Frank Jensen, Oleg I Tolstikhin, and Akiyoshi Hishikawa. "Asymmetric Dissociative Tunneling Ionization of Tetrafluoromethane in ω- 2ω Intense Laser Fields". In: *Frontiers in Chemistry* 10 (2022), p. 228.

[110] Sizuo Luo, Wenhui Hu, Jiaqi Yu, Xiaokai Li, Lanhai He, Chuncheng Wang, Fuchun Liu, and Dajun Ding. "Multielectron effects in the strong field sequential ionization of aligned CH3I molecules". In: *The Journal of Physical Chemistry A* 121.35 (2017), pp. 6547–6553.

[111] Tomoyuki Endo, Hikaru Fujise, Hiroka Hasegawa, Akitaka Matsuda, Mizuho Fushitani, Oleg I Tolstikhin, Toru Morishita, and Akiyoshi Hishikawa. "Angle dependence of dissociative tunneling ionization of NO in asymmetric two-color intense laser fields". In: *Physical Review A* 100.5 (2019), p. 053422.

[112] Akiyoshi Hishikawa, Akitaka Matsuda, and Mizuho Fushitani. "Ultrafast reaction imaging and control by ultrashort intense laser pulses". In: *Bulletin of the Chemical Society of Japan* 93.11 (2020), pp. 1293–1304.

[113] M Sharifi, F Kong, S L Chin, H Mineo, Y Dyakov, A M Mebel, S D Chao, M Hayashi, and S H Lin. "Experimental and theoretical investigation of high-power laser ionization and dissociation of methane". In: *The Journal of Physical Chemistry A* 111.38 (2007), pp. 9405–9416.

[114] Phil H Bucksbaum, Anton Zavriyev, Harm G Muller, and Douglass W Schumacher. "Softening of the H_2^+ molecular bond in intense laser fields". In: *Physical Review Letters* 64.16 (1990), p. 1883.

[115] Chengyin Wu, Haizhen Ren, Tingting Liu, Ri Ma, Hong Yang, Hongbing Jiang, and Qihuang Gong. "Laser-induced dissociation and explosion of methane and methanol". In: *Journal of Physics B: Atomic, Molecular and Optical Physics* 35.11 (2002), p. 2575.

[116] Sindhuja Sen and T Mondal. "The Jahn-Teller effect in the ground electronic state of the tetrafluoromethane cation before dissociation: a promoter of the anisotropic fragmentation". In: *Molecular Physics* 117.18 (2019), pp. 2487–2499.

[117] J M Garcıa de la Vega and E San Fabián. "Jahn-Teller effect and dissociation from the ground state of CF_4^+". In: *Chemical Physics* 151.3 (1991), pp. 335–342.

[118] M M Harb, S Cohen, E Papalazarou, F Lépine, and C Bordas. "Transfer-matrix-based method for an analytical description of velocity-map-imaging spectrometers". In: *Review of Scientific Instruments* 81.12 (2010).

[119] L J Frasinski, K Codling, and P A Hatherly. "Covariance mapping: A correlation method applied to multiphoton multiple ionization". In: *Science* 246.4933 (1989), pp. 1029–1031.

[120] Claire Vallance, David Heathcote, and Jason W L Lee. "Covariance-Map Imaging: A Powerful Tool for Chemical Dynamics Studies". In: *The Journal of Physical Chemistry A* 125.5 (2021), pp. 1117–1133.

[121] David J Manura and David A Dahl. "SIMION Version 8.0/8.1 User Manual". In: *Document Revision* 5 (2011).

[122] André T J B Eppink and David H Parker. "Velocity map imaging of ions and electrons using electrostatic lenses: Application in photoelectron and photofragment ion imaging of molecular oxygen". In: *Review of Scientific Instruments* 68.9 (1997), pp. 3477–3484.

[123] Tohru Kinugawa and Tatsuo Arikawa. "Three-dimensional velocity analysis combining ion imaging with Doppler spectroscopy: Application to photodissociation of HBr at 243 nm". In: *The Journal of Chemical Physics* 96.6 (1992), pp. 4801–4804.

[124] Felicia M Green, Maria Elena Castellani, Yifeng Jia, Anya Eyres, Natasha Smith, Steve Thompson, Paul Blenkinsopp, Michael Burt, Claire Vallance, Josephine Bunch, et al. "Development of High Throughput Microscope Mode Secondary Ion Mass Spectrometry Imaging". In: *Journal of the American Society for Mass Spectrometry* (2023).

[125] Claire Vallance, Mark Brouard, Alexandra Lauer, Craig S Slater, Edward Halford, Benjamin Winter, Simon J King, Jason W L Lee, Daniel E Pooley, Iain Sedgwick, et al. "Fast sensors for time-of-flight imaging applications". In: *Physical Chemistry Chemical Physics* 16.2 (2014), pp. 383–395.

[126] Craig S Slater, Sophie Blake, Mark Brouard, Alexandra Lauer, Claire Vallance, Jaya John John, Renato Turchetta, Andrei Nomerotski, Lauge Christensen, Jens H Nielsen, et al. "Covariance imaging experiments using a pixel-imaging mass-spectrometry camera". In: *Physical Review A* 89.1 (2014), p. 011401.

[127] Craig S Slater. *Studies of photoinduced molecular dynamics using a fast imaging sensor*. Springer, 2015.

[128] E Champenois. In: (2017). cPBASEX https://github.com/e-champenois/CPBASEX.

[129] Hironobu Fukuzawa, Kiyonobu Nagaya, and Kiyoshi Ueda. "Advances in instrumentation for gas-phase spectroscopy and diffraction with short-wavelength free electron lasers". In: *Nuclear Instruments and Methods in Physics Research Section A: Accelerators, Spectrometers, Detectors and Associated Equipment* 907 (2018), pp. 116–131.

[130] Vitali Zhaunerchyk, L J Frasinski, John H D Eland, and Raimund Feifel. "Theory and simulations of covariance mapping in multiple dimensions for data analysis in high-event-rate experiments". In: *Physical Review A* 89.5 (2014), p. 053418.

[131] Surjendu Bhattacharyya, Kurtis Borne, Farzaneh Ziaee, Shashank Pathak, Enliang Wang, Anbu Selvam Venkatachalam, Nathan Marshall, Kevin D Carnes, Charles W Fehrenbach, Travis Severt, et al. "Two-and three-body fragmentation of multiply charged tribromomethane by ultrafast laser pulses". In: *Physical Chemistry Chemical Physics* 24.45 (2022), pp. 27631–27644.

[132] J H D Eland. "The dynamics of three-body dissociations of dications studied by the triple coincidence technique PEPIPICO". In: *Molecular Physics* 61.3 (1987), pp. 725–745.

[133] Tiberiu Arion and Uwe Hergenhahn. "Coincidence spectroscopy: Past, present and perspectives". In: *Journal of Electron Spectroscopy and Related Phenomena* 200 (2015), pp. 222–231.

[134] Patrick A Robertson, David Heathcote, Dennis Milešević, and Claire Vallance. "Imaging the Dynamics of the Electron Ionization of C_2F_6". In: *The Journal of Physical Chemistry A* 126.40 (2022), pp. 7221–7229.

[135] Felix Allum, Valerija Music, Ludger Inhester, Rebecca Boll, Benjamin Erk, Philipp Schmidt, Thomas M Baumann, Günter Brenner, Michael Burt, Philipp V Demekhin, et al. "A localized view on molecular dissociation via electron-ion partial covariance". In: *Communications Chemistry* 5.1 (2022), pp. 1–10.

[136] David Heathcote and Claire Vallance. "Partial and Contingent Recoil-Frame Covariance-Map Imaging". In: *The Journal of Physical Chemistry A* 125.32 (2021), pp. 7092–7098.

[137] Leszek J Frasinski. "Covariance mapping techniques". In: *Journal of Physics B: Atomic, Molecular and Optical Physics* 49.15 (2016), p. 152004.

[138] J H D Eland, F S Wort, and R N Royds. "A photoelectron-ion-ion triple coincidence technique for the study of double photoionization and its consequences". In: *Journal of Electron Spectroscopy and Related Phenomena* 41.2 (1986), pp. 297–309.

[139] Louis Minion, Jason W L Lee, and Michael Burt. "Predicting Coulomb explosion fragment angular distributions using molecular ground-state vibrational motion". In: *Physical Chemistry Chemical Physics* 24.19 (2022), pp. 11636–11645.

[140] Shashank Pathak, Razib Obaid, Surjendu Bhattacharyya, Johannes Bürger, Xiang Li, Jan Tross, Travis Severt, Brandin Davis, René C Bilodeau, Carlos A Trallero-Herrero, et al. "Differentiating and Quantifying Gas-Phase Conformational Isomers Using Coulomb Explosion Imaging". In: *The Journal of Physical Chemistry Letters* 11.23 (2020), pp. 10205–10211.

[141] Jyoti Rajput, Diksha Garg, Amine Cassimi, X Fléchard, J Rangama, and C P Safvan. "Addressing three-body fragmentation of methane dication using "native frames": Evidence of internal excitation in fragments". In: *The Journal of Chemical Physics* 159.18 (2023).

[142] Veniamin A Borin, Sergey M Matveev, Darya S Budkina, Patrick Z El-Khoury, and Alexander N Tarnovsky. "Direct photoisomerization of CH_2I_2 vs. $CHBr_3$ in the gas phase: a joint 50 fs experimental and multireference resonance-theoretical study". In: *Physical Chemistry Chemical Physics* 18.41 (2016), pp. 28883–28892.

[143] Anuvab Mandal, Param Jeet Singh, Aparna Shastri, and B N Jagatap. "Electronic state spectroscopy of diiodomethane (CH_2I_2): Experimental and computational studies in the 30,000–95,000 cm^{-1} region". In: *The Journal of Chemical Physics* 140.19 (2014), p. 194312.

[144] Hongwei Chen, Rolf Brandt, Rolf Bandur, and Thorsten Hoffmann. "Characterization of iodine species in the marine aerosol: to understand their roles in particle formation processes". In: *Frontiers of Chemistry in China* 1 (2006), pp. 119–129.

[145] Scott A Reid. "When isomerisation is electron transfer: the intriguing story of the iso-halocarbons". In: *International Reviews in Physical Chemistry* 33.3 (2014), pp. 341–370.

[146] Sumitra Godara and Manikandan Paranjothy. "Competing Molecular and Radical Pathways in the Dissociation of Halons via Direct Chemical Dynamics Simulations". In: *The Journal of Physical Chemistry A* 123.40 (2019), pp. 8527–8535.

[147] Anna Rita Casavola, Antonella Cartoni, Mattea Carmen Castrovilli, Stefano Borocci, Paola Bolognesi, Jacopo Chiarinelli, Daniele Catone, and Lorenzo Avaldi. "VUV Photofragmentation of Chloroiodomethane: The Iso-CH_2I–Cl and Iso-CH_2Cl–I Radical Cation Formation". In: *The Journal of Physical Chemistry A* 124.37 (2020), pp. 7491–7499.

[148] Michael Odelius, Malin Kadi, Jan Davidsson, and Alexander N Tarnovsky. "Photodissociation of diiodomethane in acetonitrile solution and fragment recombination into iso-diiodomethane studied with ab initio molecular dynamics simulations". In: *The Journal of Chemical Physics* 121.5 (2004), pp. 2208–2214.

[149] Wai Ming Kwok, Chensheng Ma, Anthony W Parker, David Phillips, Michael Towrie, Pavel Matousek, and David Lee Phillips. "Picosecond time-resolved resonance Raman observation of the iso-CH_2I–I photoproduct from the "photoisomerization" reaction of diiodomethane in the solution phase". In: *The Journal of Chemical Physics* 113.17 (2000), pp. 7471–7478.

[150] John L Lyman, Brian E Newnam, James W Early, and A F G Van der Meer. "Infrared free-electron-laser photolysis of $CFCl_3$ and CF_2Cl_2". In: *The Journal of Physical Chemistry A* 101.1 (1997), pp. 49–54.

[151] Patricia K Quinn, Douglas B Collins, Vicki H Grassian, Kimberly A Prather, and Timothy S Bates. "Chemistry and related properties of freshly emitted sea spray aerosol". In: *Chemical Reviews* 115.10 (2015), pp. 4383–4399.

[152] Marıa E Corrales, Gregory Gitzinger, Jesús González-Vázquez, Vincent Loriot, Rebeca de Nalda, and Luis Banares. "Velocity map imaging and theoretical study of the Coulomb explosion of CH_3I under intense femtosecond IR pulses". In: *The Journal of Physical Chemistry A* 116.11 (2012), pp. 2669–2677.

[153] Yanmei Wang, Song Zhang, Zhengrong Wei, and Bing Zhang. "Velocity map imaging of dissociative ionization and Coulomb explosion of CH_3I induced by a femtosecond laser". In: *The Journal of Physical Chemistry A* 112.17 (2008), pp. 3846–3851.

[154] Koji Motomura, Edwin Kukk, Hironobu Fukuzawa, Shin-Ichi Wada, Kiyonobu Nagaya, Satoshi Ohmura, Subhendu Mondal, Tetsuya Tachibana, Yuta Ito, Ryosuke Koga, et al. "Charge and nuclear dynamics induced by deep inner-shell multiphoton ionization of CH_3I molecules by intense X-ray free-electron laser pulses". In: *The Journal of Physical Chemistry Letters* 6.15 (2015), pp. 2944–2949.

[155] Ken-Ichi Saitow, Yukito Naitoh, Keisuke Tominaga, and Keitaro Yoshihara. "Photo-induced reactions of CH_2I_2 in solution studied by the ultrafast transient absorption spectroscopy". In: *Chemical Physics Letters* 262.5 (1996), pp. 621–626.

[156] Jinzhong Zhang and Dan G Imre. "CH_2I_2 photodissociation: emission spectrum at 355 nm". In: *The Journal of Chemical Physics* 89.1 (1988), pp. 309–313.

[157] Steven L Baughcum and Stephen R Leone. "Photofragmentation infrared emission studies of vibrationally excited free radicals CH_3 and CH_2I". In: *The Journal of Chemical Physics* 72.12 (1980), pp. 6531–6545.

[158] Haifeng Xu, Ying Guo, Shilin Liu, Xingxiao Ma, Dongxu Dai, and Guohe Sha. "Photodissociation dynamics of CH_2I_2 molecules in the ultraviolet range studied by ion imaging". In: *The Journal of Chemical Physics* 117.12 (2002), pp. 5722–5729.

[159] M Kawasaki, S J Lee, and R Bersohn. "Photodissociation of molecular beams of methylene iodide and iodoform". In: *The Journal of Chemical Physics* 63.2 (1975), pp. 809–814.

[160] Hyoseok Kim, Young Choon Park, and Yoon Sup Lee. "Spin-orbit Effects on the Structure of Haloiodomethane Cations CH_2XI^+ (X=F, Cl, Br, and I)". In: *Bulletin of the Korean Chemical Society* 35.3 (Mar. 2014), pp. 775–782.

[161] L. J. Butler, E. J. Hintsa, S. F. Shane, and Y. T. Lee. "The electronic state-selective photodissociation of CH_2BrI at 248, 210, and 193 nm". In: *The Journal of Chemical Physics* 86.4 (1987), pp. 2051–2074.

[162] Benjamin W Toulson, Jonathan P Alaniz, J Grant Hill, and Craig Murray. "Near-UV photodissociation dynamics of CH_2I_2". In: *Physical Chemistry Chemical Physics* 18.16 (2016), pp. 11091–11103.

[163] Shun-Yi Chen, Po-Yu Tsai, Hsiang- Chin Lin, Chia-Ching Wu, King-Chuen Lin, B J Sun, and A H H Chang. "I_2 molecular elimination in single-photon dissociation of CH_2I_2 at 248 nm by using cavity ring-down absorption spectroscopy". In: *The Journal of Chemical Physics* 134.3 (2011), p. 034315.

[164] Hironobu Fukuzawa, Tsukasa Takanashi, Edwin Kukk, Koji Motomura, Shin-Ichi Wada, Kiyonobu Nagaya, Yuta Ito, Toshiyuki Nishiyama, Christophe Nicolas, Yoshiaki Kumagai, et al. "Real-time observation of X-ray-induced intramolecular and interatomic electronic decay in CH_2I_2". In: *Nature Communications* 10.1 (2019), pp. 1–8.

[165] Edwin Kukk, Koji Motomura, Hironobu Fukuzawa, Kiyonobu Nagaya, and Kiyoshi Ueda. "Molecular dynamics of XFEL-induced photo-dissociation, revealed by ion-ion coincidence measurements". In: *Applied Sciences* 7.5 (2017), p. 531.

[166] Hironobu Fukuzawa and Kiyoshi Ueda. "X-ray induced ultrafast dynamics in atoms, molecules, and clusters: experimental studies at an X-ray free-electron laser facility SACLA and modelling". In: *Advances in Physics: X* 5.1 (2020), p. 1785327.

[167] Terry N Olney, Glyn Cooper, and C E Brion. "Quantitative studies of the photoabsorption (4.5–488 eV) and photoionization (9–59.5 eV) of methyl iodide using dipole electron impact techniques". In: *Chemical Physics* 232.1-2 (1998), pp. 211–237.

[168] Norio Saito and Isao H Suzuki. "Multiple photoionization in Ne, Ar, Kr and Xe from 44 to 1300 eV". In: *International Journal of Mass Spectrometry and Ion Processes* 115.2-3 (1992), pp. 157–172.

[169] Kasra Amini, Evgeny Savelyev, Felix Braußе, Nora Berrah, Cédric Bomme, Mark Brouard, Michael Burt, Lauge Christensen, Stefan Düsterer, Benjamin Erk, et al. "Photodissociation of aligned CH_3I and $C_6H_3F_2I$ molecules probed with time-resolved Coulomb explosion imaging by site-selective extreme ultraviolet ionization". In: *Structural Dynamics* 5.1 (2018), p. 014301.

[170] J J Yeh and I Lindau. "Atomic subshell photoionization cross sections and asymmetry parameters: 1 Z 103". In: *At. Data Nucl. Data Tables* 32.1 (1985), pp. 1–155.

[171] Rebecca Boll, Benjamin Erk, Ryan Coffee, Sebastian Trippel, Thomas Kierspel, Cédric Bomme, John D Bozek, Mitchell Burkett, Sebastian Carron, Ken R Ferguson, et al. "Charge transfer in dissociating iodomethane and fluoromethane molecules ionized by intense femtosecond X-ray pulses". In: *Structural Dynamics* 3.4 (2016), p. 043207.

[172] Benjamin Erk, Rebecca Boll, Sebastian Trippel, Denis Anielski, Lutz Foucar, Benedikt Rudek, Sascha W Epp, Ryan Coffee, Sebastian Carron, Sebastian Schorb, et al. "Imaging charge transfer in iodomethane upon x-ray photoabsorption". In: *Science* 345.6194 (2014), pp. 288–291.

[173] Lothar Strüder, Sascha Epp, Daniel Rolles, Robert Hartmann, Peter Holl, Gerhard Lutz, Heike Soltau, Rouven Eckart, Christian Reich, Klaus Heinzinger, et al. "Large-format, high-speed, X-ray pnCCDs combined with electron and ion imaging spectrometers in a multipurpose chamber for experiments at 4th generation light sources". In: *Nuclear Instruments and Methods in Physics Research Section A: Accelerators, Spectrometers, Detectors and Associated Equipment* 614.3 (2010), pp. 483–496.

[174] Benjamin Erk, Jan P Müller, Cédric Bomme, Rebecca Boll, Günter Brenner, Henry N Chapman, Jonathan Correa, Stefan Düsterer, Siarhei Dziarzhytski, Stefan Eisebitt, et al. "CAMP@FLASH: an end-station for imaging, electron-and ion-spectroscopy, and pump–probe experiments at the FLASH free-electron laser". In: *Journal of Synchrotron Radiation* 25.5 (2018), pp. 1529–1540.

[175] Federico Canova and Luca Poletto. *Optical Technologies for Extreme-Ultraviolet and Soft X-ray Coherent Sources*. Springer, 2015.

[176] Stefan Düsterer et al. "Development of experimental techniques for the characterization of ultrashort photon pulses of extreme ultraviolet free-electron lasers". In: *Phys. Rev. ST Accel. Beams* 17.12 (2014), p. 120702.

[177] Pauli Virtanen et al. "SciPy 1.0: Fundamental Algorithms for Scientific Computing in Python". In: *Nature Methods* 17 (2020), pp. 261–272.

[178] Farzaneh Ziaee. "Imaging Nuclear Motion during the Photofragmentation of Halomethane Molecules Triggered by Ultraviolet Light". PhD thesis. Kansas State University, 2022.

[179] Yusong Liu, Tamás Rozgonyi, Philipp Marquetand, and Thomas Weinacht. "Excited-state dynamics of CH_2I_2 and CH_2IBr studied with UV-pump VUV-probe momentum-resolved photoion spectroscopy". In: *The Journal of Chemical Physics* 153.18 (2020), pp. 4304–4315.

[180] Spencer L Horton, Yusong Liu, Ruaridh Forbes, Varun Makhija, Rune Lausten, Albert Stolow, Paul Hockett, Philipp Marquetand, Tamás Rozgonyi, and Thomas Weinacht. "Excited state dynamics of CH_2I_2 and CH_2BrI studied with UV pump VUV probe photoelectron spectroscopy". In: *The Journal of Chemical Physics* 150.17 (2019), pp. 4201–4211.

[181] S D Price, J H D Eland, P G Fournier, J Fournier, and Ph Millié. "Electronic states and decay mechanisms of the N_2O^{2+} dication". In: *The Journal of Chemical Physics* 88.3 (1988), pp. 1511–1515.

[182] M Hochlaf and J H D Eland. "A theoretical and experimental study of the SO_2^{2+} dication". In: *The Journal of Chemical Physics* 120.14 (2004), pp. 6449–6460.

[183] Shizuka Hsieh and John H D Eland. "Secondary Dissociation Reactions of $C_2H_2N^+$ and CHN_2^+ Ions in the Charge Separation Mass Spectra of Five-membered Nitrogen Heterocycles". In: *Journal of Mass Spectrometry* 31.9 (1996), pp. 1054–1060.

[184] Marius Gerlach, Felipe Fantuzzi, Lilith Wohlfart, Karina Kopp, Bernd Engels, John Bozek, Christophe Nicolas, Dennis Mayer, Markus Gühr, Fabian Holzmeier, et al. "Fragmentation of isocyanic acid, HNCO, following core excitation and ionization". In: *The Journal of Chemical Physics* 154.11 (2021), p. 114302.

[185] Shigeki Owada, Mizuho Fushitani, Akitaka Matsuda, Hikaru Fujise, Yuuma Sasaki, Yasumasa Hikosaka, Akiyoshi Hishikawa, and Makina Yabashi. "Characterization of soft X-ray FEL pulse duration with two-color photoelectron spectroscopy". In: *Journal of Synchrotron Radiation* 27.5 (2020), pp. 1362–1365.

[186] Laurent Nahon, Agneta Svensson, and Paul Morin. "Experimental study of the 4d ionization continuum in atomic iodine by photoelectron and photoion spectroscopy". In: *Physical Review A* 43.5 (1991), p. 2328.

[187] Shigeki Owada, Kazuaki Togawa, Takahiro Inagaki, Toru Hara, Takashi Tanaka, Yasumasa Joti, Takahisa Koyama, Kyo Nakajima, Haruhiko Ohashi, Yasunori Senba, et al. "A soft X-ray free-electron laser beamline at SACLA: the light source, photon beamline and experimental station". In: *Journal of Synchrotron Radiation* 25.1 (2018), pp. 282–288.

[188] J J Yeh. *Atomic Calculation of Photoionization Cross-sections and Asymmetry Parameters*. Gordon & Breach Science Publishers, 1993. URL: https://books.google.co.uk/books?id=%5C_aK1kQEACAAJ.

[189] Kolbjørn Hagen, Reidar Stølevik, and Per Christian Sæbø. "Molecular structure and conformational composition of 1-iodopropane as determined from gas-phase electron diffraction, microwave spectroscopy data and ab initio calculations". In: *Journal of molecular structure* 346 (1995), pp. 75–82.

[190] Chikako Ikeda, Toshihiro Inagusa, and Michiro Hayashi. "Microwave spectrum, structure, and nuclear quadrupole coupling constant tensor of isopropyl bromide and iodide". In: *Journal of Molecular Spectroscopy* 135.2 (1989), pp. 334–348.

[191] Yu-Ran Luo and J Alistair Kerr. "Bond dissociation energies". In: *CRC handbook of chemistry and physics* 89 (2012), p. 89.

[192] S Leach, J H D Eland, and S D Price. "Formation and dissociation of dications of naphthalene-d8". In: *The Journal of Physical Chemistry* 93.22 (1989), pp. 7583–7593.

[193] P J Richardson, J H D Eland, and P Lablanquie. "Charge separation reactions of doubly charged benzene ions". In: *Organic mass spectrometry* 21.5 (1986), pp. 289–294.

[194] Sandra D Wiersma, Alessandra Candian, Joost M Bakker, Giel Berden, John R Eyler, Jos Oomens, Alexander GGM Tielens, and Annemieke Petrignani. "IR photofragmentation of the phenyl cation: spectroscopy and fragmentation pathways". In: *Physical Chemistry Chemical Physics* 23.7 (2021), pp. 4334–4343.

[195] C Joblin and A G G M Tielens. "25 years of PAH hypothesis". In: *European Astronomical Society Publications Series* 46 (2011), pp. 3–10.

[196] Pascale Ehrenfreund and Mark A Sephton. "Carbon molecules in space: from astrochemistry to astrobiology". In: *Faraday discussions* 133 (2006), pp. 277–288.

[197] Eric Herbst and Ewine F Van Dishoeck. "Complex organic interstellar molecules". In: *Annual Review of Astronomy and Astrophysics* 47 (2009), pp. 427–480.

[198] Alexander G G M Tielens. "Interstellar polycyclic aromatic hydrocarbon molecules". In: *Annu. Rev. Astron. Astrophys.* 46 (2008), pp. 289–337.

[199] L J Allamandola, A G G M Tielens, and J R Barker. "Interstellar polycyclic aromatic hydrocarbons-The infrared emission bands, the excitation/emission mechanism, and the astrophysical implications". In: *Astrophysical Journal Supplement Series (ISSN 0067-0049), vol. 71, Dec. 1989, p. 733-775. Research supported by NASA, DOE, and NSF.* 71 (1989), pp. 733–775.

[200] M C E Galbraith, S Scheit, N V Golubev, G Reitsma, N Zhavoronkov, V Despré, Franck Lepine, A I Kuleff, M J J Vrakking, O Kornilov, et al. "Few-femtosecond passage of conical intersections in the benzene cation". In: *Nature communications* 8.1 (2017), p. 1018.

[201] Alexandre Marciniak, V Despré, Thomas Barillot, A Rouzée, M C E Galbraith, J Klei, C-H Yang, C T L Smeenk, V Loriot, S Nagaprasad Reddy, et al. "XUV excitation followed by ultrafast non-adiabatic relaxation in PAH molecules as a femto-astrochemistry experiment". In: *Nature Communications* 6.1 (2015), p. 7909.

[202] A Boyer, M Hervé, V Despré, P Castellanos Nash, V Loriot, A Marciniak, AGGM Tielens, AI Kuleff, and F Lépine. "Ultrafast vibrational relaxation dynamics in XUV-excited polycyclic aromatic hydrocarbon molecules". In: *Physical Review X* 11.4 (2021), p. 041012.

[203] Bruno Nunes Cabral Tenorio, Jacob Pedersen, Mario Barbatti, Piero Decleva, and Sonia Coriani. "Auger–Meitner and X-ray Absorption Spectra of Ethylene Cation: Insight into Conical Intersection Dynamics". In: *The Journal of Physical Chemistry A* 128.1 (2023), pp. 107–117.

[204] Junfeng Zhen, Sarah Rodriguez Castillo, Christine Joblin, Giacomo Mulas, Hassan Sabbah, Alexandre Giuliani, Laurent Nahon, Serge Martin, Jean-Philippe Champeaux, and Paul M Mayer. "VUV photo-processing of PAH cations: quantitative study on the ionization versus fragmentation processes". In: *The Astrophysical Journal* 822.2 (2016), p. 113.

[205] Chandan Bagdia, Shubhadeep Biswas, Anuvab Mandal, Shamik Bhattacharjee, and Lokesh C Tribedi. "Ionization and fragmentation of fluorene upon 250 keV proton impact". In: *The European Physical Journal D* 75 (2021), pp. 1–7.

[206] G Reitsma, L Boschman, M J Deuzeman, S Hoekstra, R Hoekstra, and T Schlathölter. "Near edge X-ray absorption mass spectrometry on coronene". In: *The Journal of Chemical Physics* 142.2 (2015).

[207] J-P Champeaux, Patrick Moretto-Capelle, Pierre Cafarelli, Charlotte Deville, Martine Sence, and Romain Casta. "Is the dissociation of coronene in stellar winds a source of molecular hydrogen? application to the HD 44179 nebula". In: *Monthly Notices of the Royal Astronomical Society* 441.2 (2014), pp. 1479–1487.

[208] Diksha Garg, J W L Lee, DS Tikhonov, P Chopra, A L Steber, A K Lemmens, B Erk, F Allum, R Boll, X Cheng, et al. "Fragmentation dynamics of fluorene explored using ultrafast XUV-Vis pump-probe spectroscopy". In: *Frontiers in Physics* 10 (2022), p. 880793.

[209] Jason Wai Lung Lee, D S Tikhonov, P Chopra, S Maclot, A L Steber, S Gruet, F Allum, Rebecca Boll, X Cheng, S Düsterer, et al. "Time-resolved relaxation and fragmentation of polycyclic aromatic hydrocarbons investigated in the ultrafast XUV-IR regime". In: *Nature Communications* 12.1 (2021), p. 6107.

[210] Smriti Anand and H Bernhard Schlegel. "Dissociation of benzene dication $[C_6H_6]^{2+}$: exploring the potential energy surface". In: *The Journal of Physical Chemistry A* 109.50 (2005), pp. 11551–11559.

[211] Sophia Bazzi, Ralph Welsch, Oriol Vendrell, and Robin Santra. "Challenges in XUV photochemistry simulations: A case study on ultrafast fragmentation dynamics of the benzene radical cation". In: *The Journal of Physical Chemistry A* 122.4 (2018), pp. 1004–1010.

[212] Mutsumi Tasaka, Michihiko Ogata, and Hiroshi Ichikawa. "A MINDO/3 theoretical study on structure, fragmentation, and scrambling reaction in the phenyl cation". In: *Journal of the American Chemical Society* 103.8 (1981), pp. 1885–1891.

[213] Karsten Krogh-Jespersen. "Ab initio electronic structure calculations on the benzene dication and other $C_6H_6{}^{2+}$ isomers". In: *Journal of the American Chemical Society* 113.2 (1991), pp. 417–423.

[214] Ruaridh Forbes, Alberto De Fanis, Daniel Rolles, Stephen T Pratt, Ivan Powis, Nicholas A Besley, Aleksandar R Milosavljević, Christophe Nicolas, John D Bozek, and David M P Holland. "Photoionization of the I 4d and valence orbitals of methyl iodide". In: *J. Phys. B* 53.15 (2020), p. 155101.

[215] Terry N Olney, Glyn Cooper, Wing Fat Chan, Gordon R Burton, C E Brion, and K H Tan. "Absolute photoabsorption and photoionization studies of methyl bromide using dipole electron impact and synchrotron radiation PES techniques". In: *Chemical Physics* 218.1-2 (1997), pp. 127–149.

[216] Yu-Chen Cheng, Bart Oostenrijk, Jan Lahl, Sylvain Maclot, Sven Augustin, Georg Schmid, Kirsten Schnorr, Severin Meister, Dimitrios Rompotis, Bastian Manschwetus, et al. "Imaging multiphoton ionization dynamics of CH_3I at a high repetition rate XUV free-electron laser". In: *Journal of Physics B: Atomic, Molecular and Optical Physics* 54.1 (2020), p. 014001.

[217] Howard A J and Cheng C and Forbes R and McCracken G A and Mills W H and Makhija V and Spanner M and Weinacht T and Bucksbaum P H. "Strong-field ionization of water: Nuclear dynamics revealed by varying the pulse duration". In: *Physical Review A* 103.4 (2021), p. 043120.

[218] Thomas K Kjeldsen and Lars Bojer Madsen. "Vibrational excitation of diatomic molecular ions in strong field ionization of diatomic molecules". In: *Physical review letters* 95.7 (2005), p. 073004.

[219] Liang Xu, Qi Lu, Vladimir T Tikhonchuk, Bin Zhou, Runzhe Yang, Qingqing Liang, Feng He, Rostyslav Danylo, Aurélien Houard, André Mysyrowicz, et al. "Quantum and quasi-classical effects in the strong field ionization and subsequent excitation of nitrogen molecules". In: *Optics Express* 30.21 (2022), pp. 38481–38491.

[220] Timothy D Scarborough, James Strohaber, David B Foote, Collin J McAcy, and Cornelis J G J Uiterwaal. "Ultrafast REMPI in benzene and the monohalobenzenes without the focal volume effect". In: *Physical Chemistry Chemical Physics* 13.30 (2011), pp. 13783–13790.

[221] Jan H Jensen and Jimmy C Kromann. *The molecule calculator: a web application for fast quantum mechanics-based estimation of molecular properties.* 2013.

[222] Leszek J Frasinski. "Cumulant mapping as the basis of multi-dimensional spectrometry". In: *Physical Chemistry Chemical Physics* 24.35 (2022), pp. 20776–20787.

[223] Chuan Cheng, Leszek J Frasinski, Gönenç Moğol, Felix Allum, Andrew J Howard, Daniel Rolles, Philip H Bucksbaum, Mark Brouard, Ruaridh Forbes, and Thomas Weinacht. "Multiparticle Cumulant Mapping for Coulomb Explosion Imaging". In: *Physical Review Letters* 130.9 (2023), p. 093001.